ROYAUME DU MAROC
Université Mohammed V جامعة محمد الخامس
- RABAT - - الرباط -
Faculté des sciences
كلية العلوم

CENTRE D'ÉTUDES DOCTORALES - SCIENCES ET TECHNOLOGIES

N° d'ordre : 3898

THÈSE

en vue de l'obtention du : **DOCTORAT**

Centre de Recherche : Sciences et technologies
Structure de Recherche : Équipe de Science de la Matière et du Rayonnement
Discipline : Physique
Spécialité : Physique des hautes énergies

Présentée et Soutenue le : 24 / 02 / 2024

par :

Hajar BELMAHI

Thermodynamic and Optical Behaviors of Black Hole

Devant le JURY :

Yassine HASSOUNI	PES	Université Mohammed V, Faculté des sciences, Rabat	Président
Morad EL BAZ	PES	Université Mohammed V, Faculté des sciences, Rabat	Examinateur/Rapporteur
Youssef KHOULAKI	PH	Université Hassan II , Faculté des sciences Aïn chock , Casablanca	Examinateur/Rapporteur
Alaaeddine LAHBAS	PH	Université Mohammed V, Faculté des sciences, Rabat	Examinateur/Rapporteur
Carlos A.R. HERDEIRO	PES	Universidade de Aveiro, Portugal.	Examinateur
Moulay BRAHIM SEDRA	PES	Université Ibn Tofail, Faculté des sciences, Kénitra	Examinateur
Hasan EL MOUMNI	PH	Université Ibn Zohr, Faculté des sciences, Agadir	Examinateur
Adil BELHAJ	PH	Université Mohammed V, Faculté des sciences, Rabat	Directeur de thèse

Année Universitaire : 2023 - 24

✉ Faculté des Sciences, avenue Ibn Battouta, BP. 1014 RP, Rabat –Maroc
☎ 00212 (05) 37 77 18 76 🖷 00212(05) 37 77 42 61; http://www. fsr.um5.ac.ma

To my beloved family

Acknowledgments

*This thesis was carried out within the **ESMaR** (Équipe de Science de la Matière et du Rayonnement) laboratory. I want to thank all the professors and the staff members for their remarkable contributions in creating an exceptional research setting.*

*I would like to express my gratitude formost to my supervisor **Mr. Adil BELHAJ**, professor PH at the faculty of sciences, Mohammed V University in Rabat, for his support throughout my research journey. I wholeheartedly consider professor BELHAJ as my scientific father. I am profoundly grateful for his wisdom and invaluable lessons he has imparted, shaping not only my research endeavors but also my growth as a scholar.*

*My thanks also go to **Mr. Yassine Hassouni** , professor PES at the faculty of sciences, Mohammed V University in Rabat for honoring me with his presence as the president of the jury for my doctoral defense. Additionally, I would like to convey my gratitude for his kindness and benevolence towards me.*

*I express my sincere gratitude to **Mr. Morad El BAZ**, professor PES at the faculty of sciences of Mohammed V University in Rabat, for accepting to review and report the content of my doctoral thesis. I extend my heartfelt thanks to him for his remarkable personal qualities, kindness, and for being a source of a positive energy in the laboratory.*

*I also want to express my gratitude to **Mr. Alaaeddine LAHBAS**, professor PH at the faculty of sciences of Mohammed V University in Rabat, for kindly agreeing to review and report my doctoral thesis.*

*I also want to express my gratitude to **Mr. Youssef KHOULAKI**, professor at the faculty of sciences Aïn Chock of Hassan II University in Casablanca, for kindly agreeing to review and report my doctoral thesis.*

*I would like to express my sincere gratitude to **Mr. Carlos A.R. HERDEIRO**, professor PES, from the Universidade de Aveiro, Portugal, for graciously accepting to participate as an examiner for my thesis. I deeply appreciate his willingness to travel and provide valuable assistance.*

I extend my sincere thanks to ***Mr. Moulay Brahim SEDRA****, professor PES at the faculty of sciences of Ibn Tofail University, for the honor he bestowed upon me by accepting to be an examiner for this thesis and for the interest he has shown in my work.*

I extend also my particular thanks to ***Mr. Hasan El MOUMNI****, PH professor at the faculty of sciences of Ibn Zohr University in Agadir, for accepting to examine this thesis. I want to thank him immensely for his assistance and availability.*

I want to extend my warmest gratitude to all the guests who attended my thesis defense. Your presence added significant value to this important academic milestone. Thank you for sharing in this academic achievement.

This thesis is the result of fruitful collaborations. Therefore, I would like to express my gratitude to all the ***collaborators****, whether at the national or international level. I thank them for their valuable contributions and countless discussions.*

Abstract

Motivated by recent Event Horizon Telescope collaborations findings, we investigate the thermodynamics and the optics of black holes in different gravity models including higher energy physics theories. Precisely, we mainly study two relevant optical concepts being the shadow and the deflection angle of various regular and non regular black holes. Using the Hamilton-Jacobi algorithm, we find certain shadow geometries of certain black holes being corroborated by observational data. Furthermore, we discuss the deflection angle of light rays near to black holes in several gravity theories with AdS space-time geometries. Concretely, we compute and analyze such an optical quantity for certain models inspired by M-theory using brane physics. Finally, we establish a bridging scenario between the thermodynamics and the optics of AdS black holes by the means of thermal variations of the deflection angle. Interestingly, we show that the black hole thermodynamics can be approached from the deflection angle formalism. Such thermal behaviors have been also implemented in shadows of black holes in cavity systems. Precisely, we find similarities with thermodynamical properties.

Keywords: Black holes, Regular black holes, AdS space-time, phase transition, geothermodynamic, shadows, deflection angle, M-theory, SBR gravity.

Résumé

Motivés par les récentes découvertes de la collaboration Event Horizon Telescope, nous étudions la thermodynamique et l'optique des trous noirs dans différents modèles de gravité, y compris les théories de physique des hautes énergies. Plus précisément, nous étudions principalement deux concepts optiques pertinents, à savoir l'ombre et l'angle de déviation de divers trous noirs réguliers et non réguliers. En utilisant l'algorithme Hamilton-Jacobi, nous trouvons certaines géométries d'ombre de certains trous noirs qui sont corroborées par les données d'observation. En outre, nous discutons l'angle de déviation des rayons lumineux près des trous noirs dans plusieurs théories de la gravité dans l'espace-temps de type AdS. En particulier, nous calculons et analysons une telle quantité optique pour certains modèles inspirés de la théorie M utilisant la physique des branes. Enfin, nous établissons un lien entre la thermodynamique et l'optique des trous noirs AdS en utilisant une variation thermique de l'angle de déviation. En particulier, nous montrons que la thermodynamique des trous noirs peut être abordée en utilisant le formalisme de l'angle de déviation. Ces comportements thermiques ont également été mis en œuvre dans les ombres des trous noirs dans les systèmes de cavités. Précisément, nous trouvons des similarités avec les propriétés thermodynamiques.

Keywords: Trous noirs, espace-temps AdS, ombre, transition de phase, angle de déviation de la lumière, M thèorie.

Résumé détaillé

Les trous noirs dans les théories physiques non triviales sont considérés comme des sujets difficiles et intéressants qui ont reçu un intérêt remarquable. Ces objets sont d'énormes masses avec un champ gravitationnel si intense que même la lumière ne peut échapper à leur poussée une fois qu'ils traversent l'horizon des événements. L'étude de ces objets a permis de mieux comprendre les lois fondamentales de la physique, y compris la relativité générale et la mécanique quantique. Ils offrent également des informations sur la nature de l'univers et les phénomènes mystérieux qui se déroulent à l'intérieur [1–6]. En fait, le sujet des trous noirs est d'une grande importance, non seulement dans l'astrophysique, mais aussi dans les théories de la physique à haute énergie, y compris la théorie des cordes et des sujets connexes explorés pour unifier la relativité générale avec les physiques quantiques [7–18]. En général, l'enquête sur les trous noirs est développée à partir de l'examen de deux thèmes clés : la thermodynamique et l'optique.

La liaison inattendue entre les trous noirs et la thermodynamique a ouvert un nouveau domaine de recherche intrigant en physique du trou noir. En dépit d'être auparavant considérées comme des solutions exclusivement d'équations d'Einstein, les trous noirs ont montré avoir des caractéristiques thermodynamiques intéressantes qui défient notre compréhension de la nature fondamentale de l'univers. Ce changement de paradigme est rendu possible par le théorème de la zone de Hawking. Hawking a pu non seulement confirmer la conjecture de Bekenstein en établissant une relation thermodynamique entre l'énergie, la température et l'entropie, mais aussi démontrer que la superficie d'un trou noir ne peut que diminuer avec le temps. Cela apporte un aspect thermodynamique à ces objets astronomiques énigmatiques.

Dans cette perspective raffinée, la constante cosmologique dans le contexte des géométries anti-de Sitter (AdS) prend une nouvelle interprétation. Elle devient une pression thermodynamique et sa variable conjuguée est interprétée comme le volume thermodynamique. Cette conceptualisation novatrice a approfondi notre compréhension de l'interaction complexe entre la gravité et la physique quantique. La thermodynamique des trous noirs est devenue un domaine riche, offrant des aperçus profonds sur la nature de l'espace-temps, le comportement de la matière dans ses conditions les plus extrêmes en étudiant la structure de phase et la stabilité des trous noirs intégrés dans différentes théories [23–25]. Hawking et Page (HP) ont fourni une preuve théorique de l'existence de certaines transitions dans

l'espace des phases des trous noirs de Schwarzschild-AdS (SH-AdS), qui sont des solutions non rotatives et non chargées [26]. Dans ce contexte, une transition de phase du premier ordre dans le trou noir de Reissner-Nordström-AdS (RN-AdS) chargé (non rotatif) entre les phases de trou noir massif (LBH) et les phases de trou noir petit (SBH) a été étudiée. Cette étude a été étendue pour inclure d'autres notions thermodynamiques [27–34]. En particulier, les comportements critiques des trous noirs dans les milieux AdS ont été largement étudiés en relation avec divers sujets, y compris la physique sombre. Soutenus par la conjecture AdS/CFT, de tels comportements ont été étudiés dans des dimensions arbitraires en considérant certains modèles de physique des hautes énergies, y compris la théorie des cordes et la M-théorie à l'aide d'objets solitoniques. En utilisant la physique des branes, plusieurs modèles dans les supercordes de type IIB et la M-théorie ont été étudiés, en tenant compte du fait que la constante cosmologique est liée au nombre de branes. Le comportement de stabilité thermodynamique de ces trous noirs AdS dans les théories de la supergravité avec d dimensions a été dérivé [35–40].

Une inspection approfondie montre que cette étude thermodynamique a fourni de belles universalités dans la physique des trous noirs AdS [41–45]. En particulier, le comportement critique des trous noirs AdS chargés dans des dimensions arbitraires a été lié à un nombre universel dépendant uniquement de la dimension des trous noirs [46]. Ce nombre prend le rapport critique du fluide de Van der Waals pour les trous noirs RN-AdS à quatre dimensions. De plus, il a été prouvé qu'au point de transition de phase HP, deux constantes universelles peuvent être obtenues [47].

Encouragés par les découvertes observationnelles, y compris la détection des ondes gravitationnelles, cela a fourni une forte preuve de l'existence des trous noirs [48, 49]. De telles observations intéressantes sont soutenues par les images de trous noirs développées par le groupe de collaboration de l'Event Horizon Telescope (EHT). En avril 2019, cette collaboration a réalisé une avancée majeure en publiant la première image directe d'un trou noir situé au centre de la galaxie M87, confirmant la forme prédite par la théorie générale de la relativité [50–52]. Par la suite, l'EHT a présenté une autre image associée à un trou noir supermassif Sgr $A*$ [53–57]. En 2022, l'équipe de l'EHT a fourni des images de l'ombre de ce trou noir, offrant des informations précieuses sur la taille, la masse et la rotation du trou noir.

Motivés par de telles données observationnelles, l'aspect optique de divers trous noirs a été largement étudié à l'aide de différentes méthodes analytiques et numériques. Une inspection approfondie révèle que deux notions optiques pertinentes ont été explorées : l'ombre et l'angle de déviation des rayons lumineux près des trous noirs. Le concept d'ombre a été étudié en utilisant le formalisme Hamilton-Jacobi dans différents modèles de gravité [58–66]. Ainsi, les équations du mouvement de particules sans masse près de plusieurs trous noirs ont été trouvées et largement examinées en utilisant des géométries réelles algébriques. Dans quatre dimensions, par exemple, les ombres ont été étudiées en utilisant des courbes réelles unidimensionnelles avec différentes configurations géométriques [67–70]. Il a été démontré que la taille et la forme de telles courbes dépendent de l'espace des paramètres du trou noir. Concrètement, les ombres des trous noirs non rotatifs sont des cercles parfaits dont la taille peut être contrôlée par certains paramètres tels que la charge. Le paramètre de rotation, cependant, déforme de telles géométries, produisant des configurations non triviales connues sous le nom de formes en D ou de cardioïdes [71–77]. En effet, les formes en cardioïde sont apparues pour les trous noirs rotatifs dans la superstring de type IIB et la M-théorie. Il a été démontré que les ombres des trous noirs à 5 dimensions intégrées dans les géométries de superstring de type IIB présentent une apparence en D pour de faibles valeurs du nombre de branes D3 et transitent vers des formes en cardioïde pour des valeurs élevées [78–80]. Pour les ombres de trous noirs super-entropiques en dimensions arbitraires, cette transition géométrique a été étudiée et illustrée de manière élégante. Il a été prouvé que les ombres subissent certaines transitions géométriques en fonction de la dimension de l'espace-temps [81–83].

En parallèle, l'angle de déviation des rayons lumineux près des trous noirs a également été étudié. Cet angle peut fournir des informations intéressantes pouvant imposer des contraintes physiques sur les modèles de gravité dans lesquels les trous noirs peuvent être formés. De nombreux travaux sur une telle quantité optique ont été élaborés en utilisant différentes méthodes de calcul [84–91]. Plus concrètement, Gibbons et Werner ont proposé une méthode directe pour calculer un tel angle de déviation au moyen du théorème de Gauss-Bonnet [92–97]. Cette approche repose sur une métrique optique où l'angle est perçu comme un effet partiellement topologique qui peut être calculé en utilisant la courbure gaussienne de la métrique optique et en utilisant les approximations de faible déviation. Alternativement, en supprimant les hypothèses faibles, les trous noirs pourraient fortement courber les rayons lumineux et l'angle dépasserait [98–100]. Le lentillage gravitationnel est approximé par des limites de déviation forte. Dans ce cas, d'autres méthodes ont été utilisées, y compris le formalisme des intégrales elliptiques combiné avec les équations du mouvement. Plus précisément, des fonctions elliptiques complètes et incomplètes ont également été utilisées pour exprimer l'angle de déviation. Concrètement, une solution explicite a été fournie en termes de formes fonctionnelles elliptiques de Weierstrass pour divers trous noirs [101]. Cet angle a été largement utilisé pour dériver des images relativistes, leurs amplifications et les courbes critiques associées.

L'objectif central de ce travail de doctorat est d'investiguer certaines propriétés physiques des trous noirs avec des géométries AdS. Nous nous concentrons d'abord sur l'aspect de l'ombre, fournissant des prédictions pouvant être analysées à l'aide du mécanisme de falsification. En exploitant le formalisme Hamilton-Jacobi, nous obtenons diverses configurations géométriques des ombres de trous noirs. Plus précisément, nous abordons les trous noirs réguliers et irréguliers. Motivés par des théories physiques à haute énergie, nous étudions les ombres de trous noirs dans la gravité Starobinsky-Bel-Robinson (SBR) en introduisant un paramètre stringy. Nos résultats démontrent que ce paramètre peut modifier les résultats antérieurs et peut également affecter les valeurs de l'angle de déviation des rayons lumineux près de tels trous noirs. Le présent travail de doctorat révèle des géométries d'ombre diverses, s'alignant avec les données de la collaboration EHT grâce à des contraintes imposées sur les paramètres des trous noirs impliqués. De plus, nous étudions les comportements lumineux près des trous noirs AdS. Plus précisément, nous calculons et analysons l'angle de déviation des rayons lumineux près de divers trous noirs dans différents modèles, y compris ceux liés à la physique des hautes énergies. Pour les trous noirs AdS, nous calculons cette quantité optique pour les trous noirs réguliers et non réguliers, en considérant la présence ou l'absence de secteurs d'énergie sombre. Des discussions graphiques sont fournies en faisant varier les paramètres pertinents des trous noirs. En particulier, nous élargissons nos études pour couvrir des trous noirs de dimensions supérieures. Nous calculons l'angle de déviation des rayons lumineux près des trous noirs AdS à quatre et sept dimensions, dérivés des compactifications de la M-théorie. Par conséquent, nous dévoilons l'impact du nombre de branes M couplé au paramètre de rotation sur ces angles. Dans la dernière partie de notre travail, nous établiss ons une connexion entre la thermodynamique et l'optique par le calcul de l'angle de déviation. Spécifiquement, nous montrons que les comportements thermodynamiques des trous noirs AdS peuvent être obtenus à partir du formalisme de l'angle de déviation. Nous dérivons la structure de phase et les comportements de stabilité des trous noirs AdS chargés via la variation thermique de l'angle de déviation. De plus, nous explorons la transition HP à travers des variations de comportements optiques. Enfin, nous étendons ces comportements thermiques aux activités d'ombre en considérant des trous noirs dans la cavité. Concrètement, nous montrons certaines similitudes avec les comportements de transition des trous noirs.

Cette thèse est divisée en deux parties. La première partie concerne les chapitres développés, tandis que la dernière expose nos contributions scientifiques. Dans le premier chapitre, nous fournissons un aperçu concis des trous noirs dans le cadre de la relativité générale. Ensuite, nous explorons des solutions de trous noirs pertinentes pour cette thèse.

Le chapitre deux est consacré à l'étude thermodynamique des trous noirs AdS. Nous présentons la structure de phase et la stabilité de tels trous noirs, élucidant les divers comportements thermodynamiques que les trous noirs AdS peuvent présenter, y compris les transitions de phase et les comportements critiques. De plus, nous introduisons certaines quantités universelles intéressantes liées à ces aspects. Ensuite, nous présentons une étude alternative des comportements thermodynamiques en examinant la courbure de l'espace géométrique des coordonnées thermodynamiques.

Le chapitre 3 se consacre à l'investigation optique. Nous élaborons d'abord les formalismes d'ombre des trous noirs rotatifs et non rotatifs. Ensuite, nous étudions les comportements optiques des trous noirs réguliers Bardeen-AdS en examinant les ombres correspondantes à l'aide de courbes réelles unidimensionnelles dépendant de la charge de l'électrodynamique non linéaire et de la présence des secteurs d'énergie sombre. De plus, nous effectuons un examen et une analyse de l'angle de déviation pour les trous noirs AdS réguliers et non réguliers, accompagnés d'une discussion comparative. Notamment, nous discutons également des comportements optiques des trous noirs dérivés de la compactification de la M-théorie.

Dans le chapitre 4, nous construisons d'abord un magnifique scénario de pont entre l'aspect thermodynamique et l'aspect optique par l'intermédiaire de la variation thermique de l'angle de déviation. Nous présentons également la transition de phase et la géothermodynamique des trous noirs AdS en termes de variations de l'angle de déviation. Nous étendons cette approche en étudiant également la variation thermique de l'ombre des trous noirs dans des systèmes de cavité.

Dans la deuxième partie, nous présentons nos contributions scientifiques publiées dans des revues internationales. Plus précisément, nous fournissons l'essence de chaque travail suivi de la version publiée. Nous terminons ce travail de doctorat par une conclusion générale et des perspectives.

List of publications

Main articles

- A. Belhaj, H. Belmahi, M. Benali and A. Segui, *Thermodynamics of AdS black holes from deflection angle formalism*, Phys. Lett. B **817**, 136313 (2021).
- A. Belhaj, H. Belmahi and M. Benali, *Deflection light behaviors by AdS black holes*, Gen. Rel. Grav. **54**, no.1, 4 (2022).
- A. Belhaj, H. Belmahi, M. Benali, H. El Moumni, M. A. Essebani and M. B. Sedra, *Optical shadows of rotating Bardeen-AdS black holes*, Mod. Phys. Lett. A **37**, no.06, 2250032 (2022).
- A. Belhaj, H. Belmahi, M. Benali and H. Moumni El, *Light deflection by rotating regular black holes with a cosmological constant*, Chin. J. Phys. **80**, 229-238 (2022)
- A. Belhaj, H. Belmahi, M. Benali, Y. Hassouni and M. B. Sedra, *Optical behaviors of black holes in Starobinsky–Bel–Robinson gravity*, Gen. Rel. Grav. **55**, no.10, 110 (2023).
- A. Belhaj, H. Belmahi, M. Benali, M. Oualaid and M. B. Sedra, *Light trajectories and thermal shadows casted by black holes in a cavity*, JCAP 11, 094 (2023).
- N. Askour, A. Belhaj, H. Belmahi, M. Benali, H. El Moumni and Y. Sekhmani, *Deflection angle and light ray trajectories near M-theory black holes*, IJGMMP, 191 (2023).

Collaborative articles

- A. Belhaj, H. Belmahi and M. Benali, Superentropic AdS black hole shadows, Phys. Lett. B **821**, 136619 (2021).
- A. Belhaj, H. Belmahi, M. Benali, W. El Hadri, H. El Moumni and E. Torrente-Lujan, *Shadows of 5D black holes from string theory*, Phys. Lett. B **812** 136025, (2021).
- A. Belhaj, H. Belmahi, M. Benali and H. El Moumni, *Light deflection angle by superentropic black holes*, Int. J. Mod. Phys. D **31**, 07 (2022).

List of Figures

Contents

Introduction

Black holes in non trivial physical theories are considered as challenging and interesting subjects that have received a remarkable interest. These objects are immensely massive with a gravitational field being so intense that not even light can escape their pull once they cross the event horizon. The study of such objects has provided a better comprehension of the fundamental laws of physics, including the general relativity and quantum mechanics. They also offer insights into the nature of the universe and the mysterious phenomena that take place within it [1–6]. Actually, the subject of black holes is of great importance, not only in astrophysics, but also in high energy physics theories including string theory and related topics explored to unify general relativity with quantum physics [7–18]. In general, the investigation of black holes is developed from the consideration of two key topics: thermodynamics and optics.

The unexpected link between the black holes and the thermodynamics has opened up an intriguing new field of research in black hole physics. Despite being previously thought to be exclusively Einstein equation solutions, the black holes have been shown to have interesting thermodynamic features that challenge our understanding of the fundamental nature of the universe. This paradigm change is made possible by the pivotal Hawking area theorem. Hawking was able to confirm the Bekenstein conjecture by establishing a thermodynamic relationship between energy [19–22]. This brings a thermodynamic aspect to these enigmatic astronomical objects.

In this refined viewpoint, the cosmological constant in the context of the anti de Sitter

(AdS) geometries takes a new interpretation. It can be interpreted as a thermodynamic pressure and its conjugate variable interpreted as the thermodynamic volume. This novel conceptualization has deepened our understanding of the intricate interplay between gravity and quantum physics. Black hole thermodynamics has become a rich field, providing profound insights into the nature of spacetime, the behavior of matter at its most extreme by studying the phase structure and stability of black holes embedded in different theories [23–25]. Concretely, Hawking and Page (HP) have provided a theoretical evidence for the existence of certain transitions in the phase space of the Schwarzschild-AdS (SH-AdS) black holes, being non-rotating and uncharged solutions [26]. In this respect, a first-order phase transition in the charged (non-rotating) Reissner Nordstrom-AdS (RN-AdS) black hole between large black hole (LBH) phases and small black hole (SBH) phases has been investigated. This study has been expanded to include additional thermodynamic notions [27–34]. Particularly, the criticality behaviors of the black holes in AdS backgrounds have been extensively investigated in connections with various topics including the dark physics. Supported by AdS/CFT conjecture, such behaviors have been studied in arbitrary dimensions by considering certain high energy physics models including string theory and M-theory by means of solitonic objects. Using brane physics, several models in type IIB superstrings and M-theory have been studied, taking into account that the cosmological constant is related to the number of branes. The thermodynamic stability behavior of such AdS black holes in supergravity theories with d dimensions has been derived [35–40].

A close inspection shows that this thermodynamical study has provided beautiful universalities in AdS black hole physics [41–45]. Particularly, the critical behavior of charged AdS black holes in arbitrary dimensions has been linked to an universal number depending only on the dimension of the black holes [46]. This number takes the critical ratio of the Van der Walls fluid for four dimensional RN-AdS black holes. Moreover, it has been proved that at the HP phase transition point, two universal constants can be obtained [47].

Encouraged by observational findings, including the detection of the gravitational waves, it has been provided a strong evidence of the black hole existence [48, 49]. Such interesting observations are supported by the images of black holes developed by Event Horizon Telescope (EHT) collaboration groups. In April 2019, this collaboration made a groundbreaking achievement by releasing the first-ever direct image of a black hole located at the center of the galaxy M87, confirming the shape predicted by the general theory of relativity [50–52]. Subsequently, the EHT presented another image associated with a supermassive black Sgr

A$*$ [53–57]. In 2022, the EHT team provided images of the shadow of this black hole, offering valuable information about the size, the mass, and the rotation of the black hole. This image could provide data on the black holes shape.

Motivated by such observational data, the optical aspect of various black holes has been largely studied using different analytical and numerical methods. A close inspection, in such activities, reveals that two relevant optical notions have been investigated: the shadow and the deflection angle of the light rays near to black holes. The shadow concept has been investigated by using the Hamilton-Jacobi formalism in different gravity models [58–66]. In this way, the equations of motion of massless particles near to several black holes have been found and largely examined using algebraic real geometries. In four dimensions, for instance, the shadows have been studied using one-dimensional real curves with different geometrical configurations [67–70]. It has been shown that the size and the shape of such curves depend on the black hole parameter space. Concretely, the shadows of the non-rotating black holes are perfect circles where the size could be controlled by certain parameters such as the charge. The rotating parameter, however, deforms such geometries producing non-trivial configurations known as D or cardioid shapes [71–77]. Effectively, the cardioid shapes have been appeared for rotating black holes in type IIB superstring and M-theory. It has been shown that the shadows of 5D black holes embedded in type IIB superstring geometries exhibit a D-appearance for small values of the D3- brane number and transition to cardioid shapes for large values [78–80]. For superentropic black hole shadows in arbitrary dimensions, this shadow geometry transition has been studied and illustrated in beautiful manner. It has been proved that the shadows undergo certain geometric transitions depending on the space-time dimension [81–83].

In parallel studies, the deflection angle of light rays near to black holes has been also investigated. This angle could provide interesting information which may impose physical constraints on gravity models in which black holes can be built. Many works on such an optical quantity have been elaborated using different computation methods [84–91]. Concretely, Gibbons and Werner have proposed a direct method to calculate such a deflection angle by means of the Gauss-Bonnet theorem [92–97]. This approach relies on an optical space metric where the angle is perceived as a partially topological effect that can be calculated by utilizing the Gaussian curvature of the optical metric and employing the weak deflection approximations. Alternatively, removing the weak assumptions, the black holes could strongly bend light rays and the angle exceeds π [98–100]. The gravitational lensing is approximated by strong deflection limits. In this case, other methods have been used including the elliptic integral formalism combined with equations of motion. Specifically, complete and incomplete elliptic functions have also been utilized to express the deflection angle. Concretely, an explicit solution has been provided in terms of Weierstrass elliptic functional forms for various black holes [101]. This angle has been extensively employed in deriving relativistic images, their amplifications, and the associated critical curves.

The central aim of this doctoral work is to investigate certain physical proprieties of black holes with different gravity backgrounds including the AdS geometries and M-theory inspired models. We focus first on the shadow aspect, providing predictions that can be analyzed using the falsification mechanism. Exploiting the Hamilton-Jacobi formalism, we obtain various geometrical configurations of the black hole shadows. More precisely, we approach regular and irregular black holes. Motivated by high-energy physical theories, we investigate the shadows of black holes in Starobinsky-Bel-Robinson (SBR) gravity by introducing a stringy parameter. Our findings demonstrate that this parameter can modify previous results and it can also affect the deflection angle values of the light rays near to such black holes. The present doctoral work reveals diverse shadow geometries, aligning with EHT collaboration data through imposed constraints on the involved black hole parameters. Additionally, we study light behaviors near to AdS black holes. Specifically, we compute and analyze the deflection angle of light rays near various black holes in different models, including those related to high-energy physics. For AdS black holes, we calculate this optical quantity for both regular and non-regular black holes, considering the presence or the absence of dark energy sectors. Graphical discussions are provided by varying relevant black hole parameters. In particular, we enlarge our studies to cover higher-dimensional black holes. We calculate the deflection angle of light rays near to four and seven-dimensional AdS black holes, derived from M-theory compactifications. Consequently, we unveil the impact of the M-brane number coupled with the rotating parameter on these angles. In the final part of our work, we establish a connection between thermodynamics and optics through the computation of the deflection angle. Specifically, we show that the thermodynamic behaviors of AdS black holes can be obtained from the deflection angle formalism. We derive the phase structure and the stability behaviors of charged AdS black holes via the thermal variation of the deflection angle. Furthermore, we explore the HP transition through variations in optical behaviors. Finally, we extend these thermal behaviors to shadow activities by considering black holes in the cavity. Concretely, we show certain similarities with black hole transition behaviors.

This thesis is divided into two parts. The first part concerns the developed chapters, while the last one exposes our scientific contributions. In the first chapter, we provide a concise overview of the black holes within the framework of general relativity. Then, we explore pertinent black hole solutions that are relevant in this dissertation.

The chapter two is devoted to the thermodynamic study of AdS black holes. Precisely, we present the phase structure and the stability of such black holes, elucidating the diverse thermodynamic behaviors that AdS black holes can exhibit, including the phase transitions and the criticality behaviors. Additionally, we introduce some interesting universal quantities linked to these aspects. Subsequently, we present an alternative study of thermodynamic behaviors by examining the curvature of the geometrical space of thermodynamic coordinates.

The chapter 3 exposes to the optical investigation. We elaborate first the shadow formalisms of rotating and non rotating black holes. Then, we study the optical behaviors of the regular Bardeen-AdS black holes by examining the corresponding shadows using one dimensional real curves that depend on the charge of the nonlinear electrodynamics and the presence of the dark energy sectors. In addition, we perform an examination and analyse of the deflection angle for both regular and non-regular AdS black holes, accompanied by a comparative discussion. Notably, we discuss optical behaviors of black holes derived from the M-theory compactification. In the chapter 4, we first construct a beautiful bridging scenario between the thermodynamic aspect and the optical one by the intermediation of the thermal variation of the deflection angle. We present also the phase transition and geothermodynamics of the AdS black holes in terms of the deflection angle variations. We extend this approach by studying the shadow thermal variation of black holes in cavity systems.

In the second part, we present our scientific contributions published in international journals. Specifically, we provide the published version. We finish this doctoral work with a general conclusion and perspectives.

First part

Synthesis of thermodynamic and optical properties of black holes

CHAPTER 1

Black Hole Physics

In the infinite tapestry of the cosmos, few phenomena capture the imagination and the curiosity of humanity as profoundly as black holes. These enigmatic cosmic entities stand as testaments to the astonishing interplay between astrophysics and Einstein theory of general relativity. In this chapter, we explore the heart of darkness, where the gravitational pull is so intense that not even light can escape, a realm where the very fabric of space and time contorts into a cosmic abyss. Firstly, we introduce the black holes as astrophysical objects. Then, we present a concise review of general relativity formalism and black hole solutions that are of interest for this dissertation.

1.1 Black holes in astrophysics

1.1.1 Generalities on black holes

The structure of the Universe is controlled and shaped by a fundamental force being the gravitational force. This gravitational pull of any celestial body affects all objects located in its gravitational field. To escape this gravitational pull, the object should overcome the gravitational attraction and achieve a kinetic energy bigger then the gravitational potential energy [1–7]. Indeed, an escaped velocity is required. This velocity can be calculated using the following formula

$$V_{escp} = \sqrt{\frac{2GM}{R}}, \tag{1.1}$$

where G is the gravitational constant, M is the celestial object mass and R is the distance between the object and the center of the celestial body. A black hole is an extraordinary astronomical object with an incredibly strong gravitational field. Its gravitational force is so intense that the escape velocity surpasses the light speed. This means that beyond a certain critical boundary, known as the event horizon, nothing, not even light, can escape. The event horizon marks the point of no return, where any object or information that crosses it is forever trapped within the black hole, hidden from the external Universe [1–7]. Using the newtonian physics, this critical radius for an object of mass M is given by

$$R_s = \frac{2GM}{c^2}. \tag{1.2}$$

It is evident from Eq.(1.1) that a colossal mass must be compressed into an incredibly small volume to form a black hole. This process involves a tremendous concentration of the mass within a minuscule region. This central region is referred to the singularity being a region of infinite density. One of the most well-known processes that can create a black hole is the gravitational collapse of a massive star.

Throughout its life, a star is in equilibrium between two forces. The first force arises from the fusion reactions in its core, generating outward pressure that fuels its brightness and counteracts gravitational collapse. The second force is the relentless pull of gravity, attempting to compress the star under the immense weight of its own mass [9]. As the star reaches the end of its life and depletes its fuel, the balance between the fusion and the gravity is disturbed. With the loss of the energy sustaining its core, the gravity gains the upper hand, causing the core to rapidly contract. This gravitational collapse releases an immense amount of energy, leading to a huge explosion known as a supernova. During the supernova, the outer layers of star are expelled into space, leaving behind a core. If the mass of the core exceeds a critical value, the core continues to collapse and becomes increasingly compact. That it crosses the event horizon radius and a black hole is born [5, 9]. There are other proposed mechanisms for the formation of black holes including the primordial density fluctuations and high energy collisions (LHC) [10]. While the Large Hadron Collider (LHC) and other particle accelerators are primarily designed to study particle physics, there have been speculations about the potential formation of microscopic black holes during high-energy collisions.

As mass is the main parameter characterizing black holes, these objects are classified according to this parameter into four categories. The first one corresponding to stellar-Mass black holes. Their masses are ranged from a few to tens times that of the sun and they are observed as part of binary systems. They emit X-rays when they gather matter from a companion star. The second category conserns intermediate-mass black holes. The mass here can vary from hundreds to tens of thousands of solar mass. These black holes have been hypothesized to exist in dense stellar environments like globular clusters, as well as at the centers of dwarf galaxies. The third one is the supermassive black holes. They have masses ranging from millions to billions times that of the sun. they are commonly found at the centers of galaxies. The last one is a hypothetical class knowing as primordial black holes. They could have a wide range of masses. There existence linked to the extreme conditions of the early universe. Furthermore, primordial black holes have been proposed as potential contributors to the enigmatic dark matter [10]. Each type of the black holes has different processes of formation, and some aspects of their formation are still not fully understood [5, 9].

1.1.2 Black hole effects

Black holes have a profound impact on surrounding matter due to their intense gravitational pull [4,5,9]. Here, we provide the manifestations of the main effects of black holes on matter:

- **Accretion Disks:** The accretion disk forms when a black hole accretes matter from stars, gas or dust. This disc of gas and dust swirls rapidly around the black hole at extremely high speeds. It is overheated by the friction and the collisions between the particles of matter, giving it a very high temperature. As a result of this overheating, the accretion disk emits the electromagnetic radiation at different wavelengths, including X-rays, infrared and radio waves. This radiation is a distinctive feature of accretion disks and allows astronomers to detect and locate the presence of a black hole.

- **Gravitational Lensing:** The powerful gravity of the black holes can bend and distort light from distant objects behind them, causing gravitational lensing. This phenomenon creates several images or arcs of the object in the background, providing astronomers with valuable information about both the black hole and the distant source.

- **Gravitational Wave Emission:** Black holes that are in binary systems or undergo mergers emit gravitational waves. These ripples in spacetime propagate through the Universe and can be detected by gravitational wave observatories like LIGO and Virgo. The study of gravitational waves from black hole mergers provides crucial insights into their properties and the extreme conditions of their environments.

- **Jets and Relativistic Outflows**: When a black hole accretes matter from stars, gas, or dust, it can produce jets of particles and high-speed radiation emissions. These jets and radiations generally emerge from the poles of the black hole. They can extend over considerable distances in the space-time. These relativistic speeds involve a remarkable feature of the jets emitted by supermassive black holes at the center of galaxies. Certain studies suggest that the jets could be composed of an electrically neutral mixture of nuclei, electrons, and positrons. Other hypotheses consider that the jets are mainly made up of the electron-positron plasmas.

- **Tidal Forces:** Tidal forces are gravitational forces that result from variations in the gravitational field of a celestial body due to its non-uniform mass. These forces are called "tidal forces" because they are analogous to the tidal forces observed on Earth due to the gravitational attraction of the Moon and the Sun. When an object passes close to a black hole, it undergoes tidal forces due to the intense gravitational attraction of the black hole. These tidal forces can stretch the object until it tears if they exceed the breaking strength of the object material.

Fig.(1.1) presents a visualization of the main characteristics of black holes.

1.1.3 Detection of black holes

The scenario of detecting and observing black holes is a fascinating and challenging task due to their unique property of absorbing even light. This characteristic makes them invisible to traditional telescopes that rely on detecting and capturing electromagnetic radiation. To overcome this challenge, astronomers have developed indirect methods and instruments for detection. Here, we present the key methods and the breakthroughs in the detection and observation of black holes that have provided strong evidence for their existence.

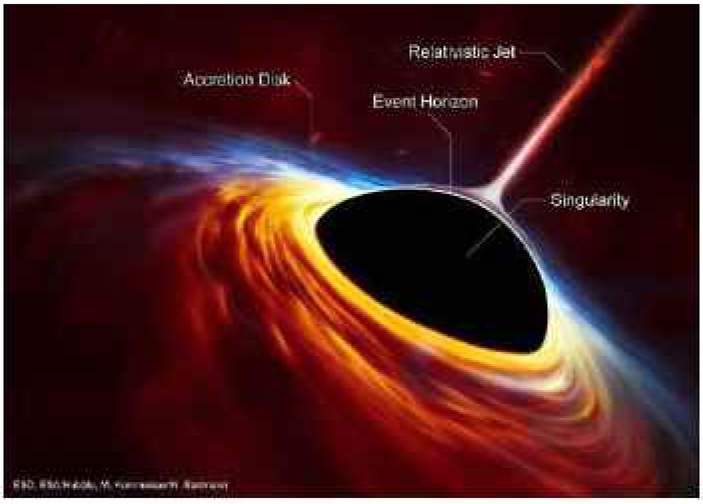

Figure 1.1: *Visualization of the main characteristics of black holes [11].*

LIGO and Virgo and gravitational wave detections

Virgo is a gravity detector built by France and Italy. It is an L-shaped interferometer with arms 3 km long. A laser beam is sent along each arm, and the reflected beams are recombined at the central point, called the beam splitter. When a gravitational wave passes through the Virgo detector, it causes a slight stretching and tightening of the space-time. This changes the lengths of the arms, causing the recombined laser beams to move relative to each other. The shifted laser beams create an interference pattern at the beam splitter. This pattern contains information about the passing gravitational wave, such as its frequency, amplitude, and polarization.

LIGO (Laser Interferometer Gravitational-Wave Observatory) is a collaborative project of two observatories. LIGO Livingston in Louisiana and LIGO Hanford in Washington State. LIGO has long arms (4 kilometers each) of L-shape to detect minute changes in the length of the arms caused by the passage of gravitational waves.

LIGO and Virgo both utilize a Michelson interferometer design. The most significant difference between them is their geographical locations. They have different operational schedules, allowing for continuous and longer observation periods. Additionally, LIGO contributes to slightly higher sensitivity compared to Virgo duo to is longer arm. However, both detectors are designed to be very sensitive to detect extremely minute changes in spacetime caused by gravitational waves. By combining the observations data from Virgo with LIGO detector, scientists can better pinpoint the location and characteristics of the sources of gravitational waves.

On 14 September 2015, the LIGO detectors picked up a signal that seemed compatible with the theoretical model of a gravitational wave signal. On December 26, 2015, the LIGO – Virgo Collaboration detectors captured another gravitational wave signal. This detection has removed the last doubts about the reality of this signal and its perfect fit with the theory of general relativity. This signal is called GW150914. It is produced when two black holes orbit each other in pairs. They slowly move towards each other, losing energy in the form of gravitational waves. This phenomenon eventually accelerates until they merge into a single black hole. During the final moments of the merger, an intense burst of gravitational waves is emitted, creating a distinctive signal that was detected [48, 49].

EHT and black hole observation

A direct image of the event horizon of a black hole would provide observational confirmation of the theory of general relativity. The initial aim of the international EHT collaboration was to achieve a technological and scientific feat by capturing an image of the event horizon of a black hole. An international collaboration between numerous observatories was essential to bring together the necessary resources and a combined data to form a global network of telescopes, enabling unprecedented resolution. The collaboration creates a virtual telescope with an aperture as large as the earth by applying the principle of very long baseline interferometry to eight telescopes placed in different specific locations. Fig.(1.2) represents the distribution of these telescopes on the earth.

Figure 1.2: *Location of the EHT collaboration telescope* [50, 51, 53].

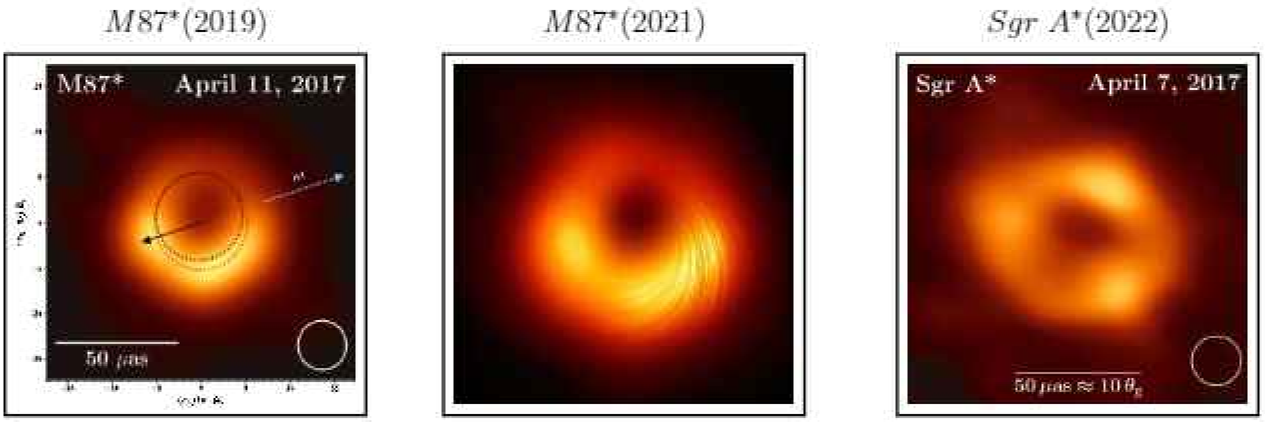
$M87^*$(2019) $M87^*$(2021) $Sgr\ A^*$(2022)

Figure 1.3: *Images of the supermassive black hole captured by the EHT.* [50, 52, 53, 55]

The signals collected by widely synchronized radio telescopes are combined to create a high-resolution imaging. This virtual observatory is capable of resolving features with an angular size of less than 20 micro-arc seconds. The data recorded by the telescopes are collected, calibrated, and then used to create images of the event horizon of the black hole. The collaboration focused mainly on imaging the supermassive black hole M87*, located at the center of the galaxy M87. This choice is based on the fact that this black hole is an active hole, meaning that it exhibits energetic phenomena at its core, likely due to the accretion of matter onto the black hole. This activity can produce observable emissions across the electromagnetic spectrum, including radio waves, which can be detected and studied. Its radiation is very intense and can be detected by telescopes. In addition, M87* is much more massive ($(6.5 \pm 0.7) \times 10^9$ of the solar mass). This means that the event horizon is much larger, offering a larger capture surface for observations. It is also located at a distance of around 55 million light-years from Earth. Despite this enormous distance, M87* appears relatively bright and is therefore accessible to detection. These make it an interesting target for observation. In April 2019, the first direct image of the event horizon of a black hole was captured. The image represents the shadow cast by the event horizon of M87*. As a result of continued observations and improved data analysis techniques, EHT had released a follow-up image of the supermassive black hole M87* in April 2021, which provided even higher resolution and greater clarity. In addition, the collaboration has revealed the first image of Sagittarius A*, the supermassive black hole at the center of the Milky Way in 2021. These images are represented in Fig.(1.3).

1.2 Black holes via general relativity

General relativity is a profound theory of gravity that revolutionized our understanding of space, time, and the nature of gravity. It was formulated by Albert Einstein in 1915 as a geometric theory of gravity, replacing Isaac Newton's classical theory of gravity. It remains a fundamental pillar of modern physics and higher energy physics. In this theory, gravity is not seen as a force between objects, but rather as the curvature of the space-time caused by mass and energy. According to that, objects with mass or energy distort the fabric of space time around them, creating what we perceive as gravity. This theory provides a framework for studying the large-scale structure of the Universe, the evolution of galaxies, the behavior of stars, the expansion of the Universe and the dynamics of objects in strong gravitational fields [2–4]. Additionally, it is crucial for accurate calculations in satellite navigation systems, global positioning systems, and the modelling of gravitational interactions in various astrophysical phenomena. One of the significant predictions of this theory is the existence of the black holes [1–6].

1.2.1 Theoretical backgrounds

The theory of general relativity is based on Riemannian geometry. This geometry provides the mathematical framework for describing the properties of curved space-times. The key idea of the Riemannian geometry is to consider properties of spaces that are invariant under continuous transformations [6, 7]. Curved spaces are not vector spaces, but physical quantities are often vectors and tensors. In this geometry, we can continue to use these notions, by denoting these quantities locally on tangent spaces. This has given rise to the concept of Riemannian variety, which is a generalization of Euclidean space. In a Riemannian variety, the distance between two points is denoted by a metric tensor. To understand tensor calculus, we first need to define some basic notions and concepts. The first one is the scalar. In the Riemannian geometry, a scalar S is a function that assigns a real or complex number to each point on a Riemannian manifold. Scalars are invariant under the coordinate transformations and do not depend on the choice of the basis or the coordinate system [6, 7]. If we consider the following coordinates transformation

$$x^{\mu} \to x'^{\mu}, \tag{1.3}$$

the scalar quantities should verify this equality

$$S'(x'^{\mu}) = S(x^{\mu}). \tag{1.4}$$

Alternatively, a vector at a particular point on a Riemannian manifold is an element of the tangent space. At that point, it can be thought of as infinitesimally small arrows attached to the manifold. Vectors are characterized by their components along a chosen basis or a coordinate system and transform as follows

$$V'^{\nu} = \frac{\partial x^{\nu}}{\partial x'^{\mu}} V^{\mu}. \tag{1.5}$$

The vector is considered as a tensor of rank (1, 0). It is recalled that the tensor is a mathematical object that generalizes scalars and vectors. The tensors represent geometric quantities that may have multiple indices, allowing them to encode complex relationships between vectors, such as measuring curvature or describing the metric structure of the manifold. The rank of a tensor determines the number of vectors or co-vectors needed to form the tensor. A tensor of rank $(0, 0)$ is a scalar, which is a single value that does not depend on any indices [4, 6, 7]. The basic tensor of the Riemannian manifold is the metric tensor which provides a way to measure distances, angles, and inner products on the manifold. The general expression for the metric tensor in curved spacetimes is given by the line element, or the metric equation. Typically, it is written as

$$ds^2 = g_{\mu\nu} dx^{\mu} dx^{\nu}. \tag{1.6}$$

ds^2 represents the space-time interval between two nearby events. dx^{μ} and dx^{ν} indicate infinitesimal displacements in each coordinate direction, where the value of indices represents the spacetime dimensions. The elements $g_{\mu\nu}$ are the components of the metric tensor, which can vary from a point to an other point in curved space-times.

To study the curvature of the space-time, we need to discus the concept of the derivative. In Riemannian geometry, this concept is typically divided into two types. Simple or ordinary derivative refers to the derivative of a function [6, 7]. The second one is the covariant derivative is the derivative operator that acts on tensors, such as vectors or more general tensor fields in a manner that takes into account the curvature of the manifold that characterized by a metric tensor. The covariant derivative is denoted as ∇ and is designed to preserve tensorial properties under coordinate transformations. This derivation can be expressed as follows

$$\nabla_\nu V^\mu = \partial_\nu V^\mu - \Gamma^\mu_{\nu\rho} V^\rho, \tag{1.7}$$

where ∂_ν is the partial ordinary derivation and $\Gamma^\mu_{\nu\rho}$ are the Christoffel symbols. These connection coefficients can be calculated from the metric of the given manifold as follows

$$\Gamma^\mu_{\nu\rho} = \frac{1}{2} g^{\mu\sigma} \left(\partial_\nu g_{\sigma\rho} + \partial_\rho g_{\nu\sigma} - \partial_\sigma g_{\nu\rho} \right). \tag{1.8}$$

For a contravariant vector, we have

$$\nabla_\nu V_\mu = \partial_\nu V_\mu + \Gamma^\rho_{\nu\mu} V_\rho. \tag{1.9}$$

The second covariant derivative, acting on a scalar S, is given by

$$\nabla_\mu \nabla_\nu S = \partial_\mu \partial_\nu S - \Gamma^\rho_{\mu\nu} \partial_\rho S = \nabla_\nu \nabla_\mu S. \tag{1.10}$$

It has the property of being symmetric under the index permutation because ordinary derivatives commute and the Christoffel symbol is symmetric [6, 7]. However, this property is not valid when the second derivative acts on a tensor of higher variance, such as a vector. In this case, we have

$$\left[\nabla_\mu \nabla_\nu - \nabla_\nu \nabla_\mu \right] V^\lambda = R^\lambda_{\sigma\mu\nu} V^\sigma, \tag{1.11}$$

where the tensor $R^\lambda_{\mu\sigma\nu}$ is written as

$$R^\lambda_{\mu\sigma\nu} = \partial_\sigma \Gamma^\lambda_{\mu\sigma} - \partial_\nu \Gamma^\lambda_{\mu\sigma} + \Gamma^\rho_{\mu\nu} \Gamma^\lambda_{\rho\sigma} - \Gamma^\rho_{\mu\sigma} \Gamma^\lambda_{\nu\rho}. \tag{1.12}$$

The covariant form of this tensor is given by

$$R_{\mu\nu\rho\sigma} = g_{\mu\tau} R^\tau_{\nu\rho\sigma}. \tag{1.13}$$

This tensor is named a Riemann curvature tensor or Riemann-Christoffel tensor. The Riemannian tensor arises when we try to measure how much a vector changes as we parallel transport it along different paths on the manifold. It is a mathematical object that encodes the curvature of a Riemannian manifold [3, 6, 7]. This tensor verifies the following properties

1. It is antisymmetric under the exchange of the first two or the last two indices

$$R_{\mu\nu\rho\sigma} = -R_{\nu\mu\rho\sigma} = -R_{\mu\nu\sigma\rho}.$$

2. It is symmetric under the exchange of the $\mu\nu$ and $\rho\sigma$ blocks:

$$R_{\mu\nu\rho\sigma} = R_{\rho\sigma\mu\nu}.$$

3. It also verifies the following cyclic identities

$$R_{\mu\nu\rho\sigma} = \frac{1}{2}(\partial_\sigma\partial_\mu g_{\nu\rho} - \partial_\sigma\partial_\nu g_{\mu\rho} + \partial_\rho\partial_\nu g_{\mu\sigma} - \partial_\rho\partial_\mu g_{\nu\sigma})$$

$$R_{\mu\sigma\nu\rho} = \frac{1}{2}(\partial_\rho\partial_\mu g_{\sigma\nu} - \partial_\rho\partial_\sigma g_{\mu\nu} + \partial_\nu\partial_\sigma g_{\mu\rho} - \partial_\nu\partial_\mu g_{\sigma\rho})$$

$$R_{\mu\sigma\rho\nu} = \frac{1}{2}(\partial_\nu\partial_\mu g_{\sigma\rho} - \partial_\nu\partial_\sigma g_{\mu\rho} + \partial_\rho\partial_\sigma g_{\mu\nu} - \partial_\rho\partial_\mu g_{\sigma\nu}),$$

which gives

$$R_{\mu\nu\rho\sigma} + R_{\mu\sigma\nu\rho} + R_{\mu\sigma\rho\nu} = 0. \tag{1.14}$$

In a locally inertial reference frame, the Christoffel symbols are zero and the covariant derivative of the Riemann tensor is written as

$$\nabla_\rho R_{\mu\nu\alpha\beta} = \frac{1}{2}\frac{\partial}{\partial x^\rho}\left(-\frac{\partial^2 g_{\mu\alpha}}{\partial x^\nu \partial x^\beta} + \frac{\partial^2 g_{\nu\alpha}}{\partial x^\nu \partial x^\beta} + \frac{\partial^2 g_{\mu\beta}}{\partial x^\nu \partial x^\alpha} - \frac{\partial^2 g_{\nu\beta}}{\partial x^\nu \partial x^\alpha}\right), \tag{1.15}$$

which proves that the tensor satisfies the Bianchi identity given by

$$\nabla_\lambda R^\mu_{\nu\rho\sigma} + \nabla_\rho R^\mu_{\nu\sigma\lambda} + \nabla_\sigma R^\mu_{\nu\lambda\rho} \equiv 0. \tag{1.16}$$

The Einstein tensor $G^{\mu\nu}$ is obtained by contracting the Bianchi identity [3,6]. This gives the Einstein identity

$$\nabla_\nu G^{\mu\nu} = \nabla_\nu \left(R^{\mu\nu} - \frac{1}{2}g^{\mu\nu}R\right) = 0, \tag{1.17}$$

where $R_{\mu\nu}$ is the Ricci curvature tensor of rank 2 obtained by contraction of the first and third index of the Riemann tensor

$$R_{\mu\nu} \equiv R^\alpha_{\mu\nu\alpha}. \tag{1.18}$$

R is the scalar curvature or the Ricci scalar. This scalar is defined as the trace of the Ricci tensor

$$R = R^{\alpha}_{\alpha} = g^{\mu\nu} R_{\mu\nu}. \tag{1.19}$$

The Einstein tensor $G_{\mu\nu}$ has several important properties. First, it is symmetric, meaning that one has $G_{\mu\nu} = G_{\nu\mu}$. This symmetry arises due to the symmetry of the Ricci curvature tensor. Second, it is divergence-free, which means that its covariant derivative vanishes. This property is a consequence of the contracted Bianchi identity [3,6,7]. This tensor considered as the only symmetric tensor that can be formed from the second derivatives of the tensor metric.

1.2.2 Equivalence principle and geodesic equations

The gravitational force has a fundamental property, known as the principle of equivalence, which distinguishes it from all the other forces of nature. This principle is based on the fact that the free-falling motion of bodies is universal, independent of their mass and composition. According to second law of motion of Newton, the force acting on an object is directly proportional to its acceleration and inversely proportional to its inertial mass [1,6,7]. Mathematically, this relationship is expressed as

$$\mathbf{F} = m_i \mathbf{a}. \tag{1.20}$$

On the other hand, a gravitational field $\mathbf{g}$ exerts on a body a gravitational force proportional to $\mathbf{g}$, where the coefficient is the gravitational mass. This law is given by

$$F_g = m_g \mathbf{g}. \tag{1.21}$$

An object placed in a gravitational field $\mathbf{g}$ acquires the acceleration

$$\mathbf{a} = \frac{m_i}{m_g} \mathbf{g}. \tag{1.22}$$

According to the theory of Newton, the mass ratio could vary from one object to another, just as the ratio of electric charge (q) to mass (m) varies in the electromagnetism. Therefore, the acceleration should be different for each object and depend primarily on the internal composition of the considered object. In fact, numerous experiments and observations have consistently confirmed the equivalence of gravitational mass and inertial mass, as stated by the Equivalence Principle. In other words, there is no local experiment that can distinguish between the gravitational force and the force experienced in an accelerating reference frame. Indeed, a uniform gravitational field is equivalent to an accelerated reference in a vacuum, with acceleration $\mathbf{a} = -\mathbf{g}$. In this context, the following principles can be stated.

- **Weak Equivalence Principle**: This principle establishes the equality of gravitational and inertial mass, stating that all objects fall with the same acceleration in a gravitational field. In general relativity, this principle is incorporated by considering that the motion of test particles, which have negligible mass, is determined by the curvature of space-time caused by the presence of the mass and the energy [3, 6, 7].

- **Equivalence principle of Einstein** : In a small region of the space-time, it is impossible to distinguish between a uniform gravitational field and an equivalent acceleration of the reference. This principle extends the weak equivalence principle to include the laws of physics beyond just the motion of objects, stating that the physical laws take the same form in a gravitational field as they do in an accelerated frame. General relativity incorporates this principle by treating gravity as a geometric phenomenon, where the curvature of space-time affects not only the motion of objects but also the behavior of light, the passage of time, and the structure of the universe itself [7].

- **Strong Equivalence Principle**: In any space-time region, it is always possible to choose a reference frame such that the laws of physics, including the gravitational field equations, are locally equivalent to those in special relativity. This principle asserts that not only do the laws of physics have the same form in a gravitational field, but the gravitational field itself behaves as if it is not present at all when viewed from a suitable locally inertial frame. In general relativity, this principle implies that the gravitational field can be fully described by the geometry of the space-time, and the motion of objects and the behavior of physical phenomena are determined by the curvature of this space-time [6, 7].

The principles of equivalence play a fundamental role in the theory of general relativity. They serve as the guiding principles for the development and formulation of the theory.

In special relativity, the space and the time are represented by a mathematical set of points called events, which form the Minkowski space-time which is a four-dimensional pseudo-Euclidean space. This means that each event P is characterized by a four-vector of real numbers, three dimensions for the space (x_1, x_2, x_3), and one for time $(x_0 = ct)$. The theory of special relativity is based on the assumption that all laws of nature are invariant under a special set of transformations in the space-time. The Minkowski space-time is a flat space. In terms of the curvature of the space-time, it has a zero curvature. This means that the geometry of the Minkowski is described by a flat metric. This metric is expressed as follows

$$\eta_{\mu\nu} = \begin{pmatrix} -1 & 0 & 0 & 0 \\ 0 & 1 & 0 & 0 \\ 0 & 0 & 1 & 0 \\ 0 & 0 & 0 & 1 \end{pmatrix}, \tag{1.23}$$

and the line element is given by

$$ds^2 = \eta_{\mu\nu}\partial x^\mu \partial x^\nu. \tag{1.24}$$

For a Riemannian manifold, it is recalled that we have

$$ds^2 = g_{\mu\nu}\partial x^\mu \partial x^\nu. \tag{1.25}$$

One can define a locally inertial reference frame X^α in which the laws of physics near each event resemble those of special relativity. Indeed, one has

$$\begin{aligned} ds^2 &= G_{\alpha\beta}\partial X^\alpha \partial X^\beta \\ &= G_{\alpha\beta}\frac{\partial X^\alpha}{\partial x^\mu}\frac{\partial X^\beta}{\partial x^\nu}\partial x^\mu \partial x^\nu \\ &= g_{\mu\nu}\partial x^\mu \partial x^\nu. \end{aligned} \tag{1.26}$$

In the neighborhood of an event P, we get the following developed form

$$G_{\alpha\beta} = \eta_{\mu\nu} + \frac{1}{2}\frac{\partial^2 G_{\alpha\beta}}{\partial X^\gamma \partial X^\delta}\,|_P\,\Delta X^\gamma \Delta X^\delta + O(|\Delta X^3|). \tag{1.27}$$

General relativity theory modifies the distinction between locally "inertial" and "non-inertial" effects by replacing the "flat" Minkowski space of special relativity with a metric that produces a non-zero curvature in space. Moreover, the space is considered asymptotically locally Minkowskian. This means in a small region around a specific point that space can be considered flat and obeys the principles of special relativity [1,6,7].

The shortest distance between two points is the geodesic. For a flat space, this is a straight line, which is not the case for the curved spaces. Indeed, in an inertial reference frame, the motion of a particle is described by the following equation

$$\frac{d^2X^\alpha}{d\lambda^2}=0, \tag{1.28}$$

where λ is the proper time measured in the center of mass reference frame. The changing of the reference gives

$$\frac{d^2x^\mu}{d\lambda^2}+\Gamma^\mu_{\nu\rho}\frac{dx^\nu}{d\lambda}\frac{dx^\rho}{d\lambda}=0, \tag{1.29}$$

where the Christoffel symbols can be expressed in terms of the referential frame vectors as follows

$$\Gamma^\mu_{\nu\rho}=\frac{\partial x^\mu}{\partial X^\alpha}\frac{\partial^2X^\alpha}{\partial x^\nu\partial x^\rho}. \tag{1.30}$$

These symbols appear in the geodesic equation in the form of a force which demonstrates how the gravitational forces arise from the space curvature .

1.2.3 Einstein equations

To describe the gravitational field completely, we need to determine the specific form of the space-time metric, which characterizes the geometry of the curved space-times. Einstein field equations allow one to find precisely the equations that the metric of the space-time must satisfy. By solving these equations, we can determine the metric tensor components, which in turn determine the curvature of the space-time in the presence of the matter and the energy. The tensor object which, in special relativity, completely describes matter is the energy-impulse tensor [1,6,7]. This tensor is given by

$$T_{\mu\nu}=\rho u_\mu v_\nu, \tag{1.31}$$

where ρ is density. u_μ and u_ν are velocities along the four dimensions of the space-time. For the special case of perfect fluids, the impulse-energy tensor is instead given by

$$T^{\nu\mu}=\frac{\epsilon+p}{c^2}v^\nu v^\mu+pg^{\nu\mu}, \tag{1.32}$$

where ϵ is the energy density and p is the pressure.

Since the gravitational field can be characterized by the ten independent components of the symmetric metric tensor $g_{\mu\nu}$, it is reasonable to seek ten field equations in the form of the equality between two symmetric tensors of rank 2. Thus, we can consider the following equality

$$G^{\mu\nu}(g, \partial g, \partial^2 g) = \zeta T^{\mu\nu}(g), \tag{1.33}$$

where $G^{\mu\nu}$ satisfies the following constraints

$$\begin{aligned} \nabla_\nu G^{\mu\nu} &= 0, & (1.34)\\ G^{\mu\nu} &= G^{\mu\nu}(g, \partial g, \partial^2 g), & (1.35)\\ G^{\mu\nu} &= 0 \quad \text{if} \quad g_{\mu\nu} = \eta_{\mu\nu}. & (1.36) \end{aligned}$$

Given these properties, the only tensor that satisfies this is the Einstein tensor. Indeed, we get

$$R^{\mu\nu} - \frac{1}{2} g^{\mu\nu} R = \zeta T^{\mu\nu}. \tag{1.37}$$

This equation establishes a profound connection between the curvature of the space-time and the distribution of the matter and the energy. In the non-relativistic limit, the Einstein equations are reduced to the usual Newtonian laws. The coupling constant ζ can be determined by imposing this constraint

$$\zeta = \frac{8\pi G}{c^4}, \tag{1.38}$$

where G is the gravitational constant and c is the speed of light.

According to [3,6,7], we can derive the Einstein equations by starting from the Einstein-Hilbert (EH) action coupled to matter

$$S = S_{EH} + S_{Matter}, \tag{1.39}$$

where the EH action is given by

$$S_{EH} = \frac{1}{2\zeta^2} \int d^4x \sqrt{-g} R. \tag{1.40}$$

The Einstein equations can be obtained by varying the action with respect to the metric tensor and applying the principles of the least action

$$\frac{1}{\sqrt{-g}} \frac{\partial S}{\partial g^{\mu\nu}} = 0. \tag{1.41}$$

The computation gives

$$R^{\mu\nu} - \frac{1}{2}g^{\mu\nu}R = \zeta T^{\mu\nu}, \tag{1.42}$$

where the energy-impulse tensor has the following expression

$$T^{\mu\nu} = \frac{-2}{\sqrt{-g}}\frac{\partial S_{Matter}}{\partial g^{\mu\nu}}. \tag{1.43}$$

1.3 Black hole solutions

In this section, we will explore various solutions of the Einstein equations in different contexts. These solutions not only give an insight into the nature of the space-time, but also reveal the diversity of black holes that emerge with distinct parameters in each case.

1.3.1 Ordinary solutions

In 1916, Karl Schwarzschild derived a fundamental exact solution to Einstein equations. This solution represents a pivotal step in understanding black holes and lays the foundation for more complex models. It describes a remarkably simple configuration of a black hole, characterized by its spherical symmetry and a solitary parameter linked to its mass [3, 6, 7]. To derive this solution, the space-time is supposed to be static

$$\frac{\partial g_{\mu\nu}}{\partial t} = 0. \tag{1.44}$$

The spherical symmetry of the space-time allows the choice of following line element

$$ds^2_{Sch} = g_{\mu\nu}dx^\mu dx^\nu = -A(r)c^2dt^2 + B(r)dr^2 + r^2d\Omega^2, \tag{1.45}$$

where $d\Omega^2 = d\theta^2 + \sin^2\theta d\phi^2$. To solve the Einstein field equations for a vacuum spherically symmetric space-time, we first calculate the Christoffel symbols

$$\Gamma^r_{rr} = \frac{1}{2B(r)}\frac{dB(r)}{dr}, \quad \Gamma^r_{\theta\theta} = -\frac{r}{B(r)}, \quad \Gamma^r_{\phi\phi} = -\frac{r\sin^2\theta}{B(r)}, \quad \Gamma^r_{tt} = \frac{1}{2B(r)}\frac{dA}{dr}, \tag{1.46}$$

$$\Gamma^\theta_{r\theta} = \Gamma^\theta_{\theta r} = \frac{1}{r}, \quad \Gamma^\theta_{\phi\phi} = -\sin\theta\cos\theta, \tag{1.47}$$

$$\Gamma^\phi_{r\phi} = \Gamma^\phi_{\phi r} = \frac{1}{r}, \quad \Gamma^\phi_{\theta\phi} = \Gamma^\phi_{\phi\theta} = \frac{\cos\theta}{\sin\theta}, \tag{1.48}$$

$$\Gamma^t_{tr} = \frac{1}{2A(r)}\frac{dA}{dr}. \tag{1.49}$$

Using the Christoffel symbols, we get the the non null components of the Ricci tensor

$$\begin{aligned}
R_{tt} &= -\frac{A''}{2B} + \frac{1}{4}\frac{A'}{B}(\frac{B'}{B} + \frac{A'}{A}) - \frac{A'}{rB}, & (1.50)\\
R_{rr} &= \frac{A''}{2A} - \frac{1}{4}\frac{A'}{A}(\frac{B'}{B} + \frac{A'}{A}) - \frac{B'}{rB}, & (1.51)\\
R_{\theta\theta} &= -1 + \frac{r}{2B}(\frac{A'}{A} - \frac{B'}{B}) + \frac{1}{B}, & (1.52)\\
R_{\phi\phi} &= R_{\theta\theta}\sin^2\theta, & (1.53)
\end{aligned}$$

where the notations ($'$) and ($''$) represent the derivative and the second derivative with respect to r. A system of differential equations involving the metric coefficients is obtained if we introduce these quantities into the Einstein equations. Solving these differential equations and applying the Newtonian limit yields

$$ds^2 = c^2(1 - \frac{2GM}{rc^2})dt^2 - (1 - \frac{2GM}{rc^2})^{-1}dr^2 - r^2(d\theta^2 + \sin^2\theta d\phi^2). \tag{1.54}$$

Detailed calculations can be found in [6]. Note that when $r \to \infty$ or $M \to 0$, we find the Minkowski space-time. An immediate analysis of Eq.(1.54) implies that the Schwarzschild solution exhibits two singularities where the solution becomes indefined or divergent. Considering system of natural units in what follows, we can prove that these singularities occur at two distinct radial coordinates $r = 0$ and $r = r_h = 2M$. The first one is considered a true singularity. It exists regardless of the choice of the coordinate system. This singularity represents an infinitely curved and a dense point where the entire mass is concentrated. The second singularity is a coordinate singularity. This means that the divergence in the solution is due to the choice of coordinates. This singularity can be removed by transforming the solution into a different coordinate system [6,7]. By calculating the Kretschmann scalar, we find

$$R_{\mu\nu\rho\sigma}R^{\mu\nu\rho\sigma} = \frac{48M^2}{r^6} \xrightarrow[r\to 0]{} \infty. \tag{1.55}$$

This quantity tends towards infinity for $r = 0$ and it takes finite value for $r = 2M$. Indeed, the first one is a physical singularity.

The study of the geodesics of the light proves that the hypersurface $r = r_h$, called the event horizon surface, separates Schwarzschild space-time into two very distinct regions. All paths in the outside region of the event horizon can lead away from the central singularity and out into space. On the other hand, all paths in inside region lead inexorably toward the central singularity $r = 0$.

An extension of this spherically symmetric solution is obtained by taking account of the mass and the electric charge parameters to describe the geometry of the space-time around a black hole. In this case, the EH action is coupled to the electromagnetic field created by the charge [6,7]. Indeed, the space-time is described by the following action

$$S = \int d^4x\sqrt{-g}\left(R - \frac{1}{4}F^{\alpha\beta}F_{\alpha\beta}\right), \tag{1.56}$$

where $F^{\alpha\beta}$ is the electromagnetic field tensor that verifies the Maxwell equations

$$\begin{aligned} \partial_\nu F^{\mu\nu} &= 0, & (1.57)\\ \partial_\sigma F^{\mu\nu} + \partial_\mu F^{\nu\sigma} + \partial_\nu F^{\sigma\mu} &= 0. & (1.58)\end{aligned}$$

Using these equations, the energy-impulse tensor distribution is derived directly from the Lagrangian

$$T_{\alpha\beta} = \mu_0^{-1}\left(\frac{1}{4}g_{\alpha\beta}F_{\mu\nu}F^{\mu\nu} - g_{\beta\nu}F_{\alpha\mu}F^{\nu\mu}\right), \tag{1.59}$$

where μ_0 is the the vacuum permeability. The solution of the Einstein equations in the presence of this energy-impulse tensor is represented by the Reissner-Nordström solution [6,7]. This solution describes a static, spherical black hole with an electric charge Q. This solution is formulated as

$$ds^2_{RN} = -\left(1 - \frac{2M}{r} + \frac{Q^2}{r^2}\right)dt^2 + \left(1 - \frac{2M}{r} + \frac{Q^2}{r^2}\right)^{-1}dr^2 + r^2(d\theta^2 + \sin^2\theta d\phi^2). \tag{1.60}$$

The event horizon is defined by $g_{tt} = 0$ producing

$$1 - \frac{2M}{r_h} + \frac{Q^2}{r_h^2} = 0. \tag{1.61}$$

This equation has multiple solutions. This gives rise to three different scenarios

- $M^2 < Q^2$, the solution corresponds to a naked singularity.
- $M^2 = Q^2$, the solution is an extremal black hole with one horizon
- $M^2 > Q^2$, the solution represents a black hole with two horizon inner and outer horizon $r_{h_\pm} = M \pm \sqrt{M^2 - Q^2}$. In the limit $Q = 0$, we obtain the schwarzschild black hole

horizon.

The third parameter that should be introduced in the black hole solution is the rotating parameter. As stars have angular momentum as a result of their rotation. This momentum is conserved when the star undergoes changes in volume, including when it collapses to form a black hole. These black holes should have a rotating parameter a. The solution has been described by the Kerr metric. A general way to obtain the metric is to use the Newman-Janis method [103,104]. This method replaces the original version used to generate the Kerr metric by following the Newman-Janis algorithm. The solution is defined as follow

$$\begin{aligned} ds_K^2 = & -\left(1-\frac{2Mr}{\Sigma}\right)dt^2 - \frac{4aMr\sin^2\theta}{\Sigma}d\phi dt + \frac{\Sigma}{\Delta}dr^2 \\ & + \Sigma d\theta^2 + \left(r^2+a^2+\frac{(2Mr)\,a^2\sin^2\theta}{\Sigma}\right)\sin^2\theta d\phi^2, \end{aligned} \tag{1.62}$$

where we have

$$\Delta = r^2 + a^2 - 2Mr \tag{1.63}$$

$$\Sigma = r^2 + a^2\cos^2\theta. \tag{1.64}$$

The rotating parameter is linked to the angular momentum via the the relation $a = \frac{J}{M}$. The properties of the space-time around a rotating black hole are significantly different from those of a non-rotating black hole. Firstly, the singularity in this case is constrained by

$$r = 0, \qquad \cos\theta = 0. \tag{1.65}$$

The singularity is not located at a precise point, but rather along a circle. More precisely, the singularity is located on a circle of the radius $r = a\cos\theta$. This represents an annular singularity. The metric form has new singularities which need to be examined. Putting $g_{tt} = 0$, we get the following solutions

$$r = M \pm \sqrt{M^2 - a^2\cos^2\theta}. \tag{1.66}$$

These solutions correspond to two specific spaces, the inner and the outer ergosphere. In these regions, the dragging of the space-time is so strong that even light cannot remain stationary and the objects within the ergosphere are forced to move in the direction of the rotation of the black hole. For the Schwarzschild black hole, this hypersurface coincides with the black hole horizon. To find the event horizon of this black hole, we solve the following equality

$$\Delta = r^2 + a^2 - 2Mr = 0. \tag{1.67}$$

The solution is given by

$$r_{h_\pm} = M \pm \sqrt{M^2 - a^2}. \tag{1.68}$$

If $M < a$, there is no horizon. For $M = a$, we have an extreme black hole with a single horizon. The last situation where $M > a$ corresponds to black hole with an inner and outer horizon. The outer horizon functions similarly to the event horizon, while the inner horizon is located closer to the singularity.

Two years after the publication of the Kerr solution, T. Newman proposed a solution for a charged and rotating black hole. This solution, known as the Kerr-Newman solution, generalizes the Kerr solution by adding the electric charge parameter. This general solution, which takes into account the three parameters being rotation, charge and mass, is formulated as follows

$$\begin{aligned} ds^2_{KN} = &-\left(1 - \frac{2Mr - Q^2}{\Sigma}\right) dt^2 - \frac{2a\left(2Mr - Q^2\right)\sin^2\theta}{\Sigma} d\phi dt + \frac{\Sigma}{\Delta} dr^2 \\ &+ \Sigma d\theta^2 + \left(r^2 + a^2 + \frac{\left(2Mr - Q^2\right)a^2\sin^2\theta}{\Sigma}\right)\sin^2\theta d\phi^2, \end{aligned} \tag{1.69}$$

where the function Δ takes the form

$$\Delta = r^2 + a^2 - 2Mr + Q^2. \tag{1.70}$$

The ergosphere equation is affected by the addition of the charge. It takes the following expression

$$r^2 + a^2\cos^2\theta = 2Mr - Q^2. \tag{1.71}$$

The event horizon solution is extended to

$$r_{h_\pm} = M \pm \sqrt{M^2 - a^2 - Q^2} \tag{1.72}$$

1.3.2 Regular black hole solutions

The irregularities present in the ordinary black hole solutions are considered as significant challenges within the context of our current understanding of the gravity and the space-time [2]. Particularly, at singularities, the curvature of the space-time becomes infinite and the laws of physics as we currently understand them collapse, making the physical theories unreliable. To avoid these irregularities, various theoretical approaches and alternative models have been explored by coupling the Einstein theory with non linear electrodynamics. The first model of regular black holes is proposed by Bardeen in 1968 [66,68,105]. The dynamics of the proposed theory is governed by the action

$$S = \int d^4x\sqrt{-g}\left(R + 16\pi\mathcal{L}(F)\right), \tag{1.73}$$

where $\mathcal{L}(F)$ is the Lagrangian density of the electromagnetic field and F is the Faraday-Maxwell tensor giving by $F = \frac{1}{4}F^{\mu\nu}F_{\mu\nu}$. The stress-energy tensor is written as

$$T_{\mu\nu} = g_{\mu\nu}\mathcal{L}(F) - \frac{\partial\mathcal{L}(F)}{\partial F}F^{\lambda}_{\mu}F_{\lambda\nu}. \tag{1.74}$$

To get the Bardeen metric, the following density has been used

$$\mathcal{L}(F) = \frac{3m^2}{4\pi g_b^3}\left(\frac{\sqrt{2g_b^2F}}{1+\sqrt{2g_b^2F}}\right)^{5/2}, \tag{1.75}$$

where g_b is the magnetic charge and m is the ADM mass. The associated line element reads as

$$ds^2 = f(r)dt^2 - f(r)^{-1}dr^2 - r^2(d\theta^2 + \sin^2\theta d\phi^2), \tag{1.76}$$

where the metric function should takes the form $f(r) = 1 - \frac{2M(r)}{r}$. From the Maxwell equations, we can prove that the mass function has the following expression

$$M(r) = \frac{mr^3}{\left(r^2 + g_b^2\right)^{3/2}}. \tag{1.77}$$

This mass generates the Bardeen regular black hole solution. To analyze the asymptotic forms, we expand the metric function as follows

$$f(r) \approx 1 - \frac{2m}{r} + \frac{3mg_b^2}{r^3}. \tag{1.78}$$

This shows that the black hole is not asymptotically Reissner-Nordstrom solution and it behaves as Schwarzschild type. For small values of r, we have

$$f(r) \approx 1 - \frac{2mr^2}{g_b^3}. \tag{1.79}$$

This can be interpreted as a de Sitter behavior inside of the black hole. The de Sitter space-time will be examined in the next section.

The second well-known regular black hole model is the Hayward black hole [106]. This class solution is valid for the following Lagrangian density

$$\mathcal{L}(F) = \frac{12}{\alpha} \frac{(\alpha F)^{5/4}}{\left(1 + \sqrt{\alpha F}\right)^{5/2}}. \tag{1.80}$$

The α parameter is linked to the Hayward magnetic charge g_h via the equation

$$\alpha = \frac{g_h^3}{m}. \tag{1.81}$$

In this case, the computation gives the following metric function

$$f(r) = 1 - \frac{2mr^2}{r^3 + g_h^3}. \tag{1.82}$$

The central singularity for these black holes is absent. The regularity can be seen by calculating the Kretschmann scalar which is given by

$$R_{\mu\nu\rho\sigma} R^{\mu\nu\rho\sigma} = \frac{48m^2 \left(18g_h^6 r^6 - 2g_h^9 r^3 + 2g_h^{12} - 4g_h^3 r^3 + r^{12}\right)}{\left(r^3 + g_h^3\right)^6}. \tag{1.83}$$

Near to the origin, we have

$$K(r \to 0) \sim \frac{96M^2}{g_h^6} - \frac{672M^2}{g_h^9} + O(r^6). \tag{1.84}$$

The infinite behavior of this scalar, for $r = 0$, is removed for this solution. This model leads to more bounded curvature and density near to the center. It should be noted that the horizon radius obtained by solving the equation $f(r) = 0$ takes the Shwarzschild radius if we put $g_b = 0$ for the first solution and $g_h = 0$ for the second one.

1.3.3 Quintessential black hole solutions

As we have seen, the solutions of the black holes depend on the density of the space-time. This density is influenced by the distribution of the mass and the energy. The behavior of the Universe as a whole, including its expansion, is affected by this distribution. In particular, the accelerated expansion of the Universe can be explained by the presence of dark energy, making it an important quantity to take into account in the theory that describes the space-time. Moreover, this energy is considered us a puzzling part of the Universe that makes up a large part of its energy content. The dark energy can be described using quintessence models. The concept of the quintessence fields provides a compelling framework for describing dark energy and its potential role in the Universe [67, 71, 72, 107]. Mathematically, the quintessence field is defined by its scalar field potential parameterized by a constant w_q where the quintessence density ρ_q and the negative pressure of the universe p_q are linked by the following relation

$$p_q = \rho_q w_q. \tag{1.85}$$

The Friedmann equations that describe the dynamics and the evolution of the universe on a large scale impose the following constraint

$$-1 < w_q < -\frac{1}{3}. \tag{1.86}$$

To study the behavior of black holes surrounding by this matter, we consider a spherically symmetric metric in the following form

$$ds^2 = e^{\nu(r)}dt^2 - e^{\lambda(r)}dr^2 - r^2\left(d\theta^2 + \sin^2\theta d\phi^2\right). \tag{1.87}$$

The energy-momentum tensor of the quintessence is given by

$$T_t^t \;\; = \;\; \rho_q(r), \tag{1.88}$$

which leads to

$$T_j^i = 3\rho_q(r)w_q\left[-(1+3B)\frac{r_i r^j}{r_n r^n} + B\delta_i^j\right], \tag{1.89}$$

where B is a free parameter. Without any loss of generality, we take

$$\lambda(r) = -\ln(1+\mu(r)). \tag{1.90}$$

The additivity and the linearity principles give

$$T_t^t = T_r^r, \tag{1.91}$$

providing

$$\lambda(r) + \nu(r) = 0. \tag{1.92}$$

This condition fixes the free parameter B to the following value

$$B = -\frac{-3\omega_q + 1}{6\omega_q}. \tag{1.93}$$

By solving the Einstein equation, we can prove that

$$\mu(r) = -\frac{2M}{r} - \frac{c_q}{r^{3\omega_q+1}} \tag{1.94}$$

where c_q is the a normalization factor. In fact, the extended Shwarzschild solution with the quintessential field is expressed as follows

$$ds^2 = \left(1 - \frac{2M}{r} - \frac{c_q}{r^{3\omega_q+1}}\right)dt^2 - \left(1 - \frac{2M}{r} - \frac{c_q}{r^{3\omega_q+1}}\right)^{-1} dr^2 - r^2\left(d\theta^2 + \sin^2\theta d\phi^2\right). \tag{1.95}$$

1.4 Black holes in different backgrounds

1.4.1 Black holes with a cosmological constant

In the process of general relativity formulation, Einstein introduces a cosmological constant Λ when he recognize that his theory could describe a dynamic universe [6,7]. This constant is an additional term that he added to the equations to account for the possibility of a Universe that neither expands nor contracts. Thus, the field equations take the following general form

$$R^{\mu\nu} - \frac{1}{2}Rg^{\mu\nu} + \Lambda g^{\mu\nu} = \frac{8\pi G}{c^4}T^{\mu\nu}. \tag{1.96}$$

The presence of this cosmological constant implies that the space-time itself is curved. Interestingly, this curvature can take different forms. When the constant curvature is positive, it is associated with a space-time known as de-Sitter (dS) space-time. On the other hand, when the constant curvature is negative, it corresponds to a space-time called Anti de-Sitter (AdS) space-time. To study cosmological black holes, we investigate an isotropic and homogeneous space-time that possesses a maximal symmetry. This means that the space-time exhibits the highest possible number of continuous symmetries or, equivalently, features the maximum number of linearly independent Killing vector fields [6,65]. In a space of dimension n, the count of such symmetries is given by

$$\underbrace{n}_{n\ translations} + \overbrace{\frac{n(n-1)}{2}}^{(n-1)rotations} = \frac{n(n+1)}{2}. \tag{1.97}$$

It can be demonstrated that space-times exhibiting maximal symmetry are characterized by the following configuration of the Riemann tensor

$$R^{\alpha}_{\rho\mu\nu} = \Bbbk\left(\delta^{\alpha}_{\mu}g_{\rho\nu} - \delta^{\alpha}_{\nu}g_{\rho\mu}\right), \tag{1.98}$$

where $\Bbbk$ is a constant. It is related to the curvature scalar R via the relation

$$\Bbbk = \frac{R}{n(n+1)}. \tag{1.99}$$

In the four-dimensional scenario, the Ricci tensor takes the following configuration

$$\begin{aligned} R_{\rho\nu} = R^{\alpha}_{\rho\alpha\nu} &= \Bbbk\left(\delta^{\alpha}_{\alpha}g_{\rho\nu} - \delta^{\alpha}_{\nu}g_{\rho\alpha}\right), \\ &= 3\Bbbk g_{\rho\nu}. \end{aligned} \tag{1.100}$$

In fact, we obtain the following filed equation

$$(\Lambda - 3\Bbbk)\mathbf{g} = \frac{8\pi G}{c^4}\mathbf{T}. \tag{1.101}$$

From this, it follows that a maximally symmetric empty space-time, when the energy-momentum tensor equals zero, must possess a cosmological constant that equals $3\Bbbk$. Furthermore, we can establish three distinct scenarios that are contingent on the value of $\Bbbk$

- For $\Bbbk = 0$, we have a Minkowski space-time.
- For $\Bbbk > 0$, the scalar curvature is positive and the space-time considered as de-Sitter.
- For $\Bbbk < 0$, the scalar curvature is negative and the space considered as Anti-de-Sitter.

It is worth noting that Minkowski space-time is no longer a solution to the Einstein equations when a cosmological constant is present in a vacuum. This means that the cosmological constant modifies the background of the space-time. In fact, it becomes essential to delve into an exploration of the metrics associated with AdS and dS space-times. This can be done by embedding the geometry of dS_4 and AdS_4 in four dimensions within the five-dimensional Minkowski spacetime choosing appropriate coordinates and transformations that preserve the curvature properties. For the dS_4 space-time, we have

$$-x_0^2 + \sum_{i=1}^{4} x_i^2 = \ell^2. \tag{1.102}$$

For AdS_4, this takes the following form

$$-x_0^2 + \sum_{i=1}^{3} x_i^2 - x_4^2 = -\ell^2, \tag{1.103}$$

where ℓ represents the radius of the space-time. For AdS_4, we have $\ell^2 = -\dfrac{3}{\Lambda}$. The spatial part of dS is spherical and the spatial part of AdS is hyperbolic. To get the metric of the dS space, we take the following coordinate transformations

$$x_0 = \sqrt{\ell^2 - r^2}\sinh\left(t/\ell\right), \tag{1.104}$$

$$x_1 = r\cos\theta, \tag{1.105}$$

$$x_2 = r\sin\theta\sin\phi, \tag{1.106}$$

$$x_3 = r\sin\theta\cos\phi, \tag{1.107}$$

$$x_4 = \sqrt{\ell^2 - r^2}\cosh\left(t/\ell\right), \tag{1.108}$$

which yields the following metric

$$ds^2 = -\left(1 - \frac{r^2}{\ell^2}\right) dt^2 + \frac{dr^2}{1 - \frac{r^2}{\ell^2}} + r^2 d\Omega^2. \tag{1.109}$$

For the AdS space-time, the considered changes of the coordinates are

$$x_0 = \sqrt{\ell^2 + r^2} \sin\left(t/\ell\right), \tag{1.110}$$

$$x_1 = r\cos\theta, \tag{1.111}$$

$$x_2 = r\sin\theta\sin\phi, \tag{1.112}$$

$$x_3 = r\sin\theta\cos\phi, \tag{1.113}$$

$$x_4 = \sqrt{\ell^2 + r^2} \cos\left(t/\ell\right). \tag{1.114}$$

The metric takes the form

$$ds^2 = -\left(1 + \frac{r^2}{\ell^2}\right) dt^2 + \frac{dr^2}{1 + \frac{r^2}{\ell^2}} + r^2 d\Omega^2. \tag{1.115}$$

By employing the approach established in [6, 64], we derive the subsequent solution for the Eq.(1.96)

$$ds^2 = -\left(1 - \frac{\Lambda r^2}{3} - \frac{2M}{r}\right) dt^2 + \left(1 - \frac{\Lambda r^2}{3} - \frac{2M}{r}\right)^{-1} dr^2 + r^2 d\Omega^2. \tag{1.116}$$

When $\Lambda > 0$, the metric is referred to as the Schwarzschild-de Sitter metric, often denoted as the Schwarzschild-dS metric. Conversely, when $\Lambda < 0$, it is termed the Schwarzschild-anti-de Sitter metric, commonly abbreviated as the Schwarzschild-AdS metric. This metric is reduced to the Schwarzschild metric for $\Lambda = 0$. According to [6, 7], the charged version of these black holes, knowing as the Reissner Nordström-AdS and the Reissner Nordström-dS black holes, is given by

$$ds^2 = -\left(1 - \frac{2M}{r} + \frac{Q^2}{r^2} - \frac{\Lambda r^2}{3}\right) dt^2 + \left(1 - \frac{2M}{r} + \frac{Q^2}{r^2} - \frac{\Lambda r^2}{3}\right)^{-1} dr^2 + r^2 d\Omega^2. \tag{1.117}$$

Applying the Janis-Newman method [103], one can obtain the following cosmological rotating and charged solution

$$\begin{aligned} ds^2 = &-\left(1 - \frac{2Mr - Q^2 + \frac{\Lambda r^2}{3}}{\Sigma}\right) dt^2 - \frac{2a\left(2Mr - Q^2 + \frac{\Lambda r^2}{3}\right)\sin^2\theta}{\Sigma} d\phi dt + \frac{\Sigma}{\Delta} dr^2 \\ &+ \Sigma d\theta^2 + \left(r^2 + a^2 + \frac{\left(2Mr - Q^2 + \frac{\Lambda r^2}{3}\right) a^2 \sin^2\theta}{\Sigma}\right)\sin^2\theta d\phi^2, \end{aligned} \tag{1.118}$$

where we have

$$\Delta = r^2 + a^2 - 2Mr + Q^2 - \frac{\Lambda r^2}{3}. \tag{1.119}$$

This solution is known as KN-AdS for ($\Lambda < 0$) and KN-dS ($\Lambda > 0$).

1.4.2 Black holes in M-theory

M-theory is a theoretical framework that seeks to unify all variants of superstring theory. Before M-theory, There are five distinct superstring theories Type I, Type IIA, Type IIB, heterotic $SO(32)$, and heterotic $E_8 \times E_8$. These theories seemed to describe different aspects of the same underlying physics, but they were not directly connected. M-theory aspires to provide a consistent description that encompasses all these superstring theories. This emerged from the realization that the different superstring theories are related by non-perturbative dualities. These dualities bridge the gap between weak and strong coupling regimes, where traditional perturbative methods break down. One of the most fundamental entities in this theory is the brane object, which can exist in higher-dimensional spacetimes. These objects are like hypersurfaces embedded in the higher-dimensional spacetime of M-theory [38, 46, 79, 80]. They can have tension, charge, and other properties that influence their behaviors and interactions. Combining the principles of supersymmetry with the concepts of general relativity brings the supergravity framework. The study of black holes in this framework achieves important investigations duo to the exploitation of the AdS/CFT correspondence [65, 74, 78]. This correspondence creates an interplay between gravitational models in d-dimensional AdS geometries and $(d-1)$-dimensional conformal field theories living in the boundary of such AdS spaces. By utilizing the physics of solitonic branes, various models within type the II superstring and M-theory have been examined. These studies involve considering the cosmological constant in the bulk, which is closely connected to the number of colors associated with the relevant branes. We consider d-dimensional AdS black holes embedded in 11-dimensional M-theory (where $(d \geq 4)$). We presume that they arise from the compactification on real spheres of dimension $(11-d)$, which are denoted as $S^{(11-d)}$. In the presence of brane objects, the corresponding 11-dimensional geometry can be written as follows

$$AdS_d \times S^{11-d}. \tag{1.120}$$

This spacetime structure could be seen as the near horizon geometry of $(d-2)$ branes in such M-theory. An analysis of the sphere compactification reveals that these higher-dimensional models should incorporate, at minimum, a gauge field $\mathcal{F}_{11-d}$ with strength $(11-d)$. This gauge field contributes with the term $\int d^d x \mathcal{F}^2_{11-d}$ to the corresponding action of the lower-dimensional black hole. This inclusion is substantiated by a $(11-d-1)$ gauge form coupled to a $(11-d-2)$-brane, which is assumed to exist within these higher-dimensional models. Upon a closer examination, it becomes evident that these proposed models present the potential for two distinct types of brane objects. These types can be classified as $(d-2)$-branes corresponding to the AdS_d geometry of the black hole and $(11-d-2)$ associated with the S^{11-d} sphere compactification. It is recalled that (1.120) is a particular case of a general statement associated with $AdS_d \times S^{d+k}$ such that $D = 2d + k$ with D is the dimension of the inspired theory. These theory is indexed by a triplet (D, d, k). In M-theory, we have

$$2d + k = 11, \tag{1.121}$$

where k is an arbitrary integer specifying the internal space of $(11-d)$ dimensions. Generally, the non-rotating solutions of the d-dimensional AdS black holes in such a theory is given by

$$ds^2 = -f(r)dt^2 + f(r)^{-1}dr^2 + r^2 d\Omega^2_{d-2}. \tag{1.122}$$

The metric function is expressed as

$$f(r) = 1 - \frac{m}{r^{d-3}} + \frac{r^2}{\ell^2_{AdS}}. \tag{1.123}$$

The physical parameter m is related to the black hole mass via the relation

$$M = \frac{(d-2)\Omega^2_{d-2} m}{16\pi G_d}, \tag{1.124}$$

where we have

$$G_d = \frac{\ell_p^{2(d-1)+k}}{\hbar \Omega_{d+k} \ell^{d+k}_{AdS}}, \qquad \Omega_{d+k} = \frac{2\pi^{(d+k+1)/2}}{\Gamma(\frac{d+k+1}{2}}, \tag{1.125}$$

The AdS radius is given by in terms of the brane number N

$$\ell_{AdS}^{2(d-1)+k} = 2^{-(d(4-d)+3)/2}\pi^{7(k+2(d-5))-4}N^{(d-1)/2}\ell_p^{2(d-1)+k}, \tag{1.126}$$

where ℓ_p denotes the Planck length. In the present investigation, we consider $(11, d, k)$ models. Particularly, we focus on 4-dimensional and 7-dimensional AdS black holes embedded in 11-dimensional M-theory associated with the triplets $(11, 4, 3)$ and $(11, 7, 3)$, involving M2 and M5-branes, respectively.

1.4.3 Black holes in Starobinsky-Bel-Robinson gravity

The EH action has been used to explain a wide range of observations, particularly in the solar system. However, it runs up against difficulties in the field of quantum gravity and the extreme energy conditions, such as those present in the early Universe (UV-regime) or for cosmological distances (IR-regime). To solve these problems, a new gravitational theory inspired by superstring theory is put forth within the framework of four-dimensional spacetime. The proposed theory is presented as the sum of the modified $R + \alpha R^2$ gravity inspired by Starobinsky inflation, along with the inclusion of the Bel-Robinson tensor squared term, which finds its origins in the dimensional reduction of the eleven-dimensional M-theory to four dimensions. The suggested Starobinsky-Bel-Robinson (SBR) action possesses solely two parameters, rendering it well-suited for empirically testable applications in domains such as black hole physics, cosmological inflation, and the phenomena of Hawking radiation during the early stages of the universe [108–110]. This action is given by

$$S_{\rm SBR} = \frac{M_{\rm Pl}^2}{2}\int d^4x\sqrt{-g}\left[R + \frac{1}{6m^2}R^2 - \frac{\beta}{32M_{\rm Pl}^6}\left(\mathcal{P}^2 - \mathcal{G}^2\right)\right], \tag{1.127}$$

where $M_{\rm Pl}$ is the reduced Planck mass, m is the mass parameter and β is the new dimensionless coupling parameter. $\mathcal{P}$ is the Pontryagin topological density and $\mathcal{G}$ is the Euler density. These densities have the following form

$$\begin{aligned} \mathcal{G} &= R^2 - 4R_{\mu\nu}R^{\mu\nu} + R_{\mu\nu\rho\sigma}R^{\mu\nu\rho\sigma} && (1.128) \\ \mathcal{P} &= \frac{1}{2}\sqrt{-g}\epsilon_{\mu\nu\rho\sigma}R^{\rho\sigma}{}_{\alpha\beta}R^{\mu\nu\alpha\beta}. && (1.129) \end{aligned}$$

Varying the action (1.127) with respect to the metric, the equations of motion are given by

$$G_{\mu\nu} + \frac{1}{6m^2} H_{\mu\nu} - \frac{\beta}{32 M_{\rm Pl}^6} K_{\mu\nu} = 0, \tag{1.130}$$

where the tensors have the following form

$$G_{\mu\nu} = R_{\mu\nu} - \frac{1}{2} g_{\mu\nu} R, \tag{1.131}$$

$$H_{\mu\nu} = 2R_{\mu\nu} R - \frac{1}{2} g_{\mu\nu} R^2 - 2\nabla_\mu \nabla_\nu R + 2 g_{\mu\nu} \Box R, \tag{1.132}$$

$$\begin{aligned} K_{\mu\nu} = \frac{1}{2} g_{\mu\nu} \mathcal{G}^2 - 2\Big[& 2\mathcal{G} R R_{\mu\nu} - 4\mathcal{G} R_\mu{}^\rho R_{\nu\rho} + 2\mathcal{G} R_\mu{}^{\rho\sigma\lambda} R_{\nu\rho\sigma\lambda} + 4\mathcal{G} R^{\rho\sigma} R_{\mu\rho\sigma\nu} \\ & + 2 g_{\mu\nu} R \Box \mathcal{G} - 2R \nabla_\mu \nabla_\nu \mathcal{G} - 4R_{\mu\nu} \Box \mathcal{G} + 4\left(R_{\mu\rho} \nabla^\rho \nabla_\nu \mathcal{G} + R_{\nu\rho} \nabla^\rho \nabla_\mu \mathcal{G} \right) \\ & - 4 g_{\mu\nu} R_{\rho\sigma} \nabla^\sigma \nabla^\rho \mathcal{G} + 4 R_{\mu\rho\nu\sigma} \nabla^\sigma \nabla^\rho \mathcal{G} \Big]. \end{aligned} \tag{1.133}$$

To get the black hole solution, the following metric form was considered

$$ds^2 = -f(r) dt^2 + \frac{1}{f(r)} dr^2 + r^2 d\Omega_2^2, \tag{1.134}$$

where the function $f(r)$, associated with the Schwarzschild solution, is

$$f(r) = 1 - \frac{2M}{r} - \beta a(r), \tag{1.135}$$

According to [108–110], the calculations give

$$f(r) = 1 - \frac{2M}{r} + \beta \frac{128\pi^3}{5} \left(\frac{2M}{r^3} \right)^3 \left(108 - \frac{194M}{r} \right). \tag{1.136}$$

To obtain the rotating metric of the SBR black hole, we could use the Newman-Janis algorithm through a series of specific steps [103, 104]. The initial step involves a modification of the relevant variables to establish a null surface with spherical symmetry. Concretely, we take the following variable change

$$du = dt - \frac{dr}{f(r)}. \tag{1.137}$$

In the Eddington-Finkelstein type coordinates, the black hole metric is expressed in the following manner

$$ds^2 = -f(r)du^2 - 2du\, dr + r^2 \left(d\theta^2 + \sin^2\theta\, d\phi^2\right). \tag{1.138}$$

The next step is to identify a null tetrad $(\ell^\mu, n^\mu, m^\mu, \overline{m}^\mu)$ that meets the following constraints

$$\ell_\mu \ell^\mu = m_\mu m^\mu = n_\mu n^\mu = \ell_\mu m^\mu = n_\mu m^\mu = 0\,, \quad \ell_\mu n^\mu = -m_\mu \bar{m}^\mu = 1. \tag{1.139}$$

The contra-variant form of the metric can be expressed as

$$g^{\mu\nu} = -\ell^\mu n^v - \ell^\nu n^\mu + m^\mu \overline{m}^\nu + m^\nu \overline{m}^\mu. \tag{1.140}$$

Utilizing the metric expression, the null tetrad vectors are determined as follows

$$\begin{aligned} \ell^\mu &= \delta_1^\mu, \qquad n^\mu = \delta_0^\mu - \frac{1}{2}\left(1 - \frac{r_s}{r} + \frac{108\beta\left(4\sqrt{2}\pi G r_s\right)^3}{5r^8}\left(\frac{1}{r} - \frac{97 r_s}{108 r^2}\right)\right)\delta_1^\mu & (1.141) \\ m^\mu &= \frac{1}{\sqrt{2}r}\left(\delta_2^\mu + \frac{i}{\sin\theta}\delta_3^\mu\right) \qquad \overline{m}^\mu = \frac{1}{\sqrt{2}r}\left(\delta_2^\mu - \frac{i}{\sin\theta}\delta_3^\mu\right), & (1.142) \end{aligned}$$

where $\overline{m}^\mu$ represents the complex conjugate of m^μ. It is noteworthy that the radial coordinate r may assume complex values. As a result, the null vectors of the tetrad are given by

$$\begin{aligned} \ell^\mu &= \delta_1^\mu, \qquad n^\mu = \delta_0^\mu - \frac{1}{2}\left[1 - \frac{r_s}{2}\left(\frac{1}{r} + \frac{1}{r*}\right) + \frac{54\beta\left(4\sqrt{2}\pi G r_s\right)^3}{5(rr*)^4}\left(\frac{1}{r} + \frac{1}{r*} - \frac{97 r_s}{54 rr*}\right)\right]\delta_1^\mu \\ m^\mu &= \frac{1}{\sqrt{2}r^*}\left(\delta_2^\mu + \frac{i}{\sin\theta}\delta_3^\mu\right), \qquad \overline{m}^\mu = \frac{1}{\sqrt{2}r}\left(\delta_2^\mu - \frac{i}{\sin\theta}\delta_3^\mu\right), & (1.143) \end{aligned}$$

where r^* is the complex conjugate of r. Roughly, the following complex coordinate changes should be adopted

$$\begin{aligned} \widetilde{u} &= u - ia\cos\theta, \qquad \widetilde{r} = r + ia\cos\theta & (1.144) \\ \widetilde{\theta} &= \theta, \qquad \widetilde{\varphi} = \varphi. & (1.145) \end{aligned}$$

The computation gives

$$\begin{aligned}
\widetilde{\ell}^{\mu} &= \delta_1^{\mu} && (1.146)\\
\widetilde{n}^{\mu} &= \delta_0^{\mu} - \frac{1}{2}\left[1 - \frac{r_s\widetilde{r}}{\widetilde{r}^2 + a^2\cos^2\widetilde{\theta}} + \frac{54\left(4\sqrt{2}\pi G r_s\right)^3}{5\left(\widetilde{r}^2 + a^2\cos^2\widetilde{\theta}\right)^5}\left(2\widetilde{r} - \frac{97r_s}{54}\right)\right]\delta_1^{\mu} && (1.147)\\
\widetilde{m}^{\mu} &= \frac{1}{\sqrt{2}(\widetilde{r} + ia\cos\widetilde{\theta})}\left(ia\sin\widetilde{\theta}\,(\delta_0^{\mu} - \delta_1^{\mu}) + \delta_2^{\mu} + \frac{i}{\sin\widetilde{\theta}}\delta_3^{\mu}\right) && (1.148)\\
\overline{\widetilde{m}}^{\mu} &= \frac{1}{\sqrt{2}(\widetilde{r} - ia\cos\widetilde{\theta})}\left(-ia\sin\widetilde{\theta}\,(\delta_0^{\mu} - \delta_1^{\mu}) + \delta_2^{\mu} - \frac{i}{\sin\widetilde{\theta}}\delta_3^{\mu}\right). && (1.149)
\end{aligned}$$

To derive the rotating metric solution, certain additional transformations are required. Specifically, these transformations are outlined as follows

$$\begin{aligned}
d\widetilde{u} &= dt - \left(\frac{r^2 + a^2}{\Delta}\right) dr && (1.150)\\
d\widetilde{\varphi} &= d\varphi - \frac{a}{\Delta}\, dr,
\end{aligned}$$

where the function Δ is given by

$$\Delta = \Delta(r) = a^2 + r^2\left(1 - \frac{2GM}{r} + \frac{1024\pi^3\beta G^6M^3\,(108r - 194GM)}{5r^{10}}\right). \tag{1.151}$$

Indeed, the covariant components of the rotating metric are

$$g_{\mu\nu} = \begin{bmatrix}
\frac{a^2\sin^2\theta - \Delta}{\Sigma} & 0 & 0 & \frac{a\sin^2\theta\left[\Delta - \left(r^2 + a^2\right)\right]}{\Sigma}\\
0 & \frac{\Sigma}{\Delta} & 0 & 0\\
0 & 0 & \Sigma & 0\\
\frac{a\sin^2\theta\left[\Delta - \left(r^2 + a^2\right)\right]}{\Sigma} & 0 & 0 & \frac{\sin^2\theta\left[\left(r^2 + a^2\right)^2 - \Delta a^2\sin^2\theta\right]}{\Sigma}
\end{bmatrix}. \tag{1.152}$$

Finally, the metric for the rotating SBR black hole can be expressed in the following form

$$\begin{aligned}
ds^2 &= -\left(\frac{\Delta(r) - a^2\sin^2\theta}{\Sigma}\right) dt^2 + \frac{\Sigma}{\Delta(r)}dr^2 - 2a\sin^2\theta\left(1 - \frac{\Delta(r) - a^2\sin^2\theta}{\Sigma}\right) dtd\phi + \Sigma d\theta^2\\
&+ \sin^2\theta\left[\Sigma + a^2\sin^2\theta\left(2 - \frac{\Delta(r) - a^2\sin^2\theta}{\Sigma}\right)\right] d\phi^2. && (1.153)
\end{aligned}$$

where one has used

$$\Sigma \; = \; r^2 + a^2 \cos^2\theta. \tag{1.154}$$

CHAPTER 2

Black Hole Thermodynamics

The thermodynamics of black holes is regarded as a cornerstone of a deep and fundamental relationship between gravitation, thermodynamics and quantum mechanics. Connecting black holes with the fancy word "thermodynamics", reveals a fascinating interplay between the laws of thermodynamics and the nature of black holes. This connection has been established by relating the area of a black hole to its entropy and the surface gravity to its temperature. This was initially explored in the early 1970s by Jacob Bekenstein. He has observed a similarity between the area law, which asserts that the event horizon area of a black hole can never diminish, and the second law of thermodynamics. Digging deeper into this analogy, the four laws of the black hole mechanics were subsequently formulated by Bardeen, Carter, and Hawking [19–21]. In addition, the cosmological constant has involved a new interpretation that brings it into the realm of thermodynamics, casting it as a sort of thermodynamic pressure. It has been treated as a dynamic variable within its own context of thermodynamics [22, 23]. This causes an extended study of the black hole thermodynamics which leads to the emergence of new quantities and thermodynamic notions. This chapter embarks on an exploration of the profound thermodynamic principles that steer the behavior of black holes, revealing a relevant interplay between the cosmic and the microcosmic aspects. Indeed, we first describe the thermodynamic laws of the black holes by defining various thermodynamic quantities. Then, we study the the thermodynamical behaviors which can be exhibited by black holes including the criticality and the phase transitions. Finally, we illustrate a beautiful established link between the geometric space of the thermodynamic variables and such behaviors.

2.1 Thermodynamical quantities of black holes

2.1.1 Laws of black hole thermodynamics

Here, we list the laws of the black hole thermodynamics:

Law 0: Considering the black hole like a cosmic vacuum cleaner that pulls everything in, the strength of this pulling is called 'surface gravity'. This strength is the same all over the outer boundary of a black hole. Since no matter at this boundary, the pulling force feels the same. Indeed, the low zero states that the surface of gravity κ is constant over the event horizon of a stationary black hole. This quantity verifies the following equation

$$\kappa^2 = \frac{-1}{2}(\nabla^a A^b)(\nabla_a A_b), \tag{2.1}$$

where A^b is the killing vector of black hole. This type of vector fields has been used in differential geometry to describe symmetries in the space-time. It represents a direction or transformation that preserves the geometry and the properties of the space under consideration. Considering the Schwarzchild space-time, as we have shown in the first chapter, the line element metric of this space reads as

$$ds^2 = -\left(1-\frac{2M}{r}\right)dt^2 + \left(1-\frac{2M}{r}\right)^{-1}dr^2 + r^2\left(d\theta^2 + \sin^2\theta d\phi^2\right). \tag{2.2}$$

The spherically symmetric manifold has three Killing vector fields satisfying the commutation relations of the $SO(3)$ group, which is a three-dimensional rotation group. These Killing vector fields create a sphere S^2. Moreover, any vacuum spherically symmetric metric possesses a timelike Killing vector [6, 34]. The two Killing vectors that lead to the conservation of the direction of angular momentum imply that $\theta = \frac{\pi}{2}$. The Killing vector of the timelike type is given by

$$k_t = \left(-\left(1-\frac{2M}{r}\right), 0, 0, 0\right). \tag{2.3}$$

The Killing vector leading to the conservation of the angular momentum magnitude is

$$k_r = \left(0, 0, 0, r^2\sin^2\theta\right) = \left(0, 0, 0, r^2\right). \tag{2.4}$$

Using the Eq.(2.1), we obtain

$$\begin{aligned} \kappa^2 &= -\frac{1}{2}\left(\nabla^t k^r \nabla_t k_r + \nabla^r k^t \nabla_r k_t\right), && (2.5) \\ &= -\nabla^t k^r \nabla_t k_r. && (2.6) \end{aligned}$$

Then, the surface gravity of the Schwarzschild black hole is expressed by the following formula

$$\kappa = \frac{1}{4M}. \tag{2.7}$$

As is evident from this equation, the zeroth law is verified. It is worth noting that the thermodynamic analogue of this law is that the temperature of a body in thermal equilibrium is constant. J. Bardeen, B. Carter, and S. Hawking demonstrated this law for any solution of the Einstein equations.

Law 1 : The first law of black hole mechanics affirms that when a small change is made to the black hole parameters, there exists a relationship corresponding to changes in the area of its event horizon δA, the angular momentum δJ, and the electric charge δQ. These relationships are mediated by the surface gravity κ, the angular velocity Ω, and the electrostatic potential Φ parameters. This law is expressed as follows

$$\delta M = \frac{\kappa}{8\pi}\delta A + \Omega\delta J + \Phi\delta Q, \tag{2.8}$$

serves as an analogue to the first law of thermodynamics. It is noteworthy that Eq.(2.8) exhibits the same structural form as the first principle of thermodynamics for a grand-canonical system, which describes the variation of its internal energy E in the following manner

$$\delta E = T + \mu\delta N - P\delta V, \tag{2.9}$$

where S represents the entropy of the system. N stands for the number of particles, P denotes pressure, and V signifies the volume. The comparison of the two expressions (2.8) and (2.9), coupled with the application of the zeroth law, allows one to establish the identification between the entropy of the black hole and its event horizon area

$$S \propto A, \tag{2.10}$$

where the area of the horizon can be calculated using the following equation

$$A = r_h^2 \int_0^{\pi} d\theta \int_0^{2\pi} \sin\theta d\phi. \tag{2.11}$$

This proportionality between the entropy and the area of the event horizon can be established by a quantum study.

Second law: This law corresponds to the area theorem, which is the counterpart of the second law of thermodynamics. This theorem states that the area of the event horizon can never decrease over time for of the Einstein equation solutions in the presence of matter. This statement provides an analogy between the increase of the entropy in classical thermodynamics and the increase of the total event horizon area in the black hole context.

Third law : The third law of thermodynamics states that it is impossible to reach absolute zero temperature. It asserts that it is fundamentally impossible to lower the temperature of a system to $T = 0$, regardless of the number of physical processes. In a similar vein, this concept can be translated as the impossibility of reaching a certain state, represented by $\kappa = 0$, by any sequence of operations.

Quantum aspect of black holes

The similarity between the mechanical laws of the black hole and those of thermodynamics is purely formal. In particular, the analogy between mass and energy, surface gravity and temperature, and horizon area and entropy might appear questionable. One key reason for doubting a thermodynamic interpretation is the fundamental characteristic of a classical black hole (it is entirely black). This means that it only absorbs incoming energy and does not emit any energy. Consequently, it is typically assigned a temperature of zero, which challenges the idea of the surface gravity being directly equated to temperature at the classical level. Therefore, the apparent connection between the mechanical laws of the black holes and the four principles of thermodynamics might seem to be nothing more than a simple analogy [19].

To address this challenge, a deeper examination of the black holes is required within the framework of quantum field theory. Within this framework, Stephen Hawking demonstrated that when quantum effects are taken into account, the black holes can undergo a process known as Hawking radiation. This process indicates that the black holes must emit photons, similar to a black body with a nonzero temperature. This quantum perspective provides a more nuanced understanding of black hole behaviors, bridging the gap between black hole mechanics and thermodynamics. This reveals that the black holes can indeed possess a temperature and emit radiations due to quantum effects.

In quantum mechanics, the vacuum is a very complex and fundamental concept. According to the following relationship

$$\Delta E \Delta T \geq \frac{\hbar}{2}, \tag{2.12}$$

a perfect vacuum does not exist because the variation in energy can be non-zero in a very short time of the order of constant of Planck divided by a time interval. The vacuum can spontaneously give rise to a particle-antiparticle pair, continually appearing and disappearing. These fluctuations are similar to the oscillations around zero of a harmonic oscillator. Under normal conditions, these fluctuations are undetectable and their average corresponds to zero energy. Near the event horizon of a black hole, the tidal forces generated by the black hole separates a particle from its corresponding antiparticle before they annihilate each other. The particle that is drawn away from the black hole by these tidal forces can escape and is recognized as the Hawking radiation. Conversely, the other particle ends up being absorbed by the black hole. Importantly, this absorption process involves a particle with a negative energy, which contributes to a reduction in the mass of the black hole [6,7,19]. Considering quantum effects, Hawking discovered that the black holes do emit radiation. This radiation exhibits a black body spectrum at a characteristic temperature

$$k_B T = \frac{\hbar \kappa}{2\pi c}, \tag{2.13}$$

where k_B is is the Boltzmann constant. Therefore, the expression for the entropy of the black hole takes the form

$$S = \frac{A k_B}{4\ell_p^2} \tag{2.14}$$

where $\ell_p = \sqrt{\frac{\hbar G}{c^3}}$ is the Plank length. To approach this entropy expression, we make an estimation using the second law of the black hole thermodynamics. For this purpose, we consider a cubic box of gas with a volume of l^3, a mass of m, and a temperature of T. Assume that the length of the box is greater than the thermal wavelength of the gas ($l \sim \hbar/T$). The descent of the gas into the Schwarzschild black hole of mass M with an air horizon

$A = 16G^2M^2$ will lead to a decreasing behavior in the entropy

$$\Delta S_{gaz} \sim -\frac{m}{T} \sim -\frac{ml}{\hbar}. \tag{2.15}$$

The cubic box will merge with the black hole when the distance ϱ between the two is of the order of l. For a Schwarzschild black hole, this distance is given by

$$\varrho = \int_{2GM}^{2GM+\delta r} \frac{dr}{\sqrt{1 - 2GM/r}} \sim \sqrt{GM\delta r}, \tag{2.16}$$

where $\varrho = l$ valid when $= l^2/GM$. The gas initially has mass m, but its energy seeing from infinity is redshifted as the box moves towards the black hole. Indeed, when the box reaches the distance $r = 2GM + \delta r$, the black hole gains the following mass

$$\Delta M \sim m\sqrt{1 - \frac{2GM}{2GM + \delta r}} \sim \frac{ml}{GM}. \tag{2.17}$$

As there is a variation in mass, it consequently leads to the following modification in the area of the black hole

$$\Delta A \sim G^2 M \Delta M \sim Gml. \tag{2.18}$$

This shows that the black hole must gain an entropy of the form

$$\Delta S_{BH} \sim -\Delta S_{gaz} \sim \frac{\Delta A}{\hbar G}. \tag{2.19}$$

Hawking was thus able to postulate that the black holes possess an entropy. This entropy is determined by the surface area A, as described by the following formula

$$S = \frac{k_B c^3 A}{4\hbar G}. \tag{2.20}$$

The calculation for the Schwarzschild black hole gives

$$S = \frac{4\pi k_B c^3 G M^2}{\hbar}. \tag{2.21}$$

On the other hand, if we consider matter falling into a black hole, the initial entropy of the matter is lost, and there is no compensation from a classical perspective. Consequently, the entropy of the Universe containing a black hole decreases over time, which contradicts the second law of thermodynamics. However, taking into account the quantum phenomena involved in the evaporation of a black hole, an entropy is created outside the black hole even as the area of the horizon decreases. This does not violate the area theorem, as the energy-momentum tensor associated with Hawking radiation does not satisfy the null energy condition [19,34]. Furthermore, by feeding matter into the black hole, the area of the horizon increases according to the first law, even if the entropy of the region outside the black hole decreases. These considerations, therefore, lead us to reformulate the second law as follows

$$S = S_{BH} + S_{\text{matter}}, \qquad \delta S \geq 0. \tag{2.22}$$

Another important concept that can be extracted from quantum studies is the lifetime of a black hole. The energy E radiated by a black hole is given by the formula of Stefan Boltzman as follows

$$\frac{dE}{dt} = A\sigma T^4, \tag{2.23}$$

where σ is the Boltzman constant. As the black hole emits more and more energy, its mass decreases, which increases its temperature and accelerates the radiation. It has been shown that a black hole of mass M, isolated in a vacuum, has a lifetime of

$$\tau = 2,095.10^{67}\left(\frac{M}{M_{\text{sun}}}\right) \text{years}. \tag{2.24}$$

A solar-mass black hole would therefore survive for approximately 2.10^{67} years after the temperature of the Universe drops below 60 nanokelvins. A black hole with a mass of 1 kg would only survive for 0.083 seconds before evaporating. Therefore, the end of a black hole evaporation is always explosive, regardless of its initial mass.

2.1.2 Thermodynamic quantities of the black holes

In the first law of the black hole thermodynamic, the mass of the black hole is interpreted as the internal energy. However, it was suggested in [25, 26, 41] that a more accurate interpretation is to consider the mass as the enthalpy which is the total energy of a system that includes the internal energy of a system and the energy required to displace the vacuum energy of its environment PdV. Notably, in this context, there is an absence of the term PdV in Eq.(2.8), which signifies a lack of consideration for volume change at ambient pressure P. This problem was solved by introducing the cosmological constant Λ [36, 37]. A natural pressure candidate emerges as $P = \Lambda/(8\pi)$. Indeed, the volume of the black hole is then defined as the thermodynamic variable conjugate to P. For an asymptotically AdS black hole space-time, the volume of the black hole is given by

$$V = \left(\frac{\partial M}{\partial P}\right)_{S,Q,J}. \tag{2.25}$$

Initially, this variable was onstructed with a geometric meaning as a finite, effective volume for the region beyond the AdS black hole horizon. Subsequently, it was highlighted that the Eq.(2.25) remains unaffected by any specific geometric volume for the majority of the black holes [34, 38, 39], emphasizing that it should be recognized as a thermodynamic volume. The formulation (2.25) was initially associated to an asymptotically AdS black hole spacetime. However, it has been revealed that taking the limit towards asymptotically flat spacetimes ($P \to 0$) often yields a finite outcome for the thermodynamic volume, seamlessly connected to its AdS counterpart. This discovery offers a method for defining the thermodynamic volume of asymptotically flat black holes. Applying this concept to the charged AdS black hole spacetime, For instance, one gets the thermodynamic volume of the Schwarzschild black hole in four dimensions as follows

$$V = \frac{4}{3}\pi r_h^3. \tag{2.26}$$

Using the concept of the heat capacity to black holes is unconventional, particularly in the context of thermodynamics. In classical thermodynamics, the heat capacity is a measure of the heat required to increase the temperature of a system by a specific amount. Similarly, in black hole thermodynamics, this concept is adapted to understand how the mass of a black hole responds to changes in its temperature. Indeed, it is formulated as follows

$$C_p = T\left(\frac{\partial S}{\partial T}\right)_{P,Q,J}. \tag{2.27}$$

The sign of the heat capacity is a crucial factor to understand how the mass of a black hole responds to changes in the temperature, providing indications of its overall stability. A positive heat capacity suggests a relatively stable system where an increase in the temperature leads to an increase in mass. A decrease in temperature results in a decrease in mass [31, 32, 34]. Indeed, the black holes can absorb or emit energy without undergoing drastic changes. They are somewhat analogous to systems with a positive heat capacity in classical thermodynamics, where the temperature changes are proportional to the added or removed energy. Conversely, a negative heat capacity means that when the temperature increases, the mass tends to decrease. Despite its counter-intuitive nature, a negative heat capacity does not necessarily imply instability. It can be tied to the emission of Hawking radiation. As the black hole loses mass through radiation, its temperature decreases, creating a self-regulating mechanism. This process stabilizes the black hole against small fluctuations in the temperature.

The Gibbs free energy, commonly known as the thermodynamic potential, holds a pivotal role in describing and predicting the behavior of physical systems, and plays the same crucial role in understanding the thermodynamic stability and phase transitions of the black holes [34]. It is defined as the maximum reversible work that can be performed by a system at constant temperature and pressure. Generally, the Gibbs free energy G is expressed by the following equation

$$G = H - TS, \tag{2.28}$$

where H is the enthalpy. We will show in the following sections that the behavior of this energy is particularly useful for understanding phase transitions in black holes, critical points, stability and system characteristics.

2.2 Black hole stability and phase transitions

In this section, we delve into the examination of both the stability and the phase structures of the black holes introduced in the first chapter. Additionally, we elucidate the various transitions that can occur. Then, we draw parallels between these transitions and classical thermodynamic ones.

2.2.1 Ordinary black holes

The thermodynamical behavior of black holes is encoded in the metric function. We start with the Schwarzschild black hole. From Eq.(1.54), the metric function is given by

$$f(r) = 1 - \frac{2M}{r} \tag{2.29}$$

Using Eqs.(2.27) and (2.28), we get the associated thermodynamical quantities

$$\begin{aligned} M &= \frac{r_h}{2}, && (2.30)\\ T &= \frac{1}{4\pi r_h}, && (2.31)\\ G &= \frac{1}{16\pi T}, && (2.32)\\ C_P &= -2\pi r_h^2, && (2.33) \end{aligned}$$

where the r_h is the horizon radius. In Fig.(2.1), we plot the variation of the Gibbs free energy in terms of the temperature. Since this potential energy and the heat capacity are positive whatever the value of the mass, the black hole has one unstable phase. The Shwarzschild black hole has no interesting features and indicates no phase transitions. To identify the effect of the second parameter, we consider the Reissner–Nordstrom solution where the metric function takes the following expression

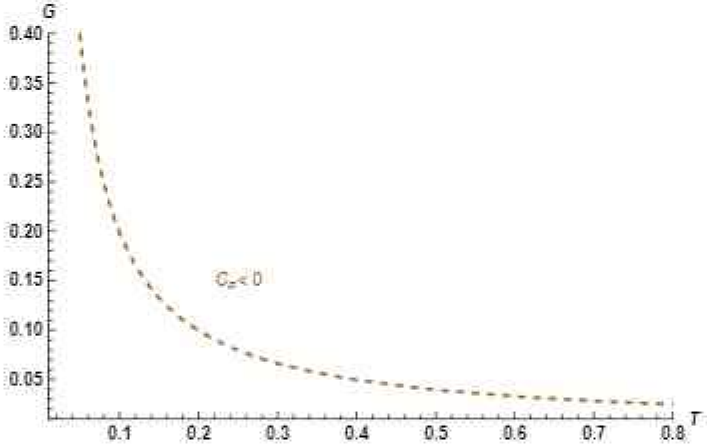

Figure 2.1: *Variation of the Gibbs free energy in terms of the temperature for Schwarzschild BH.*

$$f(r) = 1 - \frac{2M}{r} + \frac{Q^2}{r^2}. \tag{2.34}$$

The associated thermodynamic quantities are given by

$$\begin{aligned} M &= \frac{r_h^2+Q^2}{2r_h}, && (2.35)\\ T &= \frac{r_h^2-Q^2}{4\pi r_h^3}, && (2.36)\\ G &= \frac{r_h^2+3Q^2}{4r_h}, && (2.37)\\ C_p &= \frac{2\pi r_h^2(r_h^2-Q^2)}{3Q^2-r_h^2}. && (2.38) \end{aligned}$$

In this case, the specific heat capacity could be positive if the following constraint is verified

$$|Q| < r_h < \sqrt{3}|Q| \Rightarrow \frac{\sqrt{3}M}{2} < |Q| < M. \tag{2.39}$$

This provides two branches. The first one is associated with the small strongly charged black holes with positive C_p and the the second one has a negative specific heat capacity which is unstable. These two branches are clearly illustrated in Fig.(2.2) where we present the variation of the Gibbs free in terms of the temperature. As in the case of the Schwarzschild black hole, no interesting thermodynamic features are presented.

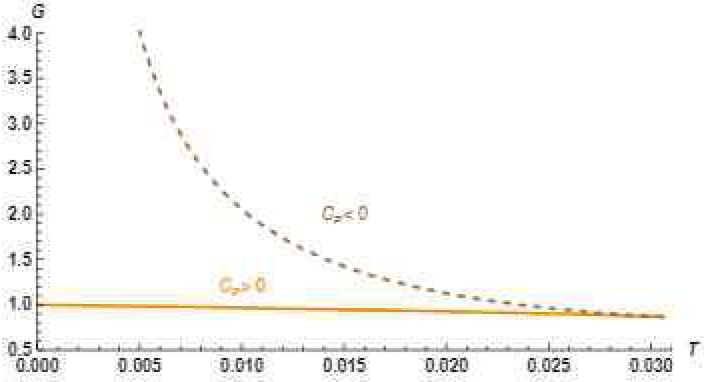

Figure 2.2: *Variation of RN-BH Gibbs free energy in terms of the temperature for* $Q=1$.

For the rotating black holes, we use the metric expression, given by Eq.(1.69) in order to obtain following thermodynamics quantities

$$
\begin{aligned}
M &= \frac{r_h^2 + a^2}{2r_h^2}, && (2.40)\\
T &= \frac{r_h}{2\pi(a^2 + r_h^2)} - \frac{1}{4\pi r_h}, && (2.41)\\
G &= \frac{3a^2 + r_h^2}{4r_h}, && (2.42)\\
C_p &= \frac{2\pi(r_h^2 - a^2)(r_h^2 + a^2)^2}{3a^4 + 6r_h^2 a^2 - r_h^4}. && (2.43)
\end{aligned}
$$

In Fig.(2.3), we plot the Gibbs free energy in terms of the temperature. The behavior of this energy closely resembles that of the charged black hole. Two branches are present. The lower one corresponds to a small fast rotating black hole with a positive specific heat capacity constrained by

$$\sqrt{3 + 2\sqrt{3}}|a| > r_h > |a| \Rightarrow M\sqrt{2\sqrt{3} - 3} < |a| < M. \qquad (2.44)$$

The upper branch of slowly rotating black holes has a higher Gibbs free energy and a negative specific heat and it is thermodynamically unstable.

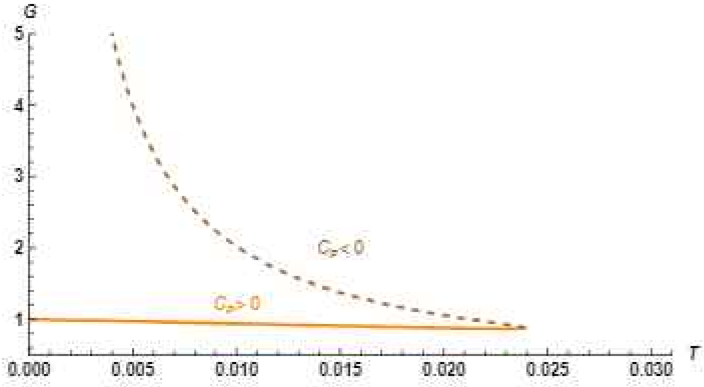

Figure 2.3: *Variation of Kerr BH Gibbs free energy in terms of the temperature for* $a = 1$.

2.2.2 AdS black holes

To explore how the cosmological constant enhances the thermodynamics of the black hole filed, we start with the simplest asymptotically AdS black hole. This black hole is described by the following Schwarzschild-AdS metric function

$$f(r) = 1 - \frac{2M}{r} + \frac{r^2}{\ell^2}. \tag{2.45}$$

As we are mentioned in the previous chapter, the AdS radius ℓ is expressed in terms of the cosmological constant

$$\ell^2 = 3/\Lambda. \tag{2.46}$$

The thermodynamic quantities read as follows

$$\begin{aligned} T &= \frac{\ell^2 + 3r_h^2}{4\pi r_h \ell^2}, & (2.47)\\ M &= \frac{r_h\ell^2 + r_h^3}{2\ell^2}, & (2.48)\\ G &= \frac{r_h\ell^2 - r_h^3}{4\ell^2}, & (2.49)\\ C_p &= \frac{2\pi r_h^2(3r_h^2 + \ell^2)}{3r_h^2 - \ell^2}. & (2.50) \end{aligned}$$

Analysing the expression of C_P, we deduce that, for $r_h > r_{\min} = \ell/\sqrt{3}$, C_P is positive. It is negative for $r_h < r_{\min}$, and indeterminable for $r_h = r_{\min}$. The minimum which corresponds to $r_{\min}$ is defined by

$$T_{\min} = \frac{\sqrt{3}}{2\pi\ell}. \tag{2.51}$$

Eqs.(2.47) and (2.49) allow us to write G as a function of the temperature. The variation of G at constant pressure is plotted in Fig.(2.4).

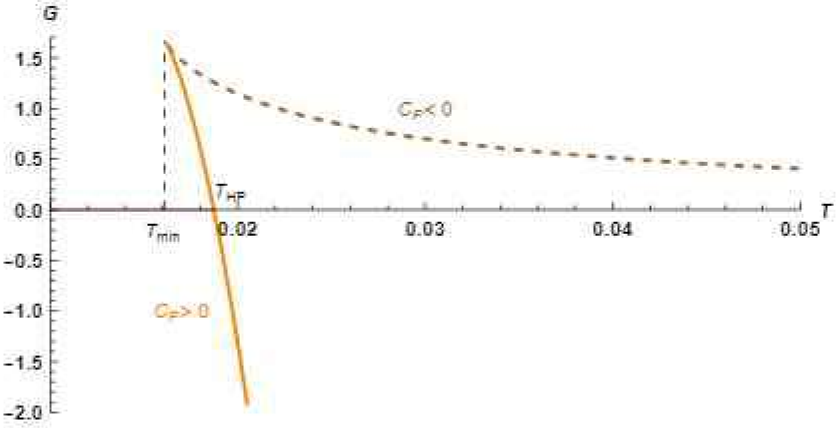

Figure 2.4: *Variation of AdS SH-BH Gibbs free energy in terms of the temperature for* $\ell = 17$.

For $T < T_{\min}$, no black hole can exist. Above this temperature, we have two branches of the black hole. The upper branch describes a black hole with a negative heat capacity. Thus, it represents an thermodynamically unstable system and cannot be in a thermal equilibrium. On the contrary, the lower part for $r_h > r_{\min}$ presents a positive heat capacity. This defines a locally thermodynamically stable system. We consider the AdS thermal space as an AdS space coupled to a radiation ($G = 0$). At a specific value of the temperature noted $T_{\rm HP}$, the Gibbs free energy is approximately zero, we observe a discontinuity in the first derivative of the Gibbs energy. Indeed, the computations gives

$$T_{\rm HP} = \frac{1}{\ell\pi}. \tag{2.52}$$

The Gibbs free energy becomes negative for $r_h > r_{\rm HP}$, marking a first-order phase transition. Thus, at $T = T_{\rm HP}$, there is a Hawking-Page phase transition a first-order transition between the large (stable) black hole and thermal radiation in anti de Sitter space. This transition has been largely studied in the context of AdS/CFT (Anti-de Sitter/Conformal Field Theory) correspondence [12]. It is linked to the duality between a gravitational theory in AdS spacetime and a non-gravitational conformal field theory defined on the boundary of that spacetime. Indeed, the black holes and the thermal AdS space are regarded as macroscopic emergent states or phases within the framework of the AdS/CFT correspondence [34,36]. It also interpreted as a confinement/de-confinement phase transition in the gluon plasma with double quarks.

The phase transition occurs when the Gibbs free energy G of the AdS black hole becomes zero, which defines the two-phase coexistence line as follows

$$P_{\rm coexistence} = \frac{3\pi}{8}T^2. \tag{2.53}$$

This line is shown in Fig.(2.5). Similar to the solid/liquid phase transition, this line continues up to an infinite pressure, where a thermal radiation acts as a solid.

To explore how the presence of the charge will affect the phase structure of the AdS black holes, we consider the metric of a RN-AdS black hole given in Eq.(1.60). The thermodynamic

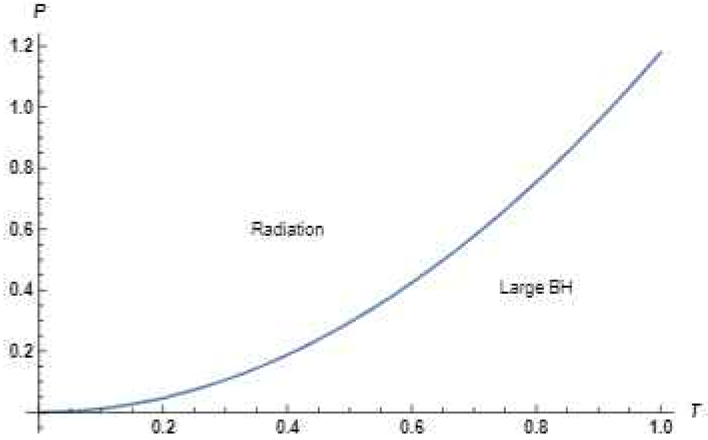

Figure 2.5: *Two-phase coexistence line in* $(P-T)$ *diagram.*

quantities take the following forms

$$
\begin{aligned}
T &= \frac{\ell^2(r_h^2-Q^2)+3r^4}{4\pi r_h^3\ell^2}, && (2.54)\\
G &= \frac{\ell^2 r_h^2-r_h^4+3Q^2\ell^2}{4\ell^2 r_h}, && (2.55)\\
C_p &= 2\pi r_h^2\frac{3r_h^4+\ell^2 r_h^2-Q^2\ell^2}{3r_h^4-\ell^2 r_h^2-3Q^2\ell^2}. && (2.56)
\end{aligned}
$$

In this case, the unstable phase is constrained by

$$
\frac{\ell\sqrt{1-\sqrt{1-36Q^2/\ell^2}}}{\sqrt{6}} < r_h < \frac{\ell\sqrt{1+\sqrt{1-36Q^2/\ell^2}}}{\sqrt{6}}, \tag{2.57}
$$

otherwise the specific heat capacity is positive. In Fig.(2.6), the behavior of the Gibbs free energy of the charged AdS black hole is displayed for a fixed value of the charge $Q = 0.11$ (canonical ensemble). The swallowtail behavior of this energy proves that this black hole exhbits a first order small-black hole/large black hole (SBH/LBH) phase transition marked by a non-analytic behavior in the Gibbs free energy, indicating the coexistence of the two phases [34].

It is worth noting that the thermodynamic properties of rotating AdS black holes in four dimensions closely resemble those of the charged AdS black holes. The thermodynamic

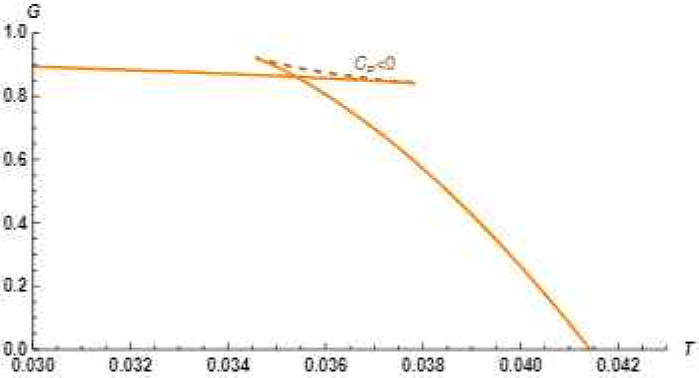

Figure 2.6: *Variation of the Gibbs free energy in terms of the temperature for $\ell = 1$ and $Q = 0.11$.*

quantities of the Kerr-AdS black holes are given by

$$T = \frac{1}{2\pi r_h}\left(\frac{(a^2+3r_h^2)(r_h^2/\ell^2+1)}{2(a^2+r_h^2)} - 1\right), \tag{2.58}$$

$$S = \frac{\pi\ell^2(a^2+r_h^2)}{\ell^2-a^2}, \tag{2.59}$$

$$G = \frac{(r_h^2+3a^2)\ell^4 - (r_h^2-a^2)^2\ell^2 + (a^2+3r_h^2)a^2r_h^2}{\ell^2 r_h(\ell^2-a^2)}. \tag{2.60}$$

The Gibbs free energy behavior is qualitatively similar to Fig.(2.6) with fixed a replacing the fixed charge. Notably, similar qualitative patterns emerge when examining the behaviors of the charged and rotating AdS black holes.

2.3 Criticality behaviors and universality

The concept of an equation of state is a fundamental aspect of thermodynamics, describing the relationship between state variables. Similar to the ordinary thermodynamic systems, black hole systems may exhibit critical behaviors near phase transitions [42,43]. The equation of state can play a crucial role in understanding and identifying critical phenomena. Moreover, the variation of the entropy in terms of the temperature is relevant in the identification of interesting universal quantities.

2.3.1 HP transition and universality behaviors

To get the equation of state of the Schwarzschild-AdS black hole, we use the associated temperature and the the pressure expressions. Indeed, we obtain the following equation

$$P=\frac{T}{v}-\frac{1}{2\pi v^2}, \tag{2.61}$$

where v is the specific volume of the fluid given by

$$v=2\left(\frac{3V}{4\pi})\right)^{1/3}=2r_h. \tag{2.62}$$

In Fig.(2.7), we present this equation of state for various temperatures. For each isotherm curves, there is a maximum point where the specific volume attains the value of $\frac{1}{\pi T}$.

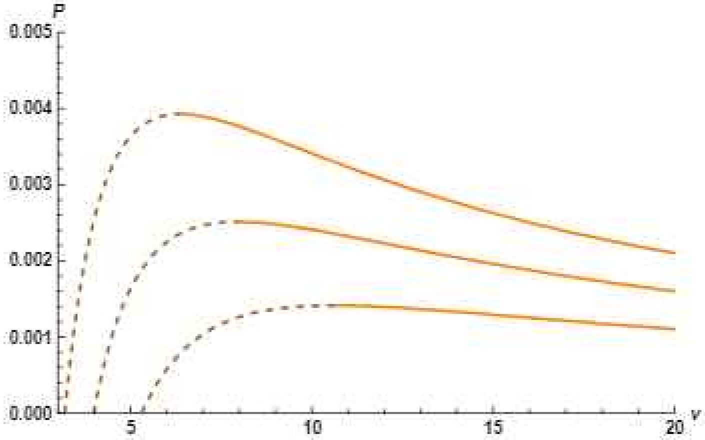

Figure 2.7: *$(P-v)$ diagram of SH-AdS black holes for $T=0.03$, $T=0.04$, and $T=0.05$.*

The section where the pressure is an increasing function is associated with small black holes, while the decreasing section corresponds to large black holes. For this black hole, non-critical points are present, as the coexistence line is continuous, and the equation of state does not exhibit any critical behavior. However, an interesting investigation shows that the Hawking-Page phase transition of AdS black holes involves two universal critical constants [46,47]. This can be starting from the the third law of thermodynamic which asserts that when the temperature approaches the absolute zero, its entropy converges towards a fixed value noted $S_{\min}$. It is worth noting that the Gibbs free energy reaches a maximum at this point. The two universal constants at the HP transition point are defined as follows

$$c_S = \frac{S_{HP} - S_{min}}{S_{min}}, \tag{2.63}$$

$$c_T = \frac{T_{HP} - T_{min}}{T_{min}}. \tag{2.64}$$

Amazingly, these two critical expressions have the same numerical values for non rotating black holes. Concretely, the calculations give

$$c_S = 2, \tag{2.65}$$

$$c_T = \frac{2-\sqrt{3}}{\sqrt{3}}. \tag{2.66}$$

Equivalently, they can be given by

$$S_{HP} = 3S_{min}, \tag{2.67}$$

$$T_{HP} = \frac{2\sqrt{3}}{3}T_{min}. \tag{2.68}$$

For the rotating AdS black holes, however, these ratios depend on other thermodynamic parameters [47].

2.3.2 Criticality in LBH/SBH phase transitions

To unveil the criticality behaviors for the charged AdS black hole, we consider the associated equation of state which is given by

$$P = \frac{T}{v} - \frac{1}{2\pi v^2} + \frac{2Q^2}{\pi v^4}. \tag{2.69}$$

The $(P - v)$ diagram of this equation is depicted in Fig.(2.8). The critical point occurs when $P(v)$ has an inflection point. Evidently, for $T < T_c$, there is an inflection point that can obtained from

$$\frac{\partial P}{\partial v} = 0, \qquad \frac{\partial^2 P}{\partial v^2} = 0, \tag{2.70}$$

which gives

$$P_c = (96\pi Q^2)^{-1}, \qquad T_c = \sqrt{6}(18\pi Q)^{-1}, \qquad v_c = 2\sqrt{6}Q. \tag{2.71}$$

The isotherm curves illustrated in Fig.(2.8) mimic qualitatively the behavior of the Van

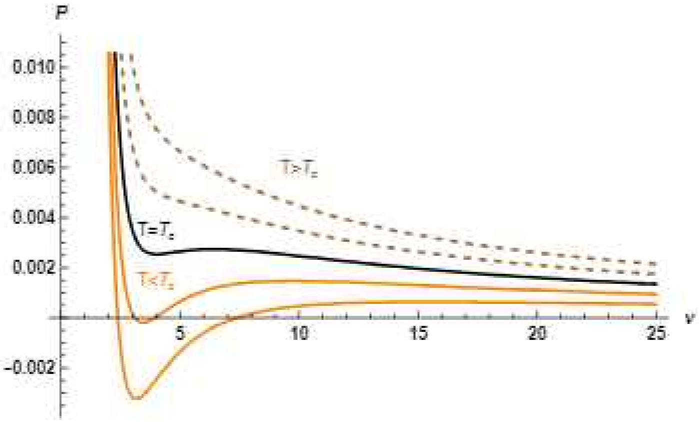

Figure 2.8: *$(P-v)$ diagram of charged black hole for $Q=1$.*

der Waals fluids. Moreover, an other critical ratio can be defined for the charged black hole linked to the above critical values. This ratio is found to be

$$\frac{P_c v_c}{T_c} = \frac{3}{8}. \tag{2.72}$$

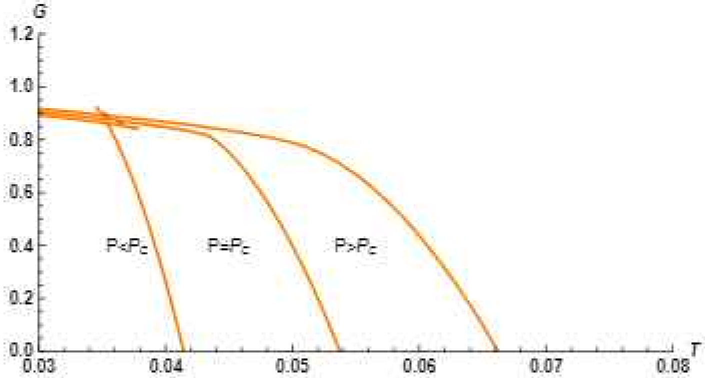

Figure 2.9: *Variation of the Gibbs free energy in terms of the temperature for $Q=1$.*

This value is precisely identical to that of the Van der Waals fluid and it stands as a universal number predicted for any RN-AdS black hole with arbitrary charge [42–44]. In Fig.(2.9), we illustrate the behaviors of the Gibbs free energy in terms of the temperature for tree values of the pressure. It is clear from the figure that the characteristic swallowtail behavior is observed only for $P < P_c$, corresponding to a small/large black hole phase transition. In this case, the corresponding coexistence line terminates at the critical point (P_c, v_c, T_c).

2.4 Geothermodynamics of black holes

In this section, we delve into the exploration of the thermodynamic geometry of black holes. This approach provides a solid tool to understand the microscopic and the phase structure of black holes. In this context, one often considers a geometric space described by thermodynamic variables as coordinates to study certain properties of black holes [111–115]. This way is motivated by the idea suggesting that the relationships and the behavior of thermodynamic systems can be effectively captured and analyzed in a geometric space.

2.4.1 Riemannian thermodynamic potential

It has been considered that the Hessian of the thermodynamic potential function $\Psi(X)$ given by

$$g_{ij} = \partial_i \partial_j \Psi(X), \tag{2.73}$$

can be thought of as a Riemannian metric on the thermodynamic state space. The coordinates X_i generate some preferred affine spaces [42]. The Ruppeiner geometry is obtained by taking $\Psi = S$. Whereas, in the Weinhold geometry, the metric is obtained from the hessian of the internal energy U [111, 114]. In the the ordinary thermodynamic, the coordinates of the space are choosing to be the extensive variables of the system. Interestingly, the two metrics are conformally related via the following identification

$$ds^2 = g^R_{ij} dM^i dM^j = \frac{1}{T} g^W_{ij} dS^i dS^j. \tag{2.74}$$

A systematic way to calculate the Ricci curvature scalar R was developed by Weinhold [115] and Ruppeiner [114]. The sign of R has been related to the type of interparticle interactions.

- $R > 0$ is associated to a repulsive interaction as the ideal Bose gas.
- $R < 0$ corresponds to o an attractive interaction as the ideal Fermi gas.
- $R = 0$ is associated with no interaction like the ideal gas.

Moreover, the critical points are defined by a divergence behavior of the scalar curvature. Interestingly, this geometric quantity can share the same divergence behaviors provided by the heat capacity. Indeed, this geometrical quantity is exploited to study the phase structure and the critical points of black holes as a nice interplay between thermodynamics and Riemannian geometrics.

2.4.2 Geothermodynamics of RN-AdS black holes

As elucidated in the preceding sections, the charged AdS black hole reveals noteworthy thermodynamic implications. Consequently, in the subsequent discussion, we examine the geothermodynamics associated with this specific category of black holes. Indeed, we express the mass in terms of the entropy

$$M = \frac{\sqrt{S}}{2} + \frac{Q^2}{2\sqrt{S}} + \frac{S^2}{2\ell^2\sqrt{S}}. \tag{2.75}$$

The Hawking temperature can be expressed also in terms of the entropy as follows

$$T = \frac{\partial M}{\partial S} = \frac{1}{4\sqrt{S}} - \frac{\sqrt{S}Q^2}{S^2} + \frac{3S}{4\ell^2\sqrt{S}}. \tag{2.76}$$

The electric potential is given by

$$\Phi = \frac{\partial M}{\partial Q} = \frac{Q}{\sqrt{S}}. \tag{2.77}$$

Using the above equations, we can get the Weinhold metric in the following form

$$ds_W^2 = \frac{1}{8S^{3/2}}\left(-1 + \frac{3S}{\ell^2} + \frac{3Q^2}{S}\right)dS^2 - 8QdSdQ + 8SdQ^2. \tag{2.78}$$

The appropriate internal energy U of the RN-AdS black hole is given by

$$U = M - \Phi Q. \tag{2.79}$$

Therefore, the Ruppeiner metric becomes

$$ds_R^2 = dUd\left(\frac{1}{T}\right) - \frac{Q}{T^2}dTd\Phi - \frac{1}{T}dQd\Phi. \tag{2.80}$$

Considering the Ruppeiner metric, the curvature scalar reads as

$$R \;=\; \frac{9}{\ell^2}\frac{\left(\frac{3S}{\ell^2}+\frac{Q^2}{S}\right)\left(1-\frac{S}{\ell^2}-\frac{Q^2}{S}\right)}{\left(1-\frac{3S}{\ell^2}-\frac{Q^2}{S}\right)^2\left(1+\frac{3S}{\ell^2}-\frac{Q^2}{S}\right)}. \tag{2.81}$$

We can also express this scalar in terms of the horizon radius

$$R=-\frac{18r_h^6\left(3Q^2-r_h^2\right)+3\ell^2r_h^2\left(10Q^4-9Q^2r_h^2+3r_h^4\right)+\ell^4\left(Q^2-r_h^2\right)^2}{\pi\ell^4\left(3r_h^4/\ell^2-Q^2+r_h^2\right)\left(3r_h^4/\ell^2+3Q^2-r_h^2\right)^2}. \tag{2.82}$$

The curvature scalar shares similarities with the divergence behaviors associated with the heat capacity in terms either of the event horizon or the entropy. At constant charges, the heat capacity should be computed. Indeed, it takes the following form

$$C_Q=T\left(\frac{\partial S}{\partial T}\right)_Q=\frac{2\pi r_h^2\left(\ell^2\left(r_h^2-Q^2\right)+3r_h^4\right)}{\ell^2\left(3Q^2-r_h^2\right)+3r_h^4}. \tag{2.83}$$

It has been observed the phase transition LBH/SBH can occur when $Q<Q_c$. We consider, for instance, specific regions of the moduli space where one has used $\ell=1$. We find that the critical value is around $Q_c=0.408$. We illustrate the heat capacity variation as a function of r_h by considering constant charges, in the left and the right of Fig.(2.10) for $Q<Q_c$ and $Q>Q_c$, respectively.

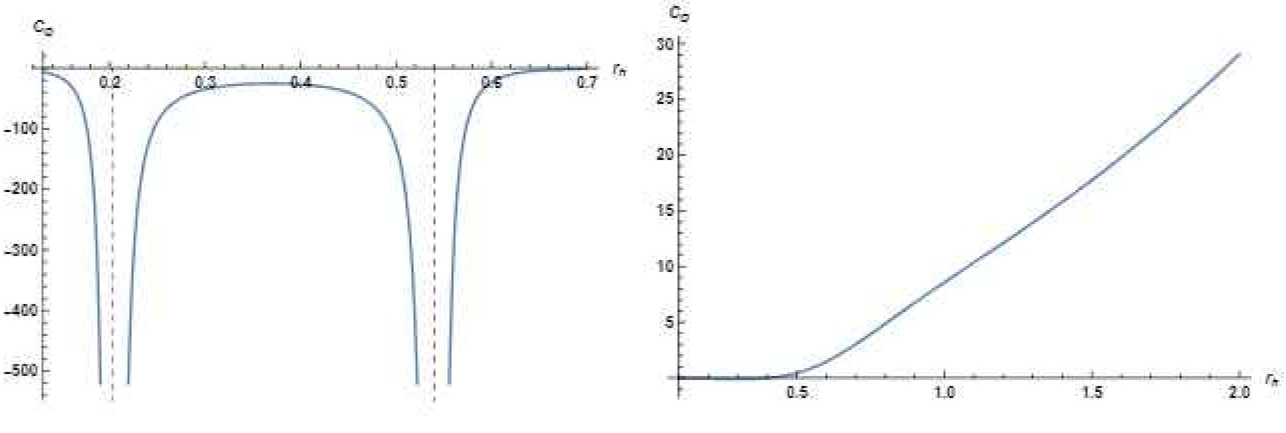

Figure 2.10: Variation of the specific heat capacity in terms of r_h for $Q=0.3$ left and $Q=0.5$ right.

For $Q<Q_c$, the phase transition is manifested, ensured by discontinuous curve behaviors. However, for $Q>Q_c$, a continuous line with non divergence behaviors is obtained showing that there is only one black hole solution. In Fig.(2.11), we depict the variation of the scalar curvature in terms of the horizon radius, using the same constant values as those employed for the heat capacity plots. The figure clearly indicates that the same critical behavior observed in the heat capacity is shared with the curvature scalar. Moreover, even for non-phase transition behavior, this scalar exhibits also continued variations.

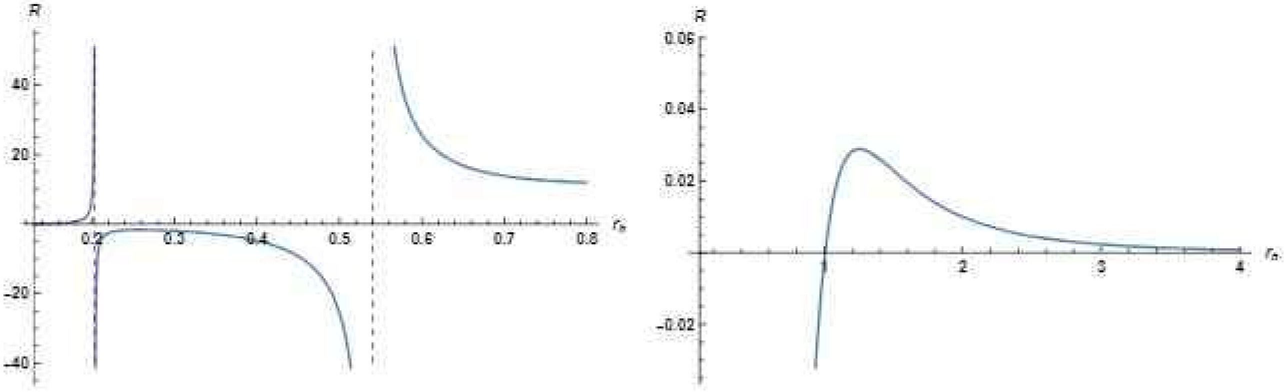

Figure 2.11: Variation of Ruppeiner curvature in terms of r_h for $Q = 0.3$ left and $Q = 0.5$ right.

CHAPTER 3

Optical Aspects of Black Holes

The study of the optical aspect of black holes becomes a warm subject being largely investigated using analytical and numerical approaches. The significant interest in this area has received backing and motivation from the empirical findings presented by EHT collaborations and gravitational wave detections [48–52]. A detailed analysis reveals that two crucial aspects have been explored: the shadow and the deflection angle of light rays in proximity to black holes [60–63, 65]. In this chapter, we investigate the characteristics of shadows and light behaviors in the vicinity of certain AdS black holes. This has been motivated by recent investigations of thermodynamical behaviors. Moreover, we provide constraints on the studied black holes from the observational EHT data.

3.1 Shadows of black holes

In this section, we first present a general review on the formalism used to obtain the shadow of rotating and non rotating black holes by considering the RN and the Kerr solutions. Then, we study shadows of rotating Bardeen AdS black holes by investigating the notions of the shape and the distortion behaviors. Furthermore, we explore the effect of the quintessential field on these shadow properties.

3.1.1 Shadow of black holes

The shadow of a black hole is defined as the apparent boundary or the critical curve which appears when light rays asymptotically approach an unstable circular orbit called photon sphere and return towards the observer. This information is encoded on the null geodesics around black holes [68–70]. Indeed, we start from the following Hamiltonian

$$\mathcal{H} = \frac{1}{2} g^{\mu\nu} p_\mu p^\nu, \tag{3.1}$$

where p_μ is the momentum vector of the photon expressed in terms of the lagrangian density of the system

$$p_\mu = \frac{\partial \mathcal{L}}{\partial \dot{x}^\mu}. \tag{3.2}$$

In this context, the dot represents the derivative concerning the affine parameter that controls the trajectory. To illustrate the calculations, we consider the metric of the RN black hole solution

$$f(r) = 1 - \frac{2M}{r} + \frac{Q^2}{r^2}. \tag{3.3}$$

Considering the equatorial plane defined by $\theta = \pi/2$, we can obtain

$$\begin{aligned} p_t &= f(r)\dot{t} = E & (3.4)\\ p_r &= \frac{\dot{r}}{f(r)} & (3.5)\\ p_\phi &= r^2\dot{\phi} = L^2, & (3.6) \end{aligned}$$

where L is the angular momentum of photon and E is the energy [68, 70]. Substituting these in Eq.(3.1), we obtain the Hamiltonian of the system which takes the form

$$\mathcal{H} = \frac{1}{2}\left(\frac{L^2}{r^2} - \frac{E^2}{f(r)} + \frac{\dot{r}^2}{f(r)}\right). \tag{3.7}$$

Applying the Hamiltonian-Jacobi formalism, we find the equations of motion of the photon

$$\begin{aligned} \frac{dt}{d\lambda} &= \frac{E}{f(r)}, \\ \frac{dr}{d\lambda} &= \pm\sqrt{f(r)\left(\frac{E^2}{f(r)} - \frac{L^2}{r^2}\right)}, \\ \frac{d\phi}{d\lambda} &= -\frac{L}{r^2}. \end{aligned} \tag{3.8}$$

The complete motion the photon is defined through a radial effective potential $V_{eff}(r)$ satisfying the following equation

$$V_{eff}(r) + \dot{r}^2 = 0. \tag{3.9}$$

Using the Eq.(3.8), we can obtain the effective potential expression

$$V_{eff}(r) = \frac{b^2}{r^2}\left(1 - \frac{2M}{r} + \frac{Q^2}{r^2}\right) - 1, \tag{3.10}$$

where b is the impact parameter of the light rays defined as follows

$$b = \frac{L}{E}. \tag{3.11}$$

The derivation of this scalar quantity with respect to r is given by

$$\frac{dV_{eff}(r)}{dr} = -2b^2\left(\frac{1}{r^3} + \frac{3M}{r^4} + \frac{2Q^2}{r^5}\right). \tag{3.12}$$

The circular orbits are defined by the following conditions

$$V_{eff}(r)\Big|_{r=r_p} = 0, \qquad \frac{dV_{eff}(r)}{dr}\Big|_{r=r_p} = 0. \tag{3.13}$$

Combining Eqs(3.10) and (3.12), we get the trajectories

$$r^2 - 3Mr + 2Q^2 = 0. \tag{3.14}$$

This equation has two solutions which read as

$$r_p^+ = \frac{3}{2}M + \frac{1}{2}\sqrt{9M^2 - 8Q^2} \tag{3.15}$$

$$r_p^+ = \frac{3}{2}M - \frac{1}{2}\sqrt{9M^2 - 8Q^2}. \tag{3.16}$$

For the SW black hole ($Q = 0$), we get one solution $r_p^+ = 3M$. For the charged one, we consider only the physical solution r_p^+. This defines the distance between the center of the black hole and a point in space at which non-massive particles can move in a circular motion [65].

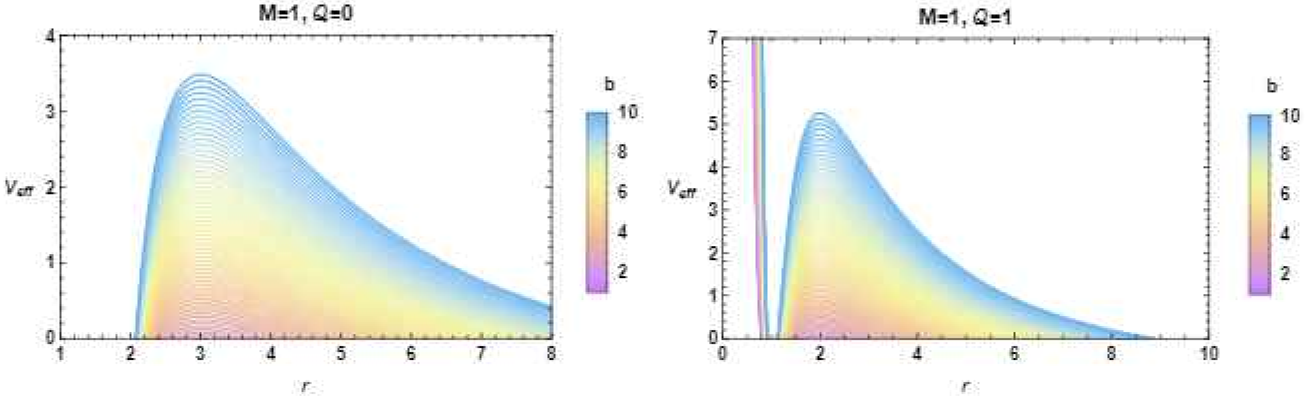

Figure 3.1: *Effective potential in terms of the radial coordinates r for different values of b .*

To understand the behavior of the light rays near to the black hole, we plot in Fig.(3.1) the variation of the effective potential in terms of radial components for charged and unchanged black holes. A close examination shows that the value of the effective potential increases with b for both types of black holes and the maximum potential corresponds to the value of the radius of the circular orbit. The behavior of the effective potential reveals that light coming from infinity can deviate by returning to infinity if $r > r_p$. If $r = r_p$, the light approaches the black hole by spiraling in to eventually describe a circle. Otherwise, the light from infinity leads to engulfment in a coiled path around a black hole.

We approach the shadow using the radial and the angular geodesic equations that appear in Eq.(3.8). Indeed, the equation of the photon orbit is formulated as follows

$$\frac{dr}{d\phi} = \pm\left(\frac{r^2}{b}\sqrt{1 - \frac{b^2 f(r)}{r^2}}\right). \tag{3.17}$$

The trajectories of the light rays are described by the following constraint

$$\left.\frac{dr}{d\phi}\right|_{r=r_p}=0. \tag{3.18}$$

Using Eq.(4.43), one can get

$$\frac{dr}{d\phi}=\pm r\sqrt{f(r)\left[\frac{r^2f(r_p)}{r_p^2f(r)}-1\right]}. \tag{3.19}$$

Considering the light rays emitted by a static observer located at r_{ob} and transmitted at an angle α_{ob}, we have

$$\cot\alpha_{ob}=\frac{\sqrt{g_{rr}}}{\sqrt{g_{\phi\phi}}}\left.\frac{dr}{d\phi}\right|_{r=r_{ob}}=\frac{1}{r\sqrt{f(r)}}\left.\frac{dr}{d\phi}\right|_{r=r_{ob}}. \tag{3.20}$$

Using Eq.(4.45), we obtain the angle of the observer

$$\sin^2\alpha_{ob}=\frac{f(r_{ob})r_p^2}{r_{ob}^2f(r_p)}. \tag{3.21}$$

In this scenario, we can establish the angular radius of the black hole shadow as a function of the radius of the photon circular orbit. Specifically, the radius of shadow observed by a stationary observer positioned at r_{ob} is expressed as

$$R_s=r_{ob}\sin\alpha_{ob}=R\left.\sqrt{\frac{f(r_{ob})}{f(R)}}\right|_{R=r_p}. \tag{3.22}$$

For a static observer located far from the black hole, we have $f(r_{ob})=1$. The apparent shape of the shadow of the black hole in such a space-time can be obtained using the celestial coordinates α and β. According to [60–63,65], these coordinates can be expressed as follows

$$\alpha = \lim_{r_{ob}\to+\infty}\left(-r_{ob}^2\sin\theta_{ob}\frac{d\phi}{dr}\right) \tag{3.23}$$

$$\beta = \lim_{r_o\to+\infty}\left(r_{ob}^2\frac{d\theta}{dr}\right) \tag{3.24}$$

where r_{ob} is the distance of the observe from the black hole. θ_{ob} indicates the angle of inclination between the line of the observer and the black hole's axis of rotation. The coordinate α represents the apparent orthogonal distance of the observed image from the axis of symmetry, while the coordinate β denotes the apparent perpendicular distance of the image from its projection onto the equatorial plane. It is noteworthy that the light has the capability to orbit around the black hole before returning to the observer, leading to the creation of the photon ring [60–63]. The region encircled by this ring is the shadow of the black hole. To illustrate this shadow, we use the celestial coordinate system. This coordinate system is illustrated in Fig.(3.2). These coordinates verify the following algebraic relationship

$$\alpha^2 + \beta^2 = R_s^2. \tag{3.25}$$

Upon close examination, it becomes evident that the non-rotating black hole shadows exhibit a circular shape. The dimension of the shadow diminishes as the charge value increases, while it enlarges with an increase in the mass value.

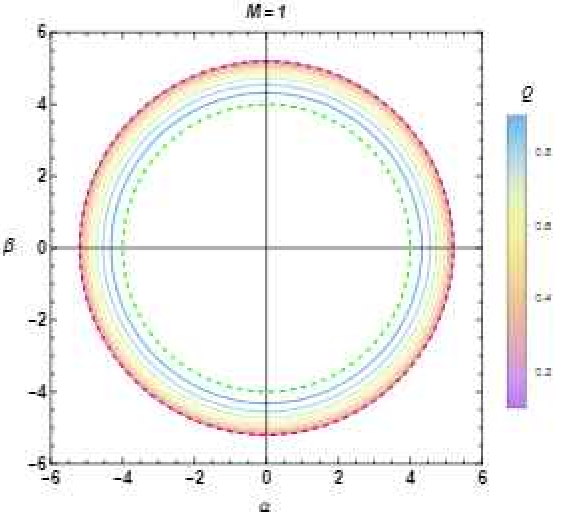

Figure 3.2: *Shadow of the RN black hole in the celestial plane for different values of the charge Q. The red and green circles correspond to the shadow of the Schwarzschild (SW) and extremal Reissner-Nordström (RN) black holes, respectively.*

To approach the shadow optical aspects of the rotating black holes, we consider the Kerr metric. The conservation of the momentum with respect to the coordinates t and ϕ is described by the following relations

$$p_t = \frac{\partial \mathcal{L}}{\partial \dot{t}} = g_{tt}\dot{t} + g_{t\phi}\dot{\phi} = -E \tag{3.26}$$

$$p_\phi = \frac{\partial \mathcal{L}}{\partial \dot{\phi}} = g_{t\phi}\dot{t} + g_{\phi\phi}\dot{\phi} = L. \tag{3.27}$$

After a calculation, we find

$$\begin{aligned}\Sigma\frac{dt}{d\lambda} &= a\left(L - aE\sin^2\theta\right) + \frac{r^2+a^2}{\Delta}\left(E\left(r^2+a^2\right) - aL\right) &(3.28)\\ \Sigma\frac{d\phi}{d\lambda} &= \left(L\csc^2\theta - aE\right) + \frac{a}{\Delta}\left(E\left(r^2+a^2\right) - aL\right). &(3.29)\end{aligned}$$

In the above equations, the separation of variables is necessary to obtain the equations of motions. Indeed, we use the Hamilton-Jacobi factorization based on the Carter method [16, 68, 70]. The Jacobi action is defined as follows

$$S = -Et + L\phi + S_r(r) + S_\theta(\theta). \tag{3.30}$$

It is denoted that $S_\theta(\theta)$ and $S_r(r)$ are functions which involve only θ and r spatial variables, respectively. This action verifies the Hamilton-Jacobi identity for massless particles given by

$$\frac{1}{2}g^{\mu\nu}\frac{dS}{dx^\mu}\frac{dS}{dx^\nu} + \frac{dS}{d\lambda} = 0. \tag{3.31}$$

Introducing the Carter constant, we can get the following system of equations

$$\begin{aligned}\Sigma^2\left(\frac{d\theta}{d\lambda}\right) + \left(L\csc\theta - aE\sin\theta\right)^2 - \left(L - aE\right)^2 &= \mathcal{K}, &(3.32)\\ \frac{\Sigma^2}{\Delta}\left(\frac{dr}{d\lambda}\right)^2 - \frac{\left(a^2E - aE + Er^2\right)^2}{\Delta} + \left(L - aE\right)^2 &= -\mathcal{K}. &(3.33)\end{aligned}$$

Immediately, we obtain

$$\begin{aligned}\Sigma\frac{dt}{d\lambda} &= a\left(L - aE\sin^2\theta\right) + \frac{r^2+a^2}{\Delta}\left(E\left(r^2+a^2\right) - aL\right) &(3.34)\\ \Sigma\frac{dr}{d\lambda} &= \sqrt{\mathcal{R}} &(3.35)\\ \sigma\frac{d\theta}{d\lambda} &= \sqrt{\Theta} &(3.36)\\ \Sigma\frac{d\phi}{d\lambda} &= \left(L\csc^2\theta - aE\right) + \frac{a}{\Delta}\left(E\left(r^2+a^2\right) - aL\right). &(3.37)\end{aligned}$$

For the rotating black holes, two impact parameters should be defined. Using the above conserved quantities, we define two parameters ξ and η as follows

$$\xi = \frac{L}{E}, \qquad \eta = \frac{\mathcal{K}}{E^2}. \tag{3.38}$$

The quantities $\mathcal{R}$ and Θ take the following forms

$$\mathcal{R} = E^2\left(\left(a^2 - a\xi + r^2\right)^2 - \Delta\left(\eta + (\xi - a)^2\right)\right) \tag{3.39}$$

$$\Theta = E^2\left(\eta - (\xi \csc\theta - a\sin\theta)^2 + (\xi - a)^2\right). \tag{3.40}$$

For the rotating model, the circular orbits are determined by the following two constraints

$$\mathcal{R}\,|_{r=r_p(a)} = 0, \quad \frac{d\mathcal{R}}{dr}\,|_{r=r_p(a)} = 0, \tag{3.41}$$

where $r_p(a)$ is the radius of the unstable circular orbit for the rotating black hole. Considering that $\Theta(\theta) > 0$ for $0 \leqslant \theta \leqslant 2\pi$, the above impact parameters can be obtained by solving Eq.(3.41). The computations provide

$$\xi = \frac{(3M - r_p(a))r_p^2(a) - a(M + r_p(a))}{a(r_p(a) - M)}, \tag{3.42}$$

$$\eta = \frac{r_p^3(a)(4a^2M - r_p(a)(3M - r_p(a))^2}{a^2(r_p(a) - M)^2}. \tag{3.43}$$

To visualize the shadow of the Kerr black hole, we could use the two celestial coordinates α and β. This can be derived from the null geodesics. Placing an observer at the inclination angle θ_{ob}, these coordinates are expressed as follows

$$\alpha = -\xi \csc\theta_{ob} \tag{3.44}$$

$$\beta = \pm\sqrt{\eta^2 + a^2\cos^2\theta_{ob} - \xi^2\cot^2\theta_{ob}}. \tag{3.45}$$

It should be noted that in the limit $a \to 0$, the two celestial coordinates are reduced to generate the geometric shape of the non-rotating shadow. By fixing the mass $M = 1$, we illustrate in Fig.(3.3) the shadow by varying a. From this figure, we can immediately deduce that a can be considered as a geometric parameter controlling the shape of the shadow by leading to a visible deformation. Indeed, for small values of the rotation parameter, the deformation of the apparent shape of the black hole is small. The main effect is to shift the shadow region in the (α, β) plane to the right. This shift is important for larger values of the rotation parameter. In order to obtain and analyze the geometric shadow data of this black hole, it is necessary to introduce the two geometric observables, the size parameter R_c and the distortion parameter δ_c which approximately characterize the shape of the shadow.

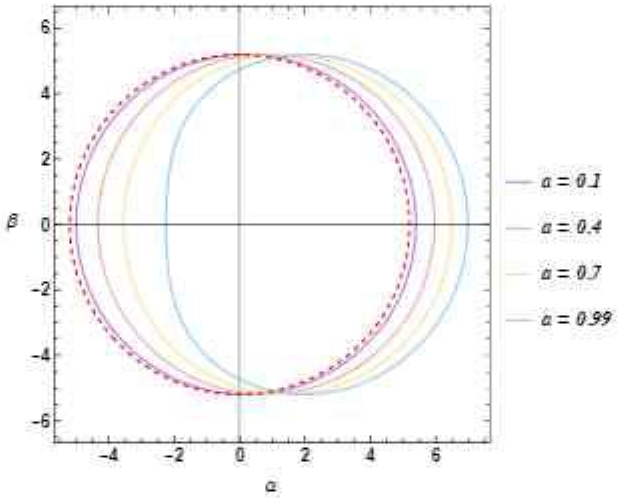

Figure 3.3: *Shadow of the Kerr black hole in the celestial plane for different values of the rotation parameter a. The red circle corresponds to the shadow of the Schwarzschild (SW) black hole.*

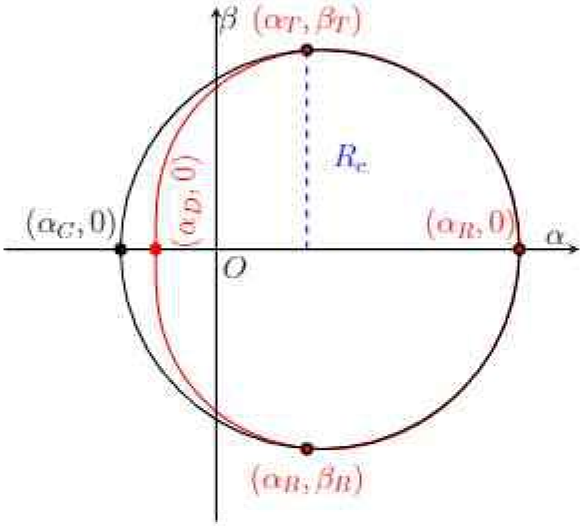

Figure 3.4: *Representation of essential parameters associated with the deformation of the black hole shadow.*

As illustrated in Fig.(3.4), the shape of the shadow is a distorted circle. Thus, we approach the shadow by a reference circle passing through the three points of the coordinates (α_T, β_T), (α_B, β_B) and $(\alpha_R, 0)$. The radius R_c of the shadow, which is defined here by the radius of the reference circle, is given by

$$R_c = \frac{(\alpha_T - \alpha_R)^2 + \beta_T^2}{2|\alpha_T - \alpha_R|}. \tag{3.46}$$

Considering the size of deformation in the left side of the shadow D_c, we define the distortion parameter δ_s of the shadow as follows

$$\delta_c = \frac{|D_c|}{R_c} = \frac{(\alpha_c - \alpha_D)}{R_c}. \tag{3.47}$$

In Fig.(3.5), we present the variation of these two observables quantities in terms of the rotating parameter. A close examination shows that the variation of the shadow size as a function of a is very small. However, the distortion of the Kerr shadow is increased by increasing the rotation parameter with a translation of the shadow from its origin.

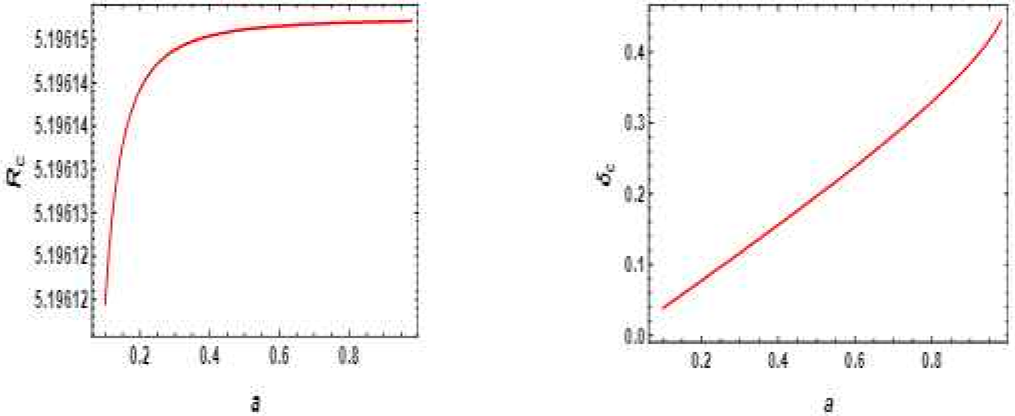

Figure 3.5: *Geometric quantities associated with the deformation of the shadow of the rotating black hole.*

3.1.2 Optical shadows of the regular rotating Bardeen AdS black holes

In this part, our focus lies on the investigations of the optical characteristics of charged rotating Bardeen black holes in four dimensions within the context of the AdS geometries. Specifically, we explore the geometric representations of the shadows, considering various parameters, among them the cosmological constant Λ. Initially, we delve into solutions that lack contributions from dark fields. Subsequently, we analyze the impact of an external dark field. This examination will be conducted within the framework of a moduli space, coordinated by pertinent parameters, including those associated with dark field sectors. Before investigating the shadows behaviors of these regular solutions, we provide a brief overview of rotating Bardeen-AdS black holes in four dimensions [116]. In Boyer-Lindquist coordinates, the line element is expressed as follows

$$ds^2 = -\frac{\Delta_r}{\Sigma}\left(dt - \frac{a sin^2\theta}{\Xi}d\phi\right)^2 + \frac{\Sigma}{\Delta_r}dr^2 + \frac{\Sigma}{\Delta_\theta}d\theta^2 + \frac{\Delta_\theta sin^2\theta}{\Sigma}\left(adt - \frac{r^2+a^2}{\Xi}d\phi\right)^2. \quad (3.48)$$

The involved reduced terms are given by

$$\begin{aligned} &\Delta_r = (r^2+a^2)\left(1+\tfrac{r^2}{\ell^2}\right) - 2m\left(\tfrac{r^2}{r^2+g^2}\right)^{\frac{3}{2}} r, && \Delta_\theta = 1 - \tfrac{a^2}{\ell^2}cos^2\theta, \\ &\Xi = 1 - \tfrac{a^2}{\ell^2}, && \Sigma = r^2 + a^2cos^2\theta. \end{aligned} \quad (3.49)$$

In this context, the symbols m and a correspond to the mass and the rotational parameter of the black hole, respectively. The variable g represents the charge associated with the nonlinear electrodynamics. Additionally, the parameter ℓ signifies the AdS radius. For this model, the radial and the polar function are expressed as follows

$$\mathcal{R}(r) = E^2\left[\left[\left(r^2+a^2\right) - a\xi\Xi\right]^2 - \Delta_r\eta\right] \quad (3.50)$$

$$\Theta(\theta) = E^2\left[\eta\Delta_\theta - \csc^2\theta\left(a\sin^2\theta - \xi\Xi\right)^2\right]. \quad (3.51)$$

These equations can be obtained by using the Kerr black hole shadow formalism. Roughly, the circular orbits conditions provide

$$\eta = \frac{16r^2\Delta_r}{\Delta_r'^2}, \quad (3.52)$$

$$\xi = \left.\frac{(r^2+a^2)\Delta_r' - 4r\Delta_r}{a\Xi\Delta_r'}\right|_{r=r_0}. \quad (3.53)$$

Here, the spatial derivative $\Delta_r' = \frac{\partial\Delta_r}{\partial r}$ has been utilized. A detailed examination indicates that in non-trivial backgrounds, employing the shadow formalism, necessitates specific considerations. For instance, the presence of the cosmological constant Λ introduces a visible way to approach such considerations. Indeed, it is essential to fix the position (r_{ob}, θ_{ob}) of the observer using the Boyer-Lindquist system coordinates [65,68]. By situating the observer within the outer communication domain $(\Delta_r > 0)$ and assuming that light ray trajectories are emitted from the position (r_{ob}, θ_{ob}) into the past [117, 118]. The observer's position can be described using the orthogonal tetrads (e_0, e_1, e_2, e_3). In relation to the metric black hole data, these tetrads are defined as

$$\begin{aligned} e_0 &= \left.\frac{(r^2+a^2)\partial_t + a\Xi\partial_\phi}{\sqrt{\Delta_r\Sigma}}\right|_{(r_{ob},\theta_{ob})} \qquad e_1 = \left.\frac{\sqrt{\Delta_\theta}}{\sqrt{\Sigma}}\partial_\theta\right|_{(r_{ob},\theta_{ob})} & (3.54) \\ e_2 &= -\left.\frac{a\sin^2\theta\partial_t + \Xi\partial_\phi}{\sqrt{\Delta_r\Sigma}\sin\theta}\right|_{(r_{ob},\theta_{ob})} \qquad e_3 = -\left.\frac{\sqrt{\Delta_r}}{\sqrt{\Sigma}}\partial_r\right|_{(r_{ob},\theta_{ob})}. & (3.55) \end{aligned}$$

In this scenario, the timelike vector e_0 represents the four-velocity of the observer. On the other hand, e_3 is specifically linked to the spatial orientation directed towards the center of the black hole. The directions $e_0 \pm e_3$ indicate vectors tangential to the principal null congruences. Within this vector representation, the parametrization of the light rays can be denoted as $\lambda(s) = (r(s), \theta(s), \phi(s), t(s))$. Additionally, one may consider the decomposition of the tangent vector $\dot{\lambda}$ as follows

$$\dot{\lambda} = \alpha(-e_0 + \sin\rho\cos\delta\, e_1 + \sin\rho\sin\delta\, e_2 + \cos\rho\, e_3), \tag{3.56}$$

where α is a scalar factor. ρ and δ are the celestial coordinates [118]. After performing the necessary calculations, one can derive

$$\alpha = g(\dot{\lambda}, e_0) = \left.\frac{1}{\sqrt{\Delta_r\Sigma}}(aL\Xi - (r^2+a^2)E)\right|_{(r_{ob},\theta_{ob})}. \tag{3.57}$$

To analyze the optical shadows of AdS black holes, it is essential to incorporate all relevant parameters, including geometric ones. Specifically, the boundaries of the optical shadows are controled by a reduced moduli space. According to [117, 118], the boundaries of these geometrical optical shadows can be characterized with the assistance of two cartesian coordinates:

$$x = -2\tan(\frac{\rho}{2})\sin\delta, \tag{3.58}$$

$$y = -2\tan(\frac{\rho}{2})\cos\delta. \tag{3.59}$$

The celestial coordinates ρ and δ are expressed in terms of ξ and η as follows

$$\sin\rho = \left.\frac{\pm\sqrt{\Delta_r\eta}}{((r^2+a^2)-a\xi\Xi)}\right|_{(r_{ob},\theta_{ob})}, \tag{3.60}$$

$$\sin\delta = \frac{\sqrt{\Delta_r}\sin\theta}{\sqrt{\Delta_\theta}\sin\rho}\left(\frac{\Xi(a-\Xi\csc^2\theta\xi)}{a\Xi\xi-(r^2+a^2)}\right)\Bigg|_{(r_{ob},\theta_{ob})}. \tag{3.61}$$

The geometric characteristics of the shadow are contingent on the parameters characterizing the rotating black holes. Notably, the charge associated with nonlinear electrodynamics is considered a significant parameter in these solutions. The corresponding shadow properties are portrayed in the (x, y) plane using the explicit expressions for x and y. For the current discussion, specific parameter values and observer positions have been taken into account. Precisely, the observer is situated at $r_{ob} = 50$ and $\theta_{ob} = \frac{\pi}{2}$. Chosen values for $\Lambda = -10^{-4}$ and $m = 1$ have been applied. The resulting behaviors are depicted in Fig.(3.6). In particular, the shadow features are illustrated by varying the two relevant parameters g and a. This study has been considered for $\frac{\pi}{2}$. However, it could be interesting to consider other observing positions.

It is crucial to note that, for a fixed value of $a = 0.9$, the shadow deviates from a perfect circle. Specifically, with $a = 0.9$, the D-shaped geometrical configurations emerge as g increases. When $g = 0.2$, the circles become distorted and displaced from the center with an increase in a. The prominence of the D-shape configuration becomes more apparent for larger values of the rotating parameter. In previous studies on the rotating AdS black holes, it has been established that the D-shape geometry is solely linked to the rotating parameter a. However, in the present scenario, the D-shape configuration is influenced not only by the rotating parameter a but also by the charge of the nonlinear electrodynamics g. Specifically, the D-shape geometry is controlled by the parameters a and g. It has been observed that the parameter g not only affects the spacetime configuration of the black hole but also influences the observed form of the shadow.

To analyze the distortion of the black hole shadows, the deformation parameters need to be reformulated. Specifically, the R_c parameter is expressed in the following form

$$R_c = \frac{(x_l - x_r)^2 + y_l^2}{2|x_l - x_r|}. \tag{3.62}$$

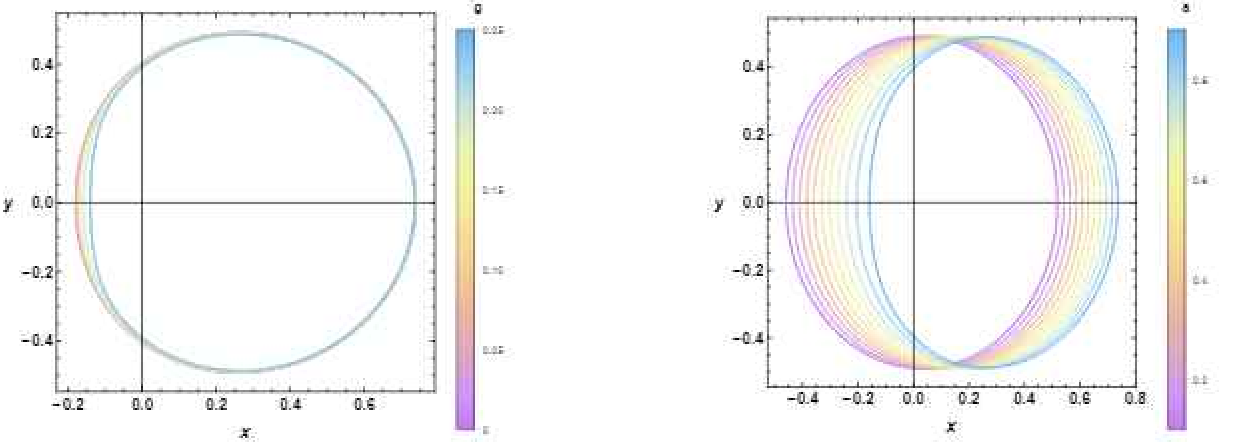

Figure 3.6: *Optical shadows of Bardeen-AdS black holes. Right panel: variation related to $a = 0.9$ for various values of g. Left panel: behavior corresponds to $g = 0.2$ for various values of a .*

In these optical behaviors, the distortion parameter reads as

$$\delta_c = \frac{|D_c|}{R_c}. \tag{3.63}$$

To broaden our analysis beyond the optical examination of rotating Bardeen-AdS black holes, we delve into the exploration of the astronomical quantities mentioned earlier. These parameters are visualized in Fig.(3.7) using a reduced moduli space defined by the coordinates (a, g). For small values of a and g, it is evident that the shadow parameter R_c, which controls

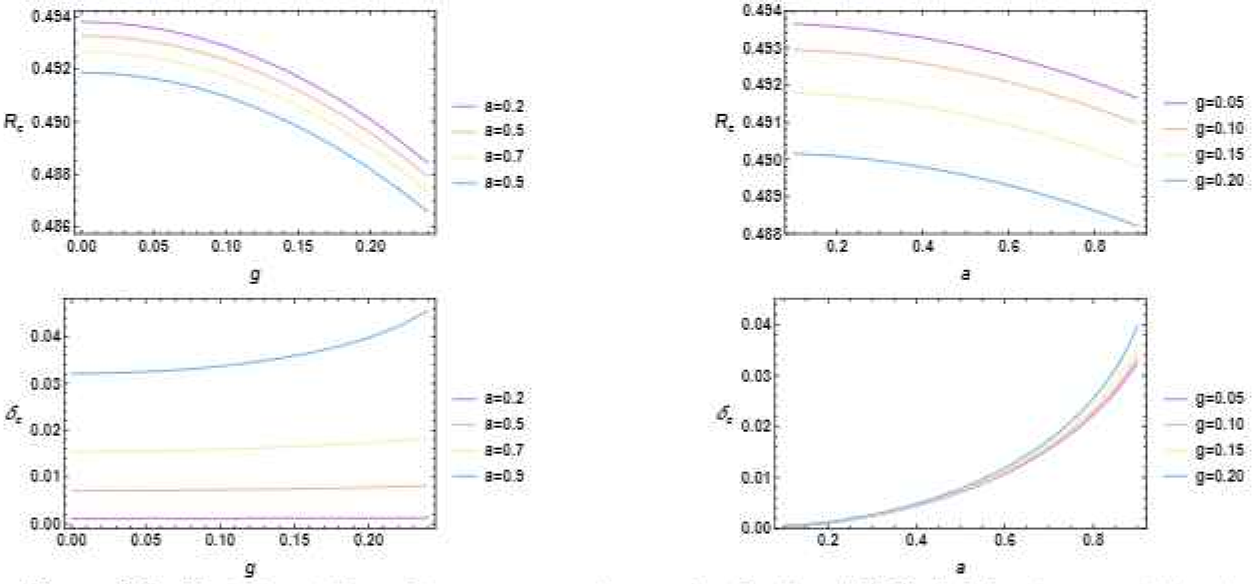

Figure 3.7: *Variation of R_c and δ_c parameters for rotating Bardeen-AdS black holes in terms of (a, g).*

the size, is large, in contrast to large values of a and g. Furthermore, when we consider large values of a, the size parameter decreases with an increase in g. This behavior aligns with the results of the regular Bardeen black hole [121, 122], where the circular geometry transforms into D-shaped configurations as a increases. Similarly, for fixed large values of g, the size parameter decreases with an increase in a.

Turning to the analysis of the distortion parameter variation δ_c, when we fix the values of a, the distortion parameter increases with g. However, for small values of a, this parameter remains small and constant. On the other hand, when we fix g, the geometric parameter δ_c increases with the rotating parameter and takes small values for small values of a. These results highlight the influence of g on both the size and the shape of the observed shadow.

Now, we extend our study to the shadow behaviors of quintessential rotating Bardeen-AdS black holes by introducing two additional parameters associated with dark field contributions [123]. Specifically, the solution is extended by incorporating external dark field contributions [123]. Our focus is particularly on dark energy (DE), utilizing quintessence field contributions. This leads to a generalization of the following delta term

$$\Delta_r^{\omega} = \left(r^2 + a^2\right)\left(1 + \frac{r^2}{\ell^2}\right) - 2m\left(\frac{r^2}{r^2 + g^2}\right)^{\frac{3}{2}} r - \frac{\alpha}{r^{3\omega+1}}, \tag{3.64}$$

The parameter α represents the intensity of dark energy (DE), while ω signifies the quintessential state parameter.

By introducing Δ_r^{ω} into the previous computations of the equations of motion, various models can be examined by fixing the state equation parameter ω. However, for the purposes of our analysis, we consider specific values that have been explored in diverse black hole contexts. Specifically, we concentrate on three ω-models with $\omega = -1, -1/3, -2/3$. In a broader context, we will explore the characteristics of the shadow by manipulating the internal and external black hole parameters. These parameters collectively generate the associated moduli space, which can be broken down as follows

$$\mathcal{M} = \mathcal{M}_{int} \times \mathcal{M}_{ext}, \tag{3.65}$$

In this context, $\mathcal{M}_{ext}$ represents the dark field sector, while $\mathcal{M}_{int}$ is the internal factor involving parameters associated with the black holes. Following a similar approach to the previous sections, one-dimensional shadow configurations can be visualized by varying one parameter while keeping the others ones. The resulting shadow geometrics are illustrated in Fig.(3.8).

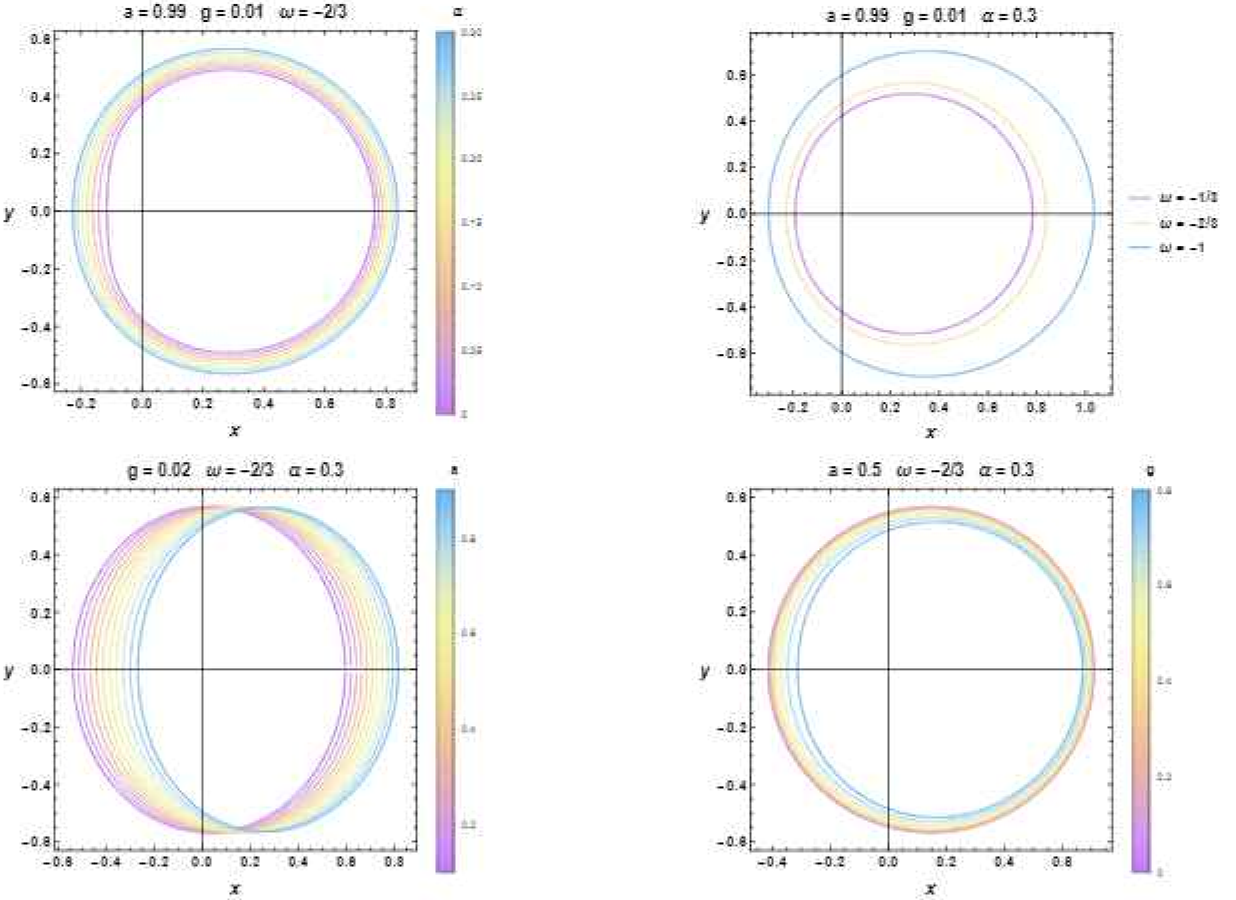

Figure 3.8: *Shadow behaviors of quintessential rotating Bardeen-AdS black holes for various values of a, g, α and ω.*

Concerning the variation of the parameter α, two regions are explored. For small values of this parameter, the shadow size decreases, and a D-shape emerges. Conversely, for large values of α, the D-shape disappears, and the size increases. These behaviors are consistent across all ω models. Notably, the size increases as ω decreases. The D-shape geometry disappears when $\alpha = 0.3$, and these configurations remain unaltered even when varying the rotation parameter a. As a increases, the circles deviate from the origin. For $\alpha = 0.3$, it is observed that the parameter g controls the shadow size, decreasing as g increases. A close examination reveals that this parameter influences the shape deformations, in contrast to the electric charge. It plays a role similar to the rotating parameter observed in many black hole shadow activities. The appearance of the D-shape geometry is linked to the existence of three parameters a, which controls the shape deformation in ordinary black hole solutions, along with g and α.

Similar to the previous section, we analyze the corresponding distorted geometries by introducing two additional parameters associated with the dark sector. Specifically, we examine their effects on the R_c and δ_c parameters. These behaviors are illustrated in Fig(3.9) by varying the dark sector parameters and the charge of the nonlinear electrodynamics.

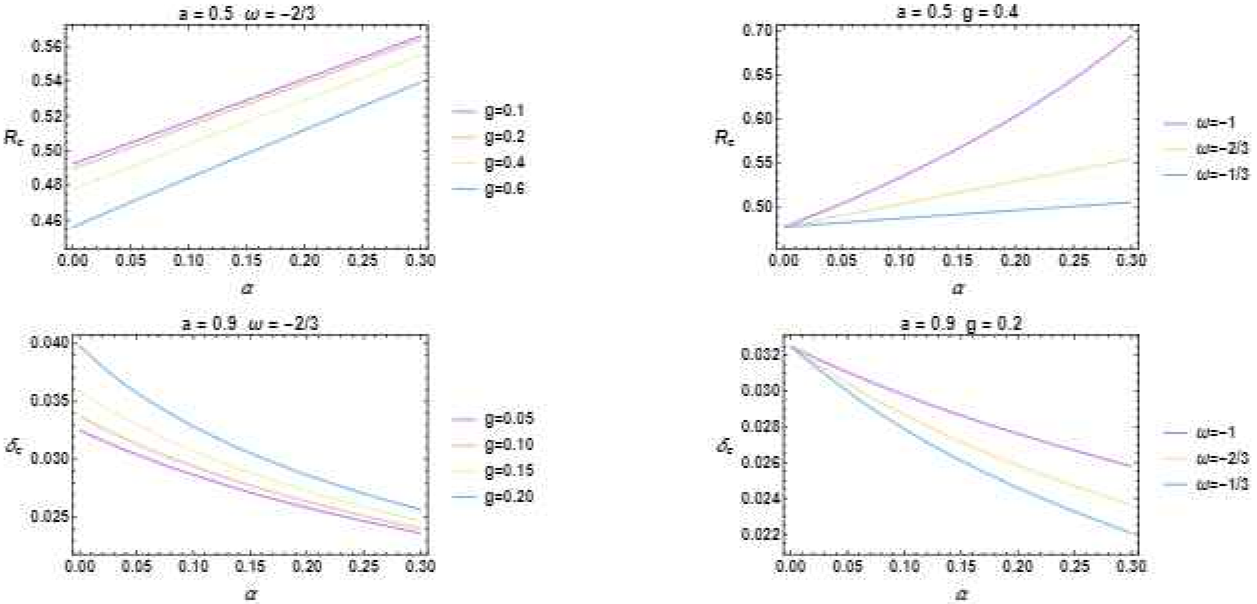

Figure 3.9: *Variations of R_c and δ_c parameters for rotating quintessential Bardeen-AdS black holes as a function of dark sector parameters.*

With fixed values for a and ω, the depicted figure illustrates that R_c exhibits a linear increase with α for various values of g, while it experiences a decrease with an increase in g. This observed pattern is also consistent for variations in ω. In contrast to R_c, δ_c diminishes with an increase in α for different values of g, and it elevates with an increase in g. The opposite trend is observed for variations in ω. For constant values of ω, the geometric parameter δ_c diminishes as α increases. These findings underscore the impact of g and α on the size and shape characteristics of the shadow.

Upon thorough examination, recent observational results from the shadows of the supermassive black hole $M87^{\star}$, as obtained by EHT, have emerged as a compelling avenue for investigating various gravity theories and alternative modified physical models. Motivated by these endeavors, there is a keen interest in establishing connections with such observational findings. Notably, it has been observed that data from observations could impose constraints on the black hole parameters [124–126]. Specifically, the behaviors of the shadows can be analyzed in terms of the external sector of the moduli space for different values of the rotation parameter a. In units of the M87* mass, we can superimpose the shadows of the M87* black hole and those from the present work by considering appropriate black hole parameters. These parameters could facilitate alignment with observational findings. The associated behaviors, considering different values of a, are illustrated in Fig.(4.13).

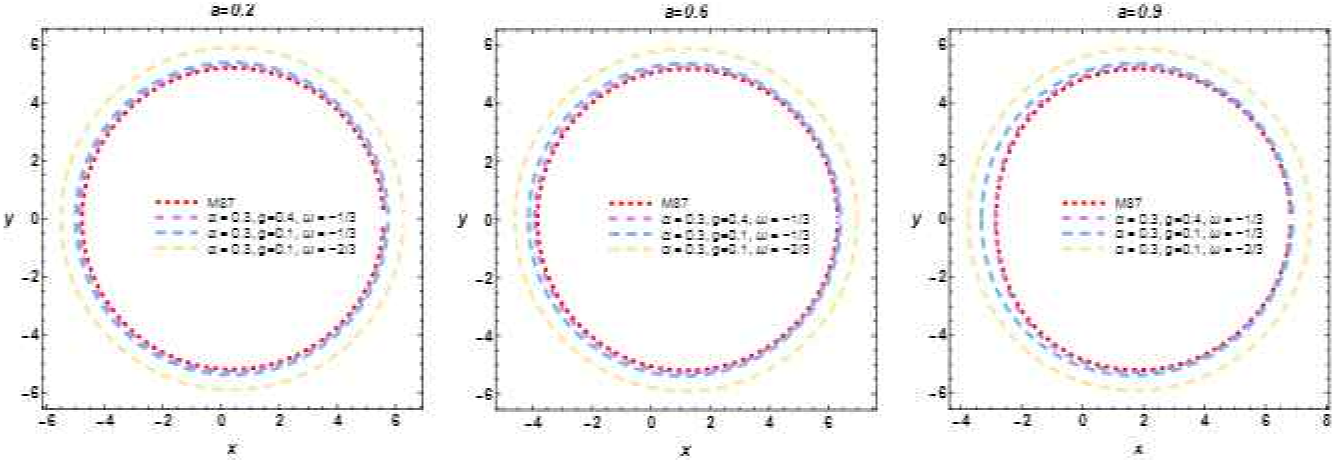

Figure 3.10: *Shadows for different values of the rotating parameter a, compared to the M87* shadow, by taking* $\lambda = -0{,}002$ *and* $M = 1$ *in units of the M87 black hole mass given by* $M_{BH} = 6.5 \times 10^9 M_\odot$ *and* $r_0 = 91.2kpc$.

Comparing the shadow radii of both black holes depicted in this figure, it is apparent that the M87* shadow aligns seamlessly with that of the rotating quintessential AdS black holes for specific values of the relevant parameters. When varying the rotating parameter, certain computations reveal that the pertinent parameters are $\alpha = 0.3$, $g = 0.4$, and $\omega = -1/3$. Additionally, for $\omega = -2/3$, it is observed that the shadows of the rotating quintessential AdS black holes can closely resemble the M87* shadows. In the case of non-distorted geometries, similar behaviors are noted, echoing those of M87. However, for $a = 0.9$ where the shadows are distorted, it becomes intriguing to discuss the distortion of the shadow in comparison to that of M87*.

It is noted that the distortion of the quintessential AdS black hole aligns with that of M87* for $\alpha = 0.3$, $g = 0.4$, and $\omega = -1/3$. However, for other parameter values, the distortion is observed to differ from that of M87*. This graphical analysis could serve to validate the specific constraints on these black hole parameters as mentioned earlier.

3.2 Deflection of light rays by black holes

The essence of gravitational lensing lies in the bending of light due to gravitational fields, as predicted by Einstein's general relativity, especially in the weak field limit [84–86, 91]. This phenomenon occurs when light passes near to massive objects like planets, black holes, or dark matter. The weak deflection, being a consequence of this gravitational lensing, is a valuable tool in detecting dark matter filaments. Understanding and studying weak deflection is crucial as it provide insights into the large-scale structure of the universe.

To calculate the deflection angle, we will adopt the approach based on the Gauss-Bonnet theorem is one of the important method to calculate the weak deflection angle using optical geometry proposed by Gibbons and Werner [92–94]. This theorem establishes a connection between the intrinsic differential geometry of a surface and its topology. Taking into account that both the observer and the source located at finite distances within the equatorial plane, the deflection angle can be formulated as

$$\Theta = \Psi_R - \Psi_S + \phi_{SR}, \tag{3.66}$$

where ϕ_{SR} represents the longitude separation angle. Ψ_R and Ψ_S denote the angles between the light rays and the radial direction at the observer and the source position, respectively [92–94]. The calculation of the deflection angle can be derived by applying the Gauss-Bonnet theorem [92]. This theorem asserts that

$$\iint_{\Sigma} K dS + \sum_{\alpha=1}^{n} \int_{C_\alpha} k_g dl + \sum_{\alpha=1}^{n} \theta_\alpha = 2\pi. \tag{3.67}$$

In this context, Σ represents a two-dimensional orientable real surface bounded by curves $C_\alpha(\alpha = 1, \ldots, n)$. θ_α denotes the external angle at the α-vertex. K indicates the Gaussian curvature of the surface Σ, and k_g is the geodesic curvature of C_α. By considering the quadrilateral ${}^{\infty}r\square^{\infty}S$ formed by light curves from the source to the observer, it has been demonstrated that Eq.(3.66) and Eq.(3.67) yield a reduced integral formula given by

$$\Theta = -\iint_{{}^{\infty}_{r}\square^{\infty}_{S}} K dS + \int_{S}^{R} k_g dl, \tag{3.68}$$

where dS represents the area element of the involved surface. The line element dl can be computed using the metric of the associated black hole. Specifically, we first consider four-dimensional black holes with the following general stationary metric form

$$ds^2 = -A(r,\theta)dt^2 + B(r,\theta)dr^2 + C(r,\theta)d\theta^2 + D(r,\theta)d\phi^2 - 2H(r,\theta)dtd\phi. \tag{3.69}$$

To define the Riemannian manifold in which light geodesics are interpreted as spatial curves, it is essential to consider the null geodesic condition $ds^2 = 0$ [84–86]. This condition effectively yields

$$dt = \pm\sqrt{\gamma_{ij}dx^i dx^j} + \eta_\phi d\phi, \tag{3.70}$$

where γ_{ij} is a spatial metric called the optical metric. In the equatorial plane ($\theta = \pi/2$) and at a constant time t of the space-time metric, one can get a 2-dimensional curved space which is represented by

$$dl^2 \equiv \gamma_{ij}dx^i dx^j. \tag{3.71}$$

In this manner, the Gaussian curvature is expressed as

$$K = \frac{R_{r\phi r\phi}}{\gamma} = \frac{1}{\sqrt{\gamma}}\left(\frac{\partial}{\partial\phi}\left(\frac{\sqrt{\gamma}}{\gamma_{rr}}\Gamma^{\phi}_{rr}\right) - \frac{\partial}{\partial r}\left(\frac{\sqrt{\gamma}}{\gamma_{rr}}\Gamma^{\phi}_{r\phi}\right)\right), \tag{3.72}$$

where one has $\gamma = \det(\gamma_{ij})$. The area element of Eq.(3.67) takes the form

$$dS = \sqrt{\gamma}drd\phi. \tag{3.73}$$

According to [92], the geodesic curvature within this Riemannian manifold is expressed as

$$k_g = -\frac{1}{\sqrt{\gamma\gamma^{\theta\theta}}}\eta_{\phi,r}. \tag{3.74}$$

Using the same principle, we can also adopt an alternative approach to derive the deflection angle by calculating ψ and ϕ_{RS} angles directly. To write down the associated formula, the following unit tangential vector along the light will be used

$$(e^r, e^\theta, e^\phi) = \epsilon\left(\frac{dr}{d\phi}, 0, 1\right), \tag{3.75}$$

where ϵ represents a radial quantity that can be derived from the solution of the black hole.

More precisely, it is defined as

$$\epsilon = \frac{A(r)D(r) + H^2(r)}{A(r)(H(r) + A(r)b)}, \tag{3.76}$$

where b represents the impact parameter, characterized as the ratio of two constants of motion derived from the orbit equation. A simplified form can be obtained by restricting the analysis to the equatorial plane. These two conserved quantities are expressed as

$$E = A(r)\dot{t} + H(r)\dot{\phi} \qquad L = D(r)\dot{\phi} - H(r)\dot{t}, \tag{3.77}$$

where the derivative with respect to the affine parameter has been used. Based on the Gauss Bonnet theorem, one can prove that the Ψ angles verify

$$\cos\Psi \equiv \gamma_{ij}e^i R^j, \tag{3.78}$$

where the components of a radial vector given by

$$R^j = (\frac{1}{\sqrt{\gamma_{rr}}}, 0, 0). \tag{3.79}$$

Exploiting Eq.(3.75) and Eq.(3.78), the $\sin\Psi$ term can be obtained from the following relation

$$\sin\Psi = \frac{H(r) + A(r)b}{\sqrt{A(r)D(r) + H^2(r)}}. \tag{3.80}$$

The calculation of the deflection angle of the light rays needs also the explicit expression of the separation angle ϕ_{SR} which is defined by

$$\phi_{SR} = \int_S^R d\phi = \int_{u_S}^{u_0} \frac{1}{\sqrt{F(u)}} du + \int_{u_R}^{u_0} \frac{1}{\sqrt{F(u)}} du, \tag{3.81}$$

where one has used

$$F(u) = \left(\frac{d\phi}{du}\right)^2, \qquad u = \frac{1}{r}. \tag{3.82}$$

It is worth noting that u_S and u_R represent the inverses of the source and the observer distances from the black hole, respectively. Additionally, u_0 denotes the inverse of the closest approach r_0 associated with the impact parameter through the constraint $F(u_0) = 0$. This representation proves more advantageous for calculating the deflection angle of the AdS black holes. We extend this formalism to d-dimensional non-rotating AdS black holes by considering the ansatz metric

$$ds^2 = -A(r)dt^2 + B(r)dr^2 + r^2 d\Omega^2_{d-2}, \qquad d\Omega^2_{d-2} \equiv d\theta^2 + \prod_{k=1}^{d-3} \sin\theta \sin\phi_k. \tag{3.83}$$

Here, $d\Omega^2_{d-2}$ denotes the metric of the $(d-2)$-dimensional unit sphere. θ and ϕ_k represent the local spherical coordinates. $A(r)$ and $B(r)$ are radial functions specified later on . The optical metric of the light rays, denoted as γ_{ij}, can be determined from the null condition, which yields

$$dt^2 = \frac{B(r)}{A(r)}dr^2 + \frac{r^2}{A(r)}d\Omega^2_{d-2}. \tag{3.84}$$

This corresponds to a $(d-1)$-dimensional Riemannian space. Within this space, the deviation of a spatial curve can be computed by choosing an equatorial plane constrained by $\theta = \frac{\pi}{2}$. This plane is defined by the radial coordinate and one periodic coordinate from the set ϕ_k, while the remaining ones are held constant. ϕ is singled out as the only non-fixed coordinate. Before proceeding further, certain conserved quantities are essential, including the energy E and the angular momentum L. These conserved quantities are expressed as follows

$$E = A(r)\frac{dt}{d\lambda} \tag{3.85}$$

$$L = r^2\frac{d\phi}{d\lambda} \tag{3.86}$$

where λ represents the affine parameter. These quantities can be combined to formulate the impact parameter b of the motion

$$b = \frac{L}{E}. \tag{3.87}$$

The computations provide

$$b = \frac{r^2}{A(r)}\frac{d\phi}{dt}. \tag{3.88}$$

The unit tangential vector of the light ray curve e^i and the radial vector R^j are defined as follows

$$e^i = \frac{dx^i}{d\lambda} = \frac{bA(r)}{r^2}\left(\frac{dr}{d\phi}, \underbrace{0, \ldots, 0}_{d\text{-}3}, 1\right), \tag{3.89}$$

$$R^j = \left(\frac{1}{\sqrt{\gamma_{rr}}}, \underbrace{0, \ldots, 0}_{d\text{-}2}\right). \tag{3.90}$$

In the plane coordinated by (r, ϕ), the angle between the light rays and the radial direction can be derived from the following relation

$$\cos\Psi \equiv \gamma^i_{ij} R^j. \tag{3.91}$$

The orbit equation can be extracted from the unity of the tangential vector as

$$F_d(r) = \left(\frac{dr}{d\phi}\right)^2 = \frac{r^4}{b^2 A(r)B(r)} - \frac{r^2}{B(r)}. \tag{3.92}$$

In the (r, ϕ) plane of the d-dimensional space, the computations simplify to those of a spherically symmetric black hole in four dimensions. This enables the consideration of the deflection angle equation related to the (r, ϕ) plane within the context of the Gauss-Bonnet theory applied to four-dimensional black holes. When accounting for finite distances between the observer (R) and the source (S), this equation is expressed as follows

$$\Theta_d = \Psi_R - \Psi_S + \phi_{RS}. \tag{3.93}$$

The separation angle can be rewritten as

$$\phi_{RS} = \int_{u_S}^{u_0} \frac{1}{\sqrt{F_d(u)}} du + \int_{u_R}^{u_0} \frac{1}{\sqrt{F_d(u)}} du. \tag{3.94}$$

From the aforementioned formalism, it is apparent that the functions $A(r)$ and $B(r)$ encompass all contributing effects, including the dimension of the black hole space-time.

With this established formalism, we can proceed to calculate the deflection angle of the light rays by various black holes in different backgrounds. This will be the focus of the upcoming investigation.

3.2.1 Deflection light behaviors by ordinarily AdS black holes

Here, we are interested in the deflection angle behaviors of the RN-AdS black holes in four dimensions. By applying the null geodesic conditions in the equatorial plane, one obtains the expression for the optical metric

$$dt^2 \;=\; \frac{1}{f(r)^2}dr^2 + \frac{r^2}{f(r)}d\phi^2, \tag{3.95}$$

where $f(r)$ indicates the metric function of RN-AdS black hole given by $f(r) = 1 - \frac{2M}{r} + \frac{r^2}{\ell^2} + \frac{Q^2}{r^2}$. Using Eq.(3.72) and Eq.(3.95), we get the expression of the Gaussian curvature

$$K \simeq \frac{1}{\ell^2} - \frac{6M}{\ell^2 r} + \frac{6Q^2}{\ell^2 r^2} - \frac{2M}{r^3} + \frac{3Q^2}{r^4} - \frac{6MQ^2}{r^5} + O(M^2, Q^3, 1/\ell^4). \tag{3.96}$$

In this situation, the determination of the optical metric determinant is achieved in the following form

$$\gamma = r^2\left(1 - \left(\frac{2M}{r} - \frac{r^2}{\ell^2} - \frac{Q^2}{r^2}\right)\right)^{-3} \tag{3.97}$$

yielding the following necessary approximation

$$\sqrt{\gamma} \simeq r + O(M^1, Q^2, 1/\ell^2). \tag{3.98}$$

To maintain the order of $O(M^2, Q^3, 1/\ell^4)$ in the calculations of deflection angles, we utilize Eq. (3.98). Indeed, the computation provides

$$\begin{aligned}\int_{\phi_S}^{\phi_R}\int_{r_o}^{\infty} K\sqrt{\gamma}drd\phi \;\simeq\; & \int_{\phi_S}^{\phi_R}\int_{r_o}^{\infty} drd\phi\,\Big(\frac{r}{\ell^2} + \frac{3Q^2}{r^3} + \frac{6Q^2}{\ell^2 r} - \frac{6M}{\ell^2} - \frac{2M}{r^2} - \frac{6MQ^2}{r^4} \\ & + \; O(M^2, Q^3, 1/\ell^4)\end{aligned} \tag{3.99}$$

To carry out these computations, the impact parameter of motion is required. Using the equation of motion, one can get

$$b = \frac{\mid L \mid}{E} = \frac{r^2}{f(r)}\frac{d\phi}{dt}. \tag{3.100}$$

The null geodesic condition gives

$$\left(\frac{du}{d\phi}\right)^2=\frac{1}{b^2}-\frac{1}{\ell^2}-u^2\left(-2Mu+Q^2u^2+1\right). \tag{3.101}$$

To solve Eq.(3.101), we need to employ the perturbative method, leading to the following result

$$u(\phi)=\frac{1}{b}\sin(\phi)+O\left(M\right). \tag{3.102}$$

Taking into account weak field approximations and small AdS radius values, the integral of Eq. (3.99) can be expanded as follows

$$\begin{aligned}
-\int_{\phi_S}^{\phi_R}\int_{r_o}^{\infty}K\sqrt{\gamma}drd\phi \;&\simeq\; \int_{\phi_S}^{\phi_R}\int_{0}^{u(\phi)=\frac{1}{b}\sin(\phi)}2M-3Q^2u+6MQ^2u^2-\frac{1}{\ell^2u^3}+\frac{6M}{\ell^2u^2}-\frac{6Q^2}{\ell^2u}dud\phi\\
&\simeq\; \frac{2M}{b}\left[\sqrt{1-(bu_S)^2}+\sqrt{1-(bu_R)^2}\right]\\
&+\; \left[\frac{6Q^2}{\ell^2}-\frac{3Q^2}{4b^2}\right]\left[\pi-\arcsin(bu_S)-\arcsin(bu_R)\right]\\
&-\; \frac{3Q^2}{4b^2}\left[bu_R\sqrt{1-(bu_R)^2}+bu_S\sqrt{1-(bu_S)^2}\right]\\
&-\; \frac{MQ^2}{3b^3}\left[\left(16+(bu_R)^2\right)\sqrt{1-(bu_R)^2}+\left(16+(bu_S)^2\right)\sqrt{1-(bu_S)^2}\right]\\
&+\; \frac{b}{2\ell^2}\left[\frac{\sqrt{1-(bu_R)^2}}{u_R}+\frac{\sqrt{1-(bu_S)^2}}{u_S}\right]-\frac{Mb}{2\ell^2}\left[\frac{1}{\sqrt{1-(bu_S)^2}}+\frac{1}{\sqrt{1-(bu_R)^2}}\right]\\
&-\; \frac{6Q^2b}{\ell^2}\left[u_S\arctan(u_Sb)+u_R\arctan(u_Rb))\right].
\end{aligned} \tag{3.103}$$

In this situation, where the coefficient $H(r,\theta)$ governing the coupling term $dtd\phi$ is absent, it has been observed that the second term in the deflection angle expression related to k_g becomes null. The integration in Eq. (3.103) seemingly exhibits a potential divergence as $bu_S\to 0$ and $bu_R\to 0$. This divergence could be associated with the impact of the cosmological constant. Combining Eq. (3.103) with Eq. (3.68) and considering the asymptotic case when $bu_S<<1$ and $bu_R<<1$, the deflection angle of the RN-AdS black hole is found to be

$$\Theta\simeq\frac{4M}{b}-\frac{3Q^2\pi}{4b^2}-\frac{32MQ^2}{3b^3}+\frac{6Q^2\pi}{\ell^2}-\frac{Mb}{\ell^2}+\frac{b}{2\ell^2}\left[\frac{1}{u_R}+\frac{1}{u_S}\right]+O(M^2,Q^3,1/\ell^4). \tag{3.104}$$

As $\ell \to \infty$, the expression corresponds to the RN black holes [65]. It is evident that the deflection angle expression displays a divergent behavior associated with the vanishing limits of the functions u_S and u_R. This behavior is linked to the presence of the cosmological constant.

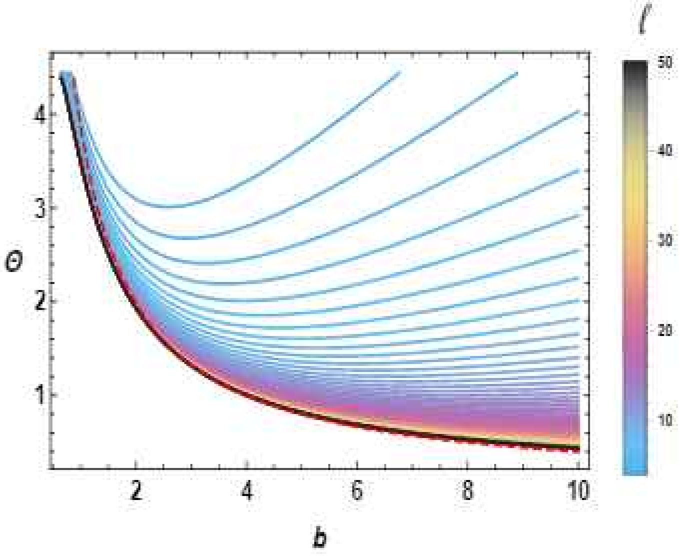

Figure 3.11: *Behaviors of the deflection angle as a function of the impact parameter for various values of ℓ, where $u_S = u_R = 0.1$, $M = 1$, and $Q = 0.2$. The dashed red curve depicts the deflection angle of the Schwarzschild black hole.*

Firstly, we examine the impact parameter-dependent behavior of the deflection angle in AdS backgrounds. The variation of this optical quantity, as derived from Eq.(3.104), is illustrated in Fig.(3.11). With the mass and the charge held constant, we investigate specific AdS radius values where their contributions become notable. The depicted figure shows a rapid decrease in the deflection angle for small impact parameter values, followed by an increase with b. As the AdS radius ℓ increases, the deflection angle tends to decrease. This observation implies that the presence of the AdS geometry can indeed influence the deviation of the light rays. For small impact parameter values, the deflection angle of the Schwarzschild black hole is slightly larger compared to the one associated with the AdS contributions. Fixing $\ell = 50$ and considering large values of b, a similar behavior is observed in the deflection angle of the Schwarzschild black hole solution. However, for $\ell < 50$, the deflection angle in the presence of the cosmological constant becomes more pronounced.

In Fig.(3.12), we investigate the impact of the charge on the deflection angle of RN

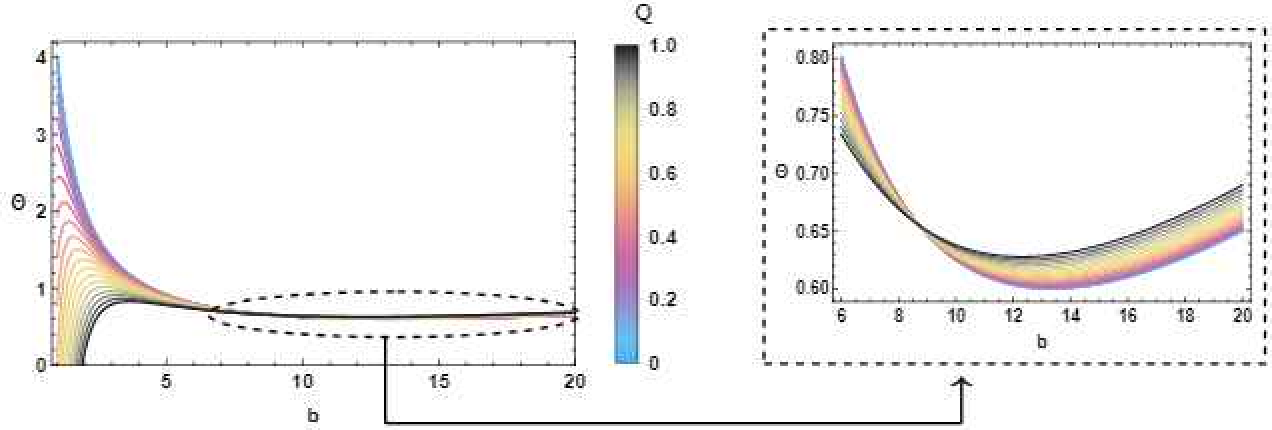

Figure 3.12: *Deflection angle in terms of the impact parameter for various charge values by taking* $u_S = u_R = 0.1$, $\ell = 20$ *and* $M = 1$.

AdS black holes. For small values of b, the deflection angle decreases with an increase in charge. However, this behavior is inverted for large impact parameter values. The reversal in behaviors commences at a specific impact parameter value, approximately $b \simeq 8.716$ for $M = 1$ and $\ell = 20$. As apparent from the figure, all curves representing different values of Q converge at a critical point b_c. This indicates that the critical value should depend solely on M and ℓ. A closer examination reveals that an explicit expression for b_c can be derived by computing the derivative of the deflection angle with respect to the charge. This computation results in

$$b_c = \frac{(\lambda\sqrt{6})^{2/3} + (6\pi)^{2/3}\ell^2}{12(\pi\lambda)^{1/3}}, \qquad \lambda = \left(\sqrt{65536M^2\ell^4 - 6\pi^2\ell^6} + 256M\ell^2\right). \tag{3.105}$$

The observed change in the behavior of the deflection angle with respect to the charge resembles the behavior seen in the quintessential RN black hole [65, 89, 96]. However, this characteristic is absent in the case of regular RN black holes. This distinction can be understood by examining the expression for the metric function $f(r)$. For small values of b, the charge effect is notable while the influence of the cosmological constant is negligible. In this scenario, the deflection angle exhibits a maximum, decreasing as the charge Q is reduced. Conversely, for large values of b, these tendencies are reversed. In this case, the impact of the cosmological constant becomes significant, resulting in linear variations in the deflection angle of light rays. We expect to observe similar optical aspects for a large class of the AdS black holes in four dimensions.

To examine the impact of the rotation parameter within the AdS geometry, we explore the deflection angle of Kerr-Newman AdS black holes. As articulated in [65], the line element characterizing this particular class of black holes is provided by

$$ds^2 = \frac{\Delta_r}{\Sigma}\left[\frac{a\sin^2\theta}{\Xi}d\phi - dt\right]^2 + \frac{\Sigma}{\Delta}dr^2 + \frac{\Sigma}{\Delta_\theta}d\theta^2 + \frac{\Delta_\theta\sin^2\theta}{\Sigma}\left[adt - \frac{r^2+a^2}{\Xi}d\phi\right]^2 \tag{3.106}$$

where the relevant elements are given by

$$\begin{aligned}\Sigma &= r^2 + a^2\cos^2\theta\,, \quad \Xi = 1 - \frac{a^2}{\ell^2}\,, \quad \Delta_\theta = 1 - \frac{a^2}{\ell^2}\cos^2\theta \\ \Delta_r &= (r^2+a^2)\left(1+\frac{r^2}{\ell^2}\right) - 2Mr + Q^2.\end{aligned} \tag{3.107}$$

The null geodesic consideration gives

$$\gamma_{rr} = \frac{r^4}{\left((a^2+r^2)\left(\frac{r^2}{\ell^2}+1\right) - 2Mr + Q^2\right)\left(r\left(\frac{r(a^2+r^2)}{\ell^2} - 2M + r\right) + Q^2\right)}, \tag{3.108}$$

$$\gamma_{\phi\phi} = \frac{l^6 r^4\left(a^2\left(\ell^2+r^2\right) + \ell^2\left(-2Mr + Q^2 + r^2\right) + r^4\right)}{\left(a^2-\ell^2\right)^2\left(r^2\left(a^2+r^2\right) + \ell^2\left(r(r-2M) + Q^2\right)\right)^2}, \tag{3.109}$$

$$\eta_\phi = -\frac{a\ell^2\left(r^2\left(a^2+r^2\right) + \ell^2\left(Q^2 - 2Mr\right)\right)}{\left(a^2-\ell^2\right)\left(r^2\left(a^2+r^2\right) + \ell^2\left(r(r-2M) + Q^2\right)\right)}. \tag{3.110}$$

The area element is found to be

$$dS \simeq rdrd\phi + O(M^1, Q^2, a^2, 1/\ell^2). \tag{3.111}$$

In the context of weak fields and slow rotation approximations, and assuming small values for the AdS radius, we can derive the expression for the Gaussian curvature. Specifically, it is formulated as

$$\begin{aligned}K \simeq\ & \frac{1}{\ell^2} - \frac{6M}{\ell^2 r} + \frac{6Q^2}{\ell^2 r^2} - \frac{14a^2M}{\ell^2 r^3} - \frac{2M}{r^3} + \frac{15a^2Q^2}{\ell^2 r^4} + \frac{3Q^2}{r^4} - \frac{6MQ^2}{r^5} + \frac{24a^2M}{\ell^2 r^5} - \frac{6a^2M}{r^5} \\ +\ & \frac{8a^2Q^2}{r^6} + \frac{12a^2MQ^2}{r^7} + O\left(M^2, Q^3, a^2, \frac{1}{\ell^4}\right).\end{aligned} \tag{3.112}$$

Using Eq.(3.102), the integral calculation yields to

$$
\begin{aligned}
-\int_{\phi_S}^{\phi_R}\int_{r_o}^{\infty} K\sqrt{\gamma}drd\phi \;\simeq\;& \frac{2M}{b}\left[\sqrt{1-(bu_S)^2}+\sqrt{1-(bu_R)^2}\right] \\
&+\left[\frac{6Q^2}{\ell^2}-\frac{3Q^2}{4b^2}\right]\left[\pi-\arcsin(bu_S)-\arcsin(bu_R)\right] \\
&-\frac{3Q^2}{4b^2}\left[bu_R\sqrt{1-(bu_R)^2}+bu_S\sqrt{1-(bu_S)^2}\right] \\
&-\frac{MQ^2}{3b^3}\left[\left(16+(bu_R)^2\right)\sqrt{1-(bu_R)^2}+\left(16+(bu_S)^2\right)\sqrt{1-(bu_S)^2}\right] \\
&+\frac{b}{2\ell^2}\left[\frac{\sqrt{1-(bu_R)^2}}{u_R}+\frac{\sqrt{1-(bu_S)^2}}{u_S}\right] \\
&-\frac{Mb}{2\ell^2}\left[\frac{1}{\sqrt{1-(bu_S)^2}}+\frac{1}{\sqrt{1-(bu_R)^2}}\right] \\
&-\frac{6Q^2b}{\ell^2}\left[u_S\arctan(u_Sb)+u_R\arctan(u_Rb))\right]+O\left(M^2,Q^3,a,\frac{1}{\ell^4}\right).
\end{aligned}
\tag{3.113}
$$

To calculate k_g terms, one should exploit Eq(3.74). Indeed, the computations of the geodesic curvature give

$$
k_g \;\simeq\; -\frac{2a}{\ell^2}-\frac{aM}{\ell^2 r}-\frac{2aM}{r^3}-\frac{3aMQ^2}{2\ell^2r^3}+\frac{2aQ^2}{r^4}+\frac{3aMQ^2}{r^5}+O\left(M^2,Q^3,a,\frac{1}{\ell^4}\right) \tag{3.114}
$$

Considering the prograde case where $dl>0$, we take the following linear approximations $r=b/\cos\vartheta$ and $l=b\tan\vartheta$. In particular, we obtain

$$
\begin{aligned}
\int_S^R k_g dl \;\simeq\;& \int_S^R -\frac{2ab}{\ell^2\cos^2\vartheta}-\frac{aM}{\ell^2\cos\vartheta}-\left[\frac{2aM}{b^2}+\frac{3aMQ^2}{2\ell^2b^2}\right]\cos\vartheta+\frac{2aQ^2}{b^3}\cos^2\vartheta+\frac{3aMQ^2}{b^4}\cos^3\vartheta d\vartheta \\
=\;& -\frac{2a}{\ell^2}\left[\frac{\sqrt{1-(bu_R)^2}}{u_R}+\frac{\sqrt{1-(bu_S)^2}}{u_S}\right]+\frac{aQ^2}{b^3}\left[\pi-\arcsin(bu_S)-\arcsin(bu_R)\right] \\
&-\frac{aM}{\ell^2}\left[\pi-\arctan(\sqrt{1-(u_Sb)^2})-\arctan(\sqrt{1-(u_Rb)^2})\right] \\
&-\left[\frac{2aM}{b^2}+\frac{3aMQ^2}{2\ell^2b^2}-\frac{2aMQ^2}{b^4}\right]\left[\sqrt{1-(bu_S)^2}+\sqrt{1-(bu_R)^2}\right] \\
&+\frac{aQ^2}{b^2}\left[u_S\sqrt{1-(u_Sb)^2}+u_R\sqrt{1-(u_Rb)^2}\right] \\
&+\frac{aMQ^2}{b^2}\left[u_S^2\sqrt{1-(u_Sb)^2}+u_R^2\sqrt{1-(u_Rb)^2}\right]+O\left(M^2,Q^3,a,\frac{1}{\ell^4}\right).
\end{aligned}
\tag{3.115}
$$

Combining Eqs.(3.114) and (3.115), for $bu_S << 1$ and $bu_R << 1$, we get the deflection angle expression

$$\begin{aligned}\Theta_{KN_{AdS}} \simeq\ & \frac{4M}{b} - \frac{3Q^2\pi}{4b^2} - \frac{4aM}{b^2} - \frac{3aMQ^2}{\ell^2 b^2} - \frac{32MQ^2}{3b^3} + \frac{aQ^2\pi}{b^3} + \frac{4aMQ^2}{b^4} + \frac{6Q^2\pi}{\ell^2} - \frac{aM\pi}{2\ell^2} \\ - & \frac{Mb}{\ell^2} + \left[\frac{b}{2\ell^2} - \frac{2a}{\ell^2}\right]\left[\frac{1}{u_R} + \frac{1}{u_S}\right] + O\left(M^2, Q^3, a, \frac{1}{\ell^4}\right). \qquad (3.116)\end{aligned}$$

From Eq.(3.116), it is evident that we can recover the contributions of the rotation parameter and charge, as obtained in the case of Kerr-Newman ordinary black holes [93,94]. Examining the gravitational bending angle of light for finite distances, where the observer and the source are located at $u_S = u_R = 0.1$, we illustrate in Fig.(3.13) the variation of the deflection angle $\Theta_{KN_{AdS}}$ with respect to the impact parameter, by varying the rotation parameter for fixed values of the mass, the charge, and the AdS radius.

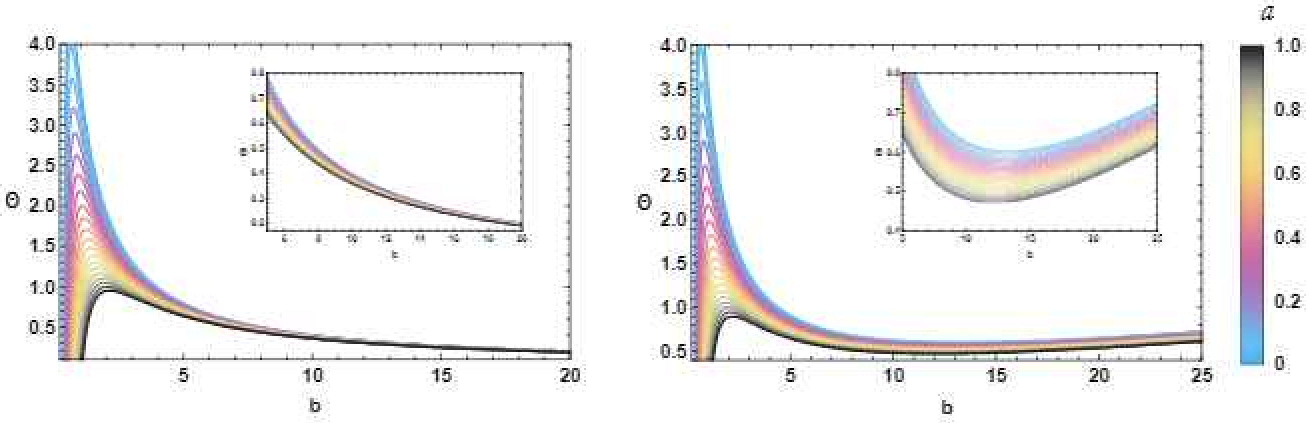

Figure 3.13: *Deflection angle variation in terms of the impact parameter by varying a and taking* $u_S = u_R = 0.1$ *, M=1 and* $Q = 0.2$*. Left panel: behavior with* $\ell = \infty$*, right panel: behavior with* $\ell = 20$*.*

To investigate the impact of the cosmological constant, we take two specific cases $\ell = \infty$ (left panel) and $\ell = 20$ (right panel). For non AdS backgrounds, the deflection angle decreases when the rotating parameter increase, remaining on a decreasing function for generic values of b. In the right panel, the deflection angle rapidly decreases for small b and then becomes an increasing function. For a generic value of ℓ, the deflection angle decreases with the rotation parameter. In fixed charge solutions, the previously observed behavior-changing point for the rotation parameter variation is not observed. Notably, in this case, the variation of the charge introduces a critical point b_c^a where the charge effect is inverted. This critical point can be obtained by using the derivative of the deflection angle with respect to the charge. Its value should depend on the three parameters ℓ, M, and a. The computation yields

$$b_c^a = b_c + a\left(\frac{\mu+\nu}{(6\pi)^{2/3}\lambda^{4/3}\left(3\pi^2\ell^2-32768M^2\right)}\right) \tag{3.117}$$

where one has used

$$\begin{aligned}
\mu &= -16777216\sqrt[3]{6}M^4\ell^2-65536\sqrt[3]{6}M^3\left(\lambda-256\mathrm{M}\ell^2\right)+512M^2\left(256\pi^{4/3}\lambda^{2/3}\ell^2-253\sqrt[3]{6}\pi^2\ell^4\right)\\
\nu &= \pi^{4/3}M\left(\lambda-256\mathrm{M}\ell^2\right)\left(515\lambda^{2/3}-509\sqrt[3]{6}\pi^{2/3}\ell^2\right)+12\sqrt[3]{6}\pi^4\ell^6\\
&- 12\pi^{10/3}\lambda^{2/3}\ell^4(6\pi)^{2/3}\lambda^{4/3}\left(3\pi^2\ell^2-32768M^2\right).
\end{aligned} \tag{3.118}$$

For a vanishing value of the rotating parameter, we retrieve the earlier equation of the non-rotating case. Now, we explore the influence of plasma on the weak deflection angle of four-dimensional AdS black holes. Particularly, we focus on the Kerr-Newman AdS solution, assuming that similar process can be applied to other models. To proceed, certain optical quantities are required. According to [90], the refractive index in terms of the photon four-momentum and velocity u^B can be expressed as

$$n^2 = 1+\frac{P_\alpha P^\alpha}{(P_B u^B)^2}. \tag{3.119}$$

For a non-magnetized cold plasma, Eq. (3.119) simplifies to the following form

$$n^2 = 1-\frac{\omega_p(r)^2}{\omega_0^2}, \tag{3.120}$$

where ω_0^2 represents the photon frequency, $\omega_p(p)$ is the electron plasma frequency. Various models have been explored, but for this discussion, we consider a special form studied in [123,124,136]. Utilizing a radial power law, the associated photon frequency can be expressed as

$$\omega_p^2(r) = \frac{k}{r^h}, \qquad h>0, \tag{3.121}$$

where k is an arbitrary constant associated with certain physical quantities. To investigate this effect, we consider a specific model based on an inhomogeneous space-time. For simplicity, we set $h=1$. Consequently, the two-dimensional optical geometry of the Kerr-Newman

AdS black hole in the presence of the plasma medium is given by

$$dl = n^2 \gamma_{ij} dx^i dx^j. \tag{3.122}$$

This represents a generalized form of Eq.(3.77). It gives the following expression for the Gaussian optical curvature

$$\begin{aligned}
K &= \frac{1}{\ell^2} + \left(-\frac{6M}{\ell^2} + \frac{3k}{2\omega_0^2\ell^2}\right)\frac{1}{r} + \left(\frac{6Q^2}{\ell^2} + \frac{3k^2}{\omega_0^4\ell^2} - \frac{15kM}{2\omega_0^2\ell^2}\right)\frac{1}{r^2} \\
&+ \left(-2M + \frac{11k^3}{2\omega_0^6\ell^2} - \frac{11k^2M}{\omega_0^4\ell^2} + \frac{7kQ^2}{\omega_0^2\ell^2} + \frac{k}{2\omega_0^2}\right)\frac{1}{r^3} \\
&+ \left(3Q^2 + \frac{9k^4}{\omega_0^8\ell^2} - \frac{33k^3M}{2\omega_0^6\ell^2} + \frac{9k^2Q^2}{\omega_0^4\ell^2} + \frac{3k^2}{2\omega_0^4} - \frac{9kM}{2\omega_0^2}\right)\frac{1}{r^4} \\
&+ \left(-6MQ^2 + \frac{27k^5}{2\omega_0^{10}\ell^2} - \frac{24k^4M}{\omega_0^8\ell^2} + \frac{12k^3Q^2}{\omega_0^6\ell^2} + \frac{3k^3}{\omega_0^6} - \frac{9k^2M}{\omega_0^4} + \frac{9kQ^2}{2\omega_0^2}\right)\frac{1}{r^5} + O\left(M^2, Q^3, a, \frac{1}{\ell^2}\right).
\end{aligned} \tag{3.123}$$

Furthermore, the geodesic curvature is found to be

$$\begin{aligned}
k_g &= -\frac{2a}{\ell^2} + \left(-\frac{2ak}{\omega_0^2\ell^2} - \frac{aM}{\ell^2}\right)\frac{1}{r} - \left(\frac{2ak^2}{\omega_0^4\ell^2} + \frac{akM}{\omega_0^2\ell^2}\right)\frac{1}{r^2} + \left(-2aM - \frac{2ak^3}{\omega_0^6\ell^2} - \frac{ak^2M}{\omega_0^4\ell^2} - \frac{3aMQ^2}{2\ell^2}\right)\frac{1}{r^3} \\
&+ \left(2aQ^2 - \frac{2ak^4}{\omega_0^8\ell^2} - \frac{ak^3M}{\omega_0^6\ell^2} - \frac{3akMQ^2}{2\omega_0^2\ell^2} - \frac{2akM}{\omega_0^2}\right)\frac{1}{r^4} \\
&+ \left(3aMQ^2 - \frac{2ak^5}{\omega_0^{10}\ell^2} - \frac{ak^4M}{\omega_0^8\ell^2} - \frac{3ak^2MQ^2}{2\omega_0^4\ell^2} - \frac{2ak^2M}{\omega_0^4} + \frac{2akQ^2}{\omega_0^2}\right)\frac{1}{r^5} \\
&+ O\left(M^2, Q^3, a, \frac{1}{\ell^2}\right).
\end{aligned} \tag{3.124}$$

By combining and integrating the above expressions in linear approximations, we can derive the deflection angle of the Kerr AdS black hole in such a medium. Assuming $bu_S << 1$ and $bu_R << 1$, we obtain this optical quantity as follows

$$\begin{aligned}
\Theta &= \Theta_{KN_{AdS}} - \frac{8ak^5}{3b^4\omega_0^{10}\ell^2} - \frac{4ak^4M}{3b^4\omega_0^8\ell^2} - \frac{2ak^2MQ^2}{b^4\omega_0^4\ell^2} - \frac{8ak^2M}{3b^4\omega_0^4} + \frac{8akQ^2}{3b^4\omega_0^2} - \frac{\pi ak^4}{b^3\omega_0^8\ell^2} - \frac{\pi ak^3M}{2b^3\omega_0^6\ell^2} \\
&- \frac{3\pi akMQ^2}{4b^3\omega_0^2\ell^2} - \frac{\pi akM}{b^3\omega_0^2} - \frac{4ak^3}{b^2\omega_0^6\ell^2} - \frac{2ak^2M}{b^2\omega_0^4\ell^2} - \frac{2\pi ak^2}{b\omega_0^4\ell^2} - \frac{\pi akM}{b\omega_0^2\ell^2} - \frac{\pi ak}{\omega_0^2\ell^2} + \frac{24k^5}{b^3\omega_0^{10}\ell^2} - \frac{128k^4M}{3b^3\omega_0^8\ell^2} \\
&+ \frac{64k^3Q^2}{3b^3\omega_0^6\ell^2} + \frac{16k^3}{3b^3\omega_0^6} - \frac{16k^2M}{b^3\omega_0^4} + \frac{8kQ^2}{b^3\omega_0^2} - \frac{9\pi k^4}{4b^2\omega_0^8\ell^2} + \frac{33\pi k^3M}{8b^2\omega_0^6\ell^2} - \frac{9\pi k^2Q^2}{4b^2\omega_0^4\ell^2} - \frac{3\pi k^2}{8b^2\omega_0^4} + \frac{9\pi kM}{8b^2\omega_0^2} \\
&- \frac{11k^3}{b\omega_0^6\ell^2} + \frac{22k^2M}{b\omega_0^4\ell^2} - \frac{14kQ^2}{b\omega_0^2\ell^2} - \frac{k}{b\omega_0^2} + \frac{bk}{4\omega_0^2\ell^2} + \frac{3\pi k^2}{\omega_0^4\ell^2} - \frac{15\pi kM}{2\omega_0^2\ell^2} + O\left(M^2, Q^3, a, \frac{1}{\ell^2}\right).
\end{aligned} \tag{3.125}$$

Setting $k = 0$, we recover the result of the ordinary solutions $\Theta = \Theta_{KN_{AdS}}$. To explore the effect of the plasma medium on the deflection angle of RN-AdS black holes, we consider two AdS radius values as before. Specifically, we vary the frequency ratio $\frac{k}{\omega_0^2}$ from 0 to 1. Fig.(3.14) illustrates these behaviors. Both the left and the right panels show that the deflection angle of the light rays remains a decreasing function with respect to the fractional frequency quantity, maintaining the same contribution even for large values of b. In the right panel, where the AdS space-time contribution is visualized with $\ell = 20$, the deflection angle increases for large impact parameter values. This behavior could be attributed to the presence of the cosmological constant, which can affect certain parameters such as the charge. However, the rotation parameter and the frequency ratio exhibit consistent behaviors for both large and small values of the impact parameter in the presence of AdS space-time.

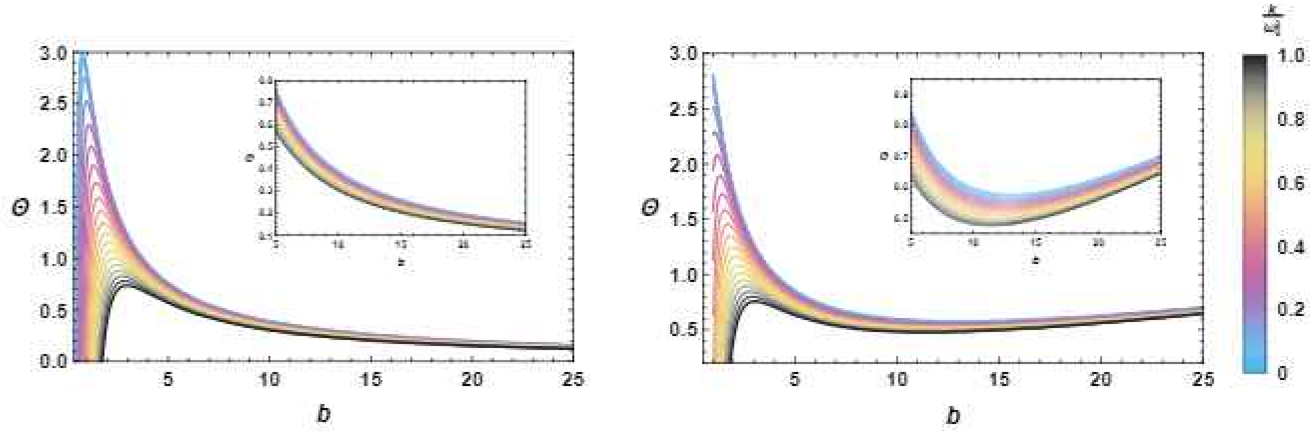

Figure 3.14: *Behaviors of the deflection angle as a function of the frequency ratio* $\frac{k}{\omega_0^2}$ *for* $u_S = u_R = 0.1$, $Q = 0.2$, $a = 0.2$ *and* $M = 1$. *Left panel: behavior with* $\ell = \infty$, *right panel: behavior with* $\ell = 20$.

3.2.2 Light deflection by cosmological rotating regular black holes

Here, we delve into the exploration of the deflection angle of the light rays in the vicinity of rotating Hayward black holes with a cosmological constant. The computations rely on the metric formulation discussed earlier. In Boyer-Lindquist coordinates, the metric is described by the following line element

$$ds^2 = -\frac{\Delta_r}{\Sigma}\left(dt - \frac{a\sin^2\theta}{\Xi}d\phi\right)^2 + \frac{\Sigma}{\Delta_r}dr^2 + \frac{\Sigma}{\Delta_\theta}d\theta^2 + \frac{\Delta_\theta \sin^2\theta}{\Sigma}\left(adt - \frac{r^2+a^2}{\Xi}d\phi\right)^2. \tag{3.126}$$

The characteristic quantities are given by

$$\begin{aligned} \Delta_r &= \left(r^2+a^2\right)\left(1-\frac{r^2\Lambda}{3}\right) - 2M\left(\frac{r^3}{r^3+g_h^3}\right)r, \qquad \Delta_\theta = 1+\frac{a^2\Lambda}{3}\cos^2\theta, & (3.127)\\ \Xi &= 1+\frac{a^2\Lambda}{3}, \qquad \Sigma = r^2+a^2\cos^2\theta, & (3.128)\end{aligned}$$

where g_h is the charge of the non-linear electrodynamics. In this case, considering the retrograde solution, one can get the geodesic equation as follows

$$\begin{aligned} \left(\frac{du}{d\phi}\right)^2 &= \frac{1}{b^2} - \frac{4aMu}{b^3} - u^2 + 2Mu^3 + \frac{\Lambda}{3} - \frac{2a\Lambda}{3b^3u^2} - \frac{8a\Lambda M}{3b^3u} + \frac{4aMu^4g_h^3}{b^3} - 2Mu^6g_h^3 \\ &+ \frac{8a\Lambda Mu^2g_h^3}{3b^3} + \mathcal{O}(M^2,\Lambda^2,a^2,g_h^4). \end{aligned} \tag{3.129}$$

The weak field and the slow rotation considerations yields to

$$b = \frac{1}{u_0} + M - 2aMu_0 + \mathcal{O}(M^2,\Lambda,a^2,g_h). \tag{3.130}$$

Performing appropriate calculations, we obtain the separation angle expression

$$\begin{aligned}
\phi_{RS} &= \phi_{RS}^{Kerr} + \left(\frac{u_R\left(2b^4u_R^4 + 5b^2u_R^2 - 15\right)}{\sqrt{1-b^2u_R^2}} + \frac{u_S\left(2b^4u_S^4 + 5b^2u_S^2 - 15\right)}{\sqrt{1-b^2u_S^2}} \right) \frac{Mg_h^3}{8b^3} \\
&+ \left(\frac{u_R\left(b^2u_R^2 - 3\right)}{\sqrt{1-b^2u_R^2}} + \frac{u_S\left(b^2u_S^2 - 3\right)}{\sqrt{1-b^2u_S^2}} \right) \frac{aMg_h^3}{b^4} \\
&- \left(\frac{u_R\left(3b^4u_R^4 - 20b^2u_R^2 + 15\right)}{\left(1-b^2u_R^2\right)^{3/2}} + \frac{u_S\left(3b^4u_S^4 - 20b^2u_S^2 + 15\right)}{\left(1-b^2u_S^2\right)^{3/2}} \right) \frac{\Lambda Mg_h^3}{12b} \\
&+ \left(\pi - \arcsin\left(bu_R\right) - \arcsin\left(bu_S\right)\right) \left(-\frac{15Mg_h^3}{8b^4} + \frac{3aMg_h^3}{b^5} - \frac{5\Lambda Mg_h^3}{4b^2} \right) \\
&+ \left(\frac{u_R}{\sqrt{1-b^2u_R^2}} + \frac{u_S}{\sqrt{1-b^2u_S^2}} \right) \frac{b^3\Lambda}{6} + \left(\frac{b\left(2-3b^2u_R^2\right)}{2\left(1-b^2u_R^2\right)^{3/2}} + \frac{b\left(2-3b^2u_S^2\right)}{2\left(1-b^2u_S^2\right)^{3/2}} \right) \frac{M\Lambda}{3} \\
&+ \left(\frac{1-2b^2u_R^2}{u_R\sqrt{1-b^2u_R^2}} + \frac{1-2b^2u_S^2}{u_S\sqrt{1-b^2u_S^2}} \right) \frac{a\Lambda}{3} + \mathcal{O}(M^2, \Lambda^2, a^2, g_h^4, Ma\Lambda, Ma\Lambda g_h^3), \quad (3.131)
\end{aligned}$$

where the Kerr contribution is given by

$$\phi_{RS}^{Kerr} = \phi_{RS}^{SW} - \left(\frac{1}{\sqrt{1-b^2u_R^2}} + \frac{1}{\sqrt{1-b^2u_S^2}} \right) \frac{2aM}{b^2}, \tag{3.132}$$

and The Schwarzschild one is expressed as follows

$$\phi_{RS}^{SW} = \pi - \arcsin\left(bu_R\right) - \arcsin\left(bu_S\right) + \left(\frac{2-b^2u_R^2}{\sqrt{1-b^2u_R^2}} + \frac{2-b^2u_S^2}{\sqrt{1-b^2u_S^2}} \right) \frac{M}{b}. \tag{3.133}$$

To express the light ray deflection angle formula, we need to get the Ψ expression. Using Eq.(3.80), we obtain

$$\begin{aligned}
\sin\Psi &= bu - bMu^2 + 2aMu^2 - \left(\frac{bM}{6} - \frac{a}{3u} + \frac{b}{6u} \right)\Lambda + \left(bu^5 - 2au^5 + \frac{b\Lambda u^3}{6} \right) Mg_h^3 \\
&+ \mathcal{O}(M^2, \Lambda^2, a^2, g_h^4, Ma\Lambda, Ma\Lambda g_h^3). \qquad (3.134)
\end{aligned}$$

The computation produces

$$\begin{aligned}\Psi_R \quad - \quad \Psi_S &= \Psi_R^{Kerr} - \Psi_S^{Kerr} + \left(\frac{b u_R^5}{\sqrt{1-b^2u_R^2}} + \frac{b u_S^5}{\sqrt{1-b^2u_S^2}}\right) M g_h^3 \\ - &\quad \left(\frac{u_R^5}{\sqrt{1-b^2u_R^2}} + \frac{u_S^5}{\sqrt{1-b^2u_S^2}}\right) 2aMg_h^3 - \left(\frac{u_R^3\,(2b^2u_R^2-1)}{(1-b^2u_R^2)^{3/2}} + \frac{u_S^3\,(2b^2u_S^2-1)}{(1-b^2u_S^2)^{3/2}}\right)\frac{b\Lambda M g_h^3}{6} \\ - &\quad \left(\frac{1}{u_R\sqrt{1-b^2u_R^2}} + \frac{1}{u_S\sqrt{1-b^2u_S^2}}\right)\frac{b\Lambda}{6} - \left(\frac{2b^2u_R^2-1}{(1-b^2u_R^2)^{3/2}} + \frac{2b^2u_S^2-1}{(1-b^2u_S^2)^{3/2}}\right)\frac{b\Lambda M}{6} \\ + &\quad \left(\frac{1}{u_R\sqrt{1-b^2u_R^2}} + \frac{1}{u_S\sqrt{1-b^2u_S^2}}\right)\frac{a\Lambda}{3} + \mathcal{O}(M^2, \Lambda^2, a^2, g_h^4, Ma\Lambda, Ma\Lambda g_h^3), \end{aligned} \tag{3.135}$$

where one has

$$\Psi_R^{Kerr} \quad - \quad \Psi_S^{Kerr} = \Psi_R^{SW} - \Psi_S^{SW} + \left(\frac{u_R^2}{\sqrt{1-b^2u_R^2}} + \frac{u_S^2}{\sqrt{1-b^2u_S^2}}\right) 2aM, \tag{3.136}$$

Moreover, one has found

$$\Psi_R^{SW} - \Psi_S^{SW} = \left(\arcsin\left(bu_R\right) + \arcsin\left(bu_S\right) - \pi\right) - \left(\frac{u_R^2}{\sqrt{1-b^2u_R^2}} + \frac{u_S^2}{\sqrt{1-b^2u_S^2}}\right) Mb \tag{3.137}$$

Using the above equations, we obtain an expression of such an optical quantity

$$\begin{aligned}
\alpha_h &= \left(\sqrt{1-b^2u_R^2}+\sqrt{1-b^2u_S^2}\right)\frac{2M}{b}-\left(\sqrt{1-b^2u_R^2}-\sqrt{1-b^2u_S^2}\right)\frac{2aM}{b^2}\\
&- \left(\frac{1-b^2u_R^2}{u_R\sqrt{1-b^2u_R^2}}+\frac{1-b^2u_S^2}{u_S\sqrt{1-b^2u_S^2}}\right)\frac{\mathrm{b}\Lambda}{6}+\left(\frac{1}{\sqrt{1-b^2u_R^2}}+\frac{1}{\sqrt{1-b^2u_S^2}}\right)\frac{b\Lambda M}{6}\\
&+ \left(\frac{\sqrt{1-b^2u_R^2}}{u_R}+\frac{\sqrt{1-b^2u_S^2}}{u_S}\right)\frac{2a\Lambda}{3}+\left(\frac{u_R\left(2b^4u_R^4+b^2u_R^2-3\right)}{\sqrt{1-b^2u_R^2}}+\frac{u_S\left(2b^4u_S^4+b^2u_S^2-3\right)}{\sqrt{1-b^2u_S^2}}\right)\frac{5Mg_h^3}{8b^3}\\
&- \left(\frac{u_R\left(2b^4u_R^4+b^2u_R^2-3\right)}{b^4\sqrt{1-b^2u_R^2}}+\frac{u_S\left(2b^4u_S^4+b^2u_S^2-3\right)}{b^4\sqrt{1-b^2u_S^2}}\right)\frac{aMg_h^3}{b^4}\\
&+ \left(\frac{u_R\left(7b^2u_R^2-15\right)}{\sqrt{1-b^2u_R^2}}+\frac{u_S\left(7b^2u_S^2-15\right)}{\sqrt{1-b^2u_S^2}}\right)\frac{\Lambda Mg_h^3}{12b}\\
&+ \left(\pi-\arcsin\left(bu_R\right)-\arcsin\left(bu_S\right)\right)\left(-\frac{15Mg_h^3}{8b^4}+\frac{3aMg_h^3}{b^5}-\frac{5\Lambda Mg_h^3}{4b^2}\right)\\
&+ \mathcal{O}(M^2,\Lambda^2,a^2,g_h^4,Ma\Lambda,Ma\Lambda g_h^3). \qquad (3.138)
\end{aligned}$$

This form can be simplified by making certain convenient approximations. Assuming $u_Sb << 1$ and $u_Rb << 1$, we can derive an equation that involves divergent contribution. These terms are essential to showcase the dependence on the cosmological background. The final expression for the deflection angle of Hayward black holes is given by

$$\begin{aligned}
\alpha_h &= \frac{4M}{b}-\frac{4aM}{b^2}-\frac{15\pi Mg_h^3}{8b^4}+\frac{3\pi aMg_h^3}{b^5}-\frac{5\Lambda\pi\mathrm{M}g_h^3}{4b^2}+\frac{b\Lambda M}{3}-\left(\frac{1}{u_R}+\frac{1}{u_S}\right)\frac{b\Lambda}{6}\\
&+ \left(\frac{1}{u_R}+\frac{1}{u_S}\right)\frac{2a\Lambda}{3}+\mathcal{O}(M^2,\Lambda^2,a^2,g_h^4,Ma\Lambda,Ma\Lambda g_h^3). \qquad (3.139)
\end{aligned}$$

Upon inspection, it becomes evident that this expression reproduces several previously established results. In the absence of cosmological contributions, the outcomes align with those of conventional Hayward solutions. Furthermore, setting the additional parameters to zero yields results consistent with the Schwarzschild black hole and the Kerr black hole. In the subsequent analysis, we investigate additional regular black holes, focusing on the deflection angle of light rays around rotating Bardeen black holes with a cosmological constant. To commence, we present the metric in Boyer-Lindquist coordinates, given by the following line element:

$$ds^2 = -\frac{\Delta_r}{\Sigma}\left(dt - \frac{a\sin^2\theta}{\Xi}d\phi\right)^2 + \frac{\Sigma}{\Delta_r}dr^2 + \frac{\Sigma}{\Delta_\theta}d\theta^2 + \frac{\Delta_\theta \sin^2\theta}{\Sigma}\left(adt - \frac{r^2+a^2}{\Xi}d\phi\right)^2. \quad (3.140)$$

This involves the following physical terms

$$\begin{aligned}\Delta_r &= \left(r^2+a^2\right)\left(1-\frac{r^2\Lambda}{3}\right) - 2M\left(\frac{r^2}{r^2+g_b^2}\right)^{\frac{3}{2}} r, \qquad \Delta_\theta = 1 + \frac{a^2\Lambda}{3}\cos^2\theta, \quad (3.141)\\ \Xi &= 1 + \frac{a^2\Lambda}{3}, \qquad \Sigma = r^2 + a^2\cos^2\theta.\end{aligned}$$

To compute the corresponding deflection angle, it is necessary to derive the orbit equation, as emphasized in the prior investigation. A careful examination yields the following relation

$$\begin{aligned}\left(\frac{du}{d\phi}\right)^2 &= \frac{1}{b^2} - \frac{4aMu}{b^3} - u^2 + 2Mu^3 + \frac{\Lambda}{3} - \frac{2a\Lambda}{3b^3u^2} - \frac{8a\Lambda M}{3b^3u} - 3Mu^5g_b^2\\ &+ \frac{6aMu^3g_b^2}{b^3} + \frac{4a\Lambda Mug_b^2}{b^3} + \mathcal{O}(M^2, \Lambda^2, a^2, g_b^3). \qquad (3.142)\end{aligned}$$

After computations, we obtain

$$\begin{aligned}\phi_{RS} &= \phi_{RS}^{Kerr} + \left(\frac{b^4u_R^4 + 4b^2u_R^2 - 8}{2b^3\sqrt{1-b^2u_R^2}} + \frac{b^4u_S^4 + 4b^2u_S^2 - 8}{2b^3\sqrt{1-b^2u_S^2}}\right)Mg_b^2\\ &- \left(\frac{3b^4u_R^4 - 12b^2u_R^2 + 8}{\left(1-b^2u_R^2\right)^{3/2}} + \frac{3b^4u_S^4 - 12b^2u_S^2 + 8}{\left(1-b^2u_S^2\right)^{3/2}}\right)\frac{\Lambda Mg_b^2}{4} + \left(\frac{6-3b^2u_R^2}{\sqrt{1-b^2u_R^2}} + \frac{6-3b^2u_S^2}{\sqrt{1-b^2u_S^2}}\right)\frac{aMg_b^2}{b^4}\\ &+ \left(\frac{u_R}{\sqrt{1-b^2u_R^2}} + \frac{u_S}{\sqrt{1-b^2u_S^2}}\right)\frac{b^3\Lambda}{6} + \left(\frac{b\left(2-3b^2u_R^2\right)}{2\left(1-b^2u_R^2\right)^{3/2}} + \frac{b\left(2-3b^2u_S^2\right)}{2\left(1-b^2u_S^2\right)^{3/2}}\right)\frac{M\Lambda}{3}\\ &+ \left(\frac{1-2b^2u_R^2}{u_R\sqrt{1-b^2u_R^2}} + \frac{1-2b^2u_S^2}{u_S\sqrt{1-b^2u_S^2}}\right)\frac{a\Lambda}{3} + \mathcal{O}(M^2, \Lambda^2, a^2, g_b^3, Ma\Lambda, Ma\Lambda g_b^2). \qquad (3.143)\end{aligned}$$

The Ψ terms are found to be

$$\begin{aligned}\sin\Psi &= bu - bMu^2 + 2aMu^2 + \left(\frac{3bu^4}{2} - 3au^4 + \frac{b\Lambda u^2}{4}\right)Mg_b^2 - \left(\frac{bM}{6} - \frac{a}{3u} + \frac{b}{6u}\right)\Lambda\\ &+ \mathcal{O}(M^2, \Lambda^2, a^2, g_b^3, Ma\Lambda, Ma\Lambda g_b^2). \qquad (3.144)\end{aligned}$$

This relation leads to

$$\begin{aligned}
\Psi_R \quad - \quad \Psi_S = \Psi_R^{Kerr} - \Psi_S^{Kerr} + \left(\frac{u_R^4}{\sqrt{1-b^2u_R^2}} + \frac{u_S^4}{\sqrt{1-b^2u_S^2}}\right)\frac{3bMg_b^2}{2} \qquad (3.145)\\
- \quad \left(\frac{u_R^4}{\sqrt{1-b^2u_R^2}} + \frac{u_S^4}{\sqrt{1-b^2u_S^2}}\right)3aMg_b^2 - \left(\frac{u_R^2\,(2b^2u_R^2-1)}{(1-b^2u_R^2)^{\,3/2}} + \frac{u_S^2\,(2b^2u_S^2-1)}{(1-b^2u_S^2)^{\,3/2}}\right)\frac{b\Lambda M g_b^2}{4}\\
- \quad \left(\frac{1}{u_R\sqrt{1-b^2u_R^2}} + \frac{1}{u_S\sqrt{1-b^2u_S^2}}\right)\frac{b\Lambda}{6} - \left(\frac{2b^2u_R^2-1}{(1-b^2u_R^2)^{\,3/2}} + \frac{2b^2u_S^2-1}{(1-b^2u_S^2)^{\,3/2}}\right)\frac{b\Lambda M}{6}\\
+ \quad \left(\frac{1}{u_R\sqrt{1-b^2u_R^2}} + \frac{1}{u_S\sqrt{1-b^2u_S^2}}\right)\frac{a\Lambda}{3} + \mathcal{O}(M^2,\Lambda^2,a^2,g_b^3,Ma\Lambda,Ma\Lambda g_b^2). \qquad (3.146)
\end{aligned}$$

Utilizing the equations mentioned above, we derive the expression for the deflection angle of light rays around cosmological Bardeen black holes

$$\begin{aligned}
\alpha_b \quad = \quad & \left(\sqrt{1-b^2u_R^2} + \sqrt{1-b^2u_S^2}\right)\frac{2M}{b} - \left(\sqrt{1-b^2u_R^2} - \sqrt{1-b^2u_S^2}\right)\frac{2aM}{b^2}\\
- \quad & \left(\frac{1-b^2u_R^2}{u_R\sqrt{1-b^2u_R^2}} + \frac{1-b^2u_S^2}{u_S\sqrt{1-b^2u_S^2}}\right)\frac{\mathrm{b}\Lambda}{6} + \left(\frac{1}{\sqrt{1-b^2u_R^2}} + \frac{1}{\sqrt{1-b^2u_S^2}}\right)\frac{b\Lambda M}{6}\\
+ \quad & \left(\frac{\sqrt{1-b^2u_R^2}}{u_R} + \frac{\sqrt{1-b^2u_S^2}}{u_S}\right)\frac{2a\Lambda}{3} + \left(\frac{b^4u_R^4+b^2u_R^2-2}{\sqrt{1-b^2u_R^2}} + \frac{b^4u_S^4+b^2u_S^2-2}{\sqrt{1-b^2u_S^2}}\right)\frac{2Mg_b^2}{b^3}\\
- \quad & \left(\frac{b^4u_R^4+b^2u_R^2-2}{\sqrt{1-b^2u_R^2}} + \frac{b^4u_S^4+b^2u_S^2-2}{\sqrt{1-b^2u_S^2}}\right)\frac{3aMg_b^2}{b^4} + \left(\frac{5b^2u_R^2-8}{\sqrt{1-b^2u_R^2}} + \frac{5b^2u_S^2-8}{\sqrt{1-b^2u_S^2}}\right)\frac{\Lambda M g_b^2}{4b}\\
+ \quad & \mathcal{O}(M^2,\Lambda^2,a^2,g_b^3,Ma\Lambda,Ma\Lambda g_b^2). \qquad (3.147)
\end{aligned}$$

This expression can be further simplified by considering certain approximations. Specifically, letting $u_S b$ and $u_R b$ approach zero, we arrive at an expression that involves divergent terms coupled with geometric contributions, reflecting the dependence on the AdS backgrounds. The final expression for the light deflection angle of the Bardeen black holes is given by

$$\begin{aligned}
\alpha_b \quad = \quad & \frac{4M}{b} - \frac{4aM}{b^2} - \frac{8Mg_b^2}{b^3} - \frac{4\Lambda M g_b^2}{b} + \frac{12aMg_b^2}{b^4} + \frac{b\Lambda M}{3} - \left(\frac{1}{u_R} + \frac{1}{u_S}\right)\frac{b\Lambda}{6}\\
+ \quad & \left(\frac{1}{u_R} + \frac{1}{u_S}\right)\frac{2a\Lambda}{3} + \mathcal{O}(M^2,\Lambda^2,a^2,g_b^2,Ma\Lambda,Ma\Lambda g_b^2). \qquad (3.148)
\end{aligned}$$

This expression retains the capability to encompass and generalize the results obtained earlier [127, 128] by removing the extra physical parameters.

With the obtained expression for the deflection angle of light rays around regular rotating black holes in the presence of a cosmological constant, we proceed to conduct a graphical analysis of the corresponding optical behaviors. Specifically, we vary the involved parameters, including the cosmological constant, and inspect different regions of the parameter space. These variations are then compared with the results obtained for Kerr solutions.

To scrutinize the variation aspects of the investigated optical quantity, we need to consider the moduli space coordinated by the involved parameters. These behaviors will be illustrated by focusing on specific regions of such a parameter space, particularly those involving cosmological contributions. Initially, we fix the black hole mass and take a negative cosmological constant, then vary the remaining parameters. The optical behaviors for the Hayward black hole solutions in these scenarios are presented in Fig. (3.15).

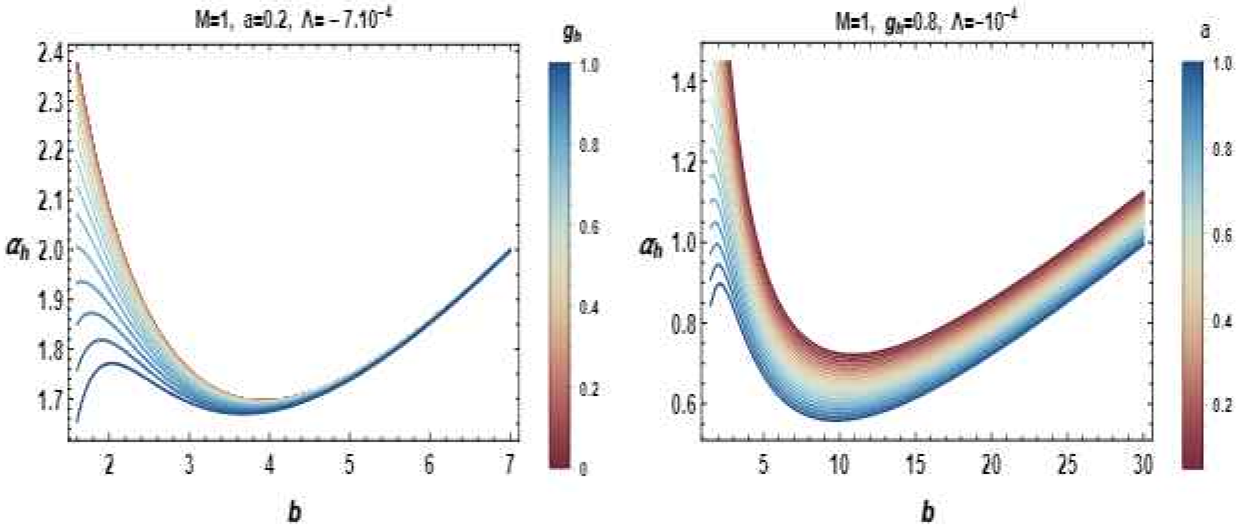

Figure 3.15: *Variation of the deflection angle of Hayward black holes with cosmological constant in terms of the impact parameter.*

For small values of the impact parameter, it is observed that the deflection angle of the light rays is a decreasing function with a noticeable effect of g_h. Specifically, it decreases with this parameter. On the other hand, for large values of the impact parameter, the deflection angle of the light rays becomes an increasing function, with one-dimensional real curves coinciding for generic values of g_h. Moreover, similar contributions are observed in the ordinary black hole solutions, where the deflection angle decreases with an increase in the rotation parameter. The obtained results confirm that the space-time of the ordinary solutions could be affected by g_h.

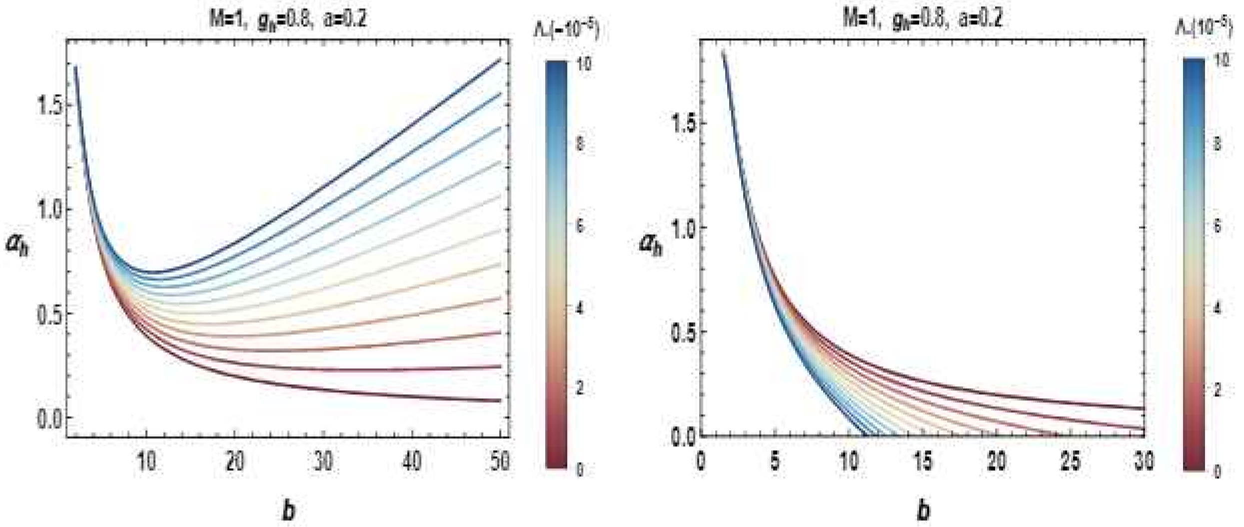

Figure 3.16: *Deflection angle variations of Hayward black holes as function of the impact parameter b with negative and positive values of Λ.*

To analyze the effect of the cosmological constant, the deflection angle in terms of b for various values of Λ will be inspected. The geometry prompts the consideration of different backgrounds by taking negative and positive values of the cosmological constant. These behaviors are presented in Fig. (3.16).

For small values b and small negative values of Λ, we observe a critical point where the deflection angle takes a minimal value. This value increases by decreasing the cosmological constant. For positive values of Λ, However, the deflection angle is a decreasing function of b.

For large values of the impact parameter, we observe that the influence of the cosmological constant becomes more pronounced. Notably, there is a linear behavior of the deflection angle.

The light deflection angle variation for the Bardeen solutions are depicted in Fig.(3.17).

Similar overall behaviors have been identified in the case of Bardeen solutions, showing consistent parameter effects with previous black hole solutions. This alignment supports the idea that the spacetime of the ordinary solutions could be influenced by g_h. However, to uncover specific local differences among regular black hole backgrounds, we conduct a comparative analysis.

Considering the Kerr solutions with cosmological contributions, the deflection angle of

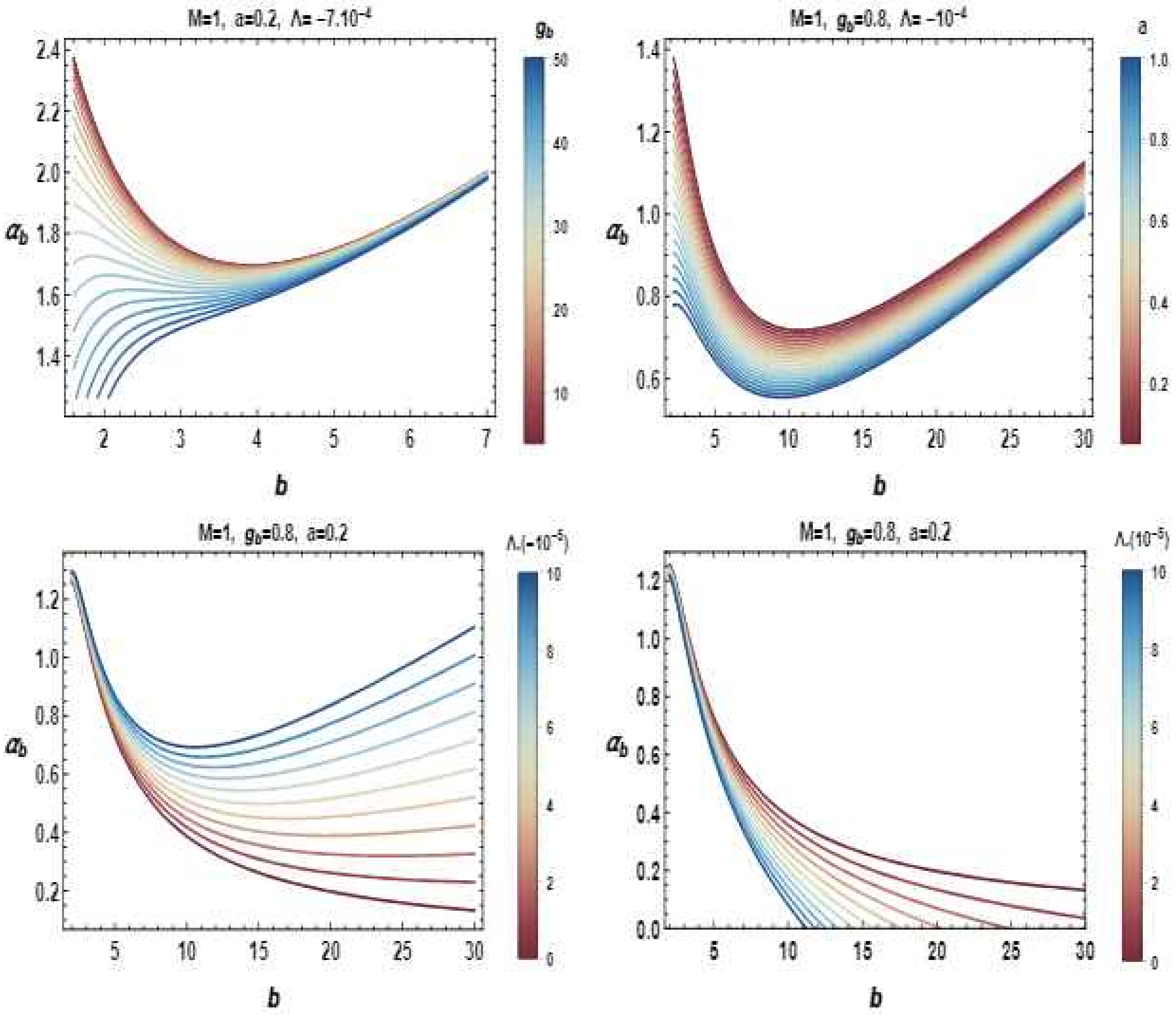

Figure 3.17: *Deflection angle variations of Bardeen black holes with cosmological constant as a function of the impact parameter.*

light rays can be approximately expressed as

$$\alpha^{\Lambda}_{Kerr} \sim \frac{4M}{b} - \frac{4aM}{b^2} + \frac{b\Lambda M}{3} - \left(\frac{1}{u_R} + \frac{1}{u_S}\right)\frac{b\Lambda}{6} + \left(\frac{1}{u_R} + \frac{1}{u_S}\right)\frac{2a\Lambda}{3}. \tag{3.149}$$

In Fig.(3.18), we plot the variation of the light deflection angle for the regular black hole solutions as a function of the impact parameter, juxtaposed with the Kerr solutions.

The analysis reveals that small ranges of b are crucial for both positive and negative values

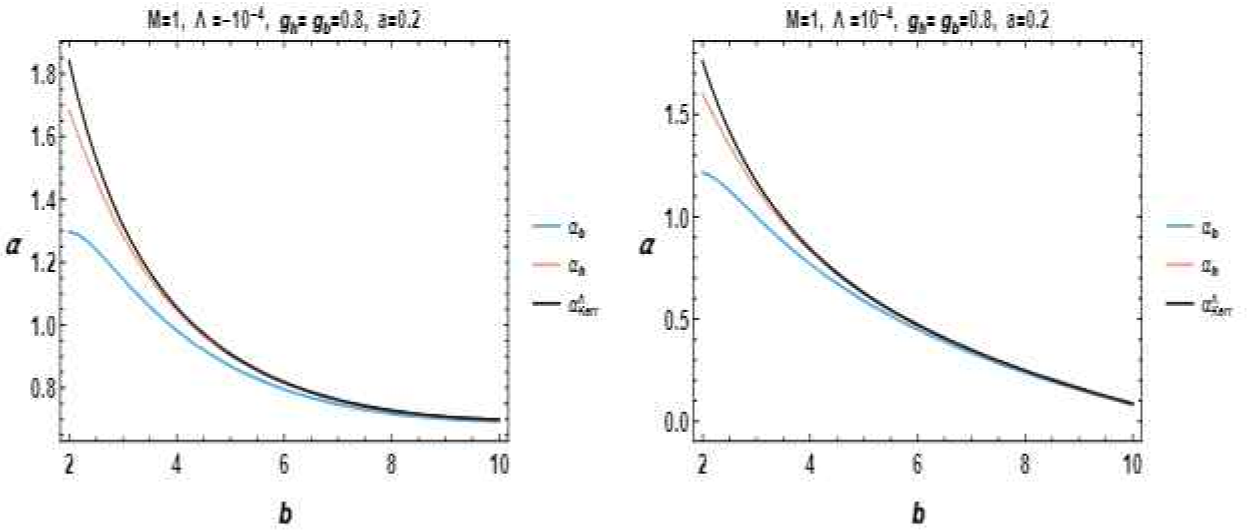

Figure 3.18: *Variation of deflection angle of Bardeen, Hayward and Kerr black holes with a cosmological constant.*

of the cosmological constant. However, for large values, notable distinctions are not apparent due to overlapping real curves. Notably, negative values of the cosmological constant result in an increased light deflection angle compared to positive ones. In particular, all solutions exhibit the same deflection angle behavior for the light rays. Consequently, our discussion primarily focuses on the first range.

It is noteworthy that the deflection angle of the light rays for the Bardeen black holes is smaller than that obtained for the Hayward solutions. Furthermore, the light deflection angle for both solutions is smaller than that of the Kerr solution. This observation supports the earlier notion that non-linear electrodynamic charges influence the spacetime geometry, contributing to a decrease in the deflection angle of the light rays.

It is anticipated that the deflection angle for both solutions tends towards that of ordinary rotating black holes with a cosmological constant. In particular, it has been verified that other findings can be recovered by setting λ to zero [127, 128].

3.3 Deflection angle and the light ray trajectories near to M-theory black holes

The study of black holes in M-theory has been an active area of research and speculation. Numerous black holes within this theoretical framework have been constructed, leading to the exploration of various aspects of their properties. A noteworthy connection has been established between the Anti-de Sitter (AdS) radius and the number of $M-(d-2)$ branes. This correlation reveals interesting thermodynamic and optical results, which are contingent upon both the dimension of the black hole and the number of branes involved. Motivated by such activities, we examine the light behaviors around 4-dimensional and 7-dimensional AdS black holes embedded in 11-dimensional M-theory associated with the triplets (11, 4, 3) and (11, 7, 3), respectively. We first deal with the corresponding deflection angle of the light rays. In the second part, we consider the study of the light trajectories.

3.3.1 Light behaviors near to black holes in the M-theory scenarios

We initiate our exploration with the non-rotating solutions corresponding to the triplet $(11,4,3)$ obtained from M-theory compactified on S^7 with N coincident $M2$-branes. The metric function in terms of the $M2$-brane number is given by

$$f(r)=1-\frac{192\ 2^{\frac{1}{6}}\pi^{\frac{2}{3}}\ell_p^2 M}{N^{\frac{7}{6}}r}+\frac{2^{\frac{1}{3}}r^2}{\pi^{\frac{2}{3}}\ell_p^2 N^{\frac{1}{3}}}, \tag{3.150}$$

where one has used

$$L_{AdS}=2^{-\frac{1}{6}}\pi^{\frac{1}{3}}N^{\frac{1}{3}}\ell_p, \qquad m=\frac{192\times 2^{1/6}\,\pi^{2/3}\,\ell_p^2\,M}{N^{7/6}}. \tag{3.151}$$

The calculation will be expanded to the leading order of m. The relevant radial equation in four dimensions is expressed as

$$F_4(u)=\frac{1}{b^2}-\frac{2^{\frac{1}{3}}}{\pi^{\frac{2}{3}}\ell_p^2 N^{\frac{1}{3}}}-u^2+\frac{192\ 2^{\frac{1}{6}}\pi^{\frac{2}{3}}\ell_p^2 M}{N^{\frac{7}{6}}}u^3. \tag{3.152}$$

Substituting the above equations in the equation (3.94) and performing the integral, the angle ϕ_{RS} can be expressed as follows

$$\begin{aligned}\phi_{RS} &= (\pi - \arcsin(bu_R) - \arcsin(bu_S)) - \left(\frac{u_R}{\sqrt{1-b^2u_R^2}} + \frac{u_S}{\sqrt{1-b^2u_S^2}}\right)\frac{b^3}{(2\pi)^{\frac{2}{3}}\ell_p^2 N^{\frac{1}{3}}} \\ &+ \left(\frac{2-b^2u_R^2}{\sqrt{1-b^2u_R^2}} + \frac{2-b^2u_S^2}{\sqrt{1-b^2u_S^2}}\right)\frac{96\ 2^{\frac{1}{6}}\pi^{\frac{2}{3}}\ell_p^2 M}{bN^{\frac{7}{6}}} + \left(\frac{3b^2u_R^2-2}{(1-b^2u_R^2)^{3/2}} + \frac{3b^2u_S^2-2}{(1-b^2u_S^2)^{3/2}}\right)\frac{48\sqrt{2}bM}{N^{3/2}}.\end{aligned} \tag{3.153}$$

According to Eq(3.91), the $\Psi_R - \Psi_S$ term takes the form

$$\begin{aligned}\Psi_R - \Psi_S &= (\arcsin(bu_R) + \arcsin(bu_S) - \pi) + \left(\frac{1}{u_R\sqrt{1-b^2u_R^2}} + \frac{1}{u_S\sqrt{1-b^2u_S^2}}\right)\frac{b}{(2\pi)^{\frac{2}{3}}\ell_p^2 N^{\frac{1}{3}}} \\ &- \left(\frac{u_R^2}{\sqrt{1-b^2u_R^2}} + \frac{u_S^2}{\sqrt{1-b^2u_S^2}}\right)\frac{96\ 2^{\frac{1}{6}}\pi^{\frac{2}{3}}\ell_p^2 bM}{N^{\frac{7}{6}}} + \left(\frac{1-2b^2u_R^2}{(1-b^2u_R^2)^{3/2}} + \frac{1-2b^2u_S^2}{(1-b^2u_S^2)^{3/2}}\right)\frac{48\sqrt{2}bM}{N^{\frac{3}{2}}}.\end{aligned} \tag{3.154}$$

Combining the above equations allows us to derive the deflection angle in terms of the $M2$-brane number N and the black hole mass. It can be expressed as follows

$$\begin{aligned}\Theta_4 &= \left(\frac{\sqrt{1-b^2u_R^2}}{u_R} + \frac{\sqrt{1-b^2u_S^2}}{u_S}\right)\frac{b}{(2\pi)^{\frac{2}{3}}\ell_p^2 N^{\frac{1}{3}}} + \left(\sqrt{1-b^2u_R^2} + \sqrt{1-b^2u_S^2}\right)\frac{192\pi^{\frac{2}{3}}2^{\frac{1}{6}}\ell_p^2 M}{bN^{\frac{7}{6}}} \\ &- \left(\frac{1}{\sqrt{1-b^2u_R^2}} + \frac{1}{\sqrt{1-b^2u_S^2}}\right)\frac{48\sqrt{2}bM}{N^{\frac{3}{2}}}.\end{aligned} \tag{3.155}$$

It has been noted that the given expression diverges when we take the limits $bu_S \to 0$ and $bu_R \to 0$. This divergence is a consequence of the space-time not being asymptotically flat. Consequently, the finite deflection angle of the light rays by AdS black holes from M-theory can be expressed as

$$\Theta_4 \sim \frac{b}{(2\pi)^{\frac{2}{3}}\ell_p^2 N^{\frac{1}{3}}}\left(\frac{1}{u_R} + \frac{1}{u_S}\right) + \frac{384\ 2^{\frac{1}{6}}\pi^{\frac{2}{3}}\ell_p^2 M}{bN^{\frac{7}{6}}} - \frac{96\sqrt{2}bM}{N^{\frac{3}{2}}}. \tag{3.156}$$

This equation indicates that the choice of the brane number value can influence the behavior of the deflection angle. Additionally, it demonstrates that the mass parameter contributes linearly, similar to the Schwarzschild black hole, with a different coefficient due to the dependence on the brane number.

3.3. Deflection angle and the light ray trajectories near to M-theory black holes

In Fig.(4.11), we depict the impact of $M2$-branes on the deflection angle. In the left panel of this figure, we illustrate the variation of the deflection angle in terms of the impact parameter for different values of N. Analyzing these AdS black holes, we observe that the deflection angle of the light rays decreases for small values of the impact parameter before becoming an increasing function. Both panels in Fig.(3.19) reveal that the $M2$-brane number leads to a decrease in the deflection angle. In the right panel, two values of the impact parameter are considered. Plotting the deflection angle against the $M2$-brane number, the two curves intersect at a specific point where the deflection angle of the AdS space transitions from a decreasing to an increasing function of the impact parameter. It should be interesting to link such behaviors with AdS/CFT conjecture.

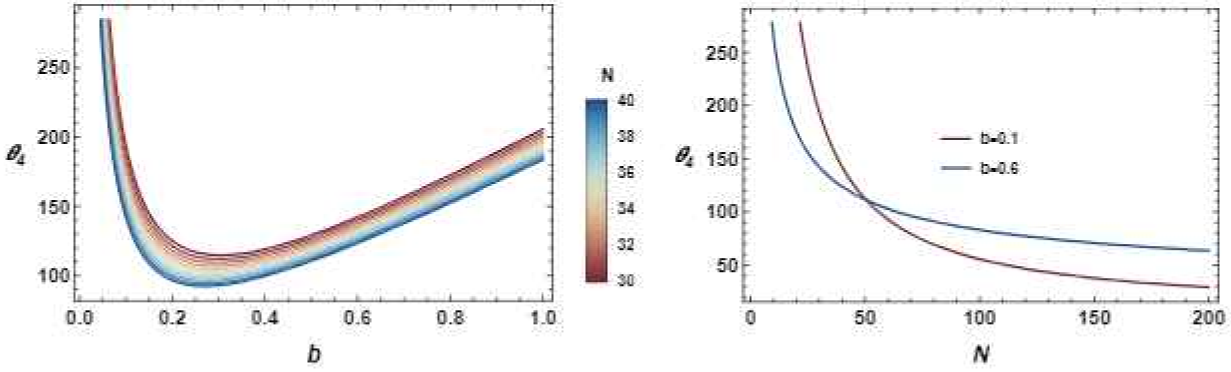

Figure 3.19: *Right panel: Variation of the deflection angle of 4-dimensional black holes in M-theory as a function of the impact parameter for various values of N. Lift panel: Variation of the deflection angle of 4-dimensional black holes in M-theory as a function of the brane number with $b = 0.1$ and $b = 0.6$.*

A close examination reveals that the behavior of the deflection angle of the AdS-Shwarzchild black holes for $M = 1$ and $L = 3$ is similar to the present one for $N \simeq 147$. The deflection angle graphs in this case exhibit a similar shape to those observed in Schwarzschild AdS black holes. They manifest as curves with noticeable positive concavities. It seems possible to extend this study of the deflection angle behaviors in M-theory by considering the rotating parameter a. According [129], indeed, the metric line element becomes

$$ds^2 = -\frac{\Delta_r}{W}\left(dt - \frac{a}{\Xi}\sin^2\theta d\phi\right)^2 + W\left(\frac{dr^2}{\Delta_r} + \frac{d\theta^2}{\Delta_\theta}\right) + \frac{\Delta_\theta \sin^2\theta}{W}\left(adt - \frac{r^2+a^2}{\Xi}d\phi\right)^2. \quad (3.157)$$

The involved terms are given by

$$\Delta_r = r^2 - mr + a^2 + \frac{r^2}{L^2}(r^2 + a^2), \qquad \Delta_\theta = 1 - \frac{a^2}{L^2}\cos^2\theta, \tag{3.158}$$

$$\Xi = 1 - \frac{a^2}{L^2}, \qquad W = r^2 + a^2\cos^2\theta. \tag{3.159}$$

In this approach, the calculation will be extended to the first order of m and a. To determine the Ψ and ϕ_{RS} angles for such a rotating black hole in four dimensions, we follow the method established in [92, 93], given the similarity in the metric form. Focusing on the equatorial plane, we can derive the orbit equation in terms of the $M2$-brane number N and the rotating parameter a. This equation is found to be

$$F_4(a,u) = \frac{1}{b^2} - u^2 - \frac{\sqrt[3]{2}}{\pi^{2/3}\sqrt[3]{N}\ell_p^2} + \frac{192\sqrt[6]{2}\pi^{2/3}Mu^3\ell_p^2}{N^{7/6}} + \frac{2\sqrt[3]{2}a}{\pi^{2/3}b^3\sqrt[3]{N}u^2\ell_p^2} - \frac{384\sqrt[6]{2}\pi^{2/3}aMu\ell_p^2}{b^3N^{7/6}} + \frac{768\sqrt{2}aM}{b^3N^{3/2}u}. \tag{3.160}$$

The longitudinal angle can be obtained as follows

$$\begin{aligned}
\phi_{RS} &= (\pi - \arcsin(bu_R) - \arcsin(bu_S)) - \left(\frac{u_R}{\sqrt{1-b^2u_R^2}} + \frac{u_S}{\sqrt{1-b^2u_S^2}}\right)\frac{b^3}{(2\pi)^{2/3}\sqrt[3]{N}\ell_p^2} \qquad (3.161)\\
&- \left(\frac{1-2b^2u_R^2}{u_R\sqrt{1-b^2u_R^2}} + \frac{1-2b^2u_S^2}{u_S\sqrt{1-b^2u_S^2}}\right)\frac{\sqrt[3]{2}a}{\pi^{2/3}\sqrt[3]{N}\ell_p^2} + \left(\frac{2-b^2u_R^2}{\sqrt{1-b^2u_R^2}} + \frac{2-b^2u_S^2}{\sqrt{1-b^2u_S^2}}\right)\frac{96\sqrt[6]{2}\pi^{2/3}M\ell_p^2}{bN^{7/6}}\\
&- \left(\frac{1}{\sqrt{1-b^2u_R^2}} + \frac{1}{\sqrt{1-b^2u_S^2}}\right)\frac{192\sqrt[6]{2}\pi^{2/3}aM\ell_p^2}{b^2N^{7/6}} - \left(\frac{2-3b^2u_R^2}{(1-b^2u_R^2)^{3/2}} + \frac{2-3b^2u_S^2}{(1-b^2u_S^2)^{3/2}}\right)\frac{48\sqrt{2}bM}{N^{3/2}}.
\end{aligned}$$

The computations give

$$\begin{aligned}
\Psi_R - \Psi_S &= (\arcsin(bu_R) + \arcsin(bu_S) - \pi) + \left(\frac{1}{u_R\sqrt{1-b^2u_R^2}} + \frac{1}{u_S\sqrt{1-b^2u_S^2}}\right)\frac{b}{(2\pi)^{2/3}\sqrt[3]{N}\ell_p^2}\\
&- \left(\frac{u_R^2}{\sqrt{1-b^2u_R^2}} + \frac{u_S^2}{\sqrt{1-b^2u_S^2}}\right)\frac{96\sqrt[6]{2}\pi^{2/3}bM\ell_p^2}{N^{7/6}}\\
&+ \left(\frac{1-2b^2u_R^2}{(1-b^2u_R^2)^{3/2}}\frac{1-2b^2u_S^2}{(1-b^2u_S^2)^{3/2}}\right)\frac{48\sqrt{2}bM}{N^{3/2}}.
\end{aligned} \tag{3.162}$$

By combining the obtained expressions, we can derive the deflection angle for four-dimensional rotating AdS black holes from M-theory in terms of the involved parameters. The computations yield to

$$\begin{aligned}\Theta_4(a) &= \left(\frac{1-b^2u_R^2}{u_R\sqrt{1-b^2u_R^2}}+\frac{1-b^2u_S^2}{u_S\sqrt{1-b^2u_S^2}}\right)\frac{b}{(2\pi)^{2/3}\sqrt[3]{N}\ell_p^2}\\ &- \left(\frac{1-2b^2u_R^2}{u_R\sqrt{1-b^2u_R^2}}+\frac{1-2b^2u_S^2}{u_S\sqrt{1-b^2u_S^2}}\right)\frac{\sqrt[3]{2}a}{\pi^{2/3}\sqrt[3]{N}\ell_p^2}\\ &- \left(\frac{1}{\sqrt{1-b^2u_R^2}}+\frac{1}{\sqrt{1-b^2u_S^2}}\right)\frac{84\sqrt{2}bM}{N^{3/2}}+\left(\sqrt{1-b^2u_R^2}+\sqrt{1-b^2u_S^2}\right)\frac{192\sqrt[6]{2}\pi^{2/3}M\ell_p^2}{bN^{7/6}}\\ &- \left(\frac{1}{\sqrt{1-b^2u_R^2}}+\frac{1}{\sqrt{1-b^2u_S^2}}\right)\frac{192\sqrt[6]{2}\pi^{2/3}aM\ell_p^2}{b^2N^{7/6}}. \end{aligned} \tag{3.163}$$

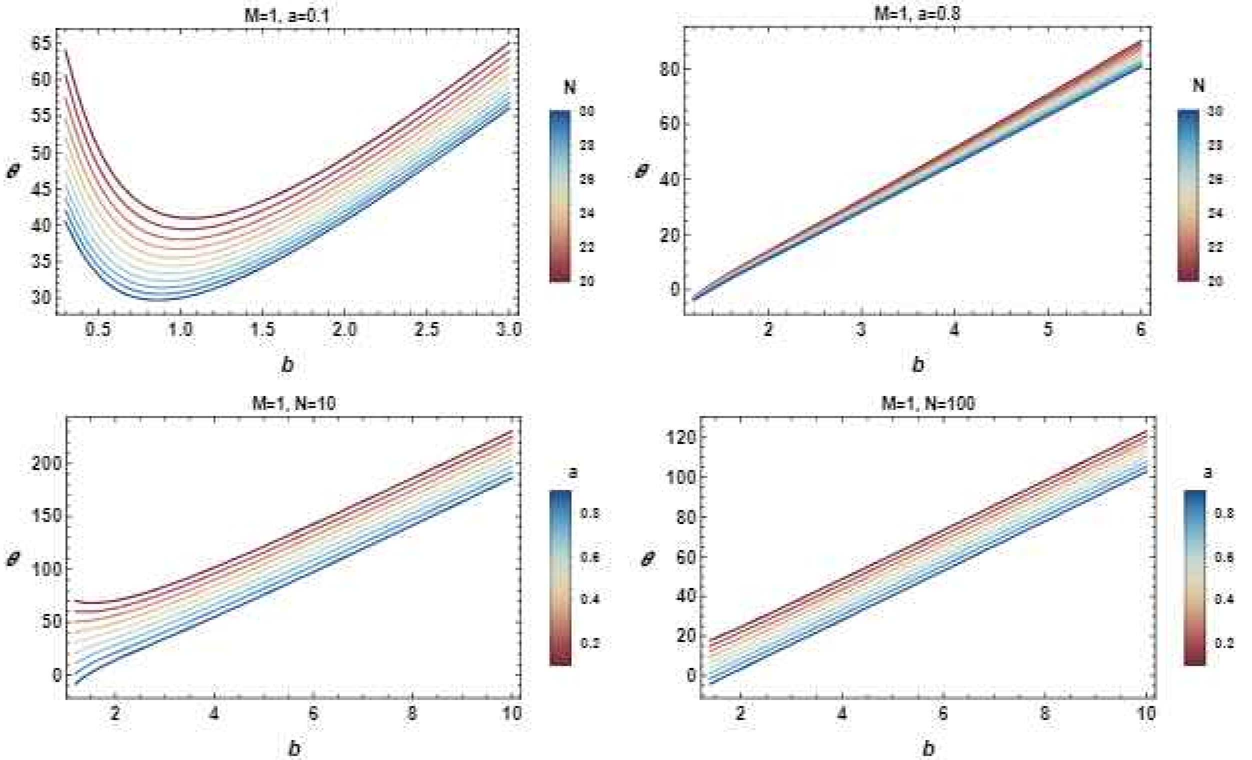

Figure 3.20: *Deflection angle as a function of the impact parameter for various values of a and N.*

When we take the finite distance limit by allowing bu_R and bu_S to approach 0, the expression for the deflection angle is simplified. Setting a to 0, we obtain the deflection angle corresponding to a non-rotating four-dimensional black hole in M-theory. A comparison with the deflection angle of a Kerr black hole reveals a linear contribution from the rotational parameter, characterized by a coefficient that depends on the brane number. Furthermore, the contribution of the Kerr deflection angle can be derived by selecting a specific value for the brane number. To investigate the influence of the $M2$-brane number on rotating black holes, we systematically vary the relevant parameters. Specifically, we explore two different values of the rotating parameter a and depict the resulting variations in the deflection angle with respect to the impact parameter b in the upper sections of both the left and right panels of Fig.(3.20). The $M2$-brane number is systematically varied within the range of 20 to 30 during these discussions. The parameter linked to the $M2$-brane number consistently leads to a reduction in the deflection angle of light rays. In the left panel, where the rotating parameter a is smaller, the deflection angle experiences an initial decrease for small values of b followed by a subsequent increase, turning into a growing function of the impact parameter. Conversely, in the right panel, where the rotating parameter has a substantial contribution, the deflection angle strictly increases with b without displaying any minimum values. In the lower part of Fig.(3.20), we explore the impact of both small (left side) and large (right side) values of the $M2$-brane number on the deflection angle while varying the rotating parameter a from 0.1 to 0.9. This investigation affirms as expected that that the rotating parameter a decreases the deflection angle. For general values of the $M2$-brane number, the deflection angle decreases as the rotating parameter a increases. Around $b = 2$, the deflection angle behavior is influenced by the $M2$-brane number, and for generic values of the rotating parameter, it increases as N decreases. This aligns with prior observations, with the only difference near to $b = 2$ being the linear behavior for high $M2$-brane number values. Notably, these optical behaviors could be associated with the AdS spacetime backgrounds.

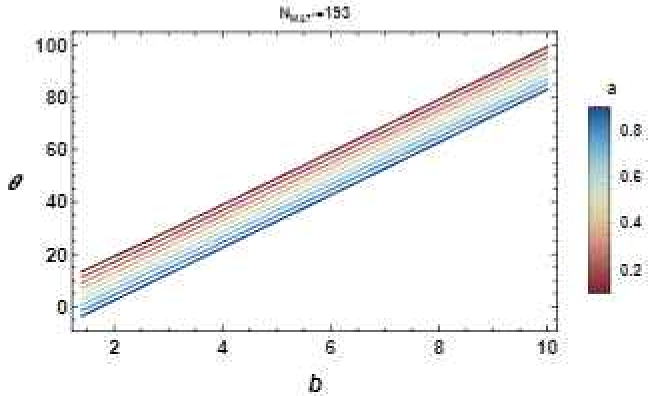

Figure 3.21: *Deflection angle in terms of the impact parameter in terms of a, with $M = 1$, $N = N_{87^*}$.*

3.3. Deflection angle and the light ray trajectories near to M-theory black holes

As we mentioned, the observational results obtained from EHT have been utilized to validate the proposed models, specifically by establishing distinct shadow boundaries for M87* and SgrA* black holes. Notably, the shadows cast by a four-dimensional black hole in M-theory precisely coincide with those of M87* black holes for $N_{87^*} = 193$. Employing this constraint mandated by EHT empirical results in the $(11, 4, 3)$ scenario, we explore the variations in the deflection angle, as illustrated in Fig.(3.21).

It follows from this figure that the deflection angle decreases by increasing the rotating parameter. It has been remarked a linear behavior in terms of the impact parameter. This behavior could be explained by the AdS backgrounds.

Here, we examine a 7-dimensional AdS black hole within the context of the triplet $(11, 7, -3)$. This model is derived from the compactification of M-theory on the four-dimensional real sphere S^4 in the presence of $M5$-branes. The associated metric function, expressed in terms of the $M5$-brane number, is as follows

$$A(r) = 1 + \frac{r^2}{4\pi^{2/3}N^{2/3}\ell_p^2} - \frac{6\pi^{5/3}M\ell_p^3}{5N^{4/3}r^4}. \tag{3.164}$$

Using the orbital equation Eq(3.92), we get

$$F_7(u) = \frac{1}{b^2} - \frac{1}{4\pi^{2/3}N^{2/3}\ell_p^2} - u^2 + \frac{6\pi^{5/3}Mu^6\ell_p^3}{5N^{4/3}}. \tag{3.165}$$

By the help of the above equation, we can compute the ϕ_{RS} term. Indeed, its is given by

$$\begin{aligned}
\phi_{RS} = {} & (\pi - \arcsin(bu_R) - \arcsin(bu_S)) - \left(\frac{u_R}{\sqrt{1-b^2u_R^2}} + \frac{u_S}{\sqrt{1-b^2u_S^2}}\right)\frac{b^3}{8\pi^{2/3}N^{2/3}\ell_p^2} \\
& + \left(\frac{-2b^5u_R^5 - 5b^3u_R^3 + 15bu_R}{\sqrt{1-b^2u_R^2}} + \frac{-2b^5u_S^5 - 5b^3u_S^3 + 15bu_S}{\sqrt{1-b^2u_S^2}}\right)\frac{3\pi^{5/3}M\ell_p^3}{40b^4N^{4/3}} \\
& - \left(\frac{bu_R\left(3b^4u_R^4 - 20b^2u_R^2 + 15\right)}{\left(1-b^2u_R^2\right)^{3/2}} + \frac{bu_S\left(3b^4u_S^4 - 20b^2u_S^2 + 15\right)}{\left(1-b^2u_S^2\right)^{3/2}}\right)\frac{3\pi M\ell_p}{80b^2N^2} \\
& + (\pi - \arcsin(bu_R) - \arcsin(bu_S))\left(\frac{9\pi^{5/3}M\ell_p^3}{8b^4N^{4/3}} - \frac{9\pi M\ell_p}{16b^2N^2}\right).
\end{aligned} \tag{3.166}$$

For the Ψ terms of these black holes, we obtain the following result

$$\begin{aligned}\Psi_R - \Psi_S = {} & (\arcsin(bu_R) + \arcsin(bu_S) - \pi) + \left(\frac{1}{u_R\sqrt{1-b^2u_R^2}} + \frac{1}{u_S\sqrt{1-b^2u_S^2}}\right)\frac{b}{8\pi^{2/3}N^{2/3}\ell_p^2} \\ & - \left(\frac{u_R^5}{\sqrt{1-b^2u_R^2}} + \frac{u_S^5}{\sqrt{1-b^2u_S^2}}\right)\frac{3\pi^{5/3}bM\ell_p^3}{5N^{4/3}} \\ & - \left(\frac{u_R^3\left(2b^2u_R^2-1\right)}{\left(1-b^2u_R^2\right)^{3/2}} + \frac{u_S^3\left(2b^2u_S^2-1\right)}{\left(1-b^2u_S^2\right)^{3/2}}\right)\frac{3\pi bM\ell_p}{40N^2}. \qquad (3.167)\end{aligned}$$

Combining Eq(3.166) and Eq(3.167), we get the needed angle expression

$$\begin{aligned}\Theta_7 = {} & \left(\frac{\sqrt{1-b^2u_R^2}}{u_R} + \frac{\sqrt{1-b^2u_S^2}}{u_S}\right)\frac{b}{8\pi^{2/3}N^{2/3}\ell_p^2} \\ & - \left(\frac{bu_R\left(2b^4u_R^4+b^2u_R^2-3\right)}{\sqrt{1-b^2u_R^2}} + \frac{bu_S\left(2b^4u_S^4+b^2u_S^2-3\right)}{\sqrt{1-b^2u_S^2}}\right)\frac{3\pi^{5/3}M\ell_p^3}{40b^4N^{4/3}} \\ & + \left(\frac{bu_R\left(7b^2u_R^2-15\right)}{\sqrt{1-b^2u_R^2}} + \frac{bu_S\left(7b^2u_S^2-15\right)}{\sqrt{1-b^2u_S^2}}\right)\frac{3\pi M\ell_p}{80b^2N^2} \\ & + (\pi - \arcsin(bu_R) - \arcsin(bu_S))\left(\frac{9\pi^{5/3}M\ell_p^3}{8b^4N^{4/3}} - \frac{9\pi M\ell_p}{16b^2N^2}\right). \qquad (3.168)\end{aligned}$$

Taking the finite distance limits, this deflection angle could be approximated by the following expression

$$\Theta_7 \sim \frac{9\pi^{8/3}M\ell_p^3}{8b^4N^{4/3}} - \frac{9\pi^2M\ell_p}{16b^2N^2} + \frac{b}{8\pi^{2/3}N^{2/3}\ell_p^2}\left(\frac{1}{u_R} + \frac{1}{u_S}\right). \qquad (3.169)$$

To analyze the associated behaviors, we depict the variation of the deflection angle of light rays by a 7-dimensional black hole in M-theory in the left panel of Fig.(3.22). Similar to the four-dimensional scenario, the deflection angle decreases for small impact parameter values until it reaches a critical value, after which it becomes an increasing function. An examination of the right panel of Fig.(3.22) shows that when we increase the number of $M2$-branes the deflection angle decreases. The critical transition of the behavior of the deflection angle from an increasing to a decreasing function is highlighted in the right panel of Fig.(4.14) through the intersection point of the two curves.

To compare the impact of the dimension on the variation of the deflection angle, we illustrate in Fig.(3.23) the variation of the deflection angle in terms of the impact parameter

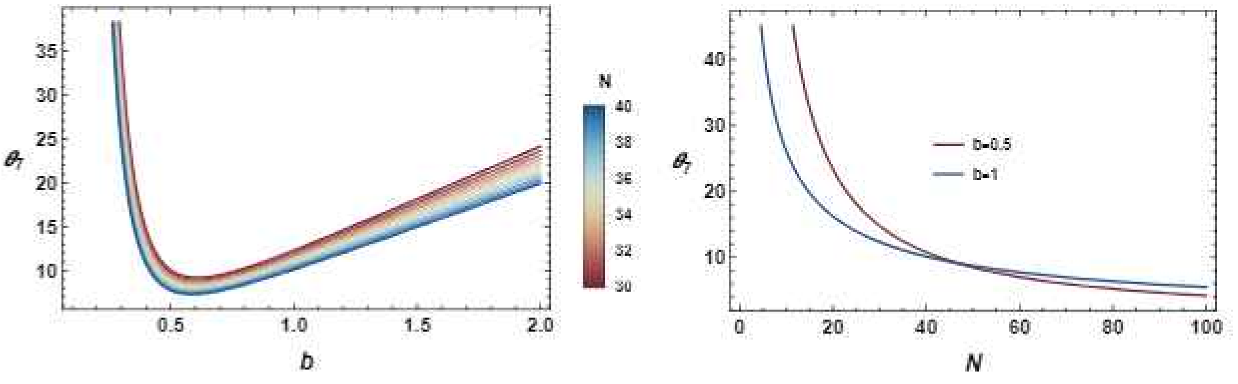

Figure 3.22: *Right panel: Variation in the deflection angle of non-rotating 7-dimensional black holes in M-theory as a function of the impact parameter for various N values. Left panel: Variation of the deflection angle of 7-dimensional black holes in M-theory as a function of brane number with $b = 0.5$ and $b = 1$.*

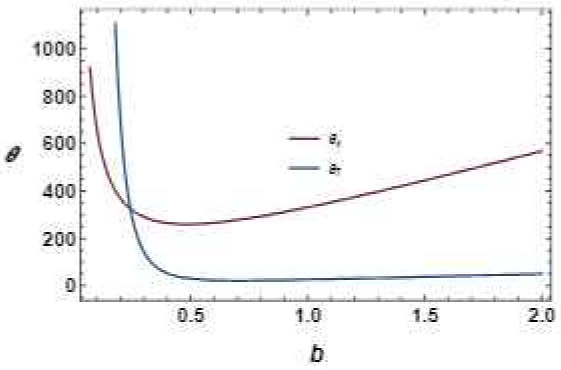

Figure 3.23: *Deflection angle as function of the impact parameter of four and seven dimensional non rotating black holes with $N = 10$.*

for both the $(11, 4, 3)$ and $(11, 7, -3)$ models by keeping N fixed. For small values of the impact parameter, the four-dimensional black hole causes a larger bending of the light rays compared to the seven-dimensional black hole. However, this behavior is reversed for large values of b. Having explored the behaviors of the deflection angle for AdS black holes in M-theory in the presence of $M2$ and $M5$-branes, we now turn our attention to investigate the corresponding trajectories. This investigation is motivated by the fact that the light trajectories around black holes rely on the orbit equation explored in the deflection angle computations. A study of the light trajectories around black holes in the context of $M2$ and $M5$-brane models could serve to validate the behavior of the deflection angle obtained in the preceding subsections.

3.3.2 Light trajectories around black holes in M-theory

In this subsection, we examine the light trajectories around the black holes in M-theory scenarios. Specifically, we explore the trajectories of the light near to AdS black holes for (11, d, k) models by varying the $M(d-2)$-brane number. It is worth noting that the investigation of light trajectories around black holes is typically approached through numerical computations applied to Eq.(3.152) and Eq.(3.165). More precisely, the behavior of the light rays around these black holes can be illustrated by solving ϕ concerning u.

To establish such trajectories, we must identify the regions corresponding to the various possibilities of the light ray trajectories. The determination of these regions is facilitated by the uses of the effective potential

$$V_d^{eff}(r) = -\left(\frac{dr}{d\lambda}\right)^2. \tag{3.170}$$

This can be expressed as follows

$$V_d^{eff}(r) = -F_d(r)\left(\frac{bA(r)}{r^2}\right)^2. \tag{3.171}$$

For the sake of simplicity, we confine our analysis to special models embedded within the 11-dimensional supergravity limits of M-theory.

We begin by examining the $(11,4,3)$ model as developed in [78]. Considering the influence of the rotating parameter, the effective potential in the presence of the $M2$-branes for the four-dimensional case is given by

$$V_4^{eff}(r) = \frac{L^2}{r^2}\left(1 - \frac{192\ 2^{\frac{1}{6}}\pi^{\frac{2}{3}}\ell_p^2 M}{N^{\frac{7}{6}}r} + \frac{2^{\frac{1}{3}}r^2}{\pi^{\frac{2}{3}}\ell_p^2 N^{\frac{1}{3}}}\right) - E^2. \tag{3.172}$$

The effective potential will be depicted as a function of the radial coordinate r for various values of the $M2$-brane number N, considering $\ell_p = 1$ and $M = 1$. As noted in [78], the maximum value of the shadow radius corresponds to $N = 80$. In Fig.(3.24), we plot this potential for two different values of the $M2$-brane number $N = 100$ and $N = 80$.

The potential exhibits an increasing trend and reaches its maximum at the photon sphere, denoted by b_{sp}. This represents the impact parameter for the spinning light rays revolving around the black holes. This observation validates the following constraint

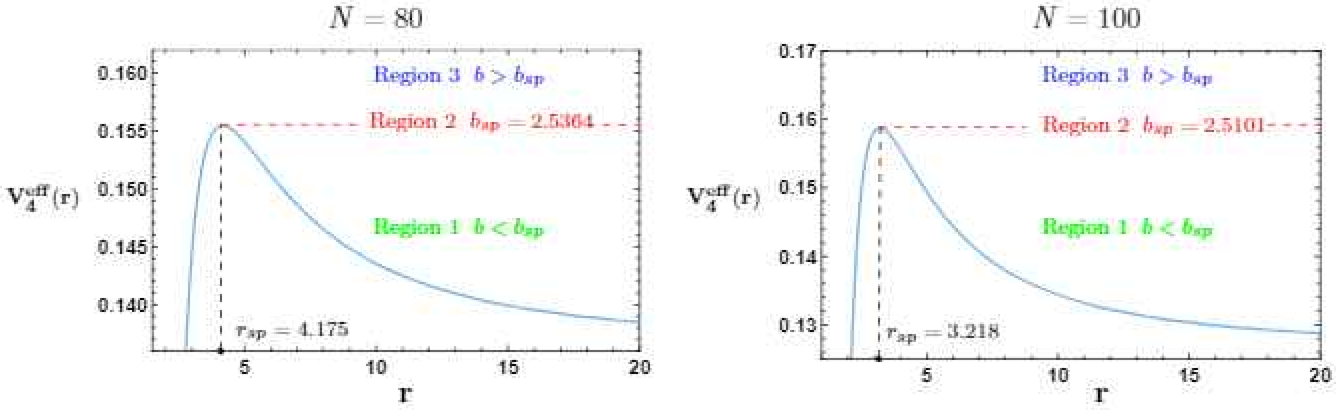

Figure 3.24: *Effective potential variation of 4-dimensional AdS black holes embedded in 11-dimensional M-theory.*

$$V^{eff}(r_{sp}) = \frac{1}{b_{sp}^2}. \tag{3.173}$$

As illustrated in Fig.(3.24), the two values of the M2-brane number $N = 80, 100$ offer two impact parameter values $b_{sp} = 2.5364$ and $b_{sp} = 2.5101$, which correspond to the photon sphere radius $r_{sp} = 4.175$ and $r_{sp} = 3.218$, respectively. By raising the M2-brane number, the corresponding impact parameter and the photon sphere radius decrease. It has been noted that the impact parameter value b_{sp} produces the light ray paths in three separate regions. These regions are designated by region 1, region 2 and region 3 which correspond to $b < b_{sp}$, $b = b_{sp}$, and $b > b_{sp}$, respectively.

The light ray falls into the black hole in the first region 1. The light ray approaching the black hole, however, can be reflected back in the third sector 3. However, in the second region 2, the light ray enters the photon sphere and makes an endless number of revolutions around the black hole due to the nonvanishing angular velocity. The corresponding orbit is unstable and circular. To illustrate these locations, we reveal the trajectories of the light beams in the polar coordinates (r, ϕ) for various values of the $M2$-brane number N in Fig.(3.25). We vary the impact parameter b to investigate the influence of the $M2$-brane on the light ray paths by using the step between two values of the impact parameter as 1/20 for all light rays.

A close examination shows that an increasing on the $M2$-brane number decreases the horizon and the sphere photon radius. However, changing the $M2$-brane number, the variation of the impact parameter b_{sp} is relatively small. For different values of the $M2$-brane

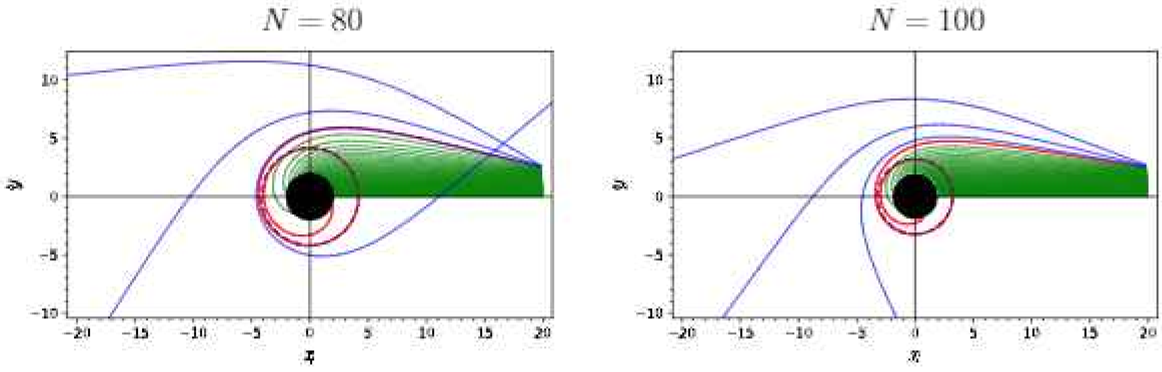

Figure 3.25: *Trajectories of the light ray for various values of $M2$-brane number. The black and the dashed red circle represent the horizon and the photon sphere of the $M2$-brane, respectively.*

number, the regions 1, 2 and 3 are the same.

Using two N values, we see that the distance between the two light rays rises with an impact parameter value closer to and larger than b_{sp} in all regions. This distance is decrease as N increases. This difference is based on the angular velocity values. An investigation reveals that decreasing the $M2$-brane number makes the reflected light beam more intense. When we compare this finding to numerous other papers on the trivial solution, [63, 65], we see a different pattern. First, by changing the N, b_{sp} becomes nearly identical. However, increasing the $M2$-brane number reduces r_{sp}. Second, we see that for small values of the impact parameter, the light ray falls into the black hole by maintaining parallel paths with the r-axis. For values near to b_{sp}, however, the light ray falls into the black hole without maintaining a parallel course with the r-axis. With the $M2$-brane number fixed, this angle grows for values approaching b_{sp} (or larger). It rises by decreasing the $M2$-brane number as N varies. This demonstrates that, in M-theory compactifications, such a $M2$-brane number can be treated as an important quantity changing the light ray behaviors near a black hole. This distinction stems from the geometry of black holes with brane backgrounds in M-theory.

We explore here the trajectory of the light beams near to the black holes in the presence of $M5$-branes in the M-theory compactification on the four-dimensional sphere S^4. Such light behaviors can be established for the $(11, 7, -3)$ model using the effective potential

$$V_7^{eff}(r) = \frac{L^2}{r^2}\left(1 + \frac{r^2}{4\pi^{2/3}N^{2/3}\ell_p^2} - \frac{6\pi^{5/3}M\ell_p^3}{5N^{4/3}r^4}\right) - E^2. \tag{3.174}$$

In Fig.(3.26), we represent the related effective potential as a function of the radial coordinate

r for two $M5$-brane numbers, $N = 1$ and $N = 80$. Using the constraint provided by Eq.(3.173), we can obtain the photon sphere values and the photon sphere critical impact parameter associated with the maximum value of the effective potential $V_7^{eff}(r)$.

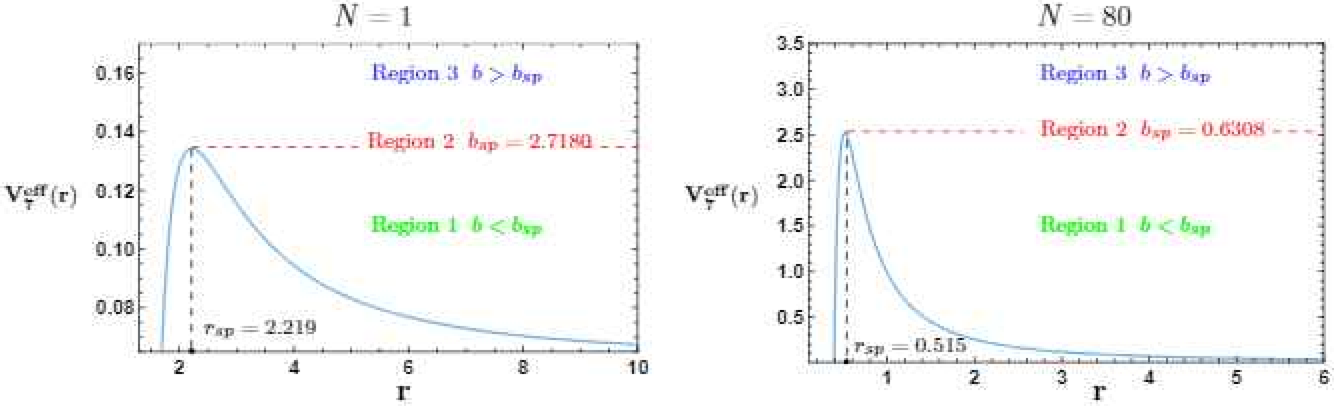

Figure 3.26: *Effective potential variation of 7-dimensional AdS black holes embedded in 11-dimensional M-theory by taking two values of the brane number.*

This implies that the $M5$-brane numbers $N = 1$ and $N = 80$ yield impact parameter values of $b_{sp} = 2.7180$ and $b_{sp} = 0.6308$, respectively, corresponding to the photon sphere radii of $r_{sp} = 2.219$ and $r_{sp} = 0.515$. As the $M5$-brane number increases, both the impact parameter and the photon sphere radius decrease. However, for a fixed value of $N = 80$, it is evident that in the $M5$-brane model, the values of b_{sp} and r_{sp} are smaller compared to the $M2$-brane model. This distinction has implications for the trajectories of light rays around black holes in the $M5$-brane model. To illustrate this, we focus on the equatorial hyperplane with $\theta_1 = \theta_2 = \frac{\pi}{2}$ and depict the light ray trajectories in polar coordinates (r,ϕ) for various $M5$-brane numbers in Fig.(3.27).

Due to the diminutive values of b_{sp}, we opt to vary the impact parameter b with a step size of $1/40$ between consecutive values for all light rays. It has been proposed that the $M5$-brane number and the extra dimension can serve as pertinent parameters influencing the behavior of light rays in the vicinity of a black hole within M-theory compactifications. These modifications arise from the altered black hole geometry resulting from the presence of $M5$-branes in M-theory compactifications. The observed behaviors align seamlessly with findings from previous works [78].

It has been observed that the previous behaviors of the $M2$-brane model corresponding to the horizon and the photon sphere radius have been conserved in the $M5$-brane model. Concretely, decreasing the $M5$-brane number increases the intensity of the reflected light

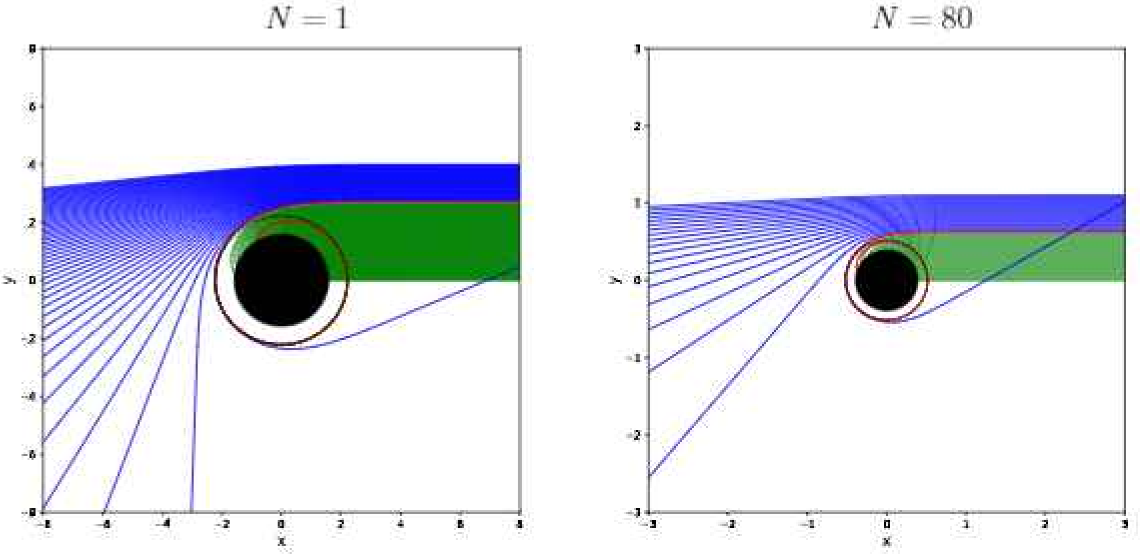

Figure 3.27: *Trajectories of the light ray for various values of $M5$-brane number. The black and the dashed red circle represent the horizon and the photon sphere of the $M5$-brane, respectively.*

ray. It has been noted that these behaviors contradict those of the $M2$-brane model. This is owing to the $M5$-brane model extra dimension contributions appearing in the related metric function. Furthermore, b_{sp} and r_{sp} vary by changing the value of the $M5$-brane number. For all impact parameter values, we see that if a light ray falls into a black hole or is refracted, it maintains a parallel course with regard to the r-axis. This behavior is radically different from the previous $M2$-brane model results. Furthermore, the angular velocity values in the $M5$-brane model differ from those in the $M2$-brane model. A close inspection reveals that the results concerning the light trajectories behaviors confirm the conclusions concerning the deflection angle behavior. It has been shown that decreasing the M-theory brane number N increases the deflection angle. Furthermore, decreasing the M-brane number increases the intensity of the light ray deflection. Both outcomes are perfectly compatible. In conclusion, the behaviors of optical quantities such as light trajectories and the black hole deflection angles for M-theory brane models are interesting and similar.

3.4 Optical behaviors of black holes in Starobinsky-Bel-Robinson gravity

3.4.1 Shadows of SBR black holes

In this section, we study the shadow behavior of black holes in SBR gravity. This investigation will be elaborated using one dimensional real curves. The null geodesic equations of motion can be used to model the current optical characteristics. We can use the Hamilton-Jacobi algorithm, as described in the first section, to generate such equations. To obtain the associated shadows, we consider the black hole solutions given by Eq.(1.136). Applying the separation method [65], we get the factorized relations

$$r^2 f(r)\left(\frac{dS_r(r)}{dr}\right)^2 - r^2\frac{E^2}{f(r)} + L^2 = -\mathcal{K}, \tag{3.175}$$

$$\left(\frac{dS_\theta(\theta)}{d\theta}\right) + L^2\cot^2\phi = \mathcal{K}. \tag{3.176}$$

The equations of motion are given by

$$\frac{dt}{d\lambda} = \frac{E}{f(r)} \tag{3.177}$$

$$r^2\frac{dr}{d\lambda} = \pm\sqrt{-r^2 f(r)\left(\mathcal{K}+L^2\right)+E^2r^4} \tag{3.178}$$

$$r^2\frac{d\theta}{d\lambda} = \pm\sqrt{\mathcal{K}-L^2\cot^2\theta} \tag{3.179}$$

$$\frac{d\phi}{d\lambda} = \frac{L}{r^2\sin^2\theta}. \tag{3.180}$$

Using the radial equation, one can get the effective potential

$$V_{eff}(r) = \frac{f(r)}{r^2}\left(\mathcal{K}+L^2\right) - E^2. \tag{3.181}$$

As shown, this effective potential should satisfy the following conditions

$$V_{eff}(r)\Big|_{r=r_c} = 0, \qquad \frac{dV_{eff}(r)}{dr}\Big|_{r=r_c} = 0, \tag{3.182}$$

where we consider that r_c represent the radius of the unstable circular orbits. This radius can be determined by solving the equation

$$f'(r) - 2f(r) = 0, \tag{3.183}$$

where the prime notation denotes the derivative with respect to the radial coordinate. The impact parameters of such a black hole in the non-rotating case are linked according to the following algebraic equation

$$\xi_{SBR}^2 + \eta_{SBR} = \frac{25r_c^{12}}{1390592\pi^3\beta G^7M^4 - 663552\pi^3\beta G^6M^3r_c - 20GMr_c^9 + 15r_c^{10}}, \tag{3.184}$$

generating one-dimensional real curves in a two-dimensional plane. Considering the celestial plane, noted here by (X, Y), the projections of the spherical photon orbits leads to

$$\xi_{SBR}^2 + \eta_{SBR} = X_{SBR}^2 + Y_{SBR}^2. \tag{3.185}$$

To obtain the shadow cast illustration, we should solve this equation by combining Eq.(3.183) and Eq.(3.184) using a numerical method. Before going ahead, we first depict in Fig.(3.28) the event horizon radius r_+ behaviors in terms of the stringy gravity parameter β. In specific regions of the moduli space, it is evident from this figure that the horizon radius of SBR black holes decreases with an increase in β. However, for values $\beta \geqslant 3.10^{-2}$, the horizon radius maintains a constant value at approximately $r_+ \simeq 1.798$.

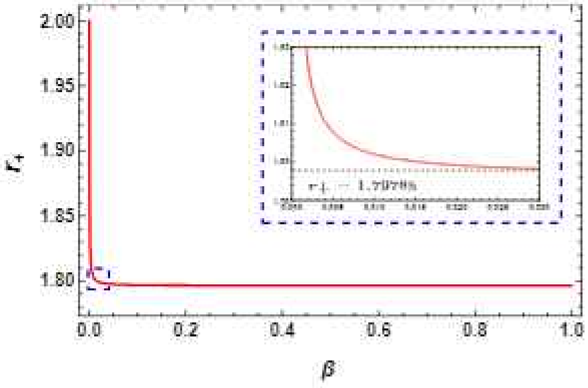

Figure 3.28: *Horizon size behaviors of SBR black holes in terms of the string parameter.*

With these constraints, we can now explore the shadow behaviors of non-rotating black holes in SBR gravity. This is done by varying the stringy gravity parameter while keeping the constants G and M fixed at 1. The shadows of SBR black holes are illustrated as a function of β in Fig.(3.29). Notably, the size of these circles is governed by the stringy gravity parameter β, diminishing as β increases. A thorough examination of the shadow behaviors reveals the necessity of imposing additional conditions on β. For $\beta > 8.10^{-2}$, it is observed that the horizon radius becomes large compared to the shadow radius. This imposes a condition on the shadow existence that aligns seamlessly with findings related to cosmological models embedded in the SBR gravity [109]. These small values of β find support in other investigations [108, 110], potentially establishing connections between inflation and black holes within the framework of SBR gravity. Having explored the non-rotating case, we now turn our attention to incorporating the rotating parameter into the shadow discussions. Here, we aim to explore the optical characteristics of the rotating black holes within the context of SBR gravity. Specifically, our focus is on examining the shadow behaviors in these black hole models inspired by M-theory. Concretely, we consider the rotating metric of the black holes in such a gravity. Using the separation method, we get

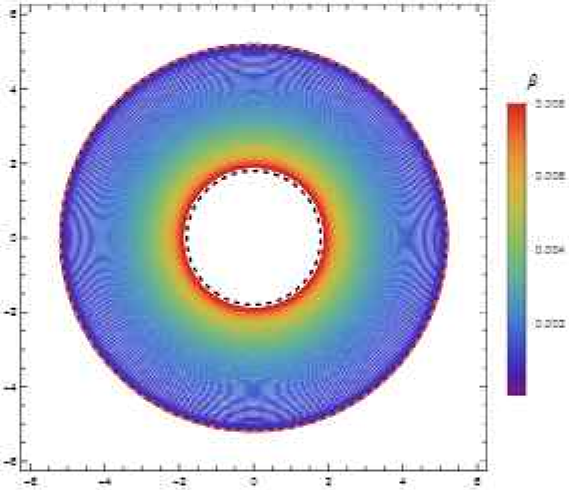

Figure 3.29: *Behaviors of the shadow of SBR black in terms of the parameter β. The orange and black dashed circle are the shadow of Schwarzschild and the horizon limit, respectively.*

$$\mathcal{R}(r) = \left((r^2 + a^2)E - aL\right)^2 - \Delta\left((aE - L)^2 + \mathcal{K}\right), \tag{3.186}$$

$$\Theta(\theta) = \mathcal{K} - \left(\frac{L^2}{\sin^2\theta} - a^2E^2\right)\cos^2\theta. \tag{3.187}$$

In this case, the impact parameters take the following expressions

$$\begin{aligned} \eta_{SBR} &= \left.\frac{r^2\left[16\Delta(r)(a^2-\Delta(r)) - r^2\Delta'(r)^2 + 8r\Delta(r)\Delta'(r)\right]}{a^2\Delta'(r)^2}\right|_{r=r_0}, && (3.188) \\ \xi_{SBR} &= \left.\frac{(a^2+r^2)\Delta'(r) - 4r\Delta(r)}{a\Delta'(r)}\right|_{r=r_0}. && (3.189) \end{aligned}$$

Using the fact that β is very small, we can write these parameters as follows

$$\begin{aligned} \eta_{SBR} &= \eta_{KR} + \beta\gamma_1 && (3.190) \\ \xi_{SBR} &= \xi_{KR} + \beta\gamma_2 && (3.191) \end{aligned}$$

where η_{KR} and ξ_{KR} are the impact parameters of the Kerr black hole which are expressed as

$$\begin{aligned} \eta_{KR} &= \frac{r_0^3\left(4a^2GM - r_0(r_0-3GM)^2\right)}{a^2(r_0-GM)^2} && (3.192) \\ \xi_{KR} &= \frac{r_0^2\left(3GM - r_0\right) - a^2\left(GM + r_0\right)}{a\left(r_0 - GM\right)}, && (3.193) \end{aligned}$$

γ_1 and γ_2 are two independent functions of β which are given by

$$\begin{aligned} \gamma_1 &= 8192\pi^3G^6M^3\Big[\frac{(a^2\left(1261G^2M^2 - 1106GMr_0 + 243r_0^2\right))}{5a^2r_0^6(r_0-GM)^3} \\ &+ \frac{r_0\left(-2619G^3M^3 + 3624G^2M^2r_0 - 1646GMr_0^2 + 243r_0^3\right)}{5a^2r_0^6(r_0-GM)^3}\Big] && (3.194) \\ \gamma_2 &= \frac{4096\pi^3G^6M^3\left(a^2(388GM - 189r_0) + r_0\left(-873G^2M^2 + 917GMr_0 - 243r_0^2\right)\right)}{5ar_0^8(r_0-GM)^2}. \end{aligned}$$

It is important to note that the impact parameters of the SBR black holes are depend on the parameter β, differing from those of the Kerr black hole. When $\beta = 0$, these impact parameters coincide with those of the Kerr black hole. As anticipated, the parameter β has the potential to influence the geometry of the shadows, impacting both their size and shape. Considering the equatorial plane, the celestial coordinates and the above impact parameters are interconnected through the following relations

$$\begin{aligned} X_{SBR} &= -\xi_{KR} + \beta\gamma_2, && (3.195) \\ Y_{SBR} &= \pm\sqrt{\eta_{KR} + \beta\gamma_1}. && (3.196) \end{aligned}$$

Vanishing β, we recover the Kerr result.

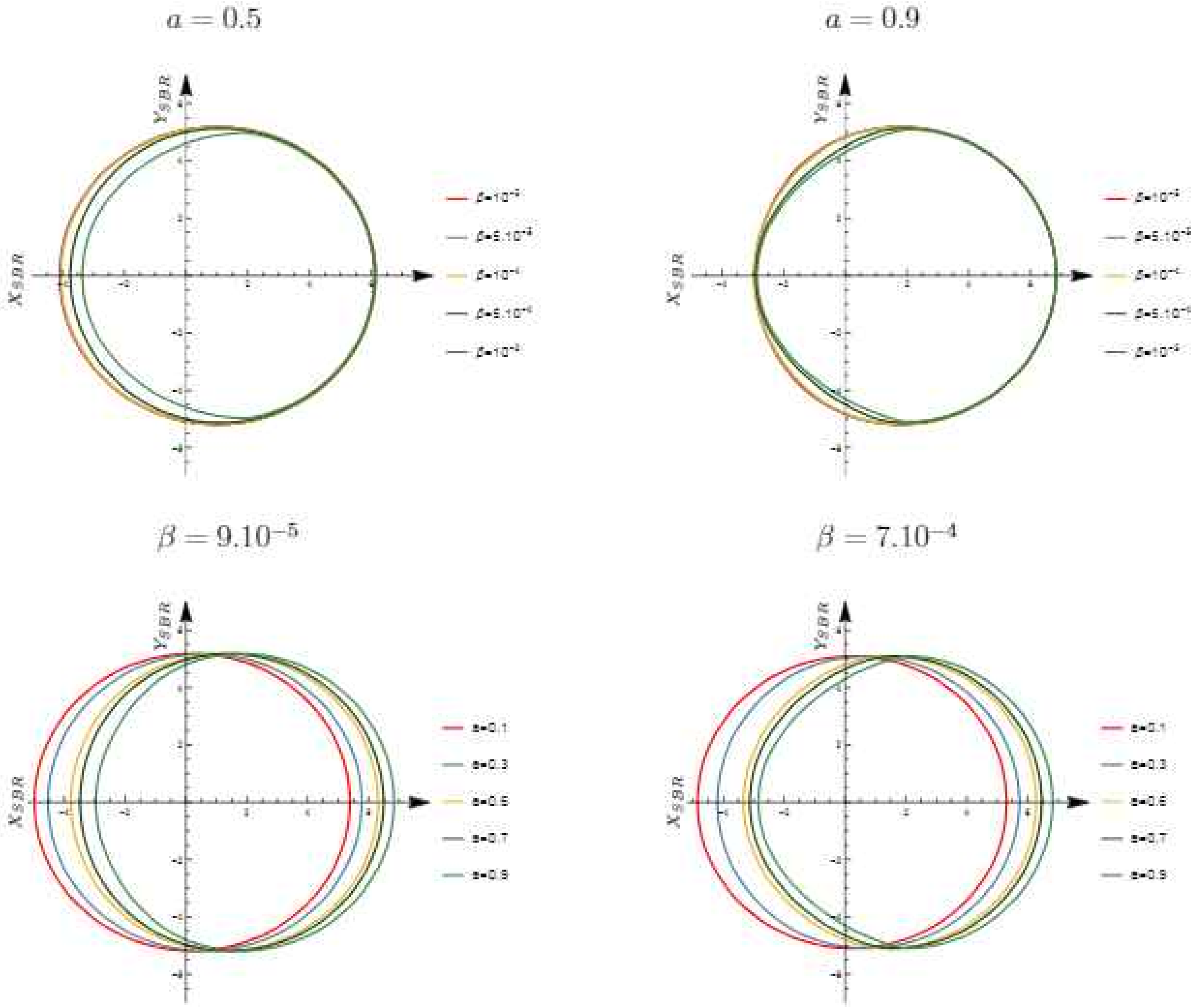

Figure 3.30: *Shadow shapes of SBR black holes in the equatorial plane by considering different values of a and β.*

In Fig.(3.30), we depict the shadow behaviors for specific values of the involved parameters, including the stringy gravity parameter β. This figure shows a variety of the shadow sizes and shapes corresponding to different combinations of a and β. When the rotating parameter is held constant, it is observed that the shadows of SBR black holes increase as β decreases. However, the deformation in the geometry of SBR black holes becomes more prominent with higher values of β. Notably, for large values of both a and β, special shadow shapes are identified, reminiscent of those observed in the case of the Kerr black hole in the presence of Gaussian plasma distributions [90]. This suggests a potential similarity in the influences of plasma and the stringy gravity parameter on the shadow shape of rotating black holes, particularly noticeable for large values of a and β.

To validate this observation, we consider two specific values of β, $\beta = 9.10^{-5}$ and $\beta = 7.10^{-4}$. For the former, the shape deformations remain negligible as the rotating parameter is varied. However, with $\beta = 7.10^{-4}$, the shape deformation becomes significant with an increase in this parameter.

The non-trivial shadow geometries of the SBR black holes require an examination of the associated deformations. Typically, geometric deformations can be analyzed in terms of two parameters: R_c controlling the size and δ_c governing the shape. In order to get such parameters, Fig.(3.31) represents the shadow deformations in terms of a reference circle with the blue color.

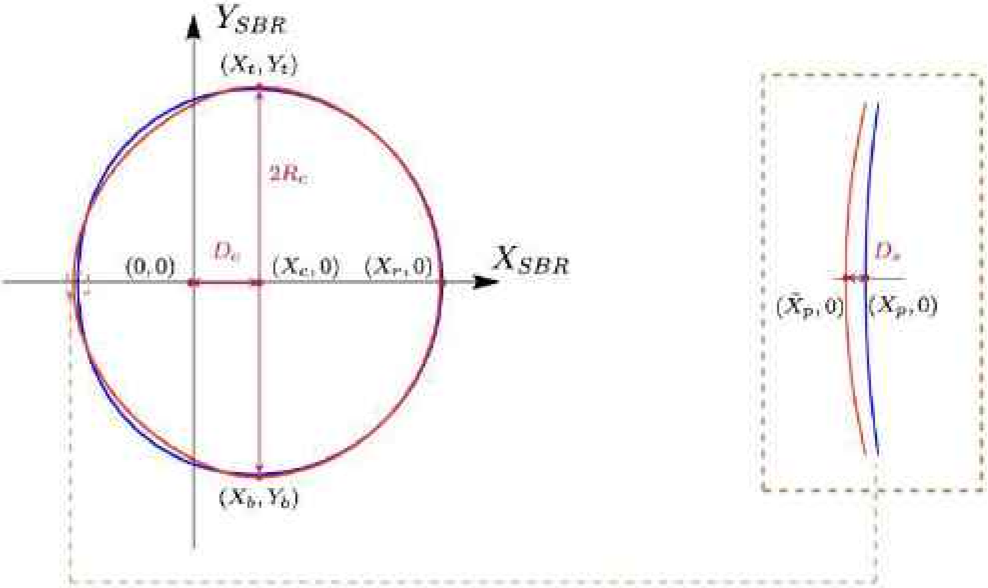

Figure 3.31: *visualisation of the shadow size and shape parameters of SBR black hole. The reference circle is the blue circle and the red geometry is associated with the shadow of the SBR black holes.*

The displacement D_c of the shadow from the centre can be obtained by taking

$$D_c = X_r - R_c, \tag{3.197}$$

where R_c is the shadow maximal radius which could be calculated using the following relation

$$R_c = \frac{Y_t - Y_b}{2}. \tag{3.198}$$

In this way, the shape parameter δ_s can be obtained from

$$\delta_c = \frac{|\tilde{X}_p - X_p|}{R_c}. \tag{3.199}$$

To study the geometric deformations, we investigate the variations in R_c, D_c, and δ_c by manipulating both the rotating and the stringy gravity parameters. The computations and the results are illustrated in Fig.(3.32).

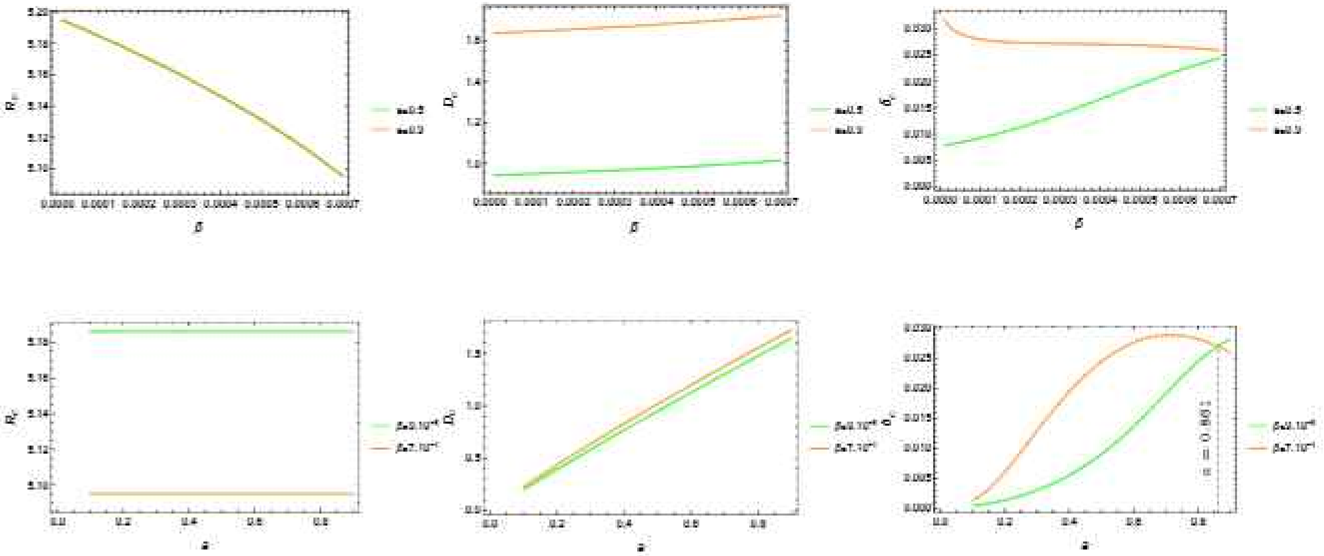

Figure 3.32: *Deformation observation parameters of SBR black hole in terms of of the rotating parameter and the string parameter.*

Taking a fixed value of the rotating parameter, the shadow size decreases by increasing β. However, the displacement of the shadow centre and the distortion deformation increases with this the stringy gravity parameter. It has been denoted that δ_c takes higher values for a higher rotating parameter. When the stringy gravity parameter β is held constant, the shadow size of SBR black holes remains nearly constant even as we vary a. However, it is observed that the rightward displacement of the shadow increases linearly with a. Additionally, the deformation of the shadow shape becomes more pronounced with an increase in the rotating parameter. For example, taking $\beta = 7.10^{-4}$ results in deformation parameter values larger than those for $\beta = 9.10^{-5}$. Upon closer examination, a critical behavior is identified for $a = 0.861$, where the curves intersect. For $\beta = 7.10^{-4}$, this intersecting point signifies a change in the distortion behavior, which could be explained by the presence of a pair of cusps in the shadow shape, consistent with earlier shadow illustrations.

Within a specific range of β, certain similarities are observed between the shadow sizes of SBR black holes and those of Kerr black holes [108–110]. Specifically, the shape deformation of SBR black holes can be compared with the case of the Kerr black hole in plasma backgrounds [90]. This observation may deserve further investigations in future studies.

Now we are in the position to impose constraints on the stringy gravity parameter utilizing observational data from EHT. Upon a careful examination, it becomes apparent that the observational data corresponding to the shadow of the supermassive black hole $M87^*$, provided by the EHT international collaborations, can serve as a valuable tool to test and probe proposed gravity models. Previous studies have demonstrated that such empirical examinations can impose constraints on the relevant black hole parameters [50, 51, 78].

In the context of $M87^*$ mass units, we can overlay the shadow behaviors of the $M87^*$ black hole given by a Kerr solution with those of the SBR black holes. By fixing the rotating parameter, we can directly compare the predictions of the present gravity model with the observational findings. Fig.(3.33) presents two shadow configurations associated with two rotating parameter values for this comparison. It has been observed that the rotating parameter and the $M87^*$ shadow data can determine the stringy gravity parameter β arising from the M-theory compactification. Upon close comparison between the shadow radius of SBR and the $M87^*$ black holes, it is evident that the SBR shadows can perfectly coincide with the $M87^*$ ones for specific values of the stringy gravity parameter. The potential compatibilities lead to the following constraint on the stringy parameter β

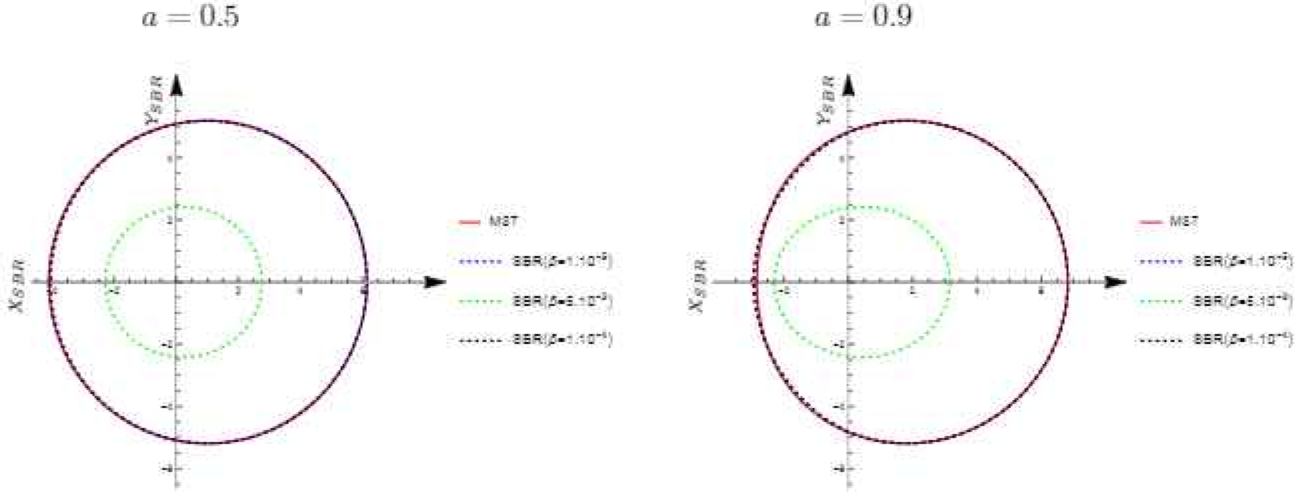

Figure 3.33: *SBR Black hole shadows for various values of β and a compared with $M87^*$. We consider the M87 black hole mass $M_{BH} = 6.5 \times 10^9 M_\odot$ and $r_0 = 91.2kpc$.*

$$\beta < 10^{-4}. \tag{3.200}$$

This constraint finds support from alternative studies related to cosmological models within the framework of SBR gravity [108–110]. For values of β greater than 10^{-4}, the distinctions between the shadows of both black holes become noticeable. In the subsequent analysis, we utilize these constraints to investigate the deflection angle of the light rays near to the proposed rotating black holes in SBR gravity.

3.4.2 Light ray behaviors near to SBR black holes

In this subsection, we investigate the light ray behaviors near to SBR black holes. To initiate the computations of the deflection angle, we begin with the non-rotating solutions of the SBR black holes. The calculations yield to

$$\begin{aligned}
\phi_{RS} &= \left(\pi - \arcsin\left(bu_R\right) - \arcsin\left(bu_S\right)\right) + \left(\frac{2-b^2u_R^2}{\sqrt{1-b^2u_R^2}} + \frac{2-b^2u_S^2}{\sqrt{1-b^2u_S^2}}\right)\frac{GM}{b} \\
&+ \left(\pi - \arcsin\left(bu_R\right) - \arcsin\left(bu_S\right)\right)\frac{15G^2M^2}{4b^2} \\
&+ \left(\frac{u_R\left(3b^4u_R^4 - 20b^2u_R^2 + 15\right)}{\left(1-b^2u_R^2\right)^{3/2}} + \frac{u_S\left(3b^4u_S^4 - 20b^2u_S^2 + 15\right)}{\left(1-b^2u_S^2\right)^{3/2}}\right)\frac{G^2M^2}{4b^2} \\
&+ \left(\frac{-5b^8u_R^8 - 40b^6u_R^6 + 240b^4u_R^4 - 320b^2u_R^2 + 128}{\left(1-b^2u_R^2\right)^{5/2}}\right. \\
&+ \left.\frac{-5b^8u_S^8 - 40b^6u_S^6 + 240b^4u_S^4 - 320b^2u_S^2 + 128}{\left(1-b^2u_S^2\right)^{5/2}}\right)\frac{G^3M^3}{6b^3} \\
&+ \left(\frac{7b^{10}u_R^{10} + 10b^8u_R^8 + 16b^6u_R^6 + 32b^4u_R^4 + 128b^2u_R^2 - 256}{\sqrt{1-b^2u_R^2}}\right. \\
&+ \left.\frac{7b^{10}u_S^{10} + 10b^8u_S^8 + 16b^6u_S^6 + 32b^4u_S^4 + 128b^2u_S^2 - 256}{\sqrt{1-b^2u_S^2}}\right)\frac{6144\pi^3\beta G^6M^3}{35b^9}.
\end{aligned} \tag{3.201}$$

For the Ψ expressions, we get

$$\begin{aligned}
\Psi_R-\Psi_S &= \left(\arcsin\left(bu_R\right)+\arcsin\left(bu_S\right)-\pi\right)-\left(\frac{u_R^2}{\sqrt{1-b^2u_R^2}}+\frac{u_S^2}{\sqrt{1-b^2u_S^2}}\right)bGM \\
&+ \left(\frac{u_R^3\left(2b^2u_R^2-1\right)}{\left(1-b^2u_R^2\right)^{3/2}}+\frac{u_S^3\left(2b^2u_S^2-1\right)}{\left(1-b^2u_S^2\right)^{3/2}}\right)\frac{bG^2M^2}{2}+\left(\frac{u_R^4\left(-8b^4u_R^4+8b^2u_R^2-3\right)}{\left(1-b^2u_R^2\right)^{5/2}}\right. \\
&+ \left.\frac{u_S^4\left(-8b^4u_S^4+8b^2u_S^2-3\right)}{\left(1-b^2u_S^2\right)^{5/2}}\right)\frac{bG^3M^3}{6}+\left(\frac{u_R^{10}}{\sqrt{1-b^2u_R^2}}+\frac{u_S^{10}}{\sqrt{1-b^2u_S^2}}\right)\frac{55296\pi^3b\beta G^6M^3}{5}.
\end{aligned} \tag{3.202}$$

Combining the obtained expressions, we obtain the deflection angle noted here by α in this form

$$\begin{aligned}
\alpha &= \left(\sqrt{1-b^2u_R^2}+\sqrt{1-b^2u_S^2}\right)\frac{2GM}{b}+\left(\pi-\arcsin\left(bu_R\right)-\arcsin\left(bu_S\right)\right)\frac{15G^2M^2}{4b^2} \\
&+ \left(\frac{15bu_R-7b^3u_R^3}{\sqrt{1-b^2u_R^2}}+\frac{15bu_S-7b^3u_S^3}{\sqrt{1-b^2u_S^2}}\right)\frac{G^2M^2}{4b^2} \\
&+ \left(\frac{13b^6u_R^6+45b^4u_R^4-192b^2u_R^2+128}{\left(1-b^2u_R^2\right)^{3/2}}+\frac{13b^6u_S^6+45b^4u_S^4-192b^2u_S^2+128}{\left(1-b^2u_S^2\right)^{3/2}}\right)\frac{G^3M^3}{6b^3} \\
&+ \left(\frac{35b^{10}u_R^{10}+5b^8u_R^8+8b^6u_R^6+16b^4u_R^4+64b^2u_R^2-128}{\sqrt{1-b^2u_R^2}}\right. \\
&+ \left.\frac{35b^{10}u_S^{10}+5b^8u_S^8+8b^6u_S^6+16b^4u_S^4+64b^2u_S^2-128}{\sqrt{1-b^2u_S^2}}\right)\frac{12288\pi^3\beta G^6M^3}{35b^9}.
\end{aligned} \tag{3.203}$$

Sending u_R and u_S to zero, we can form an approximated expression of the deflection angle of the light rays near to the non-rotating SBR black holes. Indeed, it is expressed as

$$\alpha \simeq \frac{4GM}{b}+\frac{15\pi G^2M^2}{4b^2}+\frac{128G^3M^3}{3b^3}-\frac{3145728\pi^3\beta G^6M^3}{35b^9}. \tag{3.204}$$

The deflection angle is influenced by the parameters M, b, and the stringy gravity parameter β. The earlier shadow investigation has identified specific constraints on β that should be considered. With these conditions in mind, we present the deflection angle of light rays as a function of the impact parameter while varying the stringy gravity parameter β. Fig.(3.34) visually represents this variation for different values of β.

For small values of b, a significant effect of β on the deflection angle is noticeable, specifically, it decreases with an increase in β. However, for large values of b, there is no substantial distinction observed as the curves of the deflection angle of light rays coincide. In this region

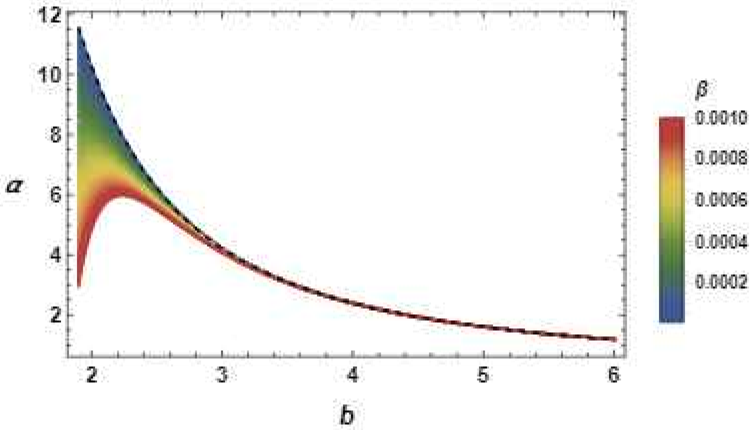

Figure 3.34: *Deflection angle of SBR black hole as function of the impact parameter for large range of the string parameter. Dashed black curve: variation of deflection angle of Schwarzschild black hole.*

of the moduli space, the deflection angle experiences a slight decrease.

Here, we explore the influence of the stringy gravity parameter β on the deflection angle of light rays around rotating black holes in the SBR gravity. Employing analogous calculations, we determine the following separation angle for slowly rotating black holes

$$\begin{aligned}\phi_{RS_a} &= \phi_{RS} - \left(\frac{1}{\sqrt{1-b^2u_R^2}} + \frac{1}{\sqrt{1-b^2u_S^2}}\right)\frac{2GMa}{b^2} + \left(\arcsin\left(bu_R\right) + \arcsin\left(bu_S\right) - \pi\right)\frac{10G^2M^2a}{b^3} \\ &+ \left(\frac{bu_R\left(6b^2u_R^2-5\right)}{\left(1-b^2u_R^2\right)^{3/2}} + \frac{bu_S\left(6b^2u_S^2-5\right)}{\left(1-b^2u_S^2\right)^{3/2}}\right)\frac{2G^2M^2a}{b^3} + \left(\frac{35b^6u_R^6-182b^4u_R^4+240b^2u_R^2-96}{\left(1-b^2u_R^2\right)^{5/2}}\right. \\ &+ \left.\frac{35b^6u_S^6-182b^4u_S^4+240b^2u_S^2-96}{\left(1-b^2u_S^2\right)^{5/2}}\right)\frac{G^3M^3a}{b^4} - \left(\frac{5b^8u_R^8+8b^6u_R^6+16b^4u_R^4+64b^2u_R^2-128}{\sqrt{1-b^2u_R^2}}\right. \\ &+ \left.\frac{5b^8u_S^8+8b^6u_S^6+16b^4u_S^4+64b^2u_S^2-128}{\sqrt{1-b^2u_S^2}}\right)\frac{110592\pi^3\beta G^6M^3a}{175b^{10}}. \qquad (3.205)\end{aligned}$$

The needed deflection angle equation can be given by

$$\begin{aligned}\Psi_{RS_a} &= \Psi_{RS} + \left(\frac{u_R^2}{\sqrt{1-b^2u_R^2}} + \frac{u_S^2}{\sqrt{1-b^2u_S^2}}\right)2GMa - \left(\frac{u_R^3\left(2b^2u_R^2-1\right)}{\left(1-b^2u_R^2\right)^{3/2}} + \frac{u_S^3\left(2b^2u_S^2-1\right)}{\left(1-b^2u_S^2\right)^{3/2}}\right)2G^2M^2a \\ &+ \left(\frac{u_R^4\left(8b^4u_R^4-8b^2u_R^2+3\right)}{\left(1-b^2u_R^2\right)^{5/2}} + \frac{u_S^4\left(8b^4u_S^4-8b^2u_S^2+3\right)}{\left(1-b^2u_S^2\right)^{5/2}}\right)G^3M^3a \qquad (3.206) \\ &- \left(\frac{u_R^{10}}{\sqrt{1-b^2u_R^2}} + \frac{u_S^{10}}{\sqrt{1-b^2u_S^2}}\right)\frac{110592}{5}\pi^3\beta G^6M^3a,\end{aligned}$$

where the notation $\Psi_{RS_a} = \Psi_{R_a} - \Psi_{S_a}$ has been used. Considering the above equations, the deflection angle of the light rays of the rotating SBR black holes is found to be

$$\begin{aligned}
\alpha_{RS_a} &= \alpha_{RS} - \frac{2aGM}{b^2}\left(\sqrt{1-b^2u_R^2} + \sqrt{1-b^2u_S^2}\right) + \frac{2aG^2M^2}{b^3}\left(\frac{2b^3u_R^3 - 5bu_R}{\sqrt{1-b^2u_R^2}} + \frac{2b^3u_S^3 - 5bu_S}{\sqrt{1-b^2u_S^2}}\right)\\
&+ \frac{10aG^2M^2}{b^3}\left(\arcsin(bu_R) + \arcsin(bu_S) - \pi\right) - \frac{aG^3M^3}{b^4}\left(\frac{8b^6u_R^6 + 35b^4u_R^4 - 144b^2u_R^2 + 96}{(1-b^2u_R^2)^{3/2}}\right.\\
&+ \left.\frac{8b^6u_S^6 + 35b^4u_S^4 - 144b^2u_S^2 + 96}{(1-b^2u_S^2)^{3/2}}\right)\\
&+ \frac{110592\pi^3 a\beta G^6M^3}{175b^{10}}\left(\sqrt{1-b^2u_R^2}\left(35b^8u_R^8 + 40b^6u_R^6 + 48b^4u_R^4 + 64b^2u_R^2 + 128\right)\right.\\
&+ \left.\sqrt{1-b^2u_S^2}\left(35b^8u_S^8 + 40b^6u_S^6 + 48b^4u_S^4 + 64b^2u_S^2 + 128\right)\right). \qquad (3.207)
\end{aligned}$$

Taking appropriate limits, we can obtain the reduced expression in the following form

$$\begin{aligned}
\alpha_a &\simeq \frac{4GM}{b} + \frac{15\pi G^2M^2}{4b^2} + \frac{128G^3M^3}{3b^3} - \frac{3145728\pi^3\beta G^6M^3}{35b^9} - \frac{4aGM}{b^2} - \frac{10\pi aG^2M^2}{b^3}\\
&- \frac{192aG^3M^3}{b^4} + \frac{28311552\pi^3 a\beta G^6M^3}{175b^{10}}. \qquad (3.208)
\end{aligned}$$

Taking $a = 0$, we retrieve the deflection angle of the non-rotating solutions obtained in the previous section. When $\beta = 0$, we recover the case of the Kerr solution. Fixing the rotating parameter, we depict in Fig.(3.35) the deflection angle as a function of b, varying the stringy gravity parameter β within the range determined by the computations associated with EHT requirements.

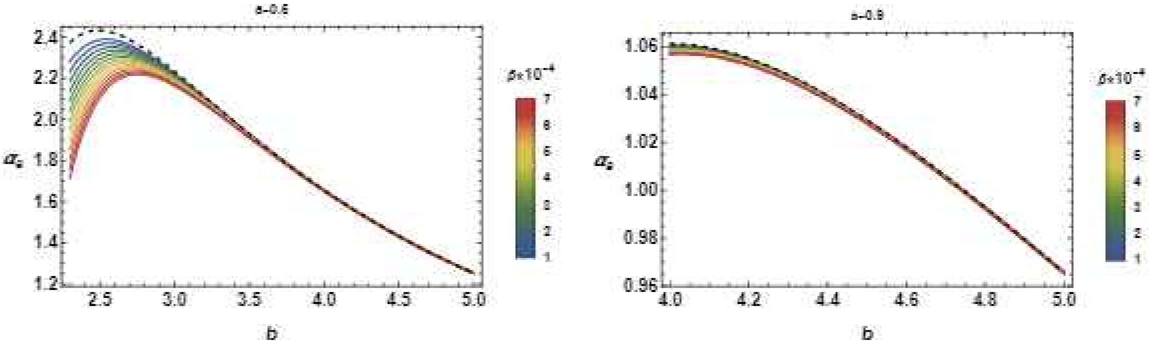

Figure 3.35: *Deflection angle of the light rays near to the rotating SBR black holes in terms of of the impact parameter by changing β values and fixing a.*

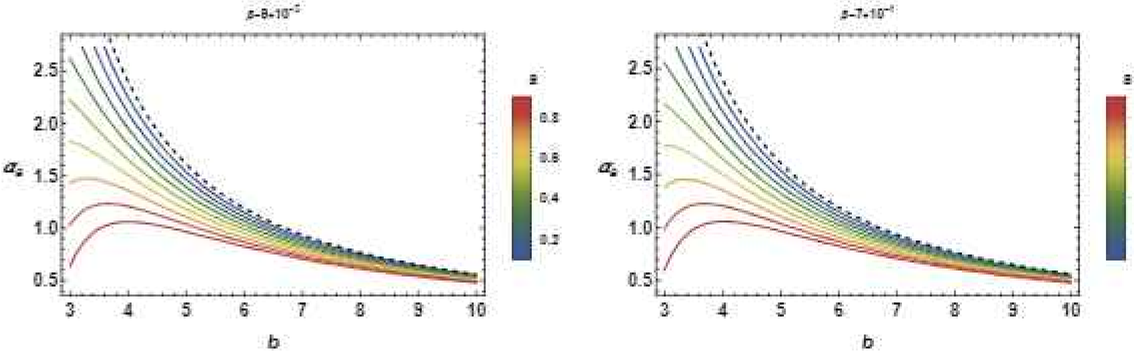

Figure 3.36: *Deflection angle of light rays near rotating SBR black holes in terms of of the impact parameter by changing the values of a and fixing β.*

For small values of the impact parameter and the rotating parameter, a notable effect of the stringy gravity parameter is observed, leading to a decrease in the deflection angle. As evident from the figure, the deflection angle also decreases with an increase in the rotating parameter. For large values of the rotating parameter, however, the β-curves become indistinguishable from the Kerr ones, suggesting that the effect of β becomes irrelevant in this regime.

In Fig.(3.36), we illustrate the variation of the deflection angle as a function of the impact parameter, varying the rotating parameter while fixing the stringy gravity parameter. In contrast to the shadow behavior, the two fixed values of β exhibit similar behaviors. Moreover, the decreasing behavior of the deflection angle depends on both the rotating parameter and the stringy gravity parameter. The associated critical impact parameter is shifted by increasing these parameters.

CHAPTER 4

Interplay Between Thermodynamic and Optical Aspects of Black Holes

The aim of this chapter is to establish a link between the thermodynamical behaviors of AdS black holes and optical aspects. Motivated by the previous activities where the shadows and critical properties have been combined [58], we first provide a bridging link between the thermodynamics of AdS black holes and deflection angle of the right rays. Using elliptic functions, we investigate the phase structure of these black holes via a thermal variation of the deflection angle. After that, we approach the HP transition and the geothermodynamic computations using the Ruppeiner metric. To enclose this chapter, we study the optical aspect of the black holes in cavity backgrounds by means of thermodynamic properties. Concretely, we discuss the light behaviors such as the photon rings and the shadows of the black holes in these non trivial systems.

4.1 Deflection angle for charged AdS black holes

To start, we consider the study of the deflection angle of light near to the four dimensional black holes with the AdS geometries. These solutions will be used to establish an interplay between and the optical aspect and the thermodynamics. More precisely, we deal with the stability and the phase structure transitions of such black holes from the deflection angle.

4.1.1 Charged AdS black holes

A priori, there are many models. However, we examine a simple one corresponding to RN-AdS black holes. As we have illustrated in the first chapter, these solutions can be obtained using the following action

$$S = \frac{1}{16\pi}\int \sqrt{-g}dx^4\left(R - F^{\mu\nu}F_{\mu\nu} + \frac{6}{\ell^2}\right). \tag{4.1}$$

Here, the scalar R indicates the Ricci curvature. Moreover, the tensor $F_{\mu\nu}$ given by

$$F_{\mu\nu} = \partial_\mu A_\nu - \partial_\nu A_\mu \tag{4.2}$$

represents the Maxwell gauge tensor, where A is the potential vector in the electromagnetism theory. Using the Boyer-Lindquist coordinate framework, one can solve the equations of motion using the line element

$$ds^2 \;\; = \;\; -f(r)dt^2 + \frac{dr^2}{f(r)} + r^2(d\theta^2 + \sin^2\theta d\phi^2). \tag{4.3}$$

where the metric function $f(r)$ is expressed as follows

$$f(r) = 1 - \frac{2M}{r} + \frac{Q^2}{r^2} + \frac{r^2}{\ell^2}. \tag{4.4}$$

It is recalled that the gauge vector potential being written as $F = dA$ can be considered as follows

$$A_\mu = \left(-\frac{Q}{r}, 0, 0, 0\right). \tag{4.5}$$

To establish the proposed interplay, certain thermodynamical quantities are needed. These quantities can be computed in terms of r_h being the radius of the event horizon. The latter is considered the largest real solution $f(r) = 0$. Indeed, exploiting the thermodynamic laws, we could calculate the important quantities. In particular, we calculate the mass M, the temperature T and the entropy S. After computations, we get

$$M = \frac{r_h^4+\ell^2 r_h^2+\ell^2 Q^2}{2\ell^2 r_h}, \tag{4.6}$$

$$T = \frac{3r_h^4+\ell^2(r_h^2-Q^2)}{4\pi\ell^2 r_h^3}, \tag{4.7}$$

$$S = \pi r_h^2. \tag{4.8}$$

4.1.2 Deflection angle computations

Having computed the most important thermodynamical quantities, we move to approach the deflection angle using the Euler-Lagrange formalism needed to find the equations of motion. To be more precise, we project the computation to the equatorial plane defined by the constraint $\theta = \frac{\pi}{2}$. In this way, the Euler-Lagrange equations can be reduced. For null geodesics, we obtain the algebraic relations providing the dynamical equations of motion

$$\dot{\phi} = \frac{L}{r^2}, \tag{4.9}$$

$$\dot{r}^2 = E^2 - f(r)\frac{L^2}{r^2}. \tag{4.10}$$

In these equations, two conserved quantities appear which are L and E. They represent the energy and the angular momentum, respectively. Using the impact parameter $b = \frac{L}{E}$, the equation (4.10) takes the following form

$$\dot{r}^2 = E^2\left(1-\frac{f(r)}{r^2}b^2\right). \tag{4.11}$$

Many situations can be discussed. However, we consider a specific one where the light rays come from the infinity. Thus, they approach to the black hole until the distance of closest approach r_0, after they come back to the infinity. In fact, the light rays are in the zone of the deflection angle. Moreover, the impact parameter should satisfy the condition $b > b_0$, where b_0 denotes the critical value. In this way, the photons generate an unstable circular orbit near to the black hole. Certain computations can be used to identify the critical value r_0. Indeed, it can be derived by means of the constraints

$$V_{eff}(r)\mid_{r=r_0}=0, \qquad \frac{dV_{eff}(r)}{dr}\mid_{r=r_0}=0, \tag{4.12}$$

where V_{eff} denotes the effective potential which can be written as

$$V_{eff}(r) = E^2 \left(\frac{f(r)}{r^2} b^2 - 1 \right). \tag{4.13}$$

Using (4.12) and (4.13), we can obtain

$$r_0 = \frac{3M + \sqrt{9M^2 - 8Q^2}}{2}. \tag{4.14}$$

Plugging r_0 in such a potential, we find the value

$$b_0 = \sqrt{\frac{r_0^2}{f(r_0)}} \tag{4.15}$$

which is a critical one. To get the deflection angle Θ, some quantities are needed including the total change in the angular variable ϕ being $2|\phi(r_0) - \phi(\infty)|$. Supposing that the trajectory is a straightaway, the above change in ϕ is π. The assumption provides

$$\begin{aligned} \Theta &= 2|\phi(r_0) - \phi(\infty)| - \pi, \\ &= 2\int_{r_0}^{\infty} | \frac{d\phi}{dr} | \, dr - \pi. \end{aligned} \tag{4.16}$$

Using the equations (4.9) and (4.10), we get

$$\left(\frac{d\phi}{dr} \right)^2 = \frac{A^2}{P(r)}, \tag{4.17}$$

where one has used $\frac{1}{A^2} = \frac{1}{b^2} - \frac{1}{\ell^2}$ and $P(r) = r^4 - A^2(r^2 - 2Mr + Q^2)$. It is recalled that $P(r)$ has four real roots given by $r_1 < r_2 < r_3 < r_4$. The largest one gives the critical value r_0. Exploiting the variable redefinitions $u = r - r_0$, ϕ can be considered as a function of u. Precisely, it is given by

$$\phi(u) = \int_0^u \frac{A du}{\sqrt{u(u + u_1)(u + u_2)(u + u_3)}}, \tag{4.18}$$

where one has $u_1 = r_0 - r_1$, $u_2 = r_0 - r_2$, $u_3 = r_0 - r_3$. A close examination shows that one could follow many roads to compute the integral of the equation (4.18). Possible ones can be can be performed using alternative methods. It has been remarked that the complete and incomplete elliptic functions have been explored in such computations. Moreover, the Weierstrass elliptic functions have been also exploited in certain investigations works. For the sake of simplicity, we use the second method. Following the techniques developed in [100], we could redefine the equation (4.18). Indeed, it takes the following form

$$\phi(x) = \lambda \int_x^\infty \frac{dx}{\sqrt{4x^3 - g_2 x - g_3}}. \tag{4.19}$$

Using the changes $\alpha = u_1^{-1} + u_2^{-1} + u_3^{-1}$, $\beta = (u_1 u_2)^{-1} + (u_3 u_1)^{-1} + (u_3 u_2)^{-1}$, $\gamma = (u_1 u_2 u_3)^{-1}$, $\lambda = \frac{A}{\sqrt{u_1 u_2 u_3}}$, $x = \frac{1}{4u} + \frac{\alpha}{12}$ in the equation (4.18), we can obtain the expressions of the arguments g_2 and g_3. Concretly, they are given by

$$g_2 = \frac{1}{4}\left(\frac{\alpha^2}{3} - \beta\right), \qquad g_3 = \frac{1}{16}\left(\frac{\alpha\beta}{3} - \gamma - \frac{2\alpha^3}{27}\right). \tag{4.20}$$

The next step is to approach the equation (4.19) using the Weierstrass elliptic function $x = \wp(\frac{\phi}{\lambda}, g_2, g_3)$. In this way, the function $\phi(r)$ is found to be

$$\phi(r) = \lambda \wp^{-1}\left(\frac{1}{r - r_0} + \frac{\alpha}{12}, g_2, g_3\right). \tag{4.21}$$

Taking the equations (4.16) and (4.21), we get the deflection angle of the rotating RN-AdS black hole being expressed as

$$\Theta = 2|\lambda \wp^{-1}\left(\frac{\alpha}{12}, g_2, g_3\right)| - \pi. \tag{4.22}$$

It has been revealed that the optical quantity Θ depends on four black holes parameters: (b, ℓ, Q, M) defining the involved parameter space. To give a graphic representation of such optical quantity, certain parameters should be fixed. Fixing the mass and the AdS radius, the deflection angle variation can be given as a function of the impact parameter by considering several values of the charge Q. This choice of the moduli space regions provide the graphic realization illustrated in Fig.(4.1). As expected, the deflection angle exhibits a continuous variation in respect of the impact parameter. From this figure, we remark that the deflection angle is a decreasing function with the charge. This result matches with many investigations providing similar optical behaviors obtained in the study of several models of AdS black holes. Having discussed optical behaviors, the main objective now is to investigate thermodynamic properties from optical ones by help of the light deflection angle around the rotating RN-AdS

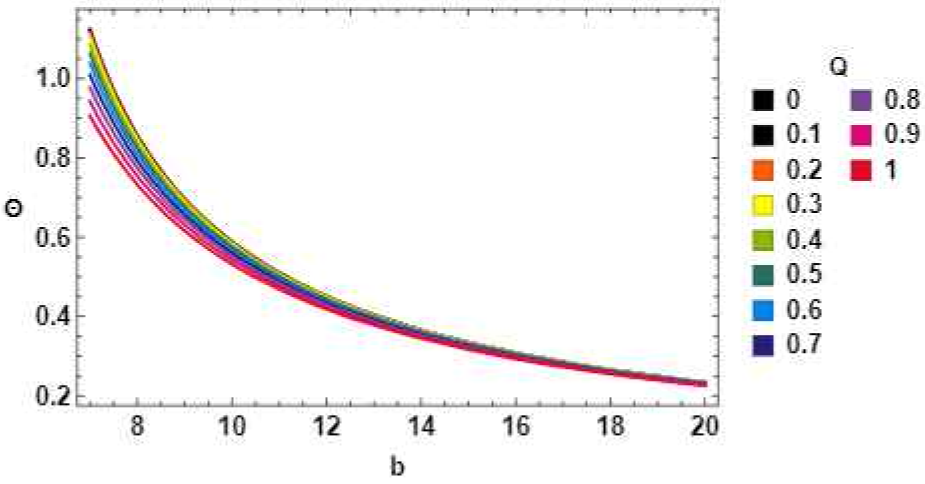

Figure 4.1: *Deflection angle as a function of b by taking certain values of the charge using $\ell = 172$ and $M = 1$.*

black holes

4.2 Black hole stability from the deflection angle variation

4.2.1 Stability behaviors

In black hole physics, the stability is a fundamental aspect of understanding their behaviors. The sign of the black hole heat capacity is a crucial indicator of its thermodynamic stability. This study can be done via the heat capacity sign, which is a primordial thermodynamic quantity needed for stability examination. The heat capacity is related to the response of the black hole mass to changes in its temperature. The stability analysis involves considering how the black hole responds to small fluctuations or perturbations in its thermodynamic parameters. To do so, we first recall the constraint

$$C = T\left(\frac{\partial S}{\partial T}\right) > 0 \tag{4.23}$$

defining a stable phase. However, the unstable is associated with the following condition

$$C = T\left(\frac{\partial S}{\partial T}\right) < 0. \tag{4.24}$$

4.2.2 Black hole stability from the deflection angle

The first link with the thermodynamics will be established in terms of the stability behaviors. Precisely, we investigate the stability of charged black holes using the deflection angle of light rays. We will see that the stability investigation can be elaborated via the deflection angle variation. Exploiting the deflection angle of light rays near to the charged black holes, the heat capacity reads as

$$C = T\left(\frac{\partial S}{\partial r_h}\right)\left(\frac{\partial r_h}{\partial \Theta}\right)\left(\frac{\partial \Theta}{\partial T}\right). \tag{4.25}$$

Assuming that $\frac{\partial S}{\partial r_h} > 0$, the primordial data on the stability aspect could be derived from the product sign $\left(\frac{\partial r_h}{\partial \Theta}\right)\left(\frac{\partial \Theta}{\partial T}\right)$. To approach this product, the temperature in terms of r_h for different values of the black hole parameters should be worked out. This analysis will be needed to examine the phase structures [34]. Concretely, the obtained information will be discussed in respect of the variation of the deflection angle. Fixing the AdS size via the relation $\ell^2 = \frac{675}{4\pi}$ and considering the equation (4.7), we can implement the temperature in the present analysis. Varying the charge, Fig.(4.2) provides the temperature variation in terms of the radius r_h of the event horizon. Considering the range $0.1 \leq Q \leq 1$, the

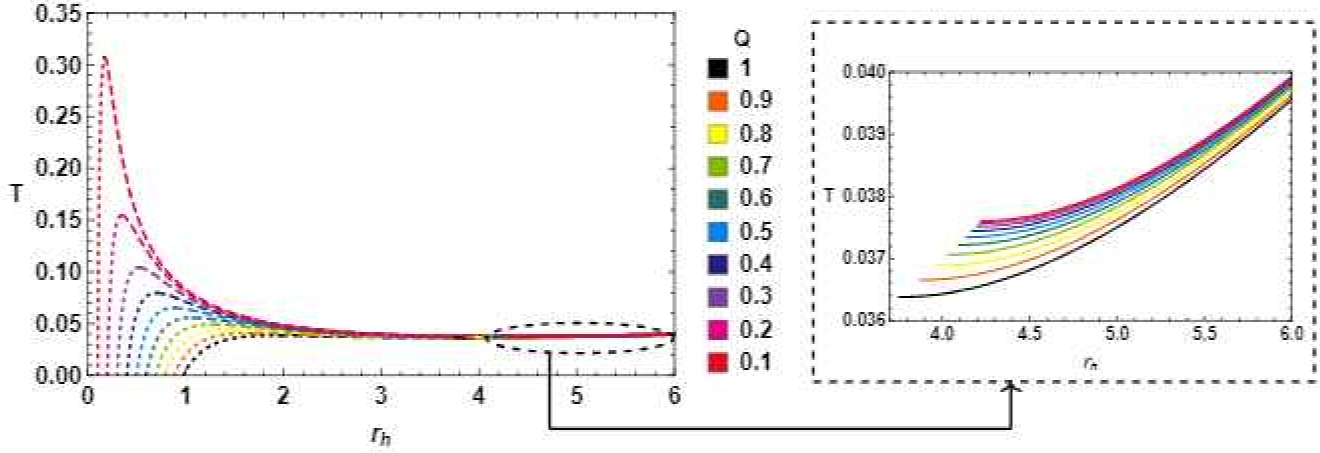

Figure 4.2: *The temperature variation in terms of r_h for $\ell^2 = \frac{675}{4\pi}$.*

temperature variation is illustrated in dashed, dotted, and solid curves. From this figure, we remark that the stable states of the charged black holes are associated with the dotted and the solid curves. For these solutions, the temperature increases with r_h. However, the dashed curves correspond to the unstable phase. It has been concluded that the phase structure of the rotating RN-AdS black holes could be discussed using the quantity $\frac{dT}{dr_h}$. In order to show the link between the deflection angle and the the phase structure, we vary Θ in respect of the event horizon radius r_h. The associated computations are plotted in Fig.(4.3). Considering generic points for the black hole parameters, we remark that the deflection angle decreases with r_h, without any critical value generating a continuous behavior with the variable r_h. The data on the phase structures can be derived from the sign of the quantity $\frac{dT}{d\Theta}$. Indeed, the unstable and the stable phase behaviors are constrained by

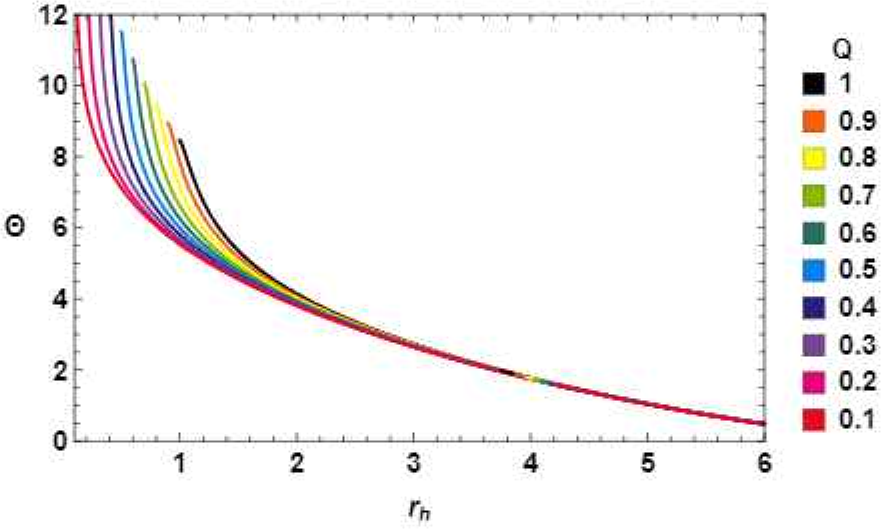

Figure 4.3: *The deflection angle variation as a function r_h for $b = 10$, $\ell^2 = \frac{675}{4\pi}$, and certain values of the charge.*

$$\frac{dT}{d\Theta} < 0 \qquad \text{unstable} \ , \qquad \frac{dT}{d\Theta} > 0 \qquad \text{stable}. \tag{4.26}$$

To elaborate the bridging scenario between the deflection angle and the phase transitions, the temperature expression given in the Eq.(4.7) will be used. These thermal aspect is illustrated in Fig.(4.4), by keeping the same the unstable and the stable phases regions corresponding to r_h. A close examination shows that the unstable and the stable phases are exhibited in the previous figure. The obtained behaviors agree with the results given in Fig.(4.2). This reveals that the phase structure could be approached via the optical aspect

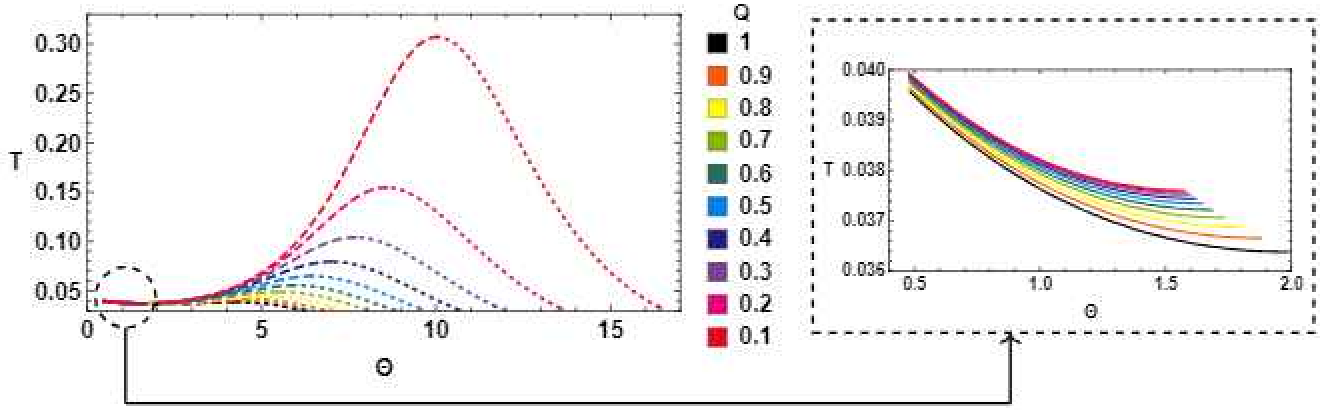

Figure 4.4: *The temperature variation as a function of the deflection angle by taking* $b = 10$ *and* $\ell^2 = \frac{675}{4\pi}$.

by help of the deflection angle variation. According to the heat capacity of the rotating RN-AdS black hole, the changing of the sign at critical points can be discussed in respect of the variation of the deflection angle. Concerning the stable phase, the deflection angle decreases with the temperature. The associated phase is illustrated by the dotted and the solid curves. However, in the unstable phase, the deflection angle is an increasing function of the temperature being illustrated by the dashed curves. The obtained results could support the idea that the deflection angle can be viewed as a relevant new tool to investigate the phase transitions of the charged black holes with AdS type geometries.

4.3 HP phase transition and geothermodynamics from deflection angle

4.3.1 HP phase transition

Here, we continue the previous analysis by providing a new connection with thermodynamical aspect. Concretely, we reconsider the study of the Hawking-Page transition of charged AdS black holes from the deflection angle variation. It has been observed that to establish a new bridge with such thermal behaviors, certain quantities should be computed including the Gibbs free energy G being a crucial thermodynamical quantity. The latter could unveil physical behaviors to approach the Hawking-Page phase transition [31, 32, 34]. In the case of the rotating RN-AdS black holes within the grand canonical ensemble with fixed electric potentials Φ, we can obtain

$$G = M - TS - \Phi Q, \tag{4.27}$$

where Φ denotes the electric potential which reads as $\Phi = \frac{Q}{r_h}$. Identifying the cosmological constant with pressure by help of $p = \frac{3}{8\pi\ell^2}$, we can calculate the needed quantities. Indeed, they are given by

$$\begin{aligned} T &= \frac{8\pi p r_h^2 - \Phi^2 + 1}{4\pi r_h}, && (4.28)\\ M &= \frac{r_h\left(8\pi p r_h^2 + 3\Phi^2 + 3\right)}{6}. && (4.29) \end{aligned}$$

Substituting (4.28), (4.29) into (4.27), the Gibbs free energy is found to be

$$G = \frac{(3r_h - 8\pi p r_h^3 - 3r_h\Phi^2)}{12}. \tag{4.30}$$

It has been remarked that the temperature $T = T(r_h, p, \Phi)$ indicates that the rotating RN-AdS black hole involves two possible critical values. The first critical value corresponds to $T_0 = \sqrt{\frac{2p(1-\Phi^2)}{\pi}}$ being the minimum value. Below such a value, no black hole can exist [34]. Now, we need to solve the horizon radius r_h in respect of the temperature T. This provides two solutions corresponding to large and small black holes, based on two different even horizon radii r_h^+ and r_h^-, respectively. In Fig.(4.5), we present the radius of the event horizon in respect of the temperature by varying the charge and taking $p = 0.04$. It is denoted that the critical value is identified with the intersection of the LBH curves, and the SBH ones. The second interesting critical value $T_{HP} = \sqrt{\frac{8p(1-\Phi^2)}{3\pi}}$ corresponds to the HP transition where the radiation and the black hole involve a zero value of the Gibbs free energy. To understand such behaviors, we illustrate the Gibbs free energy in respect of the temperature of LBH and SBH solutions in Fig.(4.6).

To establish a bridge with the deflection angle, we identify the radius of the event horizon in the deflection angle expression with the temperature. In particular, we examine the deflection angle variation $\Theta = \Theta(b, T, p, \Phi)$ with respect to T and b. Fixing Φ and p, a 3-dimensional picture is visualized in Fig.(4.7). It has been remarked a minimum temperature value which is independent of the coordinate b of the parameter space of the black hole. Taking $b > r_h^0$, where r_h^0 corresponds to T_0, b does not influence the temperature of the black hole. This could be understood via the black hole intrinsic aspect

To determine the HP transition from the deflection angle of light rays around the charged

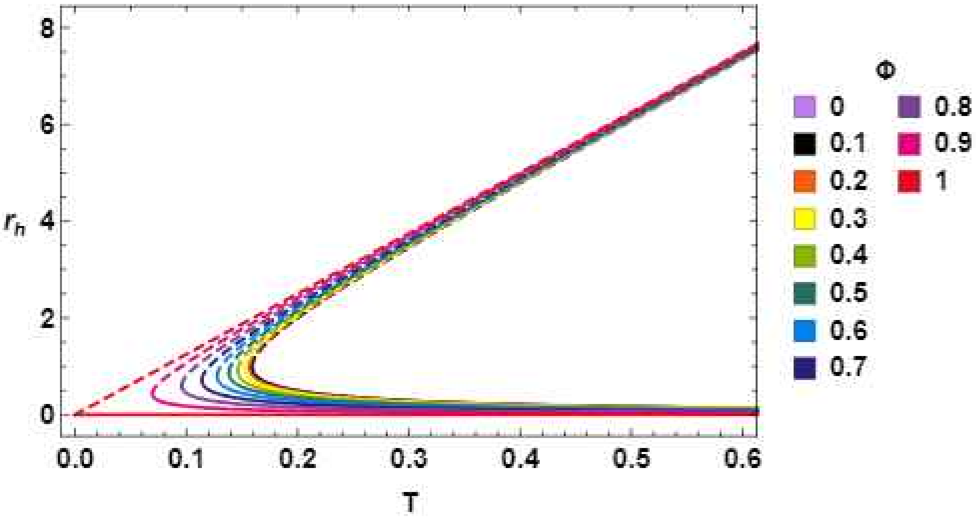

Figure 4.5: *Variation of the event horizon radius as a function of the temperature.*

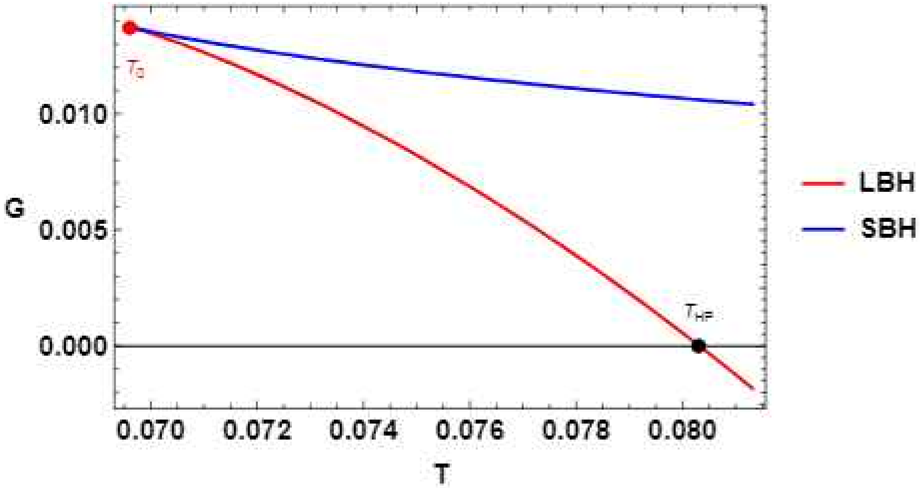

Figure 4.6: *Variation of the Gibbs free energy in respect the temperature by taking* $\Phi = 0.9$ *and* $p = 0.04$.

black holes, we examine the Gibbs free energy. The associated computations are illustrated in Fig.(4.8). For LBH, it has been obtained a zero value for the Gibbs free energy at $\Theta = \Theta_c$ imitating the Hawking-page transition by changing the role of $r_h = r_{HP}$ for which $T = T_{HP}$. It has been observed that LBH is manifested in the case where G increases with Θ. However, a solution associated with SBH has been appeared by considering G as a decreasing function. At a critical value $\Theta = \Theta_0$, the intersection point of SBH and LBH defining a minimum value of the temperature generates a Gibbs free energy maximal value. This feature matches

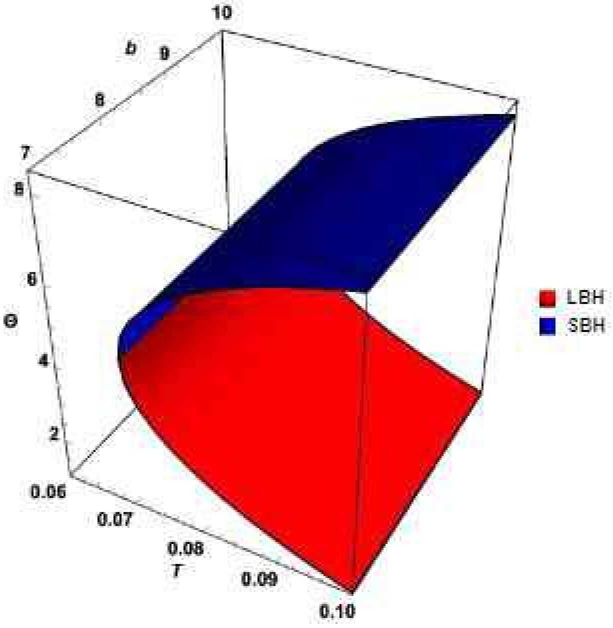

Figure 4.7: *Gibbs free energy in terms of the impact parameter and the temperature by taking* $p = 0.04$ *and* $\Phi = 0.9$.

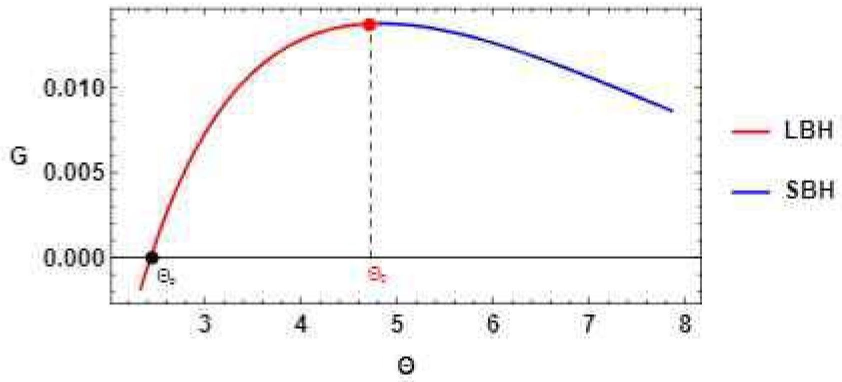

Figure 4.8: *Gibbs free energy as a function of* Θ *by considering* $p = 0.04$ *and* $\Phi = 0.9$.

with the previous results suggesting that the deflection angle can be exploited to approach transitions in black hole physics.

4.3.2 Geothermodynamics by means of the deflection angle

To complete the present study, we consider the AdS black hole geothermodynamics by examining the phase state structure. In this way, the corresponding information can be derived from a thermodynamical potential Ψ and certain conserved quantities interpreted as the coordinates of such a space. We denote them by x_i [111]. Using such coordinates, the associated metric reads as

$$g_{ij} = \frac{\partial^2 \Psi}{\partial x_i \partial x_j}. \tag{4.31}$$

A close inspection in string theory compactifications shows that the electric potential Ψ can share certain resemblances with the Kähler scalar potential. The latter is considered as a relevant piece in the study of the complex manifold metrics such as the Calabi-You spaces [112]. Various metric forms have been built needed to examine certain criticality aspects of the black holes in arbitrary dimensions [111, 113]. In particular, we exploit the Ruppeiner metric. Relating the thermodynamic potential Ψ and the entropy quantity S, and considering only two variables for the RN-AdS black hole, the above metric (4.31) can be reduced to

$$g_{ij} = -\frac{\partial S}{\partial x_i \partial x_j}, \quad i, j = 1, 2. \tag{4.32}$$

Taking $x_1 = M$ and $x_2 = Q$, the new metric (4.32) can be expressed as follows

$$g_{ij} = \begin{pmatrix} -\frac{\partial S(M,Q)}{\partial M^2} & -\frac{\partial S(M,Q)}{\partial M \partial Q} \\ -\frac{\partial S(M,Q)}{\partial M \partial Q} & -\frac{\partial S(M,Q)}{\partial Q^2}. \end{pmatrix}, \tag{4.33}$$

Following [114, 115], the curvature scalar R, carrying all information on critical behaviors, is found to be

$$R = -\frac{18r^6 \left(3Q^2 - r^2\right) + 3\ell^2 r^2 \left(10Q^4 - 9Q^2 r^2 + 3r^4\right) + \ell^4 \left(Q^2 - r^2\right)^2}{\pi \ell^4 \left(3r^4/\ell^2 - Q^2 + r^2\right) \left(3r^4/\ell^2 + 3Q^2 - r^2\right)^2}. \tag{4.34}$$

which shares similarities with the divergence behaviors corresponding to the heat capacity in respect either of the event horizon radius or the entropy function. It is has been mentioned that the phase transition has been largely studied revealing a grucial bridging between the thermodynamics and the Riemannian geometries [113]. Using a numerical discussion, these aspects from the deflection angle algorithm can be provided. For constant charges, the heat capacity should be computed. Indeed, it takes the following form

$$C_Q = T \left(\frac{\partial S}{\partial T}\right)_Q = \frac{2\pi r^2 \left(\ell^2 \left(r^2 - Q^2\right) + 3r^4\right)}{\ell^2 \left(3Q^2 - r^2\right) + 3r^4}. \tag{4.35}$$

It has been remarked that the phase transition LBH/SBH can occur when $Q < Q_c$. We consider, for instance, specific regions of the black hole parameter space where we have considered $\ell = 1$. We find that the critical value is around $Q_c = 0.408$. Using the deflection angle appearing in (4.35), the heat capacity variation is illustrated as a function of Θ by considering constant charges, in the left and the right of Fig.(4.9) for $Q < Q_c$ and $Q > Q_c$, respectively. For $Q < Q_c$, the phase transition is manifested ensured by discontinuous curves for the singular points $\Theta_1 \simeq 1.01$ and $\Theta_2 \simeq 4.15$, represented by blue dashed lines. However, for $Q > Q_c$, a continuous line with non divergence aspects is obtained showing that there is only one solution for the black hole. We examine now the curvature scalar behavior. Taking $b = 10$, we inspect the R variation by varying Θ for the charge constraints $Q < Q_c$ and $Q > Q_c$. The corresponding computations are depicted in Fig.(4.10).

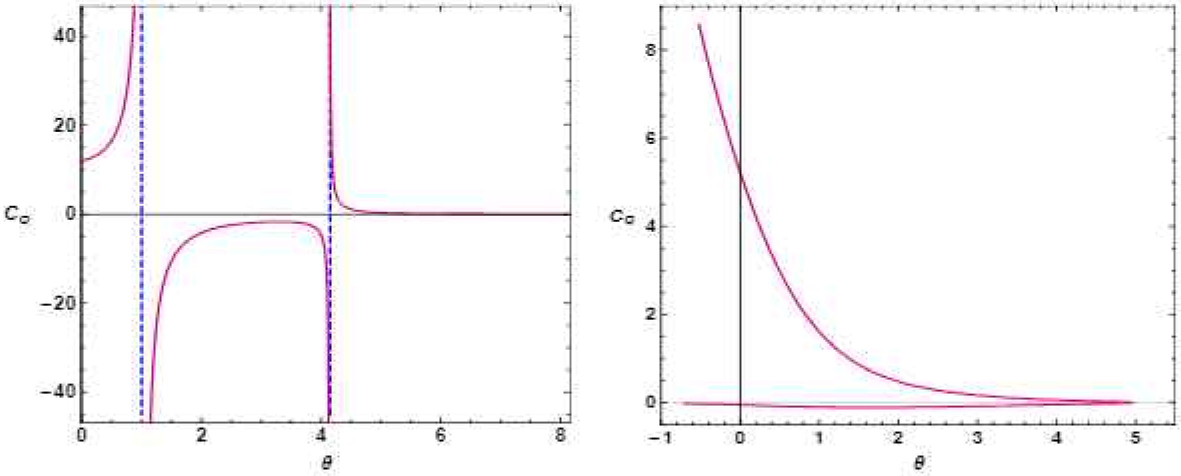

Figure 4.9: *Heat capacity as a function of* Θ. *Left side:* $Q = 0.11$. *Right side:* $Q = 0.5$.

For $Q < Q_c$, we remark that R involves a discontinuous behaviors in respect of Θ exhibiting similar divergent points of the heat capacity. However, for $Q > Q_c$, the function R is a continuous with regular points, which matches with the heat capacity behaviors. As a result, the deflection angle could be considered as a crucial optical quantity unveiling certain information on the thermodynamics of the black hole supporting the previous results.

Having discussed a bridging scenario between the thermodynamics and the optics of black holes, we move to implement the shadow aspect. A detailed examination reveals that there are many roads and methods [58]. Here, however, we follow a new method by considering black hole in cavities.

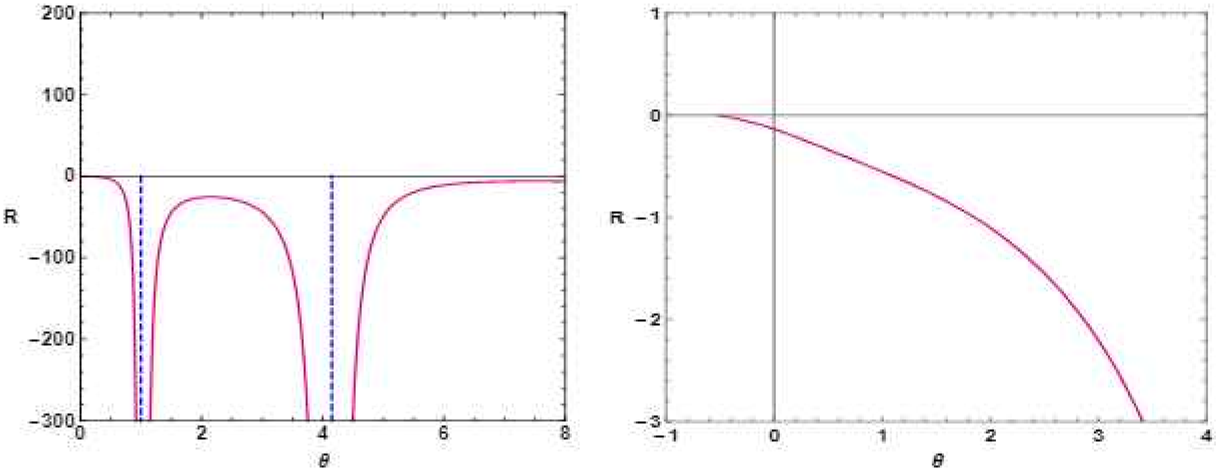

Figure 4.10: *Ruppeiner scalar as a function of* Θ*. Left side:* $Q = 0.11$*. Right side:* $Q = 0.5$*.*

4.4 Thermal behaviors of the black hole shadows in a cavity

The black hole in a cavity has been extensively studied using different approaches [130, 135]. Before giving an optical discussion, we first need to recall certain features on the associated physics. Concretely, we review the primordial notions and concepts. In the asymptotically AdS backgrounds, a black hole can be considered as a thermodynamical stable object [130, 135]. In picture, the AdS boundary can be interpreted as a reflective wall. Similarly, it has been shown that the black holes surrounded by a cavity could be also thermally stable as the AdS geometries. Putting black holes in asymptotically flat spaces with cavity boundaries, the thermodynamics stability problem could be removed. Roughly speaking, we study shadow behaviors from the thermal variation. For simplicity reasons, we consider a static and spheric metric black hole in cavity backgrounds. This can be considered as

$$ds^2 = -f(r)dt^2 + \frac{dr^2}{f(r)} + r^2(d\theta^2 + \sin^2\theta d\phi^2), \tag{4.36}$$

where $f(r)$ carries data on the used cavity. According to [135], $f(r)$ can be given by

$$f(r) = (1 - \frac{r_+}{r})(1 - \frac{Q^2}{r\,r_+}). \tag{4.37}$$

where r_+ represents the horizon radius

$$r_+ = m + \sqrt{m^2 - Q^2}, \tag{4.38}$$

In this relation, Q and m denote the charge and the mass, respectively. Taking $Q = 0$, we can recover the usual Schwarzschild black hole. It has been shown that various scenarios could be discussed depending on the positions of the observer. A simple situation can be approached by placing the observer inside the cavity geometry. This situation occurs by considering following conditions

$$r_{cav} > r_{ob}, \qquad r_{cav} > r_+, \tag{4.39}$$

which could be viewed as the optical and the thermodynamic requirements, respectively. To illustrate a black hole in a cavity using the above conditions, we provide Fig.(4.11).

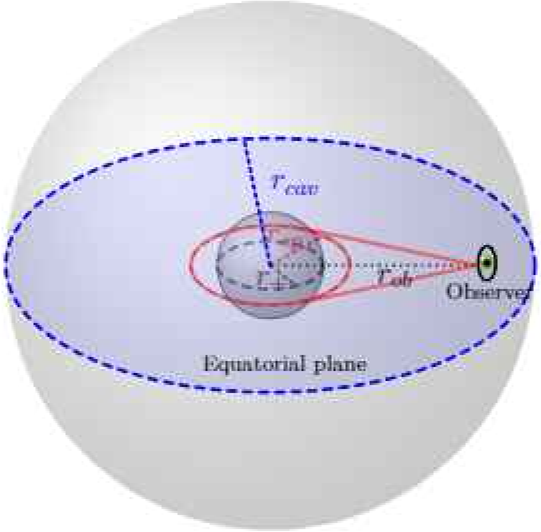

Figure 4.11: *Visualization of a black hole with cavity requirements.*

In this figure, we consider that the light rays will be directed towards the observer located at a radial distance of r_{ob} inside the cavity. This is represented by the red line. Additionally, we illustrate the equatorial plane with the blue circular surface of radius r_{cav}

4.4.1 Shadow behaviors of black holes in cavities

Now we are in the position of discuss the optical aspect the black hole in a cavity via the shadow behaviors. Since we are dealing with four dimensional black holes, we give a graphical representation of the shadows by the help of one-dimensional real closed curves [60–62]. To provide such curves, we exploit the Hamilton-Jacobi equation

$$\frac{\partial S}{\partial \tau} = -\frac{1}{2} g^{\alpha\beta} p_\alpha p_\beta. \tag{4.40}$$

S and λ denote the Jacobi action and the affine variable associated the geodesics, respectively. p^α is the black hole conjugate momentum in a cavity system.

Using the techniques of the previous chapters, the real and positive solution of $r_{sp} f'(r_{sp}) - 2f(r_{sp}) = 0$ reads as

$$r_{sp} = \frac{3(Q^2 + r_+^2) + \sqrt{9Q^4 - 14Q^2 r_+^2 + 9r_+^4}}{4r_+}. \tag{4.41}$$

The photon sphere radius r_{sp} depending on the charge and the horizon radius recovers the results obtained in the previous works. Indeed, when $Q = 0$, we get the unstable photon sphere radius of the ordinary non rotating Schwarzschild black hole studied in many investigations [65, 68, 69]. Using the radial and the angular geodesic relations corresponding to the photo, we find the orbit equation

$$\frac{dr}{d\phi} = \pm \frac{r^2}{L} \sqrt{f(r) \left(\frac{E^2}{f(r)} - \frac{L^2}{r^2} \right)}. \tag{4.42}$$

It has been observed that photon orbit is conditioned by

$$\left. \frac{dr}{d\phi} \right|_{r=r_{sp}} = 0. \tag{4.43}$$

By the help of Eq.(4.43), we get

$$\frac{dr}{d\phi} = \pm r \sqrt{f(r) \left[\frac{r^2 f(r_{sp})}{r_{sp}^2 f(r)} - 1 \right]}. \tag{4.44}$$

Using the fact that the light rays being sent from a static observer placed at r_{ob} in the cavity and transmitted into the past via an angle α_{ob}, one has

$$\cot\alpha_{ob} = \frac{\sqrt{g_{rr}}}{\sqrt{g_{\phi\phi}}}\frac{dr}{d\phi}\bigg|_{r=r_{ob}} = \frac{1}{r\sqrt{f(r)}}\frac{dr}{d\phi}\bigg|_{r=r_{ob}}. \tag{4.45}$$

Using Eq.(4.45), we obtain the observer angle in terms of certain parameters. Indeed, we have

$$\sin^2\alpha_{ob} = \frac{f(r_{ob})r_{sp}^2}{r_{ob}^2 f(r_{sp})}. \tag{4.46}$$

In particular, we obtain the angular radius of the black hole shadows in terms of the circular orbit radius of the considered photon. Indeed, the shadow radius of the black hole being observed by a static observer placed at r_{ob} reads as

$$r_s = r_{ob}\sin\alpha_{ob} = R\sqrt{\frac{f(r_{ob})}{f(R)}}\Bigg|_{R=r_{sp}}. \tag{4.47}$$

The black hole shadow geometries in the cavity geometry could be elaborated by means of the usual celestial coordinates x and y given by

$$\begin{aligned} x &= \lim_{r_0\longrightarrow\infty}\left(-r_0^2\sin\theta_0\frac{d\phi}{dr}\bigg|_{(r_0,\theta_0)}\right), \\ y &= \lim_{r_0\longrightarrow\infty}\left(r_0^2\frac{d\theta}{dr}\bigg|_{(r_0,\theta_0)}\right). \end{aligned} \tag{4.48}$$

In Fig.(4.12), we represent the shadow curves by varying the charge Q. It has been remarked that the shadow geometries are perfect circles since we are considering non rotating solutions. We could anticipate that the charge of the black hole in a cavity can be considered as a primordial parameter controlling the shadow size. It increases with the horizon radius. For a fixed value of r_+, the shadow size is increasing with the charge Q. For $Q = 0$, the shadows of the Schwarzschild black hole is recovered. To examine the shadow radius, we investigate its variation in terms of r_+ by varying the charge. The computation is given in Fig(4.13). It has been confirmed that the radius increases with the electric charge of the black hole. This could show that the charge in the cavity can control the shadow size.

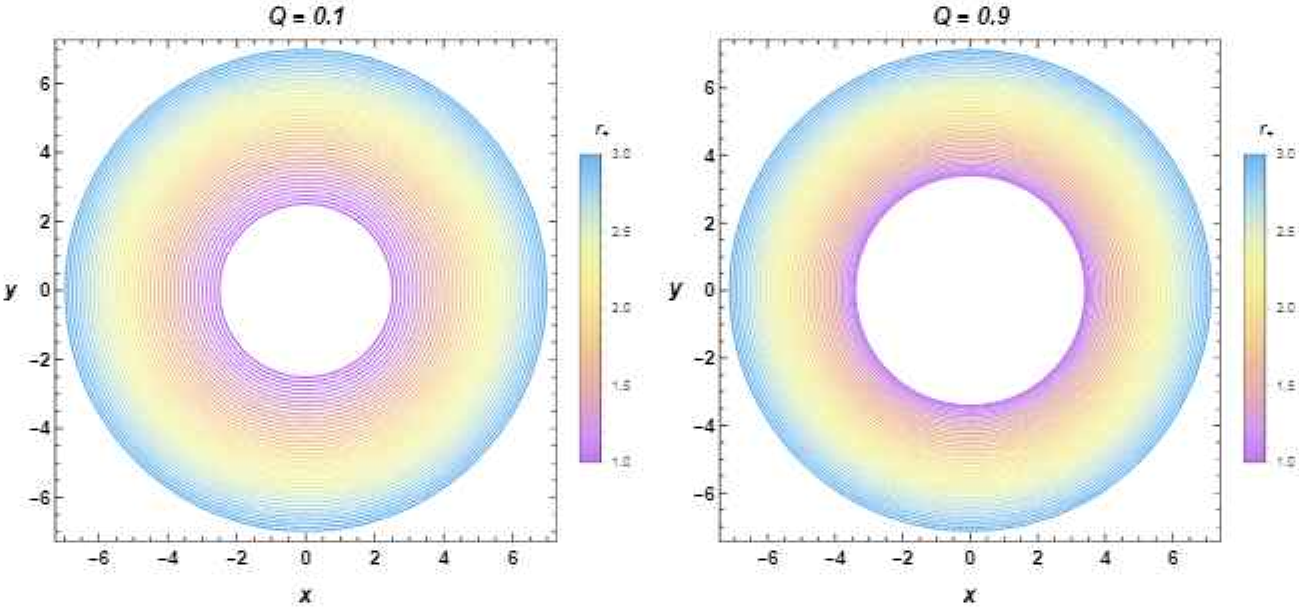

Figure 4.12: *Shadow of the black hole in the cavity in respect of* r_+ *with fixed charge values* Q*, where the observer placed in the equatorial plane with* $r_{ob} = 15$ *and* $r_{cav} = 20$.

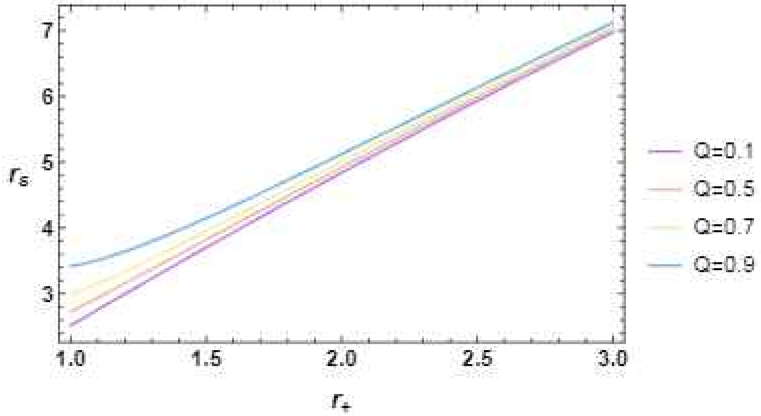

Figure 4.13: *Shadow radius in terms* r_+ *with fixed charge values, where the observer in the equatorial plane and positioned in* $r_{ob} = 15$*, and* $r_{cav} = 20$.

4.4.2 Thermal behaviors of shadow black holes

In this part, we approach the shadow aspect from the cavity temperature variation. As we have seen, the latter is a relevant quantity needed to examine the system stabilities. In the cavity system, it has been shown that the temperature is linked to the cavity radius r_{cav} via the relation

$$T_{cav} = \frac{T_H}{\sqrt{f(r_{cav})}} \tag{4.49}$$

where one has used the Hawking temperature given by

$$T_H = \frac{1}{4\pi}\frac{df(r)}{dr}\bigg|_{r=r_+}. \tag{4.50}$$

The computations of such quantities depend usually on the physical parameters. According to [130, 131, 135], one can find

$$T_{cav} = \frac{r_+^2 - Q^2}{4\pi r_+\sqrt{f(r_{cav})}}. \tag{4.51}$$

We observe that the cavity temperature T_{cav} and the shadow black hole real curves in a cavity depend on the horizon radius. For $r_{cav} > r_+$, the cavity temperature exhibits similarities with the charged AdS black hole ones. For $r_{cav} = r_+$, however, the cavity temperature T_{cav} involves divergence behaviors [135]. Similar to Fig.(4.11), the observer is situated inside the cavity to illustrate the transmitting lights by considering real closed curve shadows. Fixing the charge Q, Fig.(4.14) exposes the shadows by varying the cavity temperature T_{cav}. To do so, we take a situation associated with $r_{cav} = 20$ and $r_{ob} = 15$. The size of the shadow augments when the temperature of the cavity decreases. From this figure, we observe that the electric charge Q of the black hole decreases the shadow radius. Increasing the charge Q, the temperature behaves contrary to the horizon radius as presented in Fig.(4.13). The inverse behaviors can be understood from the relation between T_{cav} and r_+. It has been shown that when T_{cav} increases (decreases), r_+ decreases (increases). The shadow aspect of the AdS black holes is identical to the one of the black hole inside the cavity being an decreasing (increasing) function of the temperature (mass) [136]. These behaviors can be exploited to go further by considering other properties. This could support the obtained results. The corresponding energy emission rate can be approached. Near to the black hole horizon, it has been shown that the quantum fluctuations can create and annihilate pairs of possible particles. In this scenario, the particles involving positive energy values could escape along tunneling from the black hole via the Hawking radiation mechanism. To show that, we examine the associated energy emission rate in the cavity system. To do so, we consider a distant observer the thermodynamical and optical requirements associated with the cavity. Roughly, the high energy absorption cross section can provide information of the

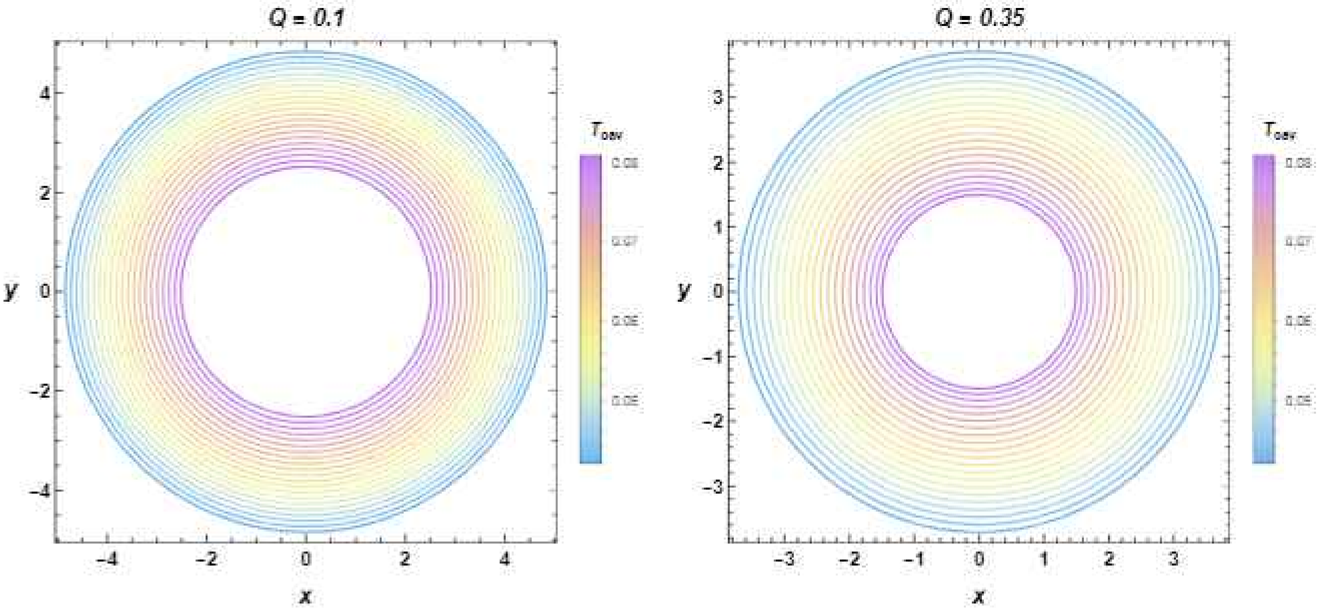

Figure 4.14: *Shadows of the black hole in the cavity system in terms of the the cavity temperature with fixed charges values where observer is placed in the equatorial plane and by considering $r_{ob} = 15$ and $r_{cav} = 20$.*

shadows of the black holes in such physical cavity systems. Indeed, it has been suggested that the absorption cross section of the black hole can oscillate near to an approximated value $\sigma_{lim} = \pi r_s^2$. In this way, the energy emission rate can be expressed as

$$\frac{d^2E(\omega)}{d\omega dt} = \frac{2\pi^3 r_s^2 \omega^3}{e^{\frac{\omega}{T_H}} - 1}. \tag{4.52}$$

Here, ω represents the emission frequency [136]. T_H indicates the corresponding Hawking temperature. Using the link with the cavity temperature, this expression takes the following form

$$\frac{d^2E(\omega)}{d\omega dt} = \frac{2\pi^3 r_s^2 \omega^3}{e^{\frac{\omega}{\sqrt{f(r_{cav})}\cdot T_{cav}}} - 1}. \tag{4.53}$$

The energy emission rate is depicted in Fig.(4.15) in respect of ω by taking different values for T_{cav} and Q. Small values of the cavity temperature show that the charge does effect the optical behaviors. Increasing the temperature, it has been remarked that the energy emission rate maximum increases by decreasing the electric charge Q. For fixed charge values, the maximum of the energy emission increases with T_{cav}, which reveals that T_{cav} and Q bring opposite effects on the studied optical aspect. This is needed to ensure the

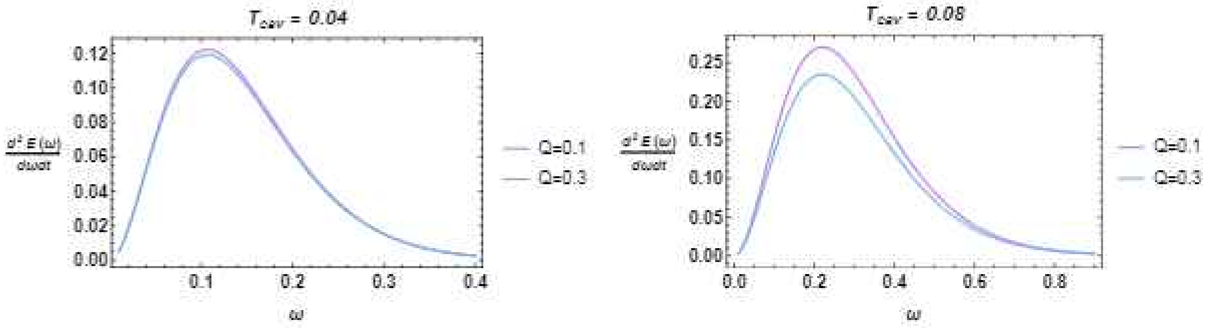

Figure 4.15: *Energy emission rate as a function of* ω *by taking certain values of* T_{cav} *and* Q*, where the observer is placed in the equatorial plane with* $r_{ob} = 15$ *and* $r_{cav} = 20$.

stability behavior. The obtained results confirm the previous findings corresponding to the black holes in cavity systems. To be more economic, we investigate the cavity temperature from the optical aspect. In Fig.(4.16), we illustrate the cavity temperature in respect of the shadow radius for various values of Q.

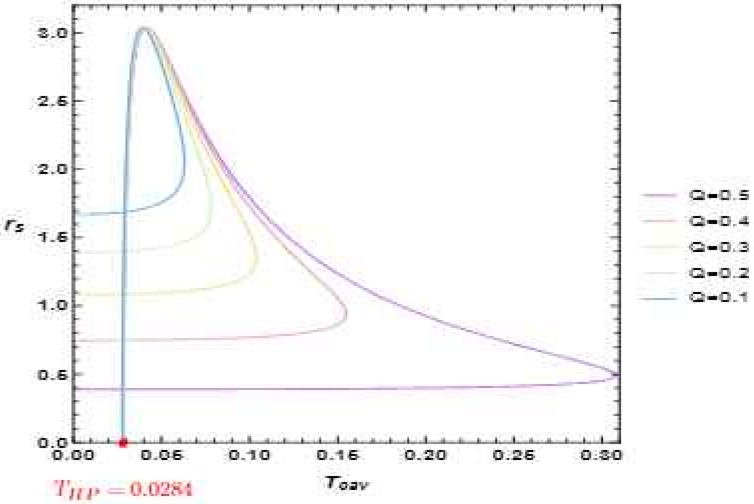

Figure 4.16: *Shadow radius as a function of the cavity temperature by taking the observer in the equatorial plane with* $r_{ob} = 3$ *and* $r_{cav} = 20$.

From this figure, we observe that the radius of the shadows increases by decreasing T_{cav} and decreases by increasing Q being supported by Fig.(4.16). This can be understood from the optical and the thermodynamical constraints given by Eq.(4.39) by taking $r_{ob} = 3$. Moreover, it has been shown that the curves in the $r_s - T_{cav}$ plane are similar to the $G - T$ ones associated with charged and rotating black holes with AdS geometries. It is recalled that G and T are the Gibbs free energy and the temperature, respectively. To understand such resemblance behaviors, we can use the thermodynamical observables. Following [135], it has been shown that the Gibbs free energy of a black hole in cavity systems can be written as

$$G = r_{cav}[7r_+r_{cav} + Q^2 r_+ r_{cav} - 812\sqrt{f(r_{cav})} + 23]. \tag{4.54}$$

The condition $G = 0$ can be exploited to obtain the phase transition temperature T_{HP}. Taking different values of the electric charge Q of the black hole, we find that this temperature being equal to

$$T_{HP} = 0.0284. \tag{4.55}$$

It has been remarked that the curves de type $r_s - T_{cav}$ exhibit the swallowtail configuration of the curve $G - T$. The T_{HP} temperature in the $G - T$ plane can be identified with T_{HP} in the $r_s - T_{cav}$ plane. It could be possible that these results could be exploited to support the interplay between the thermodynamics and the optics of the black holes in cavity systems.